Nonlinear Dynamics in III-V Semiconductor Photonic Crystal Nano-cavities

Maia Brunstein

THÈSE DE DOCTORAT
DE L'UNIVERSITÉ PARIS-SUD XI
École doctoral Ondes et Matière

Pour l'obtention du grade de Docteur de l'Université Paris-Sud XI

Présentée par

Maia Brunstein

Nonlinear Dynamics in III-V Semiconductor Photonic Crystal Nano-cavities

Date prévue de soutenance le 08 juin 2011

devant le jury composé de :

Pierre Viktorovitch	Examinateur
Raffaele Colombelli	Examinateur
Peter Bienstman	Examinateur
Marc Sciamanna	Rapporteur
Massimo Giudici	Rapporteur
Alejandro Giacomotti	Encadrant
Ariel Levenson	Directeur de thèse

A mis padres...

Abstract

Nonlinear optics concerns the modifications of the optical properties of a material induced by the propagation of light. Since its beginnings, fifty years ago, it has already found applications in almost any field of science. In micro and nano-photonics, nonlinear phenomena are at the heart of both fascinating fundamental physics and interesting potential applications: they give a handle to tailor and control the flow of light within a sub-wavelength spatial scale. Indeed, the nonlinear effects can be enhanced in systems allowing tight light confinement and low optical loses. Good candidates for this are the Photonic Crystal (PhC) nanocavities, which have been extensively studied in recent years. Among the great diversity of nonlinear processes in optics, nonlinear dynamical phenomena such as bistability and excitability have recently received considerable attention. While bistability is well known as a building block for all-optical memories, switching and logic gates, excitability has been demonstrated in optics about fifteen years ago: coming from neuroscience, it is the mechanism underlying action potential firing in neurons. In this work, we have studied bistable, self-pulsing and excitable regimes in InP-based PhC nanocavities. In order to achieve efficient light coupling into the nanocavities, we have developed an evanescent coupling technique using tapered optical microfibers. As a result, we have demonstrated for the first time excitability in a PhC nanocavity. In addition, we have accomplished the first step towards nonlinear dynamics in arrays of coupled cavities by demonstrating optical linear coupling between adjacent nanocavitites. This was achieved using far field measurements of photoluminescence. A set of coupled nonlinear resonators opens the door to a rich family of nonlinear dynamical phenomena based on spontaneous symmetry breaking. We have theoretically demonstrated this phenomenon in two evanescently coupled cavities. The first experimental studies on this regime were carried out, which establish a basis for a future demonstration of spontaneous symmetry breaking in arrays of nonlinear coupled PhC nanocavities.

Key words Nonlinear dynamics, InP-based Photonic crystal, Coupled cavities, Excitability, Bistability, Self-pulsing, Symmetry breaking.

Dynamique Non-linéaire en Nano-cavités à Cristal Photonique en Semiconducteur III-V

Résumé

L'optique non linéaire traite les modifications des propriétés optiques d'un matériau induites par la propagation de la lumière. Depuis ses débuts, il y a cinquante ans, des nombreuses applications ont été démontrées dans presque tous les domaines de la science. Dans le domaine de la micro et nano-photonique, les phénomènes non linéaires sont à la fois au cur d'une physique fondamentale fascinante et des applications intéressantes: ils permettent d'adapter et de contrôler le flux de lumière à une échelle spatiale inferieure à la longueur d'onde. En effet, les effets non linéaires peuvent être amplifiés dans des systèmes qui confinent la lumière dans des espaces restreints et avec de faibles pertes optiques. Des bons candidats pour ce confinement sont les nanocavités à cristaux photoniques (CPs), qui ont été largement étudiées ces dernières années. Parmi la grande diversité des processus non linéaires en optique, les phénomènes dynamiques tels que la bistabilité et l'excitabilité font l'objet de nombreuses études. La bistabilité est bien connue pour ces applications potentielles pour les mémoires et les commutateurs optiques et pour les portes logiques. Une réponse excitable typique est celle subjacente dans le déclanchement du potentiel d'action dans les neurones. En optique, l'excitabilité a été observée il y a une quinzaine d'années. Dans ce travail, nous avons étudié les régimes bistables, auto-oscillants et excitables dans des nanocavités semiconductrices III-V à CP. Afin de coupler efficacement la lumière dans les nanocavités, nous avons développé une technique de couplage par onde évanescente en utilisant une microfibre optique étirée. Grâce à cette technique, nous avons démontré pour la première fois l'excitabilité dans une nanocavité à CP. En parallèle, nous avons accompli la première étape vers la dynamique non linéaire dans un réseau de cavités couplées en démontrant le couplage optique linéaire entre nanocavitités adjacentes. Ceci a été réalisé en utilisant de mesures de photoluminescence en champ lointain. Un ensemble de résonateurs non linéaires couplés ouvre la voie à une famille de phénomènes dynamiques non linéaires très riches, basés sur la rupture spontanée de symétrie. Nous avons démontré théoriquement ce phénomène dans deux cavités couplées par onde évanescente. Les premières études expérimentales de ce régime ont été menées, établissant ainsi les bases pour une future démonstration de la rupture spontanée de symétrie dans un réseau de nanocavités non linéaires couplées.

Mots Clés Dynamique non-linéaire, Cristal Photonique, Cavités couplées, Bistabilité, Excitabilité, Oscillations auto-entretenues, Rupture de symétrie.

Remerciement

Tout d'abord je voudrai remercier mes encadrants, Alejandro Giacomotti et Ariel Levenson. Alejandro, merci beaucoup pour ton aide et les discussions au jour le jour et la patience infinie que t'as eu avec moi. Y por todo lo que me enseñaste, que es mucho! Ariel, toujours présent, merci pour tous tes conseils, ton soutien et ton aide pour tout.

Je voudrai remercier Pierre Viktorovitch, Raffaele Colombelli, Peter Bienstman, Marc Sciamanna et Massimo Giudici pour leur participation à mon jury de thèse.

Cette thèse c'est déroulée au Laboratoire de Photonique et des Nanostructures à Marcoussis. Je remercie le directeur du laboratoire Jean-Yves Marzin pour m'avoir accueilli au laboratoire. Je remercie également le comité C'Nano Île-de-France pour le financement de ma bourse de thèse.

Je remercie tout les gens impliqués dans la fabrication des échantillons, car sans eux cette thèse n'aurait pas été possible : A Remy Braive, pour la gravure des échantillons, Luc Le Gratiet, pour la lithographie électronique, Fabrice Raineri et Yacine Halioua, pour le collage. Merci également à Isabelle Sagnes, pas seulement pour la croissance des échantillons, mais aussi pour tout les conseils et discussions scientifiques (et non scientifiques dans les allers-retours en voiture !).

Je remercie tout les gens de l'équipe PHOTONIQ. A Paul Monnier pour les milliers de fois où tu m'a dépanné, à Rama Raj pour les discussions scientifiques, à Tim Karle pour les calculs FDTD et les dépannages informatiques, à Kamel Bencheikh pour les discussions et les manips, aussi à Patricio Grinberg pour les manips, et à Jean-Marie Moison et Nadia Belabas pour tout les prêts d'équipement et les calculs. Merci aussi aux personnes des autres équipes, Alexios Beveratos et Isabelle Robert-Philip pour toutes les discussions et pour m'avoir laissé utiliser leur banc expérimental.

Merci à Laurent Bigot pour toutes les fibres. Je sais que cela t'a pris du temps pour les mettre au point mais tu n'as jamais abandonné. Merci à Virginie Moreau pour les discussions et les manips d'imagerie.

Je remercie les gens du bureau, David Elvira, Bruno Fain et Armand Lebreton toujours très sympas et toujours attentifs au bien être de chacun de nous...nous sommes comme une petite famille! Merci aussi pour les questions de français et les traductions!

No puedo olvidarme de mi familia, mis padres, mis abuelos, mi hermano, que aunque

estén lejos nunca dejaron de apoyarme y de seguirme en el día a día. Gracias por su confianza y por apoyarme en mi decisión de partir. A mis amigos, a los de toda la vida, siempre presentes, Jesi, Mari y Fede. A los de la facu, Caro, Martin, Gri... Gracias a todos por su apoyo a pesar de la distancia.

Y a los de la facu que se volvieron más cercanos en este último tiempo, Vero y Pato, por soportarme en los momentos difíciles de escritura, por todos los favores, por todo. Gracias Celine, Coni y Fer por hacer más fácil y más amena mi estadía en Paris. Y Celine, gracias por enseñarme el Francés!

Pour finir, je voudrai remercier la personne qui est avec moi tous les jours, qui m'a aidé et qui m'aide toujours, Richard. Je n'ai pas de mot pour te remercier de tout ce que t'as fait pour moi et la liste n'aurait pas de fin. Donc je vais juste te dire, pour tout, MERCI.

Contents

Chapter 1

Introduction to nonlinear systems

The aim of this thesis is the study of nonlinear phenomena in III-V photonic crystal semiconductor nanocavities. We shall provide some background for a better understanding of this reading. "What is a nonlinear system?", "Which kind of behavior can it show?", "What is a photonic crystal nanocavity and why using it to study nonlinear effects?". In this chapter we try to answer these questions.

We will give some theoretical bases of nonlinear dynamics in systems described by one or two variables. These concepts will be useful for the interpretation of nonlinear regimes such as bistability, excitability and self-sustained oscillations. The particularities of such regimes in optical systems are discussed in the second part of this chapter, where an introduction to nonlinearities in optics is presented. Then, we will see that nonlinearities can be enhanced in nanocavities and good candidates for this are the photonic crystals. Indeed, we introduce the photonic crystal principles and the different ways to confine light, ending the section with an overview of the methods to couple light into the nanocavities, an important and non trivial problem. Finally, we develop a model for the intracavity energy, the carrier dynamics and temperature variation in a generic cavity filled with III-V semiconductor material. This model allows to capture, in a single set of simple equations, a large family of nonlinear dynamical behaviors at the heart of this thesis.

1.1 Introduction to nonlinear dynamics

"*Nonlinear dynamics concerns the study of systems whose time evolution equations are nonlinear. What is the fuss over nonlinearity? The basic idea is the following: If a parameter that describes a linear system, such as the spring constant* $\boldsymbol{k}$*, is changed, then the frequency and the amplitude of the resulting oscillations will change, but the qualitative nature of the behavior (simple harmonic oscillations in this example) remains the same. In fact, by appropriately rescaling our length and time axes, we can make the behavior for any value of* $\boldsymbol{k}$ *look just like that for some other value of* $\boldsymbol{k}$*. As we shall see, for nonlinear systems, a small change in a parameter can lead to sudden and dramatic changes in both the qualitative and quantitative behavior of the system. For one value, the behavior might be periodic, for another value only slightly different from the first, the behavior might be completely aperiodic*" [1]. We should point out that almost all real systems are nonlinear at least to some extent, from population biology to laser physics passing through planetary systems and turbulence, among others. Hence, the kind of behaviors we will discuss in this chapter can be considered to be somewhat universal in nature.

In this section we give a short introduction to nonlinear dynamics as a general description tool for the dynamics of complex systems. Different qualitative behaviors present in systems with different kinds of nonlinearities, as well as the tools to extract such behaviors from the equations are discussed. This theoretical background on nonlinear dynamics will be implemented in the next sections focusing on particular optical systems.

Nonlinear dynamics is the study of the time evolution of a system that is governed by nonlinear equations of motion. This is usually represented in two ways: by differential equations or iterated maps. Differential equations describe the evolution of the system in continuous time while iterated maps do so in discrete time. In this section we will focus on differential equations, in particular, on ordinary differential equations (ODE).

Nonlinearities in a system can make the equations difficult to solve analytically. Then, geometrical methods, which allow a qualitative description of the system behavior, become a suitable approach. As an example, let us consider a system described by:

$$\begin{aligned} \dot{x_1} &= f_1(x_1, x_2) \\ \dot{x_2} &= f_2(x_1, x_2) \end{aligned} \tag{1.1}$$

with $\dot{x}_{1,2} = dx_{1,2}/dt$. Suppose we know a solution to eq. 1.1, $(x_1(t), x_2(t))$, for a certain initial condition. If we construct an abstract space with cordinates (x_1, x_2), then, the solution corresponds to a point moving along a curve in this space, fig. 1.1.

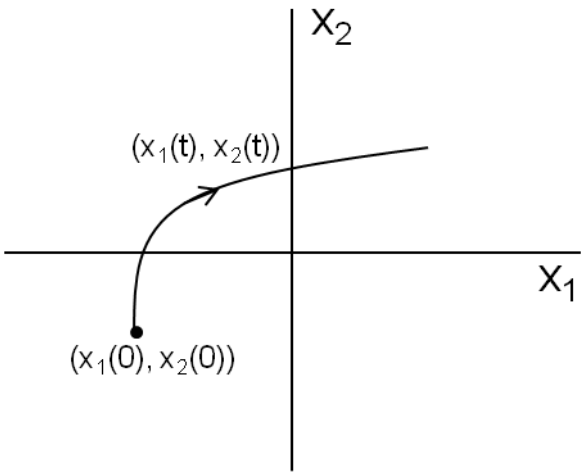

Figure 1.1: *Phase space showing a trajectory for the system described by eq. 1.1.*

The curve in fig. 1.1 is called trajectory and the space where it is plotted is called the phase space [2]. This space is completely full of trajectories since each point in the phase space is a possible initial condition for the system. Generally, the problem is addressed in the opposite way: given the differential equation we find the trajectories in the phase space.

Differential equations are classified according to the number of variables (n) or degrees of freedom needed to characterize the state of the system, which can be seen as the dimension of the phase space. Then, eq. 1.1 is a set of ODEs with a 2D phase space since the system is described by two variables (x_1 and x_2). Table 1.1 summarizes the different behaviors we can find

	n=1	n=2	n≥ 3	n»3
Linear	Exponential growth RC circuit Radioactive decay	linear oscillators RLC circuit 2-body problem	Electrical engineering Civil engineering	Coupled harmonic oscillators Solid-state physics,...
Nonlinear	Fixed points Bifurcations Overdamped systems	Pendulum Anharmonic oscillator Limit cycles Biological oscillators	Strange attractors (Lorentz) Chemical kinetics Fractals,...	Coupled nonlinear oscillator Neuronal network

Table 1.1: *Characteristic behavior found in system described by different numbers of variables (n).*

in linear and nonlinear ODEs of different dimensions [2]. As expected, the higher n is, the more complex the system can be.

1.1.1 Systems described by a single variable

In order to show the advantages of geometrical analysis over an analytical approach in nonlinear systems, let us consider a simple example: a pendulum, where the dynamics of the angular coordinate θ is governed by the equation

$$\ddot{\theta} + \gamma\dot{\theta} + \frac{g}{L}sin(\theta) = 0. \tag{1.2}$$

In the case of an overdamped pendulum ($\gamma >> 1$), eq. 1.2 reads

$$\dot{\theta} = -\alpha sin(\theta) \tag{1.3}$$

with $\alpha = g/L\gamma$. Eq. 1.3 can be solved analytically and yields

$$t = \frac{1}{\alpha} ln|\frac{cosec(\theta_0) + cot(\theta_0)}{cosec(\theta) + cot(\theta)}| \tag{1.4}$$

This result is exact but quite hard to interpret. In contrast, a graphical analysis is much easier as shown in fig. 1.2. Fig. 1.2 shows the phase space of the system in eq. 1.2: θ is a point in phase space and its time evolution is described by the vector field $f(\theta) = \alpha sin\theta$, which dictates the velocity vector ($\dot{\theta}$) at each θ. The arrows in fig. 1.2 indicate the sign of the velocity; arrows to the right means $\dot{\theta} > 0$ and to the left $\dot{\theta} < 0$. For an initial condition of $\theta(t = 0) = a$ the velocity is positive then the system evolves to higher θ; close to $\theta = 0$ the velocity tends to zero and the system converges to $\theta(t \to \infty) = 0$. On the other hand, if $\theta(t = 0) = b$ the velocity is negative and the system also converges to $\theta(t \to \infty) = 0$. Then, we say that $\theta = 0$ is a stable fixed point (θ_f). In general, all points that satisfy $\dot{\theta} = 0$ are called fixed points and we can define two kinds of them: stable (e.g. $\theta_f = 0$), which satisfy $\theta(t \to \infty) = \theta_f$, and unstable (e.g. $\theta_f = \pi$), which satisfy $\theta(t \to -\infty) = \theta_f$.

The stability of the fixed points can be found graphically as in fig. 1.2 or mathematically by linearizing the system around the fixed point. Let us consider the general case $\dot{x} = f(x)$. If x_f is a fixed point of this eq., the linearization around x_f is given by

$$\dot{x} = f(x_f) + \frac{df}{dx}|_{x_f}(x - x_f) + O(x^2) \tag{1.5}$$

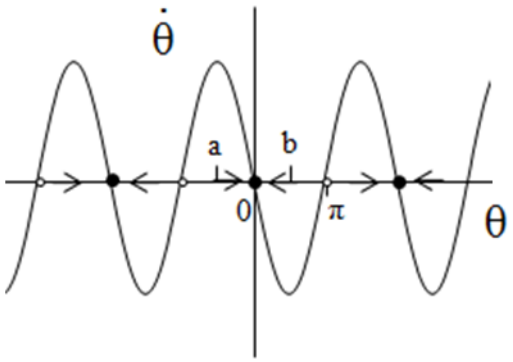

Figure 1.2: *Phase space of the system in eq. 1.3 showing the fixed points and its stability. The arrows show the sign of the velocity.*

$f(x_f) = 0$ because x_f is a fixed point. Neglecting the higher order we have

$$\dot{x} = \frac{df}{dx}|_{x_f}(x - x_f) \tag{1.6}$$

The solution to eq. 1.6 is an exponential function whose behavior is given by the eigenvalue $\lambda = \frac{df}{dx}|_{x_f}$. For $\lambda > 0$ the solution grows exponentially (then x moves away from the fixed point meaning that x_f is unstable) and for $\lambda < 0$ it decays exponentially (then x converge to the fixed point meaning that x_f is stable). If $\lambda = 0$ the higher orders of eq. 1.5 can not be neglected and a nonlinear analysis is needed.

We can thus say that fixed points dominate the dynamics in systems described by a single variable, in the sense that the trajectories can either approach or move away from a fixed point. Indeed, such behavior is all we can find in a 1D phase space. The reason is that trajectories are forced to increase or decrease monotonically or remain constant.

Now, an important question to be addressed is whether trajectories in the phase space can be qualitatively changed by varying some parameters of the system. The variation of a parameter can cause a change in the stability or the apparition/annihilation of a fixed point. This qualitatively changes the dynamics of the system: these changes are called bifurcations.

Types of bifurcations

In the following we present the most common types of bifurcations in 1D phase space.

Saddle-node bifurcation

A saddle-node is a bifurcation in which two fixed points of a dynamical system collide and annihilate each other. The prototypical example, or "normal form" in the jargon of Nonlinear Dynamics, is given by:

$$\dot{x} = \mu - x^2 \tag{1.7}$$

where μ is a parameter that can be positive, negative or zero. For $\mu < 0$ there are no fixed points; for $\mu > 0$ the system has two fixed points ($x_f = \pm\sqrt{\mu}$) and for $\mu = 0$ they coalesce. Furthermore,

for $\mu > 0$ one of the fixed point is stable while the other is unstable. Fig. 1.3 shows the value and stability of fixed points as a function of the parameter, which is called the bifurcation diagram. The bifurcation takes place at $\mu = 0$, since the vector field for $\mu > 0$ and $\mu < 0$, and hence the possible trajectories in phase space, are qualitatively different. **This bifurcation underlies optical bistability, which is one of the subjects of study of this thesis.**

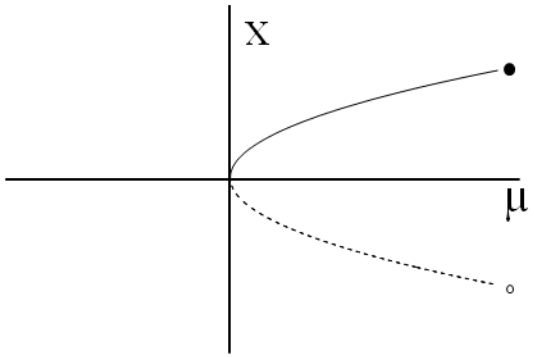

Figure 1.3: *Bifurcation diagram for the saddle-node bifurcation (eq. 1.7).*

Transcritical bifurcation

The transcritical bifurcation occurs when the parameters do not affect the independent term of the equation but the linear term. Then a fixed point exists for all values of a parameter and is never destroyed. However, it can interchange its stability with another fixed point as the parameter is varied. The normal form reads:

$$\dot{x} = \mu x - x^2 \tag{1.8}$$

Eq. 1.8 accounts for a fixed point at $x = \mu$ and another one at $x = 0$ that coalesce for $\mu = 0$. For $\mu < 0$ the fixed point at $x = 0$ is stable and the one at $x = \mu$ unstable. However, when $\mu > 0$ the situation is reversed, fig. 1.4.

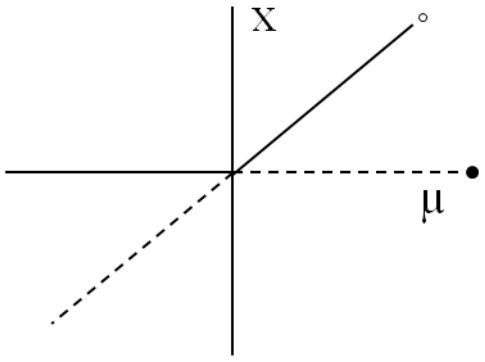

Figure 1.4: *Bifurcation diagram for the transcritical bifurcation (eq. 1.8).*

An example of this type of bifurcation is observed in a solid-state laser [3, 2]. The system consists in a collection of "laser-active" atoms embedded in a solid state matrix, bounded

by partially reflecting mirrors at either end. An external pump is used to excite these atoms. For low injected power, each atom oscillates independently and emits out of phase, then the system behaves as a lamp. However, as the pump is increased (above a certain thershold) the atoms begin to oscillate in phase. Then, laser emission takes place.

A simple model to describe this behavior was developed by Haken [3]. The dynamical variable is the number of photons ($n(t)$) in the laser field and its dynamics is given by

$$\dot{n} = gain - loss = GnN - kn \tag{1.9}$$

The gain term comes from the stimulated emission, in which photons stimulate excited atoms to emit additional photons. This process is proportional to the number of photons (n) and excited atoms ($N(t)$). The parameter G is the gain coefficient and the losses account for photons lost through the mirrors forming the optical cavity. k is a constant rate ($k > 0$) and is the inverse of the photon lifetime inside the resonator.

Once an atom has emitted a photon it returns to its fundamental state; indeed, there is a relation between N and n. If, in the absence of laser effect, the pump produces N_0 excited atoms, then the laser effect decrease this number as:

$$N(t) = N_0 - \alpha n \tag{1.10}$$

with $\alpha > 0$ corresponding to the rate of atoms that return to their fundamental state. Replacing eq. 1.10 in eq. 1.9, this reads

$$\dot{n} = (GN_0 - k)n - (\alpha G)n^2 \tag{1.11}$$

Note the equivalence between eq. 1.11 and eq. 1.8, meaning that the system presents a transcritical bifurcation, although in this case only $n > 0$ has a physical meaning. For $N_0 < k/G$ the system has a stable fixed point at $n_f = 0$ meaning that it behaves as a lamp, fig. 1.5. A bifurcation occurs at $N_0 = k/G$ where $n_f = 0$ changes its stability. Finally, for $N_0 > k/G$ a stable fixed point appears at $n_f = (GN_0 - k)/\alpha G > 0$ that corresponds to a laser effect. $N_0 = k/G$, the value at which the laser action appears, is called the laser threshold in this simple representation.

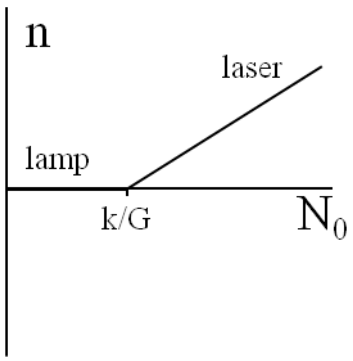

Figure 1.5: *Bifurcation diagram for a solid-state laser described by eq. 1.11.*

Pitchfork bifurcation

The pitchfork bifurcation is common in systems having a symmetry. In this kind of bifurcation a fixed point changes its stability and gives birth to two other fixed points, which "inherit" the original stability of the first. The normal form of this bifurcation is:

$$\dot{x} = \mu x \pm x^3 \tag{1.12}$$

Note that eq. 1.12 remains invariant under $x \to -x$ transformations.

Taking the minus sign in eq. 1.12, for $\mu < 0$ there is one stable fixed point at $x = 0$. For $\mu > 0$ there are three, $x_f = \pm\sqrt{\mu}$ which are stable and $x = 0$ is unstable, fig. 1.6.a. This type of behavior is called supercritical pitchfork.

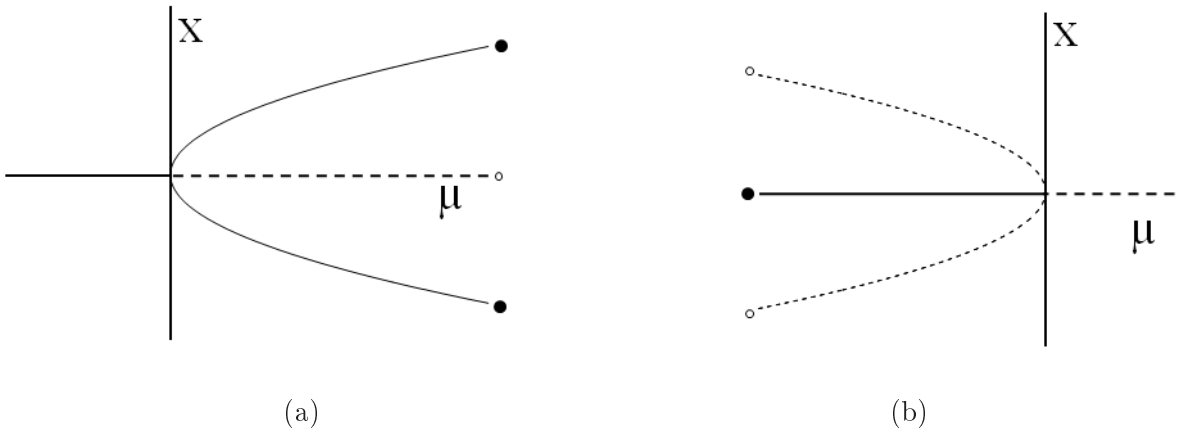

(a) (b)

Figure 1.6: *Bifurcation diagram of a (a) supercritical and (b) subcritical pitchfork bifurcation (eq. 1.12).*

Taking the plus sign in eq. 1.12, we obtain the opposite behavior. For $\mu < 0$ there are three fixed points, $x_f = \pm\sqrt{-\mu}$ which are unstable and $x = 0$ that is stable, fig. 1.6.b. And for $\mu > 0$ there is one unstable fixed point at $x = 0$. This type of behavior is called subcritical pitchfork.

Both super and subcritical pitchfork bifurcations are at the origin of the spontaneous symmetry breaking in coupled (optical) cavity systems. This phenomenon is studied in detail in the last part of this manuscript.

The pitchfork bifurcation is related to systems having a symmetry. However, the symmetry is just a mathematical approximation of real systems. Then, in order to model a real system, we need to add a perturbation (h) to eq. 1.12. This perturbation leads to a disconnection of the pitchfork bifurcation into two branches. An upper piece that consists entirely of stable fixed points and a lower branch that presents stable and unstable fixed points. Changing μ from negative to positive values the lower branch can only be reached by adding a perturbation in the phase space of the system.

1.1.2 Systems described by two variables

We have seen that systems described by a single variable have restricted behaviors, i.e. the variable either evolve monotonically or it remains constant. In higher dimensional phase spaces, a wider range of dynamical behaviors becomes possible.

Classification of fixed points

As we have seen in the previous paragraphs, the nonlinear dynamical approach to analyze the stability of fixed points is based on the local properties (i.e. in the vicinity of the fixed point) of the vector field. For this, the vector field is linearized.

Recall that the general way to model the dynamics of a system in a 2D phase space is:

$$\begin{aligned} \dot{x_1} &= f_1(x_1, x_2) \\ \dot{x_2} &= f_2(x_1, x_2) \end{aligned} \tag{1.13}$$

We can linearize eq. 1.13 around a fixed point ($x_f = (x_{1f}, x_{2f})$) in the following way:

$$\begin{aligned} \dot{x_1} &= \frac{\partial f_1}{\partial x_1}|_{x_f} x_1 + \frac{\partial f_1}{\partial x_2}|_{x_f} x_2 + O(x^2) \\ \dot{x_2} &= \frac{\partial f_2}{\partial x_1}|_{x_f} x_1 + \frac{\partial f_2}{\partial x_2}|_{x_f} x_2 + O(x^2) \end{aligned} \tag{1.14}$$

and simplify this expression by writing $\dot{x} = Ax + O(x^2)$, where $\dot{x}$ and x are vectors and A is the matrix with the partial derivatives (Jacobian matrix). If the matrix A is diagonalizable ($det(A) \neq 0$) we can transform the problem into two uncoupled one-dimensional linear problems, where the time evolution in each transformed coordinate is determined by the associated eigenvalue. Let us now consider the eigenvalues (λ_1 and λ_2) of A:

$$\lambda^2 - \tau\lambda + \Delta = 0 \tag{1.15}$$

with τ the trace of A ($\tau = \lambda_1 + \lambda_2$) and Δ the determinant ($\Delta = \lambda_1 \times \lambda_2$). Then

$$\lambda_{1/2} = \frac{\tau \pm \sqrt{\tau^2 - 4\Delta}}{2} \tag{1.16}$$

In the following we will detail all possible situations. In the general case, the real part of both eigenvalues is different form zero ($Re(\lambda_{1/2}) \neq 0$). We call the fixed point a node if both eigenvalues are real; in particular, stable node if they are both negative and repulsor if they are both positive. If one eigenvalue is positive and the other one negative we call the fixed point a saddle point. Finally, when the eigenvalues are complex (then $\lambda_1 = \lambda_2^*$), we call it a focus. There are two types of focus: spiralling inward if $Re(\lambda_1) < 0$ and spiralling outward if $Re(\lambda_1) > 0$. In the special case in which $Re(\lambda_{1/2}) = 0$ we call the fixed point a center. There are other classifications but it is not our purpose on being exhaustive and we will only consider these ones. Fig. 1.7 shows the features of each bi-dimensional fixed point.

Analyzing the determinant (Δ) and the trace (τ) of the matrix A we can determine the type and the stability of a fixed point. If $\Delta < 0$ the eigenvalues are real and have opposite signs, then the fixed point is a saddle, fig. 1.8. On the other hand, for $\Delta > 0$, the eigenvalues are either real with the same sign (nodes) or complex conjugated (spirals). Nodes satisfy $\tau^2 - 4\Delta > 0$ while spirals $\tau^2 - 4\Delta < 0$. When $\tau < 0$, both eigenvalues have negative real parts, so the fixed point is stable. On the contrary, for $\tau > 0$ it is unstable and for $\tau = 0$ the fixed point is a center. If $\Delta = 0$, then the fixed point is not an isolated point, there is either a whole line of fixed points, or a whole plane if $A = 0$.

Let us now consider an example to clarify these points. The most studied example of this type of system is the pendulum, whose equation of motion is eq. 1.2. In the absence of damping and external driving, the dynamics of the pendulum is given by

$$\ddot{\theta} + \frac{g}{L} sin\theta = 0 \tag{1.17}$$

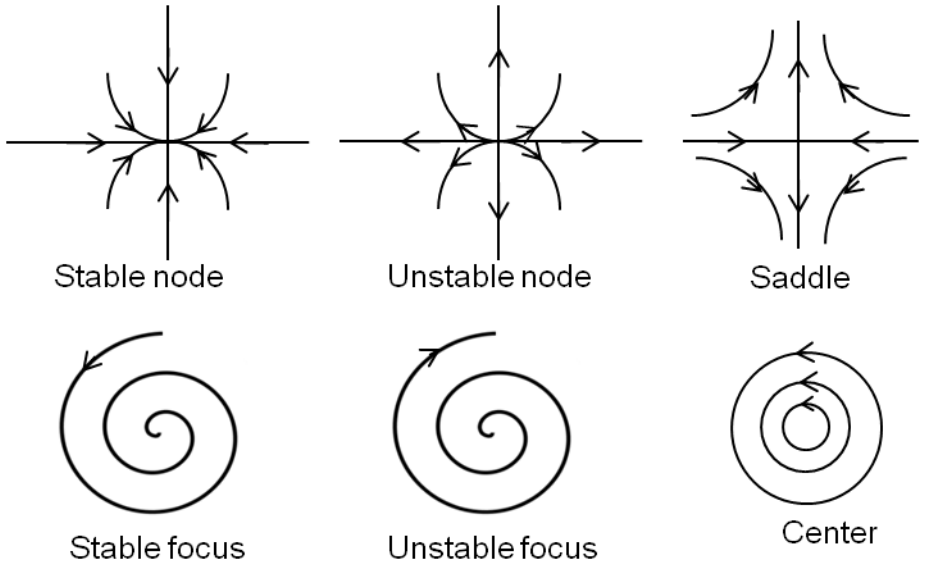

Figure 1.7: *Types of singularities in systems described by two variables.*

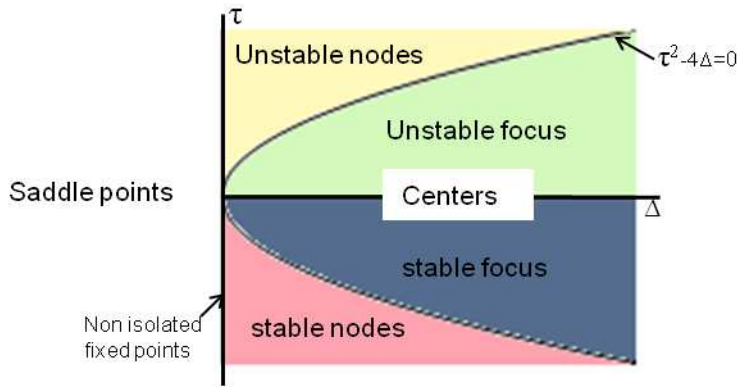

Figure 1.8: *Summary of the types of singularities and their stability as a function of the trace (τ) and the determinant (Δ) of the Jacobian matrix.*

where θ is the angle with the downward vertical, g is the acceleration due to gravity and L the pendulum length. Introducing $\omega = \sqrt{g/L}$ and $\tau = \omega t$, and writing the system in form of two coupled first order ODEs we have

$$\begin{aligned} \dot{\theta} &= \nu \\ \dot{\nu} &= -sin\theta \end{aligned} \tag{1.18}$$

with ν the dimensionless angular velocity. The fixed points are $X_f = (\theta_f, \nu_f) = (k\pi, 0)$ with k an integer. Since the vector field is periodic we will focus on $X_{f,1} = (0,0)$ and $X_{f,2} = (\pi, 0)$. Linearizing eq. 1.18 around $X_{f,1}$ and taking the eigenvalues of A we find that $Re(\lambda_{1/2}) = 0$, then the fixed point is a center. Considering $X_{f,2}$, the eigenvalues of A are real and one is positive and the other negative, then the fixed point is a saddle. Fig. 1.9 shows the phase portrait in the vicinity of the fixed point. Applying energy conservation considerations we can join the trajectories between the fixed points. From fig. 1.9, if the state of the system is near the origin it performs small oscillations around this point whereas if the system starts at $X_{f,2}$ the slightest perturbation causes the pendulum to move away from this point.

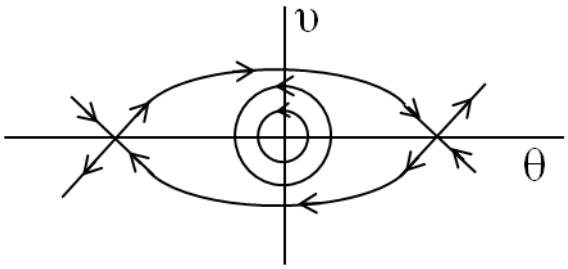

Figure 1.9: *Phase portrait in the vicinity of the fixed points of eq. 1.17 which describes the kinetics of a pendulum.*

Bifurcations in systems described by two variables

The bifurcations we have discussed so far for systems described by a single variable have an analogue in 2D (and in larger dimensions). Actually, nothing different happens by adding further dimensions to the problem. The interesting dynamics is confined to the subspace where the bifurcation takes place. Such subspace is called the "center manifold". However, there are bifurcations that only appear for dimensions higher than one, such as the Hopf bifurcation.

Hopf bifurcation

The Hopf bifurcation occurs when a fixed point looses stability as a pair of complex conjugate eigenvalues crosses the imaginary axis of the complex plane as a parameter is varied.

The normal form of this type of bifurcation is given by the equations:

$$\begin{aligned} \dot{\rho} &= \mu\rho + Re(\alpha)\rho^3 \\ \dot{\varphi} &= \omega + Im(\alpha)\rho^2 \end{aligned} \tag{1.19}$$

where ρ and φ are cylindrical coordinates describing trajectories in phase space.

There are three parameters in eq. 1.19: μ which controls the stability of the fixed point (0,0), ω that gives the frequency of infinitesimal oscillations and $Im(\alpha)$ which controls the dependence of frequency on amplitude for larger amplitude oscillations. Considering $Re(\alpha) = -1$ we observe that, as the parameter μ is varied from negative to positive values, the stable focus at (0,0) changes to an unstable focus and a stable periodic orbit with $\rho = \sqrt{\mu}$ appears, see fig. 1.10. This orbit (fig. 1.10 dashed line) is called a limit cycle. The limit cycle is an isolated closed trajectory, where the term "isolated" means that neighboring trajectories are not closed, rather they are spirals either towards or away from the limit cycle.

Self-sustained oscillations: The van der Pol oscillator

In nonlinear dynamical systems, oscillations usually take place through a Hopf bifurcation. In general, the normal form given by eq. 1.19 is only valid very close to the bifurcation point ($\mu \sim 0$). Beyond, higher order nonlinearities play an important role and the limit cycle becomes

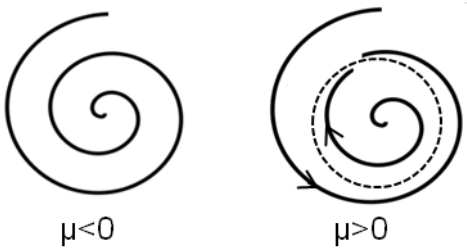

Figure 1.10: *Phase portrait of a Hopf bifurcation (eq. 1.19).*

nonlinear itself. In the following we illustrate this through a typical solution of the so-called van der Pol oscillator. The van der Pol oscillator is given by the equation

$$\ddot{x} + \mu(x^2 - 1)\dot{x} + x = 0 \tag{1.20}$$

where $\mu \geq 0$ is a parameter. This equation looks like a simple harmonic oscillator but with a nonlinear damping term $\mu(x^2 - 1)\dot{x}$. Here we will consider the case of strong coupling $\mu >> 1$. We can rewrite eq. 1.20 as:

$$\begin{aligned} \dot{x} &= \mu[y - F(x)] \\ \dot{y} &= -\frac{1}{\mu}x \end{aligned} \tag{1.21}$$

with

$$F(x) = \frac{1}{3}x^3 - x, \quad y = \frac{\dot{x} + \mu F(x)}{\mu} \tag{1.22}$$

It is useful to analyze the nullclines of the system, which are manifolds such that $\dot{x} = 0$ or $\dot{y} = 0$. The first nullcline, $\dot{x} = 0$, is the $y = F(x)$ curve, and the second one, $\dot{y} = 0$, is the y axis of the phase space. If the initial condition (point A in fig. 1.11.a) is not too close to the cubic nullcline, the condition $\mu >> 1$ leads to $|\dot{x}| >> |\dot{y}|$; besides, in the first stage (from A to B), $|\dot{x}| > 0$. Indeed, the trajectory is practically horizontal and it approaches the nullcline. Close to the nullcline (point B in fig. 1.11.a), $y - F(x) << 1$ then $|\dot{x}| \sim |\dot{y}|$ and the trajectory crosses the nullcline vertically and eventually moves along it slowly until it reaches the kink at point C, and it jumps sideways again with a fast and almost horizontal trajectory. This is followed by a slow movement along the nullcline until the next jump point (point D in fig. 1.11.a) is reached. This movement continues periodically: we approach a limit cycle.

This analysis shows that the limit cycle has two different time scales, governed by μ and $1/\mu$. These time scales are revealed in the time trace of x, fig. 1.11.b, obtained through numerical integration of eq. 1.21 with $\mu = 20$ and $(x_0, y_0) = (1, 1)$. From fig. 1.11.b we observe a periodic motion: we say that the system exhibits self-sustained oscillations, meaning that it oscillates even in the absence of periodic forcing. Several systems in nature present this kind of behavior: the heart beating, the periodic firing of a pacemaker neuron, daily rhythms in human body temperature and hormone secretion, among others. **We will study these oscillations in an optical system: an optical cavity.**

Excitability: The forced van der Pol oscillator

Suppose the van der Pol oscillator is biased by a constant force, then eq. 1.20 takes the form

$$\ddot{x} + \mu(x^2 - 1)\dot{x} + x = a \tag{1.23}$$

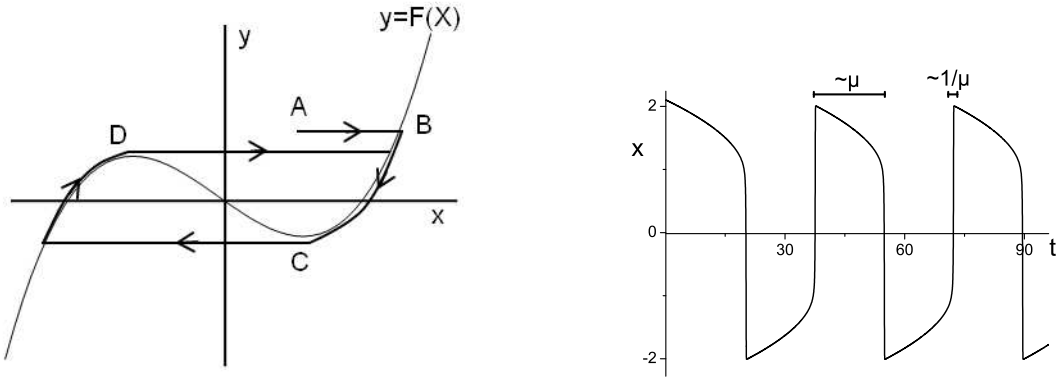

(a) (b)

Figure 1.11: *(a) Nullclines of eq. 1.21 in the phase space. The line with the arrows represents an example of a possible trajectory. (b) Time trace for* $\mu = 20$ *and* $(x_0, y_0) = (1, 1)$.

Following the same procedure as before, eq. 1.23 can be written as

$$\begin{aligned} \dot{x} &= \mu[y - F(x)] \\ \dot{y} &= \frac{-x + a}{\mu} \end{aligned} \tag{1.24}$$

with $F(x)$ and y as in eq. 1.22. The fixed points are given by the intersection of nullclines (see fig. 1.12) that yields $x_f = (a, F(a))$. Linearizing the system around the fixed point, we obtain the determinant and the trace of the Jacobian matrix, $\Delta = 1$ and $\tau = -\mu(a^2 - 1)$ respectively. From fig. 1.8 we have that the fixed point is unstable if $-1 < a < 1$ and stable otherwise. Furthermore, $\tau^2 - 4\delta = \mu^2(a^2 - 1)^2 - 4$ will be positive for sufficiently large values of $|a|$ ($|a| > a_c$), implying that the fixed point will be a node. For $\mu >> 1$ and $-1 < a < 1$ we have a case analogue the the one described in the previous paragraphs. However, for $|a| > a_c$ the fixed point is stable, with no limit cycles, as the trajectory approaches the cubic nullcline, it moves slowly along it and towards the fixed point, fig. 1.12. If a slight perturbation kicks the state of the system away from the fixed point, then, the system jumps to the negative branch of the cubic function, moves along the nullcline, jumps again when it reaches the maximum and finally moves slowly towards the fixed point. This type of behavior is called excitability. An excitable system is characterized by two properties: it has a unique, globally attracting rest state, and a large enough stimulus can send the system on a long excursion through phase space before it returns to the quiescent state.

Types of excitability

In the previous paragraph we have introduced the concept of excitable system, which is of central importance to this thesis. Here we will discuss excitability in more detail.

Excitability is a regime well known in biology since it underlies spiking behavior in many biological systems such as neurons and cardiac tissue. Excitability can also be found in chemistry, namely in the Belousov-Zhabotinsky reaction, and in physics from the driven mechanical pendulum to lasers and amplifiers [4]. Excitability is usually defined in a phenomenological way

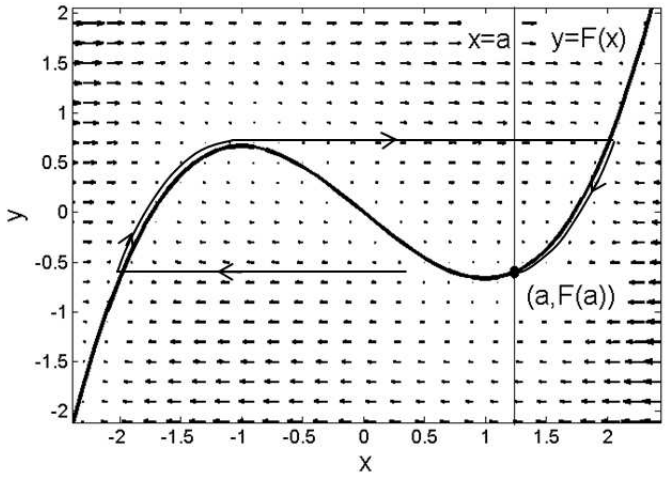

Figure 1.12: *Nullclines of eq. 1.24 in the phase space. The line with the arrows represent an example of a possible excitable trajectory. The small arrows show the velocity vector direction at each point of the phase space.*

[5]: a small perturbation from the single stable fixed point can result in a large and long lasting excursion away from the fixed point before the system comes back to equilibrium. Furthermore, as an external parameter is changed, the global attractor in the form of the stationary point bifurcates into a stable periodic orbit, and the excitability behavior undergoes oscillatory dynamics, as discussed in the previous paragraphs. There are three qualitatively different types of excitability, called type I, II and III, which are distinguished by the distinct bifurcations leading to the oscillatory dynamics [6]. This is manifested in different properties of the frequency of the emergent oscillations [7].

Type I excitability arises from an attractor (stable node) close to a saddle-node in an attractive invariant circle, as sketched in fig. 1.13.a (left), as in the Terman−Wang model of neuronal excitability [8]. The fact that the attractor and the saddle point are close together means that the system is close to a saddle-node bifurcation on a limit cycle. A perturbation that makes the system cross the saddle point leads to a large amplitude excursion around the invariant circle. This corresponds to a single pulse in the time trace as depicted in fig 1.13.a (right). Type II excitability is due to an S-shape slow nullcline in slow-fast systems (as the biased van der Pol oscillator discussed previously), as sketched in fig. 1.13.b (left). This type of excitability is found in the FitzHugh-Nagumo model of neuron spiking [4, 9]. A sufficiently large perturbation brings the system from the attractor (black dot) to the white dot, then the system makes a quick jump to the right branch of the nullcline, follows it before it jumps back to the left branch of the nullcline reaching then the steady state. This leads to square-shaped pulses as shown in fig. 1.13.b (right). Note that in both types of excitability the amplitude of the excursion is independent of the perturbation, because the invariant circle and the slow nullcline determine the maximum of the pulse. The phase portrait of a type III excitability is depicted in fig 1.13.c (left). The off solution (y=0) is an attractor (black dot) but a perturbation can push the system above the stable nullcline to the white dot. From there the system produces a single pulse and then relaxes slowly following the slow nullcline to the attractor. The pulse of this type of excitability is shorter than in fig. 1.13.a-b (right) [10]. This type of excitability was observed in laser with saturable absorber [10]. **In this work we will focus on type II excitability as will see in chapter 6.**

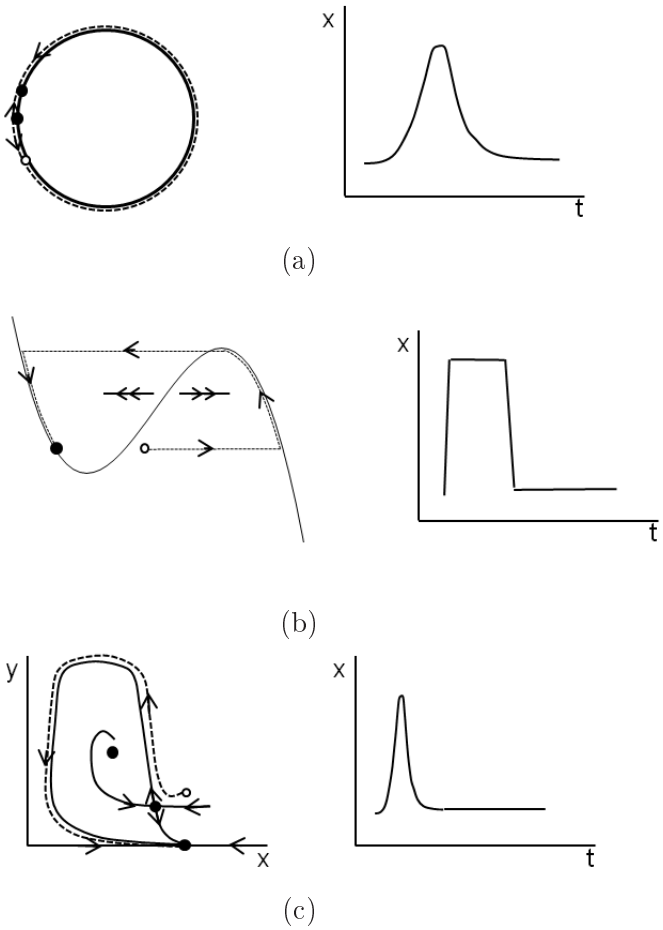

Figure 1.13: *Phase portrait (left) and time traces (right) for the type I (a), type II (b) and type III (c) excitability. The black dot denotes the fixed points and the white dot is the initial condition. The plots are inspired by [10]*

Once the system has reacted to an external perturbation with an excitable pulse, a second response can not be initiated immediately. Instead, a finite time, known as the refractory period, must elapse before another excitable pulse is generated from a second stimulus. This refractory period has been extensively studied in biology, e.g. in neuronal systems, where it has been shown to lye in the ms range [11]. In optics, the refractory times can be much shorter, typically from sub-ns to millisecond timescale. Such fast dynamics makes time-resolved measurements quite challenging in optics. In chapter 6 we will see how this quantity can be measured in an optical (photonic crystal) excitable nanocavity.

In this section we have described some fundamentals on nonlinear dynamical systems. The methods used to solve nonlinear equations and the different behaviors that can be obtained were discussed. In the next section we will apply these tools to a particular kind of systems: the nonlinear optical systems.

1.2 Nonlinear optics in III-V semiconductor

Nonlinear optics is the branch of optics that accounts for phenomena in which the properties of light propagation in a medium depend on light intensity. This can be described by a nonlinear

dependency of the dielectric polarization of the material on the electric field. Nonlinear optical phenomena are typically observed for high light intensities.

In most cases, the physical origin of the nonlinear polarization relies on the microscopic characteristics of the material in which light is propagating. Due to the great diversity of microscopic properties of matter, many different nonlinear processes can be expected.

In this section we will focus on a particular class of nonlinear properties: third order nonlinearity. Specifically, we will consider third order nonlinear effects due to charge carriers in active III-V semiconductor nanostructures induced by one photon absorption process. Such carrier density leads to both absorption and refractive index change.

This section is organized as follows: we begin with an introduction to nonlinear optics and active materials. We continue with the description of particular nonlinear regimes: optical bistability, excitability and self-sustained oscillations. Finally, we will introduce an important regime in coupled nonlinear cavities: the spontaneous symmetry breaking.

1.2.1 Principles of nonlinear optics

In classical optics, the linear response of a medium to an oscillating electric field of amplitude $E(\omega)$ is characterized by the macroscopic polarization (P):

$$P(\omega) = \epsilon_0 \chi(\omega) E(\omega) \tag{1.25}$$

where $\chi(\omega)$, the linear electric susceptibility, is a scalar or tensor function which describes the macroscopic optical properties of the material. This can be written as $\chi = \epsilon - 1$, with ϵ the relative dielectric permittivity. We can also adopt a microscopic point of view considering the material as an ensemble of charged particles: electrons and ions. When an electromagnetic field is applied to this system the positive and negative charges move in opposite directions following the field. In a metal, these charges are free carriers subjected to an oscillating driving force. In dielectric materials, however, electric charges do not flow through the material, but only slightly shift from their average equilibrium positions inducing a dielectric polarization. Under the action of an electric field with frequency ω the charges will react as dipoles oscillating at a frequency ω. As the electron mass is much smaller than the ion mass we can consider that only the electrons oscillate. A good classical representation of this is the oscillation of a mass attached to a spring.

Within this framework, the nonlinear regime can be thought of as a situation where the spring is brought to the stretching limit (high injected intensities). Then the electron displacement (and hence the polarization) is no longer linear with the injected field. Therefore, a model of an anharmonic oscillator needs to be implemented. The material polarization (P) can thus be expanded in a Taylor series of the incident field E as:

$$P = \epsilon_0 [\chi^{(1)} E + \chi^{(2)} E^2 + \chi^{(3)} E^3 + ...] \tag{1.26}$$

In this expression $\chi^{(1)}$ corresponds to the linear susceptibility while $\chi^{(2)}$, $\chi^{(3)}$, ..., to the nonlinear susceptibilities. The real part of the susceptibility is related to the refractive index of the material and the imaginary part to the optical absorption.

The processes governed by the second term in eq. 1.26 are called second order nonlinear processes. This type of nonlinearity gives rise to the mixing of frequencies. Among the most

important second order nonlinear phenomena we find the second harmonic generation, sum frequency generation, optical parametric amplification, spontaneous parametric down conversion [12]. All these are examples of what is known as parametric processes. Even though these processes are not strictly associated to second order non linearities, they have been shown to be largely predominant with second order nonlinearities rather than higher orders. Most importantly, in parametric processes the energy of the incident wave is not transferred to the material through absorption.

The nonlinear effects associated to the third term in eq. 1.26 are called third order nonlinear processes. This type of nonlinearity gives rise to several interesting phenomena, among which, we can distinguish those for which the energy of the incident field, in resonance with material spectral transitions, leads to energy transfer between light and matter. Then, the energy of the field is stored in the material for a period that depends on the excitation dynamics and the carrier relaxation time. This type of non linearities induces a change in the absorption coefficient and refractive index with the incident field. In this work we will focus on this type of nonlinearities. Note that semiconductor materials are meanly characterized by the existence of a band gap for the electronic transitions, i.e. a region where there is not available electronic state. This region separates the last electronic occupied band, called valence band, from the first non occupied band, called conduction band. Compare to insulator materials, this band gap is sufficiently small in energy so that an optical external field can easily promote an electron from the valence to the conduction band. As a consequence, intrinsic or absorptive nonlinear responses can be achieved, simply by setting the excitation energy within or higher the band gap energy. This is schematic in fig. 1.14. Note that this electronic dispersion diagram corresponds to a direct semiconductor, which is the case of III-V considered here, and it is oversimplify. Namely, only two bands are represented and the dispersion relation is parabolic. Nevertheless, this description is sufficient to all the situation experimentally encountered in this work.

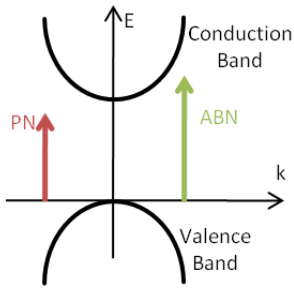

Figure 1.14: *Scheme of the energy of the excitation in a parametric process (PN) and in a absorptive-based process (ABN). For the first the energy of the incident field is not absorbed by the material while in the second one an energy transfer takes place.*

In the following paragraphs we turn our attention to the properties of absorption and dispersion in semiconductors. We will see that it is possible to control these parameters by changing the carrier density through optical excitation.

1.2.2 Absorption and nonlinear refractive index in III-V semiconductors

When a semiconductor is excited with an incident field, as long as the incoming energy is higher than the semiconductor gap (Eg), electrons are promoted from the valence to the conduction bands leaving an equal number of "holes" in the former. As a consequence, the absorption and

refractive index are modified, within the electron-hole recombination lifetime. In steady state, since the carrier density is a function of the electromagnetic field intensity, we can write, at first order in $|E|^2$,

$$n = n_0 + n_2|E^2| \tag{1.27}$$

with n_0 the linear refractive index and n_2 the nonlinear refractive index, which is proportional to $\chi^{(3)}$ and gives the rate at which the refractive index increases or decreases with increasing optical intensity [12]. Different types of nonlinearities may induce a nonlinear refractive index change effects in semiconductors. Two well known effects can be distinguished: the Drude effect, when a photogenerated electron-hole plasma modifies the refractive index and this change is proportional to the carrier density [13]; and band filling effect, which produces a decrease of the absorption through photoexcited carrier generation. If two pulses are sent to the sample, a strong (pump) pulse followed by a weak (probe) pulse, the occupation of the conduction and valence bands generated by a pump pulse induces a decrease in the absorption probability of the probe [14]. This change in the absorption induces a refractive index modification.

The detailed calculation of the refractive index and the absorption in a general case is quite cumbersome. In order to simplify the problem, a first assumption is to consider a direct gap semiconductor described by parabolic bands. In this case the susceptibility can be calculated using descriptive tools such as the joint density of states ($\rho_j(E)$), i.e. the density of two level systems optically coupled by a photon of energy E. In this model, the semiconductor is represented as a continuous sum of two-level systems, of homogeneous broadening $\gamma = (T_2)^{-1}$, weighted by the occupation function of electrons (f_e) and holes (f_h). Then we can express the susceptibility ($\chi(\omega) = \chi_r(\omega) + i\chi_i(\omega)$) as:

$$\chi_r(\omega) = A\int_0^\infty dw'\rho_j(\hbar\omega')[1 - f_e(\omega') - f_h(w')]\frac{(\omega - \omega')}{(\omega - \omega')^2 + \gamma^2} \tag{1.28}$$

$$\chi_i(\omega) = A\int_0^\infty dw'\rho_j(\hbar\omega')[1 - f_e(\omega') - f_h(w')]\frac{\gamma}{(\omega - \omega')^2 + \gamma^2} \tag{1.29}$$

with A a proportionality constant characteristic of the material. The occupation functions introduce the nonlinear mechanisms through the dependency of carrier density with the field. χ_r describes the refractive index which can be translated into a third order term in the susceptibility, $\chi^{(3)}_{eff}$. The induced polarization can thus be expressed with a cubic dependence of the electric field and the total refractive index with a linear dependence of the intensity. On the other hand, the imaginary part of the susceptibility (χ_i) describes the absorption.

In situations of quasi-equilibrium, $f_e(\omega)$ and $f_h(\omega)$ can be described by the Fermi-Dirac distribution:

$$f(\omega) = (\frac{e^{\hbar\omega - E_F}}{k_B T_F} + 1)^{-1} \tag{1.30}$$

with T_F the lattice temperature, E_F the Fermi level and K_B the Boltzmann constant. In most cases $h/T_2 << k_B T_F$ (i.e. $\gamma \to 0$), then, the Lorentzian distribution of eqs. 1.28 and 1.29 can be considered as a Dirac distribution, leading to an expression for the absorption of the form:

$$\alpha(\omega) = \alpha_0(\omega)[1 - f_e(\omega) - f_h(\omega)] \tag{1.31}$$

with α_0 the absorption coefficient of the material in absence of excitation. Note that α/α_0 gives direct access to the population factors f_e and f_h.

The information about the nonlinear refractive index in energy windows close to the spectral gap of a semiconductor is of major interest for devices such as nonlinear Fabry-Perot resonators. The direct measurement of this magnitude requires interferometric methods of high accuracy. However, the experimental measurement of the absorption spectra is easier and the refractive index can be deduced from it by means of the Kramers-Kronig transformation:

$$\Delta n(\omega) = \frac{c}{\pi} \int_0^\infty d\omega' \frac{\Delta\alpha(\omega')}{\omega'^2 - \omega^2} \tag{1.32}$$

Application of bulk semiconductors to nonlinear optical devices is limited since their nonlinear properties are restricted within fixed energy intervals, mainly determined by the band gap energy. Therefore, materials whose absorption properties can be adjusted to a certain spectral range, depending on the application, are highly desirable. In the following we describe this kind of materials.

Absorption and refractive index change in active materials

Active nanostructured materials, such as quantum dots, wires and wells, allow the modification of the spectral range where the absorption and refractive index change takes place. We will see that specific properties as the energy gap can be tailored by changing the size of these structures.

The quantum wells (QW) are semiconductors were the charge carriers are confined within a plane (2D) in the space. In quantum wires (QR) confinement takes place in a line and in QDs the carriers are confined in the three dimensions (0D), fig. 1.15. This confinement is achieved by introducing an energy barrier for the electrons.

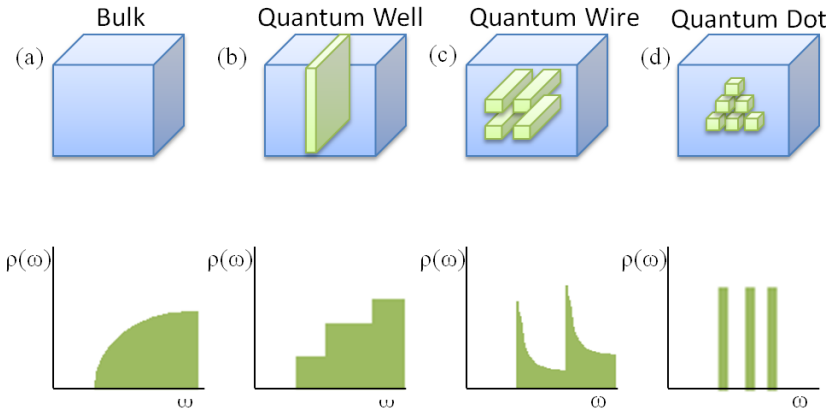

Figure 1.15: *Active region (top) and density of states (bottom) for confinement in no dimensions (i.e., bulk material) (a), in one dimension (i.e., quantum well) (b), in two dimensions (i.e., quantum wire) (c) and in three dimensions (i.e., quantum dot) (d).*

For example, the quantum dots can be formed by introducing a nanometric "box", i.e. a well in the three dimensions, of a semiconductor with low bandgap in a semiconductor with higher bandgap. For well sizes of the order or smaller than the electronic De Broglie wavelength, i. e. ~ 120 nm in III-V semiconductors, the strong spatial confinement of the carrier inside the dots yields to a discretization of the energy levels. Moreover, this discretization depends on the

QD size. Provided that the difference in the energy bandgaps of the QD and the bulk is higher than the thermal energy, the carrier are trapped in the dots. For these reasons the QDs are also called artificial atoms.

The spatial confinement and the discretization of the energy levels in the QDs make them interesting as an active material in semiconductor lasers. They can give rise to a decrease of the laser threshold, low sensitivity to temperature, an increase of the gain and a decrease of the frequency chirp. Some of these structures are nowadays extensively used in technology. They are used in quantum information processing, as single-electron transistors, in diode lasers, amplifiers and biological sensors, among others.

In this work we are interested in InAs/InP III-V semiconductors QDs. The advantages of these nanostructures is their emission at the telecommunication wavelengths (1-2 μm). We will use this type of QDs in photoluminescence measurements, since its broad emission ($\sim$ 150 nm) and low density ($\sim 10^{10} cm^{-3}$) allow to easily detect the photonic crystal cavity modes, as we will see in chapter 3. Let us now consider QW structures that are at the center of our nonlinear studies.

Quantum Wells

The quantum wells can be formed by introducing a very thin ($<$ 120 nm) 2D layer of a semiconductor with low bandgap surrounded by a semiconductor with higher bandgap (fig. 1.15.b). The boundary conditions in this layer determine the wave functions of carriers, hence, the potential energies. Because these wave functions depend on the quantum well dimensions, the energies allowed in the well are tunable by adjusting the well dimension, which yields a change of the bandgap energy. The effects of quantum confinement (discrete energy spectrum) take place when the quantum well thickness becomes comparable to the De Broglie wavelength of carriers (generally electrons and holes), leading to discrete energy levels, fig. 1.16. The lateral confinement in the QW produces a restriction of the carrier movement in this direction, giving rise to the discrete energy spectrum. However, carriers are free to move in the parallel direction leading to a dense distribution of states in the parallel plane.

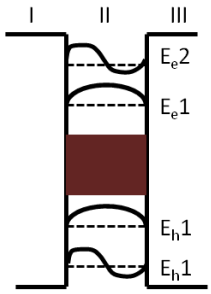

Figure 1.16: *Discrete energy levels in a QW semiconductor. I and III correspond to the high bandgap semiconductor (the barrier) and II to the low one (the well). The quantum confined carrier energies are E_e1 or E_e2 for electrons and E_h1, E_h2 for holes. The wave functions of carriers at these allowed energies are standing waves.*

QWs structures are extensively used in technology. One of the most common applications of these systems is laser diodes, including red lasers for DVDs and laser pointers, infra-red lasers

in fiber optical transmitters, blue lasers, among others.

Let us now study the absorption spectra and the refractive index change in this kind of structures. Experimental measurements of α and Δn (through Kramers-Kronig tranformation) as a function of energy for different injected intensities in multiple GaAs quantum wells were carried out by Koch et al. [15], fig. 1.17. The exponential tail below the band gap (dashed line in fig. 1.17.a) in the absorption vs energy plot is called the Urbach tail. This tail can be attributed to transitions between band tails below the band edges. Such tails can result from disorder of the perfect crystal, e.g. from defects or doping and the fluctuation of electronic energy bands due to lattice vibrations [16].

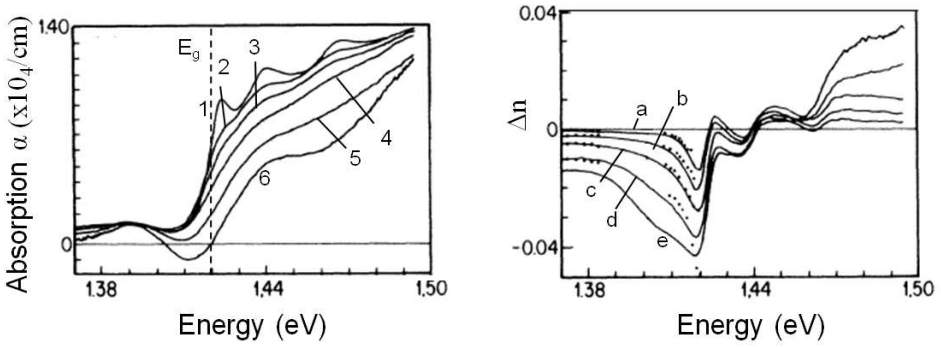

(a) (b)

Figure 1.17: *Nonlinear absorption spectra (a) and refractive index change (b) of multiple quantum wells for (from 1 to 6 and a to e, respectively) increasing excitation powers. The refractive index change was deduced from the measurements of the absorption by Kramers-Kronig transformation. Images from [15]*

Note the decrease of the absorption with the incident power regardless the energy. This can be seen in eq. 1.31 when $f_e + f_h \leq 1$ and it is called the absorption saturation. Note also that, for the higher injected power (fig. 1.17.a.6), the absorption is negative for a range of energies, i.e. optical gain. This is obtained when $f_e + f_h \geq 1$ in eq. 1.31. We observe in fig. 1.17.b that the variation of the refractive index can be positive or negative depending on the wavelength. Furthermore, its value is strongly dependent on the excitation energy.

In this work we will take advantage of this change in the refractive index to spectrally shift the modes of photonic crystal cavities.

1.2.3 Nonlinear dynamical processes in optical resonators

The optical properties of nonlinear materials can be varied by changing the intensity of the incident light. Therefore, if light is confined in small volumes inside the material, field enhancement inside this volume is achieved, thus the material properties can be changed with lower excitation powers. This light confinement can be achieved in optical resonators or cavities. As an example, micro and nano-photonic devices give a handle to tailor and control the flow of light within a sub-wavelength spatial scale. Indeed, the nonlinear effects can be enhanced in systems allowing tight light confinement and low optical losses. Among all the nonlinear phenomena that can be observed in optical resonators, optical bistability has been extensively investigated in the last decades, mostly due to its potential for optical memories and switching. In optical

bistability the system presents two possibles output signals for an equal injection. By definition, bistability only deals with static regimes and one dynamical variable, but it is often the precursor of exciting dynamical regimes, which can be found in several natural systems including neurons, cardiac tissues and chemical reactions. Dynamical nonliearities allow rich and complex non-stationary phenomena such as excitability and self-sustained oscillations. In self-sustained oscillation regime the nonlinear system reacts emitting a periodical signal while excited with a CW beam. In the excitable regime the system develops all-or-non calibrated optical responses to a small perturbation.

In the following we give some insights about these three particular nonlinear behaviors: bistability, excitability and self-pulsing regime in optical cavities.

Optical bistability

Optical bistability is the simplest and more robust paradigm for the realization of all-optical transistors and memories. Two ingredients are needed in order to obtain bistable operation in an optical system: a resonance capable of localizing the light intensity in the spectral domain, and a nonlinear property that changes the spectral response as a function of the light intensity. Under certain conditions for the injection of a nearly resonant beam, two stable states for the transmission/reflection through the device can coexist, in the sense that either one output level or another can take place for the same input parameters. This type of phenomenon has been theoretically demonstrated for the first time in optics by Szoke [17] and experimentally by [18]. The optical bistability has been studied in several works due to its possible application to information processing. Although, the phenomenon is not inherent to optical system, actually it is a common behavior in electronic systems.

Optical bistability typically occurs in nonlinear optical resonators. Depending on the physics behind the resonator different mathematical representations can be adopted to describe the system, e.g. the equations that govern the optical field in a cavity via the Maxwell Bloch equations. In order to theoretically describe the optical bistability in an optical resonator, let us consider the following system: a cavity filled with a nonlinear material of index $n = n_0 + n_2 I$ optically injected though a waveguide, fig. 1.18.

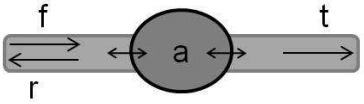

Figure 1.18: *Sketch of a cavity coupled to a waveguide. The field is injected through the left port (f). The cavity is filled with a third order nonlinear medium with* $n = n_0 + n_2 I$.

The system in fig. 1.18 can be described by a Coupled Mode Theory (CMT) formalism [19, 20] which will be detailed in section 2.2.

In this framework, the field amplitude inside the cavity (a) is described by [20]:

$$\frac{da}{dt} = [j(\omega_0 - \delta\omega) - \frac{1}{\tau}]a + df \tag{1.33}$$

where we have considered an injection only through the left port. ω_0 is the cavity resonance frequency, τ the photon lifetime, f the injected field and $d = jexp(j\phi/2)/\sqrt{\tau}$, where the phase ϕ depends on the structure. $\delta\omega$ accounts for the nonlinear resonance frequency shift:

$$\delta\omega = \pm\frac{|a|^2}{P_0\tau^2} \tag{1.34}$$

where P_0 is the characteristic nonlinear power of the cavity [21]. The term $\delta\omega$ can be seen as a correction of the cavity resonance frequency due to the intensity inside the cavity and accounts for the nonlinear refractive index. The sign in eq. 1.34 gives the sign of the nonlinear resonance shift. We choose $\delta\omega = -|a|^2/P_0\tau^2$, i.e. nonlinear blue-shift, without loss of generality. Considering $a = a(t)exp(j\omega_{in}t)$ the steady states of eq. 1.33 are given by:

$$0 = [j(\delta + \frac{|a|^2}{P_0\tau}) - 1]a + je^{j\phi/2}\sqrt{\tau}f \tag{1.35}$$

where $\delta = \tau(\omega_0 - \omega_{in})$ is the detuning of the optical injection with respect to the resonance. The squared modulus of eq. 1.35 becomes:

$$\tau P_{in} = [\delta^2 + A^2 + 2\delta A + 1]A \tag{1.36}$$

where $A = |a|^2/P_0\tau$ and $P_{in} = |f|^2$. The transmitted power ($P_{out} = |t|^2$) is related to the intracavity energy (A) through $P_{out} = |a|^2/\tau = AP_0$. Then, eq. 1.36 yields

$$\frac{P_{out}}{P_0} = \frac{P_{in}/P_0}{1 + (P_{out}/P_0 + \delta)^2} \tag{1.37}$$

Eq. 1.37 contains a cubic dependence of P_{in} as a function of P_{out}. Indeed, the curve has either zero or two critical (i.e. zero derivative) points depending on δ. P_0 does not affect the shape of the curve, it becomes a rescaling factor. The bistable regime corresponds to the case where the curve has two critical points, which requires a detuning higher than $|\delta| > \sqrt{3}$. In addition, since P_{out} is positive by definition, $\delta < -\sqrt{3}$. From eq. 1.36, the transmission T as a function of the P_{in} has the feature of fig. 1.19, provided $|\delta| > \sqrt{3}$.

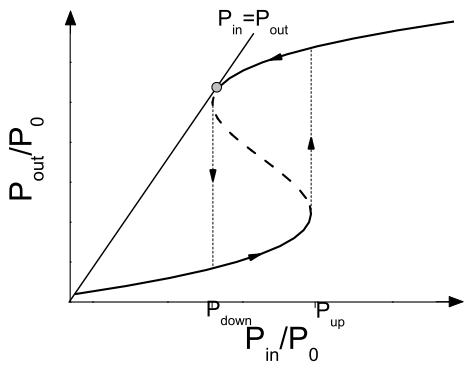

Figure 1.19: *Transmitted power as a function of the injected signal showing the typical feature of a bistable optical system. The solid line corresponds to the stable states while the dashed line to the unstable states. The arrows show the sense of the hysteresis cycle. The solid line corresponds to: $P_{in} = P_{out}$; the bistability threshold can be approximated as the intersection between this line and the curve (grey dot).*

From fig. 1.19, if the system is injected with an increasing power, the transmitted signal (P_{out}) remains low until P_{in} is increased beyond some critical value (P_{up}) then P_{out} increases. The transmission remains high even if P_{in} is decreased until another critical value (P_{down}) is reached and the system jumps to the lower branch. Such hysteresis cycle is usually considered as the experimental evidence of optical bistability. A magnitude that characterizes a bistable

system is the bistability threshold, which is defined as the minimum power for which the system presents two possible states (P_{down} in this case). This value can be estimated as the input power needed for 100% transmission [21], which corresponds to the intersection of the curve given by eq. 1.37 with the line $P_{in} = P_{out}$, see fig. 1.19, giving [21]:

$$P_{th,in} = P_0|\delta| \tag{1.38}$$

Note that if the system is injected with powers such as $P_{down} < P_{in} < P_{up}$ the system present two stable fixed points and one unstable fixed point in between. Besides, the range of power for which the multistability takes place is given by two saddle node bifurcations.

The bistability can be observed in the spectral domain as a bending of the cavity resonance. From eq. 1.36 the detuning (δ) as a function of the transmitted signal for a fixed injected power (different from zero) is given by:

$$\delta = -\frac{P_{out}}{P_0} \pm \sqrt{\frac{P_{in}}{P_{out}} - 1} \tag{1.39}$$

For an injected power in the range of the bistable regime, the cavity resonance bends to higher or lower wavelengths depending on the sign of the nonlinearity (in this case the resonance bends to the blue), see fig. 1.20. If the detuning is lower than a certain value (δ_{up} in fig. 1.20) the system response remains on the tail of the resonance. Beyond δ_{up} the transmission suddenly jumps to the upper branch and remains high even if δ decreases, until another critical value, δ_{down}, is reached and the system jumps back to the tail of the resonance. Note that both δ_{up} and δ_{down} depend on the injected power.

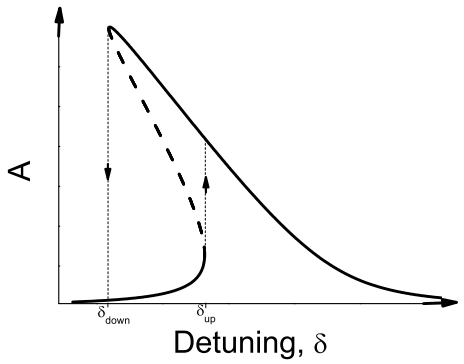

Figure 1.20: *Resonance bending. Transmitted signal as a function of the detuning for a fixed injected power in the range of the bistable regime (see fig. 5.1).*

From the experimental point of view, optical bistability has been extensively studied in the last decades due to its potential application to optical memories. In particular, it has been investigated in detail in Fabry-Perot etalons [22, 23], monolithic vertical cavities [24, 25], micropillars [26] and microdisks [27]. Fig. 1.21 shows the hysteresis cycles in GaAs/AlGaAs multiple quantum well microresonator pillars [24].

In fig. 1.21 the threshold power is less than 70 μW while the threshold in the unetched structure was of the order of 1 mW [26]. This reduction of the threshold power is due to the lateral confinement. According to [28, 21] the threshold scales as V/Q^2, with V the optical

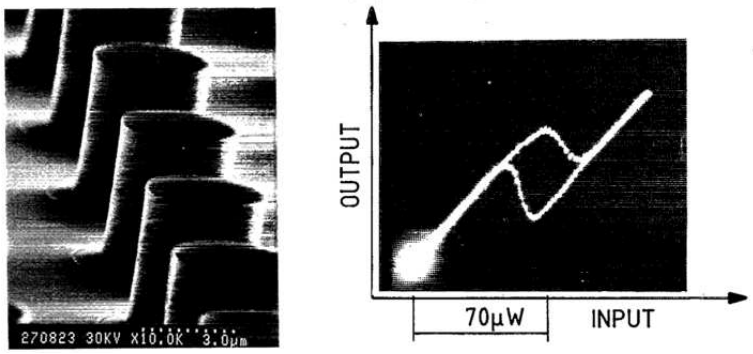

(a) (b)

Figure 1.21: *(a) Scanning electron micrograph of 4 μm-diameter microresonators. (b) Oscilloscope traces showing a wide hysteresis loop in a micropillar. Image from [26].*

mode volume and Q its quality factor. For example, in [27] Si microdisks with high Q ($Q \sim 3 \times 10^5$) and small volumes ($V \sim 40(\lambda/n_{si})^3$) bistability thresholds as low as 60 μW have been observed. As a general rule, optical cavities with high quality factors and small volumes are needed in order to reduce the bistability threshold. Such reduction is crucial for the applications to information processing. Excellent candidates for obtaining high quality factors and small volumes are photonic crystal nanocavities, as we will see in section 1.3.

Self-sustained oscillations and excitability

By definition, bistability only deals with static regimes. The dynamical nature of nonlinearities in active resonators allows, in principle, rich and complex non-stationary phenomena. In particular we will focus on two interesting regimes: excitability and self-sustained oscillations.

As it has been previously discussed, the excitable and spiking (or self-sustained oscillations) regimes are nonlinear dynamical processes that involve variables with different time scales: a fast one, responsible for the firing of the excitable pulse, and a slow one, that determines the full recovery to the quiescent state. Usually, in semiconductors, the fast variable is given by the carrier recombination time and the slow one by the thermal relaxation in the material. In standard resonators, as the one used in [29], the time scale for thermal relaxation is of the order of a ms. In microphotonic resonators such as microdisks or photonic crystals, the thermal relaxation time becomes much faster, due to the small dimensions playing a role in heat diffusion. In [27], self-induced optical modulation of the transmission through a high quality factor (Q) microdisk was reported; the thermal recovery time was of the order of μs. Furthermore, studies on optomechanical oscillations driven by radiation pressure have also shown two time-scale self-sustained oscillations in ultrahigh Q microtorus [30]. More generally, the world of microphotonic devices concerns high and ultrahigh Q resonators [31] which, under light injection, enhance carrier absorption and radiation pressure thus involving ubiquitous thermal or mechanical dynamical effects, respectively.

In the previous section we have studied the excitable and the self-sustained oscillation regime in general systems. In optics, such behaviors are manifested as optical output pulses that depend on the input power. When a constant input signal leads to a time-varying output signal we have self-sustained oscillations. On the other hand, if a constant input signal plus an optical perturbation (shorter than the oscillation period) triggers an optical pulse, provided the

perturbation energy is above a certain value, and if the output pulse shape is independent of the perturbation, we have excitability.

Excitability offers interesting prospects for applications in all-optical circuits, such as clock recovery and pulse reshaping [32]. The self-pulsing behavior in a network of resonators is potentially interesting for an optical realization of reservoir computing [33]. A photonic implementation of a reservoir computing offers the promise of massively parallel information processing with low power and high speed [34, 35, 36].

Self-oscillation regimes are well known in optics. For instance, passive Q-switching and mode-locking lasers are classical self-oscillating phenomena. In recent years, self-pulsing regimes were studied in semiconductor materials in [37, 38] and experimentally observed in lasers with optical feedback [39], in lasers with saturable absorber [40], in etalons [41] and in microdisks [27]. More recently, opto-mechanical oscillations were observed in micro-torus [30].

Unlike bistability and self-sustained oscillations, well known in optics, few works have investigated excitability in optical systems. In particular, some experimental demonstration of excitability in nonlinear optical cavities have been carried out in the last fifteen years. These studies concerned semiconductors lasers with optical feedback [42, 43, 44, 45], gas and solid state lasers with saturable absorber [46, 47], thermo-optical pulsation in broad-area semiconductor amplifiers [29, 48], as well as semiconductors ring lasers [49, 50] and optically injected QD lasers [51]. As an example let us consider a semiconductor laser with optical feedback [42]. The excitable regime is observed while feeding the system with a fixed pump current close to the laser threshold and adding to the pumping current pulses whose amplitude and width can be varied. For perturbation amplitudes less than 2.6 mA no output pulses are observed, fig. 1.22.a. However, for perturbations higher than 3 mA an excitable response is obtained 1.22.b, showing the existence of a threshold.

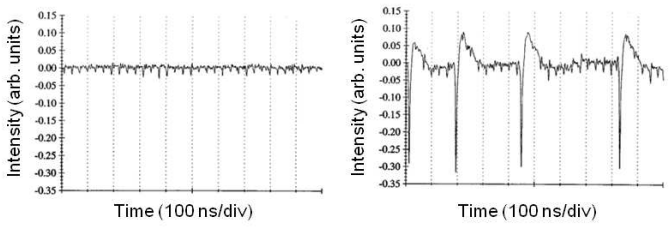

Figure 1.22: *Excitability in a laser with optical feedback. Intensity of the system when a small amplitude perturbation is added to the pumping current; amplitude of the pulse: 2.6 mA (a) and 3 mA (b). Images from [42].*

Excitability in optics has received considerable attention because of its prospects for applications in optoelectronic devices, primarily for optical switching, clock recovery, pulse reshaping (a dispersed input pulse can trigger a large "clean" output pulse), tunable pulses, and for generating a coherent resonance output pulse in communication networks [32]. However, for many of such applications low threshold and ultrafast excitability and self-pulsing are needed in systems that allow integration and miniaturization. We will see in section 1.3 that good candidates to achieve these requirements are the photonic crystal nanocavities.

The regimes studied so far involved a single optical system. In the following we will

introduce an interesting phenomenon arising from the coupling of two (or more) nonlinear optical resonators.

1.2.4 Coupled resonators

Several works have studied the coupling between resonators in different configurations: in "photonic molecules" [52, 53, 54, 55, 56], microdisks [57, 58, 59, 60], microspheres [61] and micropillars [62]. As an example, let us consider the coupling of GaInAsP microdisks studied by Baba et al. [57]. Figs. 1.23.a and b show the system under study and the mode splitting: note that the modes split into a bonding and antibonding mode. The spectral distance between these two modes decreases with the microdisk separation, fig. 1.23.c. This mode split, indeed, depends on the coupling strength as we will analyze in detail in chapter 7.

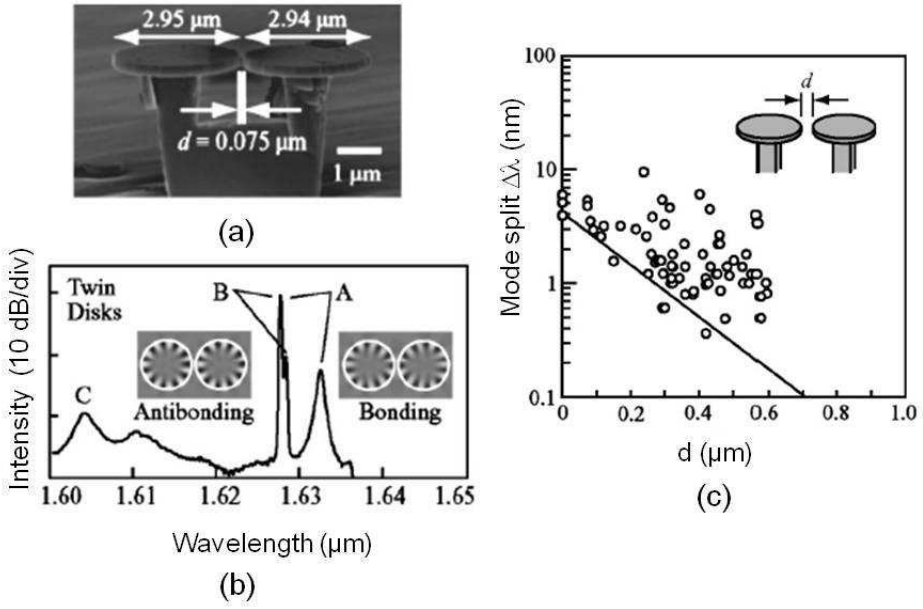

Figure 1.23: *(a) Scanning electron images of twin microdisks. (b) Lasing spectra. Inset figures are magnetic field profiles of bonding and antibonding states of the eleventh order whispering gallery mode. (c) Mode split ($\Delta\lambda$) vs interdisk spacing (d) characteristic of twin disks. The dots and the line are measurement and calculated results, respectively. Images from [57]*

In this paragraph we have introduced the coupling between optical resonators, in the following we will introduce a key and elusive phenomenon in coupled nonlinear resonators.

Nonlinear coupled resonators: Spontaneous symmetry breaking

Coupling sets of nonlinear resonators opens up the possibility of spatio-temporal control of light. The phenomenon underlying the family of rich nonlinear dynamical behaviors in such coupled system is called spontaneous symmetry breaking. This phenomenon is the process by which a symmetrical system, under symmetrical excitation ends up in an asymmetric state, while linearly, the intensity inside each resonator would be equal. This behavior opens up a whole new range of applications such as photonic reservoir computing [36], slow light engineering [63], and all-optical flip-flop operation [64]. Imagine we have a system of two cavities with right-left symmetry. If the system is linear, the original symmetry is preserved. Since both modes are excited with the same

strength, a superposition of equal inputs from left and right results in equal outputs to the left and right. In the nonlinear case, this excitation shifts the resonance frequencies of the modes. Because of the coupling of cavity intensities through the middle channel, it is possible that the symmetric situation is no longer stable at a certain input power. Therefore, the system will drift to a situation where one cavity is more excited than the other, and thus, an asymmetric state arises.

Maes et al. [64] have predicted, both analytically and through numerical simulations, this kind of behavior in two coupled nonlinear cavities with a symmetric excitation through two ports, fig. 1.24.

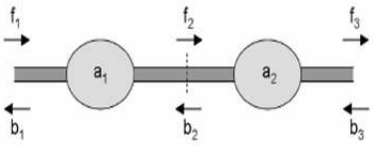

Figure 1.24: *(a) Sketch of two coupled cavities coupled to the outside by two ports. Image from [64]*

Instantaneous Kerr nonlinearity is used, where the index depends on the intensity of the local field. Using coupled-mode theory (CMT, see section 2.2) they presented a simple analytical description of the processes. Fig. 1.25 shows the output power (trough the left or right ports) as a function of the input power. Note that there is a range of incident powers for which the output powers through the left and right ports are not equal. This means that the symmetric solution has become unstable and the system has switched to an asymmetric state. Indeed, we have spontaneous symmetry breaking. Note that the symmetry breaking arises and ends with a pitchfork bifurcation.

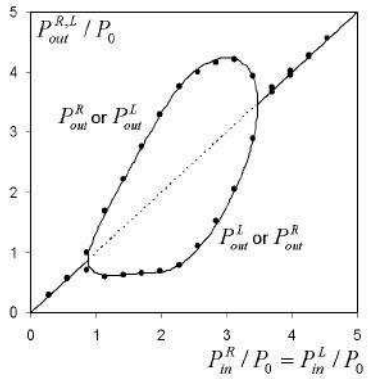

Figure 1.25: *Output power versus input power. Stable and unstable states are shown with solid and dashed lines, respectively. Dots show rigorous simulation results. Note that for a range of injected powers, the symmetric solution becomes unstable and the system switches to an asymmetric state. Image from [64]*

In this thesis we propose the experimental demonstration of spontaneous symmetry breaking on the bases of two evanescently coupled InP-based photonic crystal cavities, symmetrically

excited through a microfiber. We will come back to this in Part III.

We have mentioned that photonic crystals are good candidates for light confinement in small volumes and with high quality factors. In the next section we give a short introduction to photonic crystals, with particular emphasis in light confinement in small volumes and light input coupling methods.

1.3 Photonic crystals

Light confinement in high quality factor resonators or cavities leads to enhanced nonlinearities, i.e. stronger refractive index changes. Hence, lower bistability, excitability and self-sustained oscillations thresholds can be obtained. The light confinement in a dielectric or semiconductor medium can be obtained by two different phenomena: the total internal reflection mechanism or the interferences in a medium with a periodicity in the refractive index.

1.3.1 Mechanisms of light confinement

Total internal reflection

A simple way to confine light in a dielectric or semiconductor is by means of refraction index contrast between two materials. Let us consider two layers with refractive indices n_1 and n_2, such that $n_1 < n_2$, fig. 1.26.a. If the incident light propagates through the material with n_2, total internal reflection can be achieved provided the angle of incidence is higher than $\theta_{in} > arcsin(n_1/n_2)$. This is the confinement mechanism in regular optical fibers but also in microdisks (fig. 1.26.b) and microspheres where the materials of higher and lower index can be, for example, III-V semiconductor or Si and air, respectively. Using this phenomenon we can confine light in 1, 2 and 3 directions of space leading to waveguides or cavities.

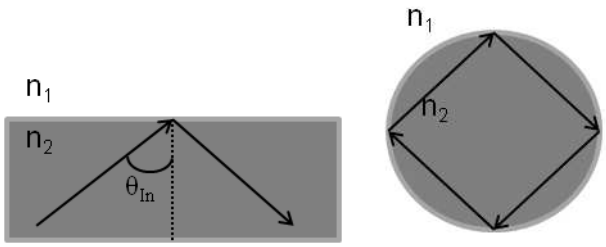

Figure 1.26: *Light confinement in a layer (a) and in a microdisk (b). The confinement is given by total internal reflection on the interface of two media with different refractive index.*

Confinement by interference

Another way to confine light is via light interference of a wave propagating in a periodic medium, like a photonic crystal (PhC). PhC are dielectric materials with a periodic structure of the refractive index in a scale of the order of the wavelength. This periodicity affects the propagation of light in the same way as a atomic periodic potential in a crystal affects the motion of electrons, by defining allowed and forbidden electronic energy bands. In particular, structures with photonic bandgaps that prevent the light to propagate in certain directions with certain frequencies can

be realized. The periodicity can be in 1 direction (i.e. 1D PhC), 2 directions (2D PhC) or 3 directions (3D PhC). In the following we describe the origin of this confinement.

1.3.2 Band structure in photonic crystals

The physics of light propagation in periodic media is contained in the dispersion relation. For simplicity let us first consider a 1D photonic crystal, a Bragg mirror. The structure is given by layers of index n_1 and thickness d_1 and layers with n_2 and d_2. Then, the structure period is $d_1 + d_2$. If for a certain wavelength the phase shift is such that $n_1 d_1 = n_2 d_2 = \lambda_0/4$, destructive interference takes place between the reflected and transmitted waves at each interface. Hence, the structure behaves as a mirror for a wave of wavelength λ_0, which is the central wavelength of the forbidden band of propagation. Indeed, there exists a whole range of frequencies that cannot propagate in the system, called the photonic bandgap. This bandgap can be seen in the dispersion relation or band diagram of the structure, where the frequencies are plotted as a function of the wave vector ($\omega(k)$). As for electron standing Bloch waves in a crystal, the band diagram represents the allowed frequencies (bands) and forbidden frequencies (bandgaps) for an optical Bloch wave propagating in the periodic medium. It contains information of the dispersion characteristics $\omega(k)$ of the photonic crystal. Fig. 1.28 shows the band diagram for the case $n_1 = n_2$ (left) and for $n_1 = 3.6$ and $n_2 = 1$ (right). Note the photonic bandgap in the latter.

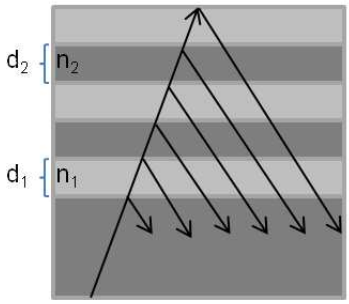

Figure 1.27: *Scheme of the multiple reflections on the successive interfaces of a structure with a periodicity in the refractive index (Bragg mirror).*

Total reflectivity in more dimensions can be obtained by adding a periodicity in the other directions. As a result, 2D or 3D photonic crystals can be realized. These structures also show photonic bandgaps, which lead to a range of wavelengths that cannot propagate in the structure. Using this concept we can make an analogy with the band theory for the electrons in a crystal. The periodic variation of the refractive index resembles the periodic potential in a crystal. Therefore, we can use the same formalism for the propagation equation due to the wave nature of the photons and electrons.

Writing the Maxwell equation for a periodic system ($\epsilon(r) = \epsilon(r+R)$, with ϵ the dielectric function), the eigenmodes of the PhC (h_k) are Bloch modes characterized by a vector $\overrightarrow{k}$ as

$$H_k(r) = e^{ikr} u_k(r) \tag{1.40}$$

where $u_k(r)$ is a periodic function: $u_k(r) = u_k(r + R)$ for all lattice vectors R [65]. Note the system is invariant under the transformation $k \rightarrow k + m2\pi/a$ (with m an integer). Indeed,

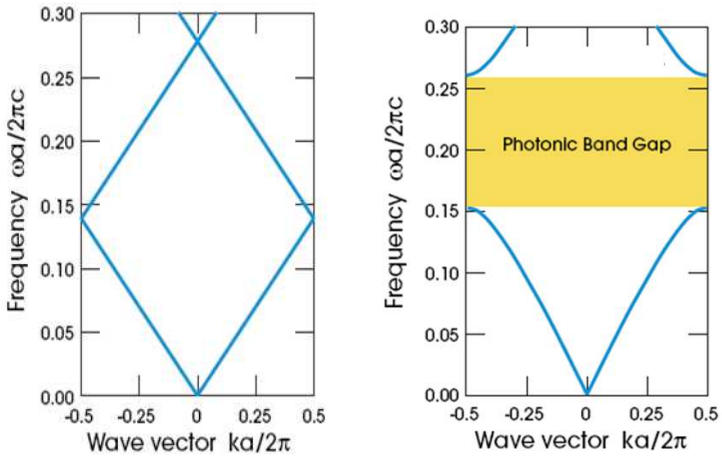

(a) (b)

Figure 1.28: *Photonic band structure for a propagation perpendicular to the structure for (a) $n_1 = n_2$ and (b) $n_1 = 3.6$ and $n_2 = 1$. Note that for different refractive index the degeneracy at the crossing points is lifted, giving rise to photonic bandgaps.*

in order to fully describe the physics of propagation we can restrict ourselves to the interval $-\pi/a < k \leqslant \pi/a$: this region in k space is called the Brillouin zone.

Let us now consider a particular case of a PhC: a 2D photonic crystal with triangular lattice, fig. 1.29.a. The periodicity is given by air holes (n=1) embedded in a high refractive index material. The key to understanding photonic crystals in two dimensions is to realize that the fields in 2D can be divided into two polarizations by symmetry: Transverse-electric (TE) modes where the magnetic field is normal to the plane and the electric field lies on the plane, and transverse-magnetic (TM) modes where the magnetic field is in the plane and the electric field is normal to the latter. The band structure for the TE and TM modes can be completely different, fig. 1.29.b. In particular, it may occur that a photonic bandgap exists for one polarization while no bandgap exists for the other one. Frequency bands for which propagation is forbidden both for TE and TM modes are called total bandgaps.

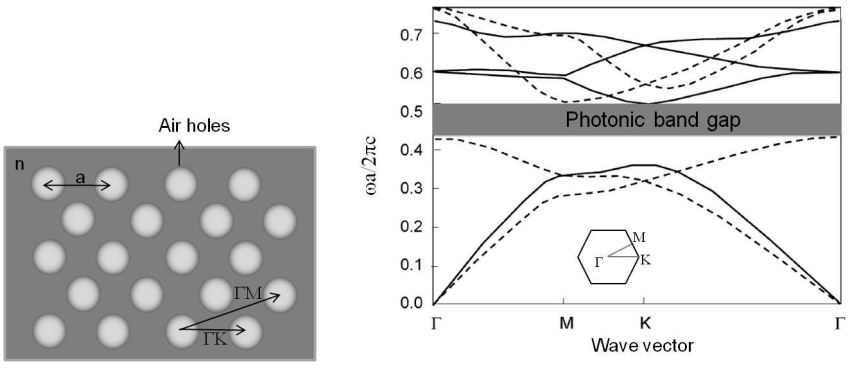

(a) (b)

Figure 1.29: *(a) 2D Photonic crystal of triangular lattice. The periodicity is given by air holes of radius r in a material with dielectric constant $\epsilon = 10.89$. (b) Band diagram for the structure in (a). The solid lines represent the TE modes while the dashed lines the TM modes. The inset shows the Brillouin zone.*

The triangular lattice is usually chosen over the square one because the bandgap is wider in the first case and leads to more flexibility to get a complete cavity effect with better confinement.

2D PhC have two drawbacks: firstly, the confinement cannot be achieved in the normal direction, and secondly, they are difficult to fabricate due to the high aspect ratio-etching process needed to obtain 2D cylinders. Nowadays, almost all the 2D PhC are 2D photonic crystal slabs. In such structures the confinement in the direction perpendicular to the slab can be achieved by total internal reflection. However, confinement is not prefect: photons incident with angles smaller than the total internal reflection critical angle can escape from the structure and couple to the continuum of radiation modes.

In this thesis we are interested in a particular type of 2D slab: the 2D PhC suspended membrane. Here the lateral confinement is given by the PhC periodicity and the vertical confinement through guided modes in the suspended membrane.

1.3.3 Photonic crystal cavities

The photonic bandgap can be used to confine light in reduced volumes. Imagine we include a defect in a PhC for instance by removing some holes in the lattice: if this defect has the appropriate size to support a mode surrounded by the photonic band gap, then the light gets trapped into this defect. As a result, an optical cavity is realized. These cavities can have very small volumes and high quality factors (Q), where Q represents the rate of energy loss relative to the stored energy of the oscillator. It is given by $Q = \tau\omega/2 = \omega/\Delta\omega$, with τ the photon lifetime inside the cavity, ω the cavity resonance frequency, and $\Delta\omega$ the resonance width.

Photonic crystal nanocavities can be formed by removing and/or modifying one or more holes (i.e. by changing the hole size or the refractive index) in an otherwise perfectly periodic lattice. Such a breaking in the periodicity of the lattice introduces new energy levels within the photonic band gap. Here we will present two kinds of cavities: defect cavities and double heterostructure cavities.

Defect photonic crystal cavities

The simplest defect cavity in a bi-dimensional photonic crystal consists of removing one hole [66] in a perfect triangular lattice of holes. This cavity is called H1. However, these typically have quality factors of a few hundreds, which exclude them as good candidates for nonlinear optics.

In recent years, a considerable amount of effort has been devoted to improve PhC cavity design in terms of both Q factors and mode volumes. In particular, it has been shown that given a defect cavity, the quality factor of the structure can be improved by shifting the position of the nearby holes or increasing/decreasing their size. This is the case of the L3 modified cavity in a suspended PhC membrane. Such cavities are given by three missing holes in a line of a triangular periodic lattice, fig. 1.30.a. Noda et al. [67] have demonstrated that a slight shift of the two holes closing the cavity increases the cavity quality factor by almost one order of magnitude, fig. 1.30.b. Sauvan et al. [68, 69] have given a successful interpretation of this phenomenon. The elements that affect the quality factor of a cavity are: an increase of the reflectivity of the surrounding "mirrors" of the cavity by shifting the holes positions which better adapt the mode profile in the cavity to that of the mirrors; and a decrease of the group velocity of the cavity modes. Thanks to this shift, high quality factors (Q) in this kind of cavities were achieved,

e.g. $Q \sim 10^4$ in GaAs and $Q \sim 45000$ in Si. We have implemented this kind of cavities in InP suspended membranes for nonlinear studies.

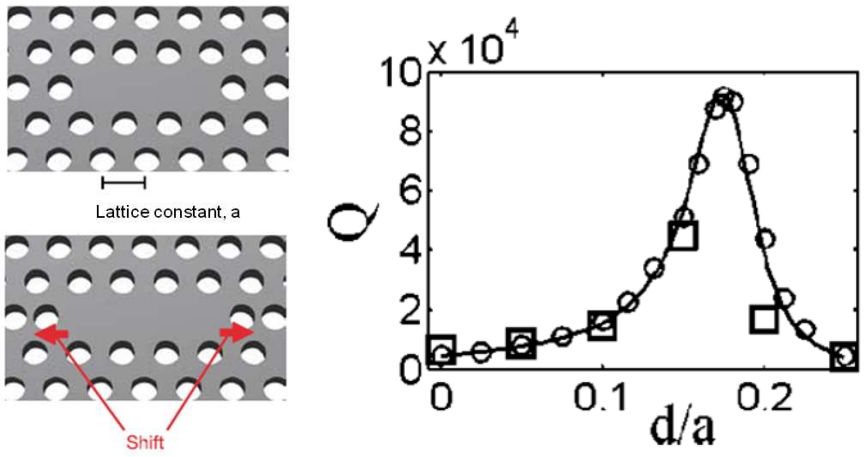

(a) (b)

Figure 1.30: *(a) Sketch of a L3 cavity with a lattice constant a, where the two holes closing the cavity are shifted away a distance d. Image from [67]. (b) Quality factor of the L3 cavity as a function of the holes shift, d. Squares correspond to the experimental results in [67] while the line and the circles correspond to the numerical results from [69]. Image from [69].*

Double heterostructure cavity

Extended defects in a photonic crystal, i.e. a whole missing line of holes or a line with smaller holes, lead to optical waveguides. Examples of this confinement are W1 waveguides (fig. 1.31.a), where the guide is formed by removing a row of holes in the $\Gamma - K$ direction from an otherwise perfect triangular lattice. Light that propagates in the waveguide with a frequency within the band gap of the crystal is confined into the defect and can be directed along it. The introduction of this defect results in a frequency band for light propagation lying inside the PhC band gap, fig. 1.31.b.

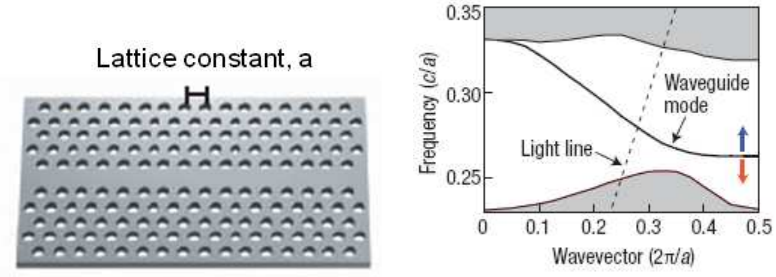

(a) (b)

Figure 1.31: *(a) Sketch of a W1 guide, i.e. a whole missing line of holes. (b) Band diagram of this structure. The PhC bandgap takes place inside the white region. Note that a band of the waveguide lies within this bandgap. Images from [70].*

The position of the guided-mode band, fig. 1.31.b, depends on the PhC period and hole

diameter. Changing such parameters allows fine tuning of the guided mode frequency. Moreover, this allows the realization of optical cavities within the waveguide. These are called double heterostructure cavities. Noda et al. [70] proposed one type of double heterostructure cavity, where the cavity is formed by a local increase (over two periods) of the longitudinal lattice period (from a to a') along the waveguide, fig. 1.32.a. As a result, an inner waveguide with lattice period a' is sandwiched between two outer waveguides with lattice constant a. In the case $a' > a$, the inner waveguide mode is red-shifted respect to the outer waveguides mode. Therefore, light is confined in the former, fig. 1.32.b. We will call this kind of cavity Noda-type cavity. We have also used these cavities, to a lesser extent, for our studies.

In these cavities, due to the close similarities between the inner and outer waveguides, the reflectivity of the mirrors, formed by the outer waveguide, is almost $\sim 99.99\%$. Besides, the cavity mode has low group velocity (due to the flatness of the dispersion curve, fig. 1.31.b). As a result, high quality factors can typically be obtained with these cavities. Quality factors of the order of 10^6 in Si were achieved [70] while in III-V semiconductors (in absence of 1-photon absorption) cavities with $Q \sim 10^5$ were realized in GaAs [71, 72].

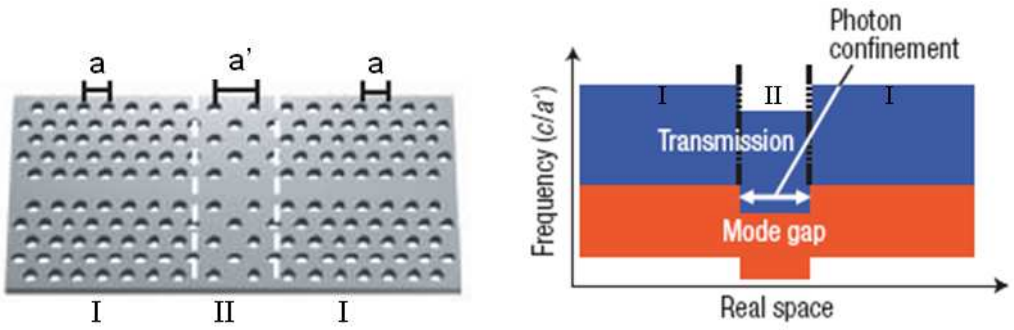

(a) (b)

Figure 1.32: *(a) Sketch of a Noda-type cavity given by an inner waveguide (II) with lattice constant a' and outer waveguides (I) with lattice constant a. (b) Representation of the optical confinement in this kind of structure. Photons of a specific energy can only exist in the inner waveguide (II). Images from [70]*

1.3.4 Coupled PhC cavities

Coupling of microcavities allowing energy transfer introduces new grounds for the development of fast lasers [73], delay [54] and non-linear [74] optical lines, bistability-based ultrafast generators, switchable lasers [75], optical memories [76, 77] and other elements of future integrated photonics circuits. Generally, coupling results in a frequency splitting and, in some circumstances, in a splitting of the modal loss.

The coupling between PhC cavities has been investigated in several works [52, 53, 54, 55, 78, 56]. In particular, Notomi et al. [78] have experimentally demonstrated the coupling between cavities in a large (N>100) array of PhC nanocavities. Moreover, the ultrahigh value of Q and small size has enabled them to achieve slow light pulse propagation with a group velocity well below 0.01c and a long group delay.

The coupling in L3 PhC cavities was studied in [56] where the mode splitting and the

quality factors splitting is studied in detail. Fig. 1.33 shows this splitting as a function of the distance between cavities (a) for four different geometries. We observe that the mode at higher energy can be symmetric (also called bonding) or antisymmetric (anti-bonding) depending on the geometry and the separation. Note also that the splitting not only depends on the separation but also on the geometry. We will see later that this splitting is associated to the coupling strength.

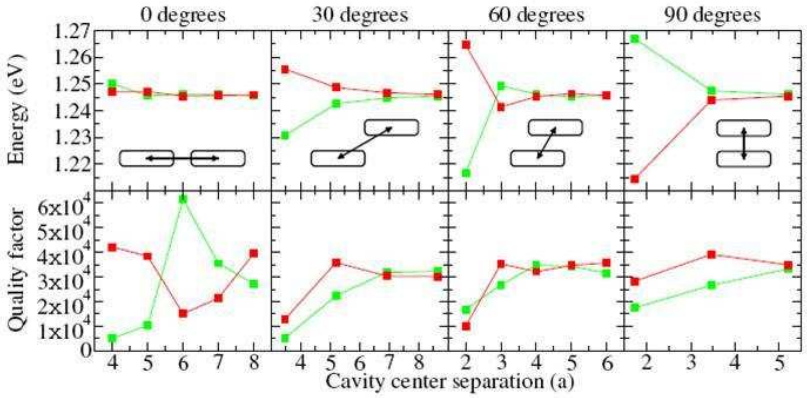

Figure 1.33: *Theoretical plots of the energies and quality factors of the split fundamental modes of parallel L3 cavities coupled along lines defined relative to those of the cavities. Green lines represent bonding (B) states, red lines represent anti-bonding (AB) states. Images from [56]*

The study of the mode splitting builds confidence in the evanescent coupling between cavities. A systematic study of the cavities coupling was carried out by Vignolini et al. [79] where the anticrossing of modes was observed. Fig. 1.34.a shows a schematic image of the sample. This kinds of cavities (individually) presents two main modes spatially extended along the two orthogonal direction x and y, and they have different polarization properties. In order to control the coupling between the modes of the two PhC cavities, one of the cavities is injected with a solution that allows to modify its modes: the cavity modes shift with the evaporation of this solution. This evaporation is induced by heating the sample through the photoluminescence setup. Fig. 1.34.b shows the spectral position of the first four modes (P1, P2, P3 and P4) of the coupled system as a function of the exposure time at high excitation density. P1 and P2 (P3 and P4) arise from the coupling between the fundamental (first excited) modes of each cavity. After 500 min of exposure time, an anticrossing between the two first modes (P1 and P2) is observed with a minimum splitting of 17 nm. After an exposure time of 1300 min an anticrossing between P2 and P3 is observed. These anticrossings of modes are clear evidence of the coupling between cavities.

In Chapter 8 the coupling between PhC cavities is investigated using another approach: the phase coherence between the cavities fields.

1.3.5 Light coupling methods

We have seen that cavities with high quality factors and small volumes are possible in photonic crystal devices. However, due to their small volumes and complex radiation patterns compared to either standard optical fiber modes or free-space diffraction-limited optical beams, the efficient coupling of light into PhC devices is quite challenging. Different approaches can be implemented to achieve this coupling. The most usual one is the integration of optical waveguides into the PhC, fig. 1.35, [80, 81, 82]. This is an interesting approach since it allows integration, miniaturization and repeatability, among others. However, it presents some drawbacks such us injection,

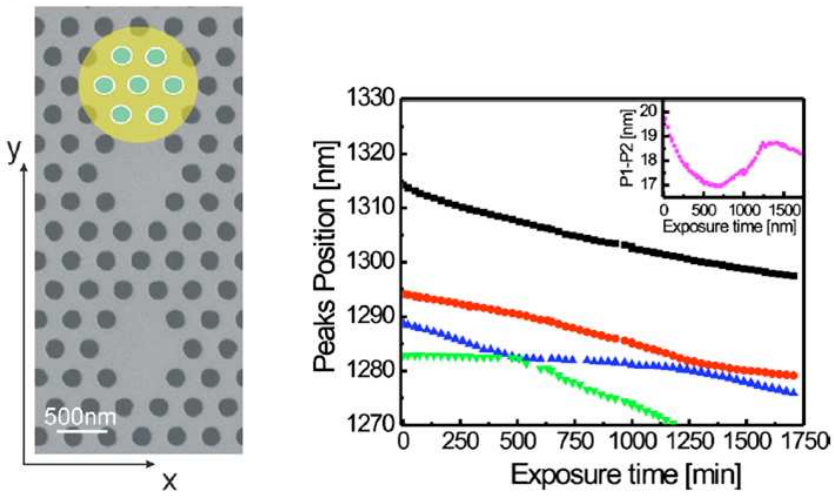

(a) (b)

Figure 1.34: *(a) Schematic image of the studied sample. On the upper cavity, the implementation of the tuning techniques is also schematically drawn, where the turquoise (white) dots represent the water infiltration and the yellow highlighted area (brighter) represent the laser spot. (b) Spectral position of the first four modes of the system as a function of the exposure time for: (■) P1, (●) P2, (▲) P3, and (▼) P4. In the inset the splitting of P1 and P2 is reported as a function of the exposure time. The anticrossing corresponds to a minimum splitting at 500 min. Images from [79].*

propagation and absorption losses in the waveguides.

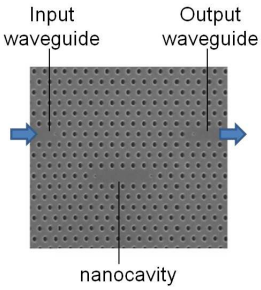

Figure 1.35: *Photonic crystal cavity coupled by an integrated waveguide. Image from [82].*

Another interesting approach is the evanescent coupling from PhC cavities to tapered optical fibers, [80, 83, 84, 85]. This coupling is obtained as far as the spatial overlap of the cavity mode and the microfiber mode is different from zero. Evanescent coupling between a tapered fiber and a PhC waveguide or cavity (fig. 1.36) is well adapted to on-chip input and output coupling using silica optical fibers. This evanescent coupling technique is also suitable for adaptation to planar lightwave circuit technology, allowing for the interfacing between fiber optics and PhCs in a mechanically robust and scalable way.

Braclay et al. [83] and Hwang et al. [85] have studied the coupling characteristics between a cavity and a tapered fiber as a function of different parameters. In particular, the coupling efficiency as a function of the gap between the fiber and the cavity [85] through FDTD

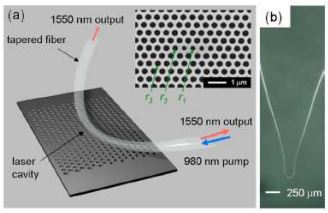

Figure 1.36: *(a) Coupling geometry between a PhC waveguide and a tapered fiber. Inset: SEM image of the PhC. (b) Picture of the tapered fiber. Images from [85].*

numerical simulations was investigated, with the efficiency defined as the intensity collected by the fiber (in both senses) over the intensity inside the cavity. Fig. 1.37 shows this coupling efficiency (η) and the loaded quality factor (Q_{loaded}) as a function of the gap; the filled circles correspond to simulations with an ideal cavity while the open circles to simulations using a SEM image of the PhC cavity. The Q_{loaded} corresponds to the quality factor obtained trough the resonance measured with the tapered fiber and η corresponds to the ratio between the signal collected through the fiber and the total intracavity power. Note that the maximum coupling efficiency is given for a gap different form zero (gap=100 nm): a maximum of $\eta \sim 80\%$ was theoretically achieved. Moreover, experimental studies were also carried out in [85] where coupling efficiencies of $\eta \sim 70\%$ were reported, using specific cavity design in order to maximize the efficiency. Such high coupling efficiencies allow the application of this system to single photon generators and to efficiently probe structures with high absorption coefficients, among others.

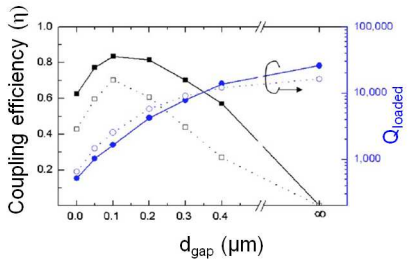

Figure 1.37: *Fiber coupling efficiency (squares) and total quality factor (circles) as functions of distance between the cavity and the fiber. The open symbols are results from numerical simulations using a SEM image of the sample, while the filled symbols corresponds to the ideal cavity structure. Image from [85].*

In this thesis we have implemented this coupling system to address the nonlinear behavior of photonic crystal nanocavities, as we will see in chapter 3.

1.3.6 Optical bistability and excitability in PhC: State of the art

Only few works were devoted to the understanding and implementation of nonlinear dynamics in nanoresonators. They have mainly dealt with optical bistability of thermal origin since thermal effects are usually dominant against ultrafast nonlinearities. Notomi et al. [82, 86] have studied the all-optical bistable switching operation in Si PhC nanocavities. Fig. 1.38.a shows the output signal as a function of the input power for different detuning. Note the similarities with fig. 1.19. A power threshold of $\sim 40\ \mu W$ was found, which is one order of magnitude smaller than the threshold for microresonators and vertical cavities discussed in section 1.2. Electronic nonlinear-

ities in nanoresonators are more difficult to achieve due to technological issues and due to their fast time scales (ps-ns scale). Nonetheless, some works have recently demonstrated bistability of electronic origin in PhC nanocavities [87, 88]. Kim et al. [87] have also studied optical bistability in InP PhC nanocavities (fig. 1.38.b), with the particularity of using a microfiber to couple light in and out of the cavity. They have also found a bistability threshold, measured in the vicinity of the cavity, of $\sim 37\ \mu W$. These results confirm that the bistable threshold can be reduced in PhC optical cavities.

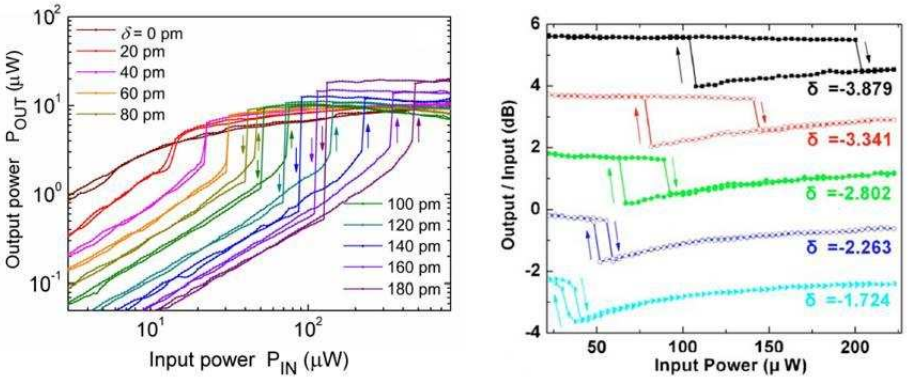

(a) (b)

Figure 1.38: *Bistability in PhC nanocavities. Output signal as a function of the input signal, showing bistability, for different detunings* $\delta = (\lambda_{in} - \lambda_0)/\gamma$ *(with* $_{in,0}$ *the injected/resonance wavelength and* γ *the HWHM of the resonance) for (a) a Si PhC cavity coupled through waveguides (showing thermal bistability) and (b) InP PhC nanocavity coupled by a microfiber (showing electronic bistability).*

Regarding excitability in 2D PhC resonators, Yacomotti et al. [89] have demonstrated self-sustained oscillations and type II excitability in Bloch mode resonators in InP PhC. The system under study was an extended resonator that exhibits a flat band edge at the Γ point. As a result, light can be coupled resonantly into this low group velocity Bloch mode when it is injected normal to the PhC surface, fig. 1.39.a. Injecting the system with a near-resonant constant signal and measuring the reflected signal, self sustained oscillations were observed, fig. 1.39.a. Decreasing the injected signal under the spiking threshold and adding a perturbation to this configuration (an incoherent pump sent by the surface) an excitable regime was obtained, fig. 1.39.b. Note the similarities between fig. 1.39.a and the time trace for the van der Pol oscillator (fig. 1.11.b). The excitability is manifested in fig 1.39.b as an all-or-none optical response. For perturbation energies lower than U_p=1.6 pJ no output pulse is observed. However, for perturbation energies higher than 1.9 pJ an excitable pulse of 300-ns-width is observed in the reflected signal.

Excitability and self-pulsing, already observed in extended resonators [89], have never been reported in PhC nanocavities. In such a case, self-pulsing and excitable threshold are expected to be considerably reduced. One of the main goals of this thesis is the experimental demonstration of such regimes in PhC nanocavities (chapter 6).

In the following section we derive an original and simple model that accounts for nonlinear behaviors of a PhC cavity that incorporates an active medium and which is coupled to the external continuum through a generic optical waveguide.

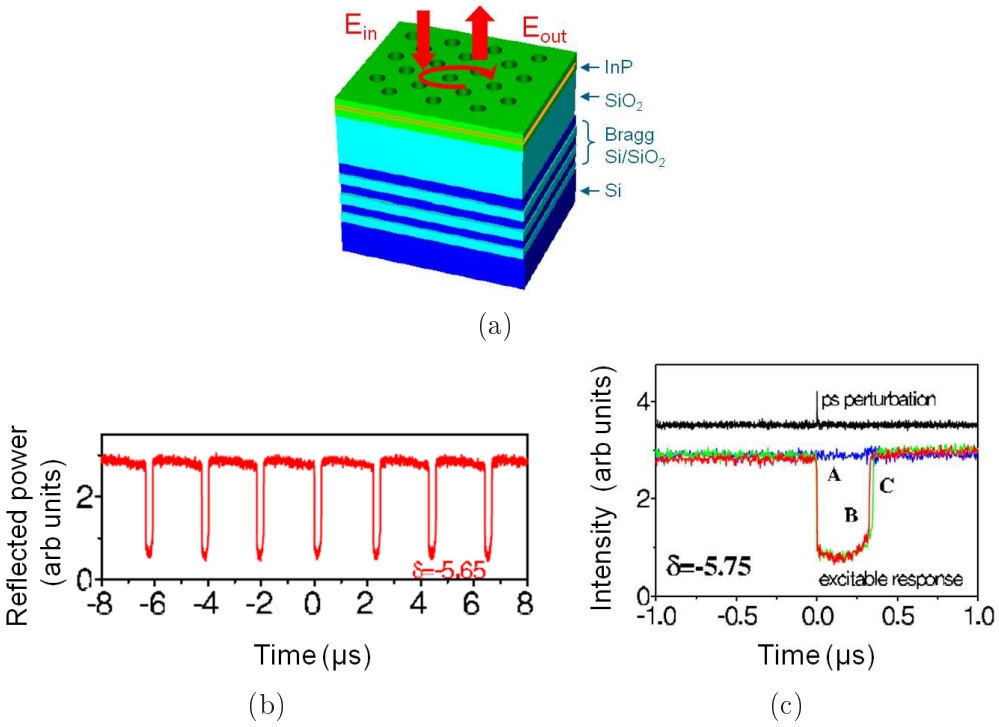

Figure 1.39: *Excitability in a PhC band-edge Bloch mode. (a) Sketch of the 2D PhC. (b) Self-sustained oscillations regime in a InP Bloch mode resonator, for a detuning of $\delta = -5.65$ and an injected power of 5.1 mW. (c) Excitable behavior for a detuning of $\delta = -5.75$ and a perturbation energy of U_p=1.6 pJ (label A), 1.9 pJ (label B), and 2.5 pJ (label C). Images from [89].*

1.4 Dynamical model equations for active III-V optical cavities.

As it has already been discussed in section 1.2, optical bistability involves a single nonlinear effect, either electronic or thermal, while thermo-optical excitability and self-sustained oscillations involve both of them. In this section we develop a model to capture the main features of such phenomena in a single set of equations, namely amplitude equations of the electromagnetic field in a cavity filled with an active (III-V semiconductor) medium. We will focus on the experimental device, given by a suspended membrane with a PhC nanocavity coupled to the external continuum by a microfiber, where the suspended membrane contains a layer of active material (i.e. QWs). The equations accounting for all those phenomena must describe the time evolution of three main coupled variables: the electromagnetic field, the charge carrier density inside the active material and the temperature. For the first, a coupled mode theory (CMT) formalism is used. The basic ideas of such formulation are given in section 2.2 where the linear equations of the time evolution of the electromagnetic field inside a cavity are deduced. Let us stress that such equations remain valid for generic optical cavities filled with active III-V semiconductor media.

1.4.1 Field amplitude equation

The intracavity field amplitude (a) in CMT with two nonlinear terms, one given by electronic effects and another given by thermal effects, normalized such that $|a|^2$ is the intracavity energy,

is governed by the following equation

$$\frac{da}{dt} = [j(\omega_0 + \Delta\omega_e + \Delta\omega_{th}) - \frac{1}{\tau}]a + df \tag{1.41}$$

with ω_0 the cavity resonance in the absence of any nonlinear effect; $\Delta\omega_{e/th}$ the nonlinear frequency shift of the cavity resonance given by electronic or thermal effects, respectively; d is the coupling coefficient from the outside and f the injected field. $1/\tau = 1/\tau_c + 1/\tau_{rad} + 1/\tau_a$, where τ_c is the coupling time; τ_{rad} the radiative losses time and τ_a the absorption time. The absorption is given by active semiconductor nanostrustures, in particular we consider QWs. Then, we can relate τ_a to the absorption (α), dependent on the frequency and charge carrier density (N), and the confinement factor (Γ) as:

$$\frac{1}{\tau_a} = \frac{c\Gamma\alpha(\omega, N)}{2n_{g_0}} \tag{1.42}$$

where n_{g_0} is the group velocity in the dielectric (here semiconductor) slab and c the speed of light. The confinement factor (Γ) is defined as the fraction of the propagating wave that is seen by the active medium, which extends from $x = 0$ to $x = w$, in the following way [90]

$$\Gamma = \frac{\int_0^w |E(x)|^2 dx}{\int_{-\infty}^{\infty} |E(x)|^2 dx} \tag{1.43}$$

This value can be approximated as the ratio of the active medium thickness to the whole structure thickness ($\Gamma \sim w/D$), with w and D the active material and structure thickness, respectively.

Moreover, we can define the small signal (unsaturated) absorption, α_0, as

$$\frac{1}{\tau_{a_0}} = \frac{c\Gamma\alpha_0}{2n_{g_0}} \tag{1.44}$$

It is straightforward to relate the material permittivity to the complex refractive index. Its real part is given by both the slab effective refractive index (n_s) and the change in the refractive index given by the active medium (Δn_e), while its imaginary part is related to the extinction coefficient (κ) in the following way

$$\epsilon = (n_s + \Gamma\Delta n_e + j\Gamma\kappa)^2 \tag{1.45}$$

Considering that $\kappa = \alpha\lambda/4\pi$ and neglecting $O(\Gamma^2)$ terms we obtain

$$\alpha = \frac{2\pi}{n_s\lambda}\epsilon_e'' = \frac{2\pi}{n_s\lambda}\chi_e'' \tag{1.46}$$

$$\Delta n_e = \frac{\chi_e'}{2n_s} \tag{1.47}$$

where χ_e' and χ_e'' are the real and imaginary parts of the material susceptibility, respectively, which depend on the frequency (ω) and the carrier density (N). Assuming $\chi_e(\omega, N) \cong \chi_e(\omega_0, N)$ and expanding $\chi_e''(\omega_0, N)$ to first order in N around the carrier density in transparency (equal number of electrons in the conduction than in the valence band) N_t, eq. 1.46 yields

$$\alpha = \alpha_0(1 - \frac{N}{N_t}) \tag{1.48}$$

Furthermore, eqs. 1.46 and 1.47 can be related to the Henry factor, which is the ratio of the real to the imaginary parts of the differential susceptibility, namely:

$$\alpha_H = \frac{\frac{\partial\chi'}{\partial N}|_{N=N_t}}{\frac{\partial\chi''}{\partial N}|_{N=N_t}} \tag{1.49}$$

In order to derive an expression forΔn_e, let us consider a linear approximation of the slab effective index close to ω_0:

$$n_s \cong n_0 + \Delta n_s(\Delta\omega) \tag{1.50}$$

with

$$\Delta n_s(\Delta\omega) = \frac{\Delta\omega}{\omega_0}(\frac{c}{v_{g_0}} - n_0) \tag{1.51}$$

being v_{g_0} the group velocity in the slab, $n_0 \equiv n_s(\omega_0)$ and Δn_s the refractive index change due to the mode dispersion in the slab. Using $n = n_s + \Gamma\Delta n_e$ (eq. 1.45), the total refractive index change associated to a frequency shift $\Delta\omega_e$ is $\Delta n = \Delta n_s(\Delta\omega_e) + \Gamma\Delta n_e$. Considering $\Delta n/n_0 \simeq -\Delta\omega_e/\omega_0$, eqs. 1.46 to 1.51 lead to

$$\Delta\omega_e = \frac{\alpha_H}{\tau_{a_0}}(\frac{N}{N_t} - 1) \tag{1.52}$$

Eq. 1.52 shows a linear dependence of the frequency shift with the carrier density.

1.4.2 Dynamical equation for carrier density

Now we focus on carrier dynamics. A simple model to describe the time evolution of the 3D carrier density N is a rate equation. The variation of the number of carriers in the QWs is given by the recombination process and the excitation of carriers by the intracavity field and/or an incoherent pump rate (R). Two main recombination processes can be taken into account: a nonradiative recombination process with a time constant τ_{nr}, and a radiative recombination process or bimolecular recombination at a rate BN, B being the bimolecular recombination coefficient, which is expected to play an important role for high carrier densities [91]. The carrier excitation by the intracavity field is proportional to the density of photons inside the cavity (S), then the rate equation for N(t) is given by [92, 93]

$$\frac{dN}{dt} = -\frac{N}{\tau_{nr}} - BN^2 - v_{g_0}\sigma S(N - N_t) + R \tag{1.53}$$

with $\sigma \simeq \alpha_0/N_t$. We can express S as a function of the intracavity energy as:

$$S = \frac{1}{h\nu V_{cav}}|a|^2 \tag{1.54}$$

where V_{cav} is the cavity volume. Defining the saturation energy ($|a_{sat}|^2$) as

$$|a_{sat}|^2 \equiv \frac{V_{cav}h\nu}{v_{g_0}\tau_{nr}\sigma} \cong \frac{V_{cav}h\nu N_t}{v_{g_0}\tau_{nr}\alpha_0} \tag{1.55}$$

Eq. 1.53 leads to

$$\frac{dN}{dt} = \frac{1}{\tau_{nr}}[-N - B\tau_{nr}N^2 - \frac{|a|^2}{|a_{sat}|^2}(N - N_t)] + R \tag{1.56}$$

Let us compute the steady states of N. Considering low carrier densities (i.e. we neglect the bimolecular recombination and saturation) and no incoherent pump, the steady state (N_{st}) yields

$$\frac{N_{st}}{N_t} \sim \frac{|a|^2}{|a_{sat}|^2} \tag{1.57}$$

meaning that the carrier density is proportional to the intracavity energy. Replacing eq. 1.57 into eq. 1.52 we have

$$\Delta\omega_{e,st} = \frac{\alpha_H}{\tau_{a_0}}(\frac{|a|^2}{|a_{sat}|^2} - 1) \tag{1.58}$$

In addition to a linear shift of the cavity frequency, eq. 1.58 accounts for nonlinear frequency shift. Note that the shift of the cavity resonance frequency driven by charge carriers becomes proportional to the intracavity energy.

1.4.3 Thermal relaxation dynamics

Finally, we consider the thermal loading of the material inside the cavity. We will assume that the dynamics of the temperature increase, say at the center of the cavity, with respect to the substrate temperature is governed by the following equation:

$$\frac{d\Delta T}{dt} = \frac{-1}{\tau_{th}}(\Delta T - \Delta T_{st}) \tag{1.59}$$

where ΔT_{st} denotes the steady state of the temperature change and τ_{th} the thermal relaxation time. Separating contributions from incoherent pump and intracavity power, ΔT_{st} reads

$$\Delta T_{st} = \frac{1}{\rho C_p}(\frac{\eta_{pump} P_{pump} \tau_{dis,pump}}{V_{pump}} + \frac{P_{abs}\tau_{dis,cav}}{V_{cav}}) \tag{1.60}$$

where ρ is the density, C_p the specific heat capacity in the pumping region, η_{pump} is the fraction of the incident power absorbed, τ_{dis} is the heat dissipation time and $P_{abs} = 2|a|^2/\tau_{a_0}$ is the absorbed power (neglecting saturation), as we will see in chapter 2. Note that eq. 1.59 models temperature free relaxation in the material as an exponential process, which will be justified in chapter 4. Considering resonant injection only, we can write ΔT_{st} as a function of the intracavity energy $|a|^2$ as

$$\Delta T_{st} = |a|^2 \frac{dT}{dU} \tag{1.61}$$

where

$$\frac{dT}{dU} \equiv \frac{\Gamma \alpha_0 \tau_{dis,cav} v_{g_0}}{\rho C_p V_{cav}} \tag{1.62}$$

is the temperature increase as a result of the intracavity energy increase. Thus, eq. 1.59 becomes

$$\frac{d\Delta T}{dt} = \frac{-1}{\tau_{th}}(\Delta T - |a|^2 \frac{dT}{dU}) \tag{1.63}$$

Finally, the thermally induced frequency shift $\Delta\omega_{th}$ can be written in terms of the temperature variation ΔT in the following way:

$$\Delta\omega_{th} = -\omega_0 \frac{\Delta n_{th}}{n_{g_0}} = -\frac{\omega_0}{n_{g_0}} \frac{dn}{dT} \Delta T(t) \tag{1.64}$$

Let us now turn to steady states. The stationary thermally-induced frequency shift (eq. 1.64) then reads

$$\Delta\omega_{th} = -\frac{\omega_0}{n_{g_0}} \frac{dn}{dT} \frac{dT}{dU} |a|^2 \tag{1.65}$$

meaning that the nonlinear term in eq. 1.41, driven by thermal loading, is proportional to the intracavity energy, similar to eq. 1.58. However, we stress two differences: i) the relaxation dynamics, governed by τ_{th}, is much slower compared to electronic induced nonlinearities, and ii) the opposite sign of the nonlinear effects, namely thermal red-shift and electronic blue-shift.

1.4.4 Three-variable model for an active cavity

Writing eq. 1.41, 1.56 and 1.63 together we have the set of equations that describes the nonlinear dynamics of the system:

$$\frac{da}{dt} = [j(\omega_0 + \Delta\omega_e + \Delta\omega_{th}) - \frac{1}{\tau}]a + df$$

$$\frac{dN}{dt} = \frac{1}{\tau_{nr}}[-N - B\tau_{nr}N^2 - \frac{|a|^2}{|a_{sat}|^2}(N - N_t)] + R \tag{1.66}$$

$$\frac{d\Delta T}{dt} = \frac{-1}{\tau_{th}}(\Delta T - \frac{dT}{dU}|a|^2)$$

with $|a_{sat}|^2 = V_{cav}h\nu/\sigma\tau_{nr}v_{g0}$ and $dT/dU = \Gamma\alpha_0\tau_{dis,cav}v_{g0}/\rho C_p V_{cav}$ and

$$\begin{aligned} \Delta\omega_e &= \frac{\alpha_H}{\tau_{a_0}}(\frac{N}{N_t} - 1) \\ \Delta\omega_t &= -\frac{\omega_0}{n_{g0}}\frac{dn}{dT}\Delta T(t) \\ \frac{1}{\tau_a} &= \frac{1}{\tau_{a0}}(1 - \frac{N}{N_t}) \end{aligned} \tag{1.67}$$

In the case of having only thermal nonlinear effects and considering the steady states of the full system, eq. 1.66 yields

$$0 = [j(\delta - \frac{|a|^2}{U_{0,th}}) - 1]a + d\tau f \tag{1.68}$$

where $U_{0,th} = n_{g0}(dU/dT)/2Q(dn/dT)$ is the characteristic intracavity energy for thermal bistable threshold. Note that, since $dU/dT \propto V_{cav}$, $U_{0,th} \propto V_{cav}/Q$. Besides, the intrinsic bistability threshold, i.e. the power coupled into the cavity at threshold ($P^{(thermal)}_{intrinsic,thr}$), is proportional to $P^{(thermal)}_{intrinsic,thr} \propto U_{0,th}/\tau$, thus, $P^{(thermal)}_{intrinsic,thr} \propto V_{cav}/Q^2$, as pointed out in section 1.2.3.

On the other hand, considering only electronic nonlinear effects and the full steady states, eq. 1.66 becomes

$$0 = [j(\delta + \frac{|a|^2}{U_{0,e}}) - 1]a + d\tau f \tag{1.69}$$

where $U_{0,e} = \tau_{a_0}|a_{sat}|^2/\alpha_H\tau$ is the characteristic intracavity energy for electronic bistable threshold. Note that we have approximated $\tau_a \sim \tau_{a_0}$ in eq. 1.69 provided $\alpha_H >> 1$, which is the case in III-V semiconductors for injected wavelengths in the Urbach tail. As in the case of thermal bistability, since $U_{0,e} \propto V/Q$, $P^{(elec)}_{intrinsic,thr} \propto V_{cav}/Q^2$.

Considering an L3-type cavity in an InP suspended membrane with QW as active medium, we can estimate the intrinsic bistability threshold both for thermal and electronic origin. The constants needed for this calculation are obtained from the literature values and from the experiences that will be shown all along this manuscript. Table 1.2 resumes all these constants. Using these values, we have obtained intrinsic bistability thresholds of the order of $P^{(thermal)}_{intrinsic,thr} \sim 2$ μW and $P^{(elec)}_{intrinsic,thr} \sim 3$ μW, for the thermal and electronic thresholds, respectively. Note that both values are of the same order of magnitude. Moreover, they are three orders of magnitude smaller than typical thresholds reported in monolithic vertical cavities [24] and ring resonator

$V_{cav} \sim 0.08\ \mu^3$[95]	$\rho C_p = 1.5 J cm^{-3} K^{-1}$
$n_{g_0} \sim 3$	$\Gamma = 0.2^*$
$(dn/dT)/n \sim 0.63 \times 10^{-4} K^{-1}$[96]	Q=3750*
$\alpha_0 = 66 cm^{-1}$*	$\tau_{dis,cav} \sim 186$ ns[97]
$\tau_{nr} \sim 200$ ps[91]	$\lambda = 1.55\ \mu m$
$\alpha_H = 10$	$\tau \sim 6$ ps

Table 1.2: *Table summarizing all the constants involved in the calculation of the bistability threshold both of thermal and electronic origin. *See chapter 5.*

devices [94].

Note that eq. 1.68 and eq. 1.69 are analogous to the bistability equation developed in section 1.2 (eq. 1.33).

In addition, from this set of equation we can calculate the nonlinear refractive index (eq. 1.27). From $\Delta n/n_0 \simeq -\Delta\omega_e/\omega_0$ and eq. 1.52, considering the steady states of the carrier density (eq. 1.57), Δn yields

$$\Delta n = -\frac{n_0 \alpha_H}{\omega_0 \tau_{a_0}} \left(\frac{|a|^2}{|a_{sat}|^2} - 1\right) \tag{1.70}$$

Considering an uniform slab (i.e. neglecting distributed feedback effects) for simplicity, we can write $|a|^2 = (V_{cav} 2/v_{g_0}) I$. Now using eqs. 1.44 and 1.55 for τ_{a_0} and $|a_{sat}|^2$, respectively, eq. 1.70 reads

$$\Delta n \equiv n_2 I \sim -\Gamma \left[\frac{\alpha_0^2 \alpha_H \lambda^2 \tau_{nr}}{2\pi h c N_t}\right] I \tag{1.71}$$

According to the table 1.2, eq. 1.71 gives $n_2 \sim -3.5 \times 10^{-10} cm^2/W$. This value is six orders of magnitude higher than the nonlinear refractive index in silica ($SiO_2 : n_2 \sim 3 \times 10^{-16} cm^2/W$ [98]). The marked difference between this two values is a clear evidence of the advantages of single photon absorption in III-V semiconductors over intrinsic Kerr effects.

The set of equations (eq. 1.66) allows us to study nonlinear dynamical regimes of our system such as bistability, self-pulsing and excitability. Moreover, it contains the characteristic time scales of each process, such as the thermal relaxation time (τ_{th}) and the nonradiative recombination time (τ_{nr}). We will return to this set of equations along this manuscript and we will apply it to the particular cases studied during this thesis.

1.5 Conclusion

The bases of nonlinear dynamics in systems described by one and two variables were presented at the beginning of this chapter. By simple graphical methods we have deduced the behavior of systems with complex differential equations, such as the van der Pol oscillator with and without bias. Through these examples we have introduced important concepts for the understanding of this thesis, like the self-sustained oscillation regime and the excitable regime.

Some key concepts about nonlinear optical systems were introduced in section 1.2, in particular the parametric processes and the dynamical processes, although we focus on the latter. Dynamical processes allow interesting phenomena such as bistability and excitability. The first one has been extensively studied in the last four decades, partly for its potential application

to optical memories. The second one has been investigated in optical systems only recently. In particular it has never been reported in optical nanocavities, which motivated us to study in detail this regime in PhC nanocavities.

A model that involves the intracavity energy, the carrier density and the temperature was proposed in order to predict a large family of nonlinear dynamical behaviors in a PhC suspended membrane filled with an active medium. This model includes, in a simple set of equations, the dynamics of qualitatively different behaviors such as bistability (which involves a single nonlinear variable) and excitability (which involves two nonlinear variables). These equations will allow us to get physical insight into the different regimes observed along this thesis in PhC nanocavities.

Part I

Tapered fiber-assisted coupling into a nanocavity: Description, characterization and application.

This thesis aims to study nonlinear dynamical behaviors in 2D photonic crystal nanocavities. For this, the type of cavity and the method to couple light inside this cavity needs to be established. In the first chapter, we investigate the adequate type of cavity to obtain nonlinear behaviors and the coupling method: evanescent coupling via a tapered fiber. A theoretical model and numerical simulations are carried out in order to characterize and study the parameters that optimize this coupling.

A detailed characterization of the sample is given in the second chapter. Images and photoluminescence spectra are shown. Details of the tapered fiber fabrication and the positioning system are given. A detailed characterization of the coupling method can be found at the end of this chapter.

In the last chapter we apply this coupling method to measure important characteristic times of the sample. First, we determine the characteristic thermal relaxation time of the photonic crystal membrane. Next, a pump and probe technique is applied to measure the carrier recombination time. Both magnitudes will be useful in the following part for understanding non-linear dynamical regimes in active photonic crystal nanocavities.

Chapter 2

Theoretical and numerical calculations

Photonic crystals allow high degrees of freedom when designing an optical nanocavity. Much progress has been recently accomplished in realizing high quality factors and ultra small volume nanocavities. Among them, several cavity designs have been shown to be performant and robust, such as heterostructure cavities, H0 and L3 cavities. Cavities based on L3 configuration turn out to be adequate geometries for our porposes since high Q, small volumes and straightforward sets of evanescently coupled cavities can be realized. In the first part of this section we discuss some characteristics of these cavities, such as near and far field spatial distributions and quality factors obtained by FDTD simulations.

A mayor challenge in the context of nonlinear optics in nanocavities concerns efficient input light coupling methods. Several approaches can be adopted to achieve this, the usual one relying on integrated waveguides. Although this is an attractive option it presents some drawbacks such us the reduction of the coupling efficiency due to injection losses and material absorption. For this reason, we chose an alternative road: to couple light inside the cavity by evanescent waves via a tapered fiber. Therefore, the first question that emerges is how efficient this coupling can be. To answer this, in this section we develop a coupled mode theory formalism to characterize and quantify the coupling strength. In order to test this theory, numerical simulations are carried out for a simplified version of the cavity-fiber system. The results of such study are also discussed in this chapter.

2.1 FDTD simulations of a L3 Photonic Crystal cavity

Among all the different types of PhC cavities that can be studied, we have mostly worked with L3 type cavity, although we will see in chapter 8 some studies over heterostructure cavities. The L3 cavities allows high Q factor and they are well suited to be evanescently coupled through a tapered fiber. In order to characterise these cavities, FDTD (finite-difference-time-domain method) numerical simulations [99] of the system shown in fig. 2.1 have been carried out[1]. This method consists in computing the time-dependent Maxwell's equations (in partial differential form) in a discretized mesh using central-difference approximations to the space and time partial derivatives. The resulting finite-difference equations are solved as follows: the electric field vector in a volume of space are solved at a given instant in time; then the magnetic field vector components in the same spatial volume are solved at the next instant in time; and the process is repeated until the desired transient or steady-state electromagnetic field behavior is fully evolved [100]. In order to use the FDTD method, the spatial grid (spatial resolution) and the material (air, metal

[1]This simulations were developed in collaboration with Timothy Karle, post-doc in our group.

or dielectric), with the corresponding refractive index, in each of those points must be established.

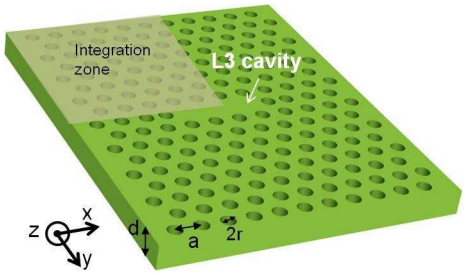

Figure 2.1: *Scheme of the L3 cavity simulated in FDTD. The parameters are: a=435 nm, r=0.3a.*

In the following, we simulate a modified L3 cavity in a PhC membrane, i.e. a L3 cavity with the two end holes shifted away a given distance. We have carried out simulations with a spatial resolution of $a/20 = 21.75$ nm in x and z-directions, $a\sqrt{3}/2 = 20.9$ nm in y-direction, and a material refractive index of 3.3. The PhC period and hole radius are a=435 nm and r=0.3a, respectively, where the two holes closing the cavity are shifted away 0.15a, and the dimensions of the sample are 12.2 μm x 8.3 μm. In order to exploit the symmetries of the system, the integration volume corresponds to one eight of the complete structure (grey zone in fig. 2.1). Then, the electromagnetic field is extended to the rest of the structure with the boundary conditions for the electric field depicted in fig. 2.2. The total integration time was 1 ps. The output of the FDTD simulation is used as the input data into a harmonic inversion algorithm (Harminv) [101, 102] in order to extract central frequencies and decay times, the latter being used to calculate quality factors. The system is excited with an electric dipole polarized in the y-direction laying in the center of the cavity.

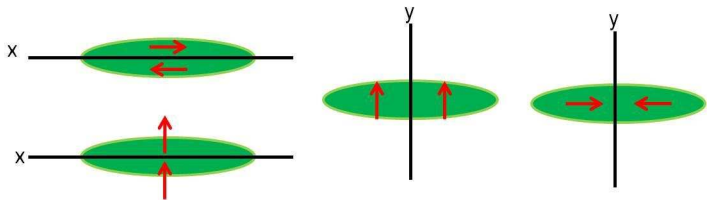

Figure 2.2: *Scheme of the boundary conditions for the electric field used in the FDTD simulations.*

For the system in fig. 2.1, the resonant mode is found at 1.598 μm with a quality factor of ~ 23000. For this mode, the electric and magnetic fields polarization (in x, y and z-direction) in near field (at the center of the membrane) have been recorded (fig 2.3). We observe the electromagnetic field concentrated in the cavity region and the principal component of the electromagnetic field in the y-axis, corresponding to an almost linearly polarized mode in the y-direction.

The far field emission profile in k-space is shown in fig. 2.4 calculated as the spatial Fourier transform of electromagnetic field monitors located at twice the membrane thickness (2a from the slab surface) in z-direction. We observe two lobes at $\sim 70°$ meaning that the emission of the cavity mode is not perpendicular to the surface but with a strong angle. For this reason, a resonant signal injected perpendicular to the surface do not couple to the cavity mode. Indeed

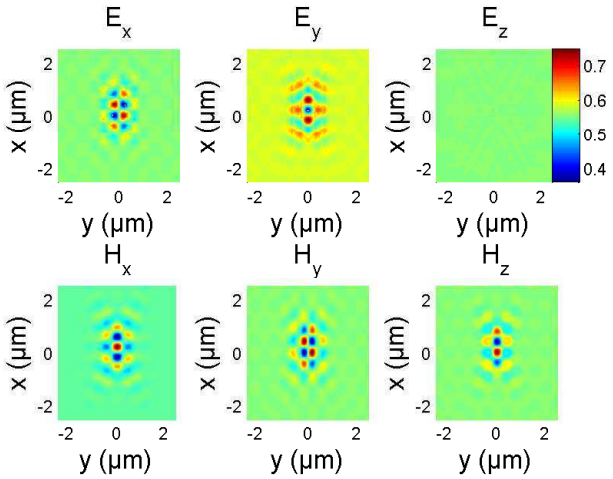

Figure 2.3: *Field spatial distribution at the membrane center for the system depicted in fig. 2.1.*

a different method to coupled light inside the cavity is likely to be implemented.

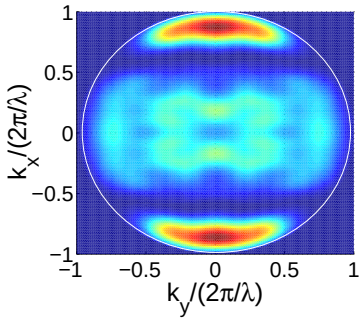

Figure 2.4: *Far field emission profile for the system depicted in fig 2.1 calculated as the Fourier transform of the field stored on a monitor positioned at twice the lattice period (~ 0.9 μm from the membrane surface).*

2.2 Coupling between a cavity and a fiber

The goal of this section is to describe the light confinement in an optical resonator coupled to the outside through an optical microfiber. Such a device can be directly modelled by means of e.g. FDTD methods [99], but such technique can be very time and memory-consuming in this case since the integration zone becomes much larger, both in the propagation direction and in z-direction, than the integration zone used for the configuration of fig. 2.1. In order to get physical insight into the different parameters, a simple theoretical framework is highly desirable. A good candidate is the well-known Coupled Mode Theory (CMT). The basic idea of coupled-mode theory is to decompose all propagating light into a linear superposition of the known modes of the uncoupled device (in our case the cavity and waveguide separated away), and then to calculate the coupling strength in presence of some coupling mechanism (cavity-waveguide evanescent coupling in our case). This requires, in principle, a strong approximation: the coupling does not change the intrinsic modes. This assumption remains valid as long as the

coupling strength is weak. However, even for strong coupling conditions, the intrinsic modes might be renormalized to take into account changes due to the coupling. The CMT is often technically and conceptually much more convenient than, e.g., recalculating the propagation modes for the actual situation in which light propagates in the full device.

In the following the coupling of a PhC cavity to a microfiber is described on the basis of the temporal coupled mode formalism developed by Fan et al. in [19]. The transmitted and reflected signals of one single-mode cavity coupled to the outside by two ports will be calculated, fig. 2.5. We first consider that the losses are only given by these two ports. From fig. 2.5 the injected/output fields are given by $S_{1+/-}$ and $S_{2+/-}$, for the left and right port respectively, d corresponding to the coupling from the cavity to the ports and κ from the ports to the cavity.

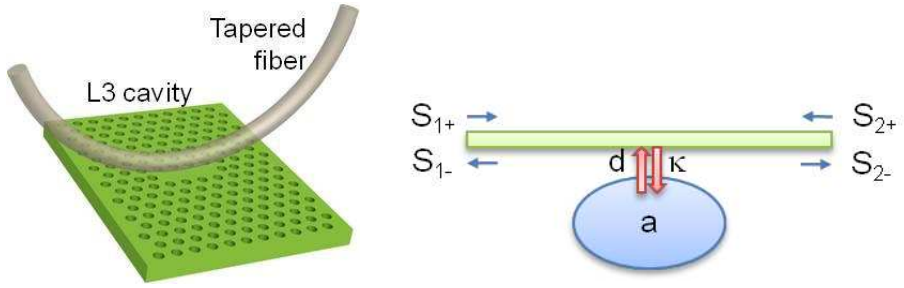

(a) (b)

Figure 2.5: *(a) System of interest: PhC nanocavity evanescently coupled to the outside by a tapered fiber. (b) Simplify scheme of the system in (a), a cavity coupled to the outside by two ports.*

In the following we apply the Dirac notation used in [19], where the kets represent column vectors. We will consider a general case where the coupling to each port can be different: $\kappa_{1/2}$ and $d_{1/2}$ correspond to the coupling to the left/right port. This generalization will be useful in part II where several cavities and ports will be studied. Let us start by writing the dynamic equation for the field amplitude (a) inside the cavity:

$$\frac{da}{dt} = (i\omega_0 - 1/\tau)a + (\langle\kappa|^*)|s_+\rangle \tag{2.1}$$

The first term in eq. 2.1 gives the resonance frequency ω_0; the second one accounts for the photon lifetime inside the cavity (τ) and the third represents the optical injection ($|S_+\rangle$) multiplied by the coupling constant ($|\kappa\rangle$).
The output signals depend on the injected field and on the field inside the cavity that couples to the ports, in the following way:

$$|s_-\rangle = C|s_+\rangle + a|d\rangle \tag{2.2}$$

where C is the (unitary) matrix for the direct process, meaning the incoming field can be directly coupled to the ports, and

$$|d\rangle = \begin{pmatrix} d_1 \\ d_2 \end{pmatrix}; |s_+\rangle = \begin{pmatrix} s_{1+} \\ s_{2+} \end{pmatrix}; |\kappa\rangle = \begin{pmatrix} \kappa_1 \\ \kappa_2 \end{pmatrix}; \langle\kappa|^* = (\kappa_1, \kappa_2) \tag{2.3}$$

where $d_{1/2}$ is the coupling strength between the cavities and the left/right port. Replacing $a(t) \to a'(t)e^{i\omega t}$ and $f(t) \to fe^{i\omega t}$, the steady state is given by:

$$a' = \frac{(\langle\kappa|^*)|s_+\rangle}{j(\omega - \omega_0) + 1/\tau} \tag{2.4}$$

In the following we recall Fan considerations (conservation of energy and time reversal symmetry) for determining relations among parameters, such us κ, d and C. For an external input $|S_+\rangle$ the scattering matrix, defined as $S|s_+\rangle = |s_-\rangle$, is given by:

$$S = C + \frac{|d\rangle\langle\kappa|^*}{j(\omega - \omega_0) + 1/\tau}, \tag{2.5}$$

where we have used eq. 2.4. Since S must be symmetric because of time-reversal symmetry, we have

$$|d\rangle\langle\kappa|^* = |\kappa\rangle\langle d|^* \tag{2.6}$$

meaning that the coefficients are not independent and must satisfy $d_1\kappa_2 = d_2\kappa_1$.

- Conservation of energy. Instead of exciting the cavity externally lets now consider the system in the absence of external input ($|s_+\rangle = 0$) and with finite amplitude inside the cavity at $t = 0$, so the energy ($U = |a|^2$) yields:

$$\frac{dU}{dt} = -2|a|^2/\tau = -\langle s_-|s_-\rangle = -|a|^2\langle d|d\rangle \tag{2.7}$$

  Hence

$$\langle d|d\rangle = 2/\tau \tag{2.8}$$

  It is a common assumption to consider identical ports ($d_1 = d_2 \equiv d$) which, in the case of the microfiber, means that the photon inside the cavity has equal probability to couple to the right and to the left side of the fiber:

$$\langle d|d\rangle = 2|d|^2 \tag{2.9}$$
$$|d| = \sqrt{1/\tau} \tag{2.10}$$

  This means that the coupling constant is related to the photon lifetime inside the cavity, as expected.

- Time reversal. The time reversal transformation, i.e. $t \to -t$, for the exponential decay process has the following solution

$$a_R = \frac{(\langle\kappa|^*)|s_+\rangle}{j(\omega - \omega_0) + 1/\tau} \tag{2.11}$$

  The time reversal situation can be represented as feeding the resonator with exponentially growing waves at complex frequency $\omega = \omega_0 - j(1/\tau)$, with amplitudes at $t = 0$ equal to $|s_-\rangle^*$ (i.e. $|s_+\rangle = |s_-\rangle^*$) and taking the complex conjugate, namely

$$a_R = a^* = \frac{(\langle\kappa|^*)|s_+\rangle}{j(\omega - \omega_0) + 1/\tau} = \frac{(\langle\kappa|s_-\rangle)^*}{2/\tau} = \frac{(\langle\kappa|d\rangle a)^*}{2/\tau} \tag{2.12}$$

  Therefore

$$\langle\kappa|d\rangle = 2/\tau = (\langle\kappa|d\rangle)^* \tag{2.13}$$

  This, together with eq. 2.6 and eq. 2.8, leads to the following important result

$$|\kappa\rangle = |d\rangle \tag{2.14}$$

meaning that the port-cavity coupling constants are equal to the cavity-port ones, as expected.

Moreover, since no output signal comes out while exciting with time-reversed excitation $|s_-\rangle^*$ we have

$$0 = C|s_-\rangle^* + a^*|d\rangle = a^*C|d\rangle^* + a^*|d\rangle \tag{2.15}$$

This leads to

$$C|d\rangle^* = -|d\rangle \tag{2.16}$$

Eq. 2.16 allows to demonstrate that the scattering matrix given by eq. 2.5 is unitary, which ensures self-consistency.

Finally, we consider intrinsic (radiative and/or absorption) losses with photon lifetime τ_0. In this case:

$$\frac{1}{\tau} = \frac{1}{\tau_c} + \frac{1}{\tau_0} \tag{2.17}$$

where

$$\frac{1}{\tau_0} = \frac{1}{\tau_{rad}} + \frac{1}{\tau_a} \tag{2.18}$$

with $\tau_{rad/a}$ the radiative/absorption time. The intrinsic losses can be considered as carried by an external port (so the theory remains unchanged) or as an "energy sink" (without considering extra ports). We chose this latter approach since it is independent of the nature of losses (radiative or due to absorption). In doing this, the scattering matrix (eq. 2.5) is no longer unitary because the incoming and outgoing power through ports are not equal, i.e. $\langle s_+|s_+\rangle \neq \langle s_-|s_-\rangle$. The difference is given by the radiated or absorbed power

$$P_{loss} = \langle s_+|s_+\rangle - \langle s_-|s_-\rangle \tag{2.19}$$

Using eq. 2.5 we have

$$\langle s_-|s_-\rangle = \langle s_+|s_+\rangle + |a|^2\langle d\rangle + 2Re[\langle d|C_+\rangle a^*] \tag{2.20}$$

Multiplying both sides of eq. 2.16 by C^+ to the left, and applying $^+$ to both sides we get $\langle d|C = -\langle d|^*$, so the last term in eq. 2.20 becomes

$$\begin{aligned} 2Re[\langle d|C|s_+\rangle a^*] &= -2Re[(\langle d|^*)|s_+\rangle a^*] && (2.21)\\ &= -2Re[(\langle \kappa|^*)|s_+\rangle a^*] && (2.22)\\ &= -2Re[|a|^2(j(\omega-\omega_0)+1/\tau)] && (2.23)\\ &= -2|a|^2/\tau && (2.24) \end{aligned}$$

As a result, eq. 2.19 becomes

$$P_{los} = 2|a|^2/\tau_0 \tag{2.25}$$

showing that the dissipated (i.e. radiated and/or absorbed) power is twice the energy per intrinsic photon lifetime as expected. This justifies the formula for the absorbed power used in section 1.4.

Including the intrinsic losses in eq. 2.5, the scattering matrix becomes

$$S = C + \frac{|d\rangle\langle d|^*}{i(\omega-\omega_0) + 1/\tau_c + 1/\tau_0} \tag{2.26}$$

In order to write down the full expression of the coefficients d and κ, the direct process has to be defined. We analyse the particular case of a cavity coupled by a tapered fiber, therefore evanescent coupling. The direct process can be described by the following unitary matrix:

$$C = \begin{pmatrix} 0 & exp(j\phi) \\ exp(j\phi) & 0 \end{pmatrix} \tag{2.27}$$

where ϕ is the accumulated phase through the fiber. C, given by eq. 2.27, relates S_{1-} with S_{2+} and S_{2-} with S_{1+}, see fig. 2.5.

Considering $d = exp(j\phi_d)/\sqrt{\tau}_c$, eq. 2.16 leads to $cos(\phi/2 - \phi_d) = 0$. This condition is satisfied with $\phi_d = \phi/2 + \pi/2$ which gives [20]

$$d = j\ exp(j\phi/2)/\sqrt{\tau}_c \tag{2.28}$$

In the following we consider the injection through the left port only ($|S_+\rangle = (f, 0)$) which accounts for the experimental conditions (see section 3.2). Using eq. 2.28 in eq. 2.26 we calculate the normalized transmission ($T = |s_{2-}|^2/f^2$) and the reflection ($R = |s_{1-}|^2/f^2$) signal as

$$T = \frac{(1 + 4\Delta^2 Q_0^2)Q_c^2}{2Q_0Q_c + Q_c^2 + Q_0^2(1 + 4\Delta^2 Q_c^2)} \tag{2.29}$$

$$R = \frac{Q_0^2}{Q_0^2 + 2Q_0Q_c + Q_c^2 + 4\Delta^2 Q_0^2 Q_c^2} \tag{2.30}$$

where $\Delta = (\omega - \omega_0)/\omega_0$, $Q_0 = \tau_0\omega_0/2$ and $Q_c = \tau_c\omega_0/2$ (the intrinsic and coupling quality factors, respectively) [103].

To fix ideas, let us study three particular cases of eqs. 2.29 and 2.30. Fig. 2.6.a shows the transmitted and reflected signal for an overcoupled cavity (i.e. when the intrinsic losses can be neglected, $Q_0 >> Q_c$). We observe a 100% contrast in the transmission dip. Fig. 2.6.b shows a more realistic situation where the two quality factors are of the same order of magnitude, in particular, we consider critical coupling, i.e. $Q_0 = Q_c$. Note that the resonance contrast in transmission is $\sim 75\%$ meaning that this configuration, where the coupling losses equals the intrinsic ones, is still suitable to probe the cavity resonance. Note that $R + T \neq 1$, which is due to the dissipation losses. In the particular case where $Q_0 << Q_c$, the undercoupled case, the resonance contrast significantly decreases, fig. 2.6.c, and the cavity can no longer be efficiently probed with the microfiber.

We can conclude from fig. 2.6 that the resonance contrast depends on the relation between Q_0 and Q_c. This resonant contrast is of great interest since it quantifies the coupling efficiency. In order to obtain the resonance contrast we calculate from eq. 2.29 the ratio of the "in resonance" ($\delta = 0$) transmitted power (P_t) to the input power ($P_{in} = |f|^2$) as follows:

$$T(\delta = 0) = \frac{P_t}{P_{in}} = \frac{1}{(1 + \frac{Q_0}{Q_c})^2} = \frac{1}{(1 + \frac{\tau_0}{\tau_c})^2} \tag{2.31}$$

Eq. 2.31 shows that the resonance contrast is given by the ratio $\frac{\tau_0}{\tau_c}$.
It is important to point out that a real tapered fiber has losses between the fiber input and cavity position and between the cavity position and the fiber output, fig. 2.7. The powers at the fiber input and output can be related to the power near the cavity as:

$$P_{in} = P_{input}e^{-\alpha_1 L_1} \tag{2.32}$$

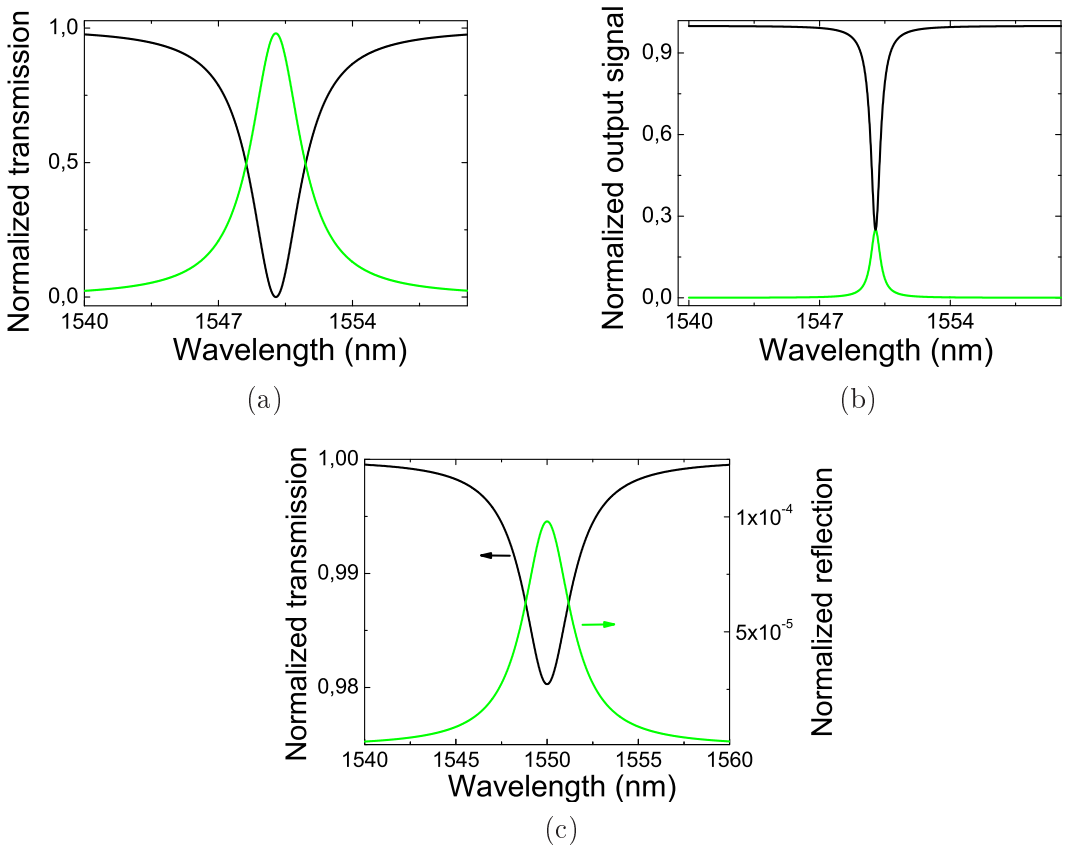

Figure 2.6: *Transmitted (black line) and reflected signal (green line) for a cavity coupled to the outside by two ports and excited through one of them. Three particular cases are studied: overcoupled cavity ($Q_0 = 50000$ and $Q_c = 500$)(a), for $Q_0 = Q_c = 5000$ (b) and undercoupled cavity ($Q_0 = 500$ and $Q_c = 50000$)(c).*

$$P_{t,output} = P_t e^{-\alpha_2 L_2} \tag{2.33}$$

where L is the fiber length and $\alpha_{1/2}$ are the input/output distributed losses in the fiber.

We can also relate the injected power (P_{in}) with the power off-resonance measured in transmission as:

$$P_{off,output} = P_{in} e^{-\alpha_2 L_2} \tag{2.34}$$

Taking the ratio of eqs. 2.33 and 2.34 we have

$$\frac{P_{t,output}}{P_{off,output}} = \frac{P_t}{P_i} \tag{2.35}$$

Eq. 2.35 means that the ratio of the "in resonance" transmitted power to the input power in the vicinity of the cavity is equal to the ratio of the powers measured at the fiber end: the transmitted signal in and off resonance, respectively.
We then define the coupling efficiency (η) as the probability that a photon inside the cavity couples to the fiber (in either direction, hence $\wp_c \propto 1/\tau_c$) with respect to the photon emission probability throughout all the coupling channels ($\wp_{tot} \propto 1/\tau_c + 1/\tau_0$), namely

$$\eta_c \equiv \wp_c/\wp_{tot} = \frac{1}{1 + \frac{\tau_c}{\tau_0}} = \frac{1}{1 + \frac{Q_c}{Q_0}} \tag{2.36}$$

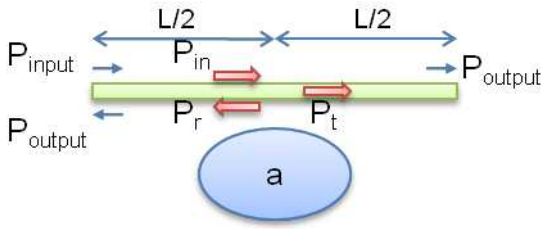

Figure 2.7: *Scheme of the distributed losses in the microfiber.*

Then, we can write the coupling quality factor as a function of the coupling efficiency as

$$Q_c = Q_0(\frac{1}{\eta} - 1) \tag{2.37}$$

The particular case studied in fig. 2.6. a, b and c corresponds to $\frac{Q_0}{Q_c}$ =100, 1 and 0.01, which gives η =0.97, 0.5 and 0.01, respectively. We point out that a strong coupling $\tau_c \ll \tau_0$ gives $\eta_c \to 1$, meaning that the lower Q_c/Q_0 is, the higher the coupling efficiency will be.

2.3 Numerical simulations

As we have previously seen, efficient coupling between a cavity and a tapered fiber can be obtained provided Q_c is of the order of (or much smaller than) Q_0. In order to test the CMT model developed in the previous paragraphs in a more realistic system, CAMFR (Cavity Modelling Framework) [104, 105] simulations of a cavity and a waveguide are carried out. This method is based on a principle called eigenmode expansion. Rather than working in time domain as in FDTD method, the structure is divided in a number of "slabs" where the refractive index profile is uniform in the z-direction. Instead of specifying the fields explicitly at a number of grid points, the fields in each layer are written as a sum of the local eigenmodes of that particular layer. This leads to a much more compact representation of the field and therefore shorter computation times. Moreover, contrary to spatial discretisation, the calculation time of a layer is independent of the length of that layer. Also, periodicity or quasi-periodicity is exploited in a more powerful way.

This method requires a discrete set of modes in each slab. In order to achieve this, the structure under study is typically enclosed in a metal box. Unfortunately, this can create parasitic reflections: radiation that would otherwise travel freely towards infinity is now completely reflected at the metal boundaries, returns to the structure, and disturbs the simulation results. In order to overcome this problem, CAMFR makes use of advanced boundary conditions, the most prominent of which are perfectly matched layers (PMLs). These layers can be thought as layers with a real refractive index, but with a complex thickness. This complex thickness provides reflectionless absorption of the incident field, regardless the incidence angle, wavelength or polarisation. The use of these advanced boundary conditions not only improves the accuracy of the model, but also speeds up the computation time, as the simulation boundaries can now be placed much closer to the structure [106]. In our simulations PML boundary conditions separated from the structure by 5 μm have been used.

Since the system must have at least one invariant direction for a simplest implementation of the CAMFR code, the system has to be 2D. For this reason we simulate a 1D periodic

waveguide (wg), fig 2.8 in dark grey, as a simplified version of the PhC structure. The parameter ϵ is chosen so as to respect the same filling factor as the PhC in fig. 2.1, then $\epsilon = \pi d/8$. The field propagation is in the x-direction and the system is invariant in the z-direction.

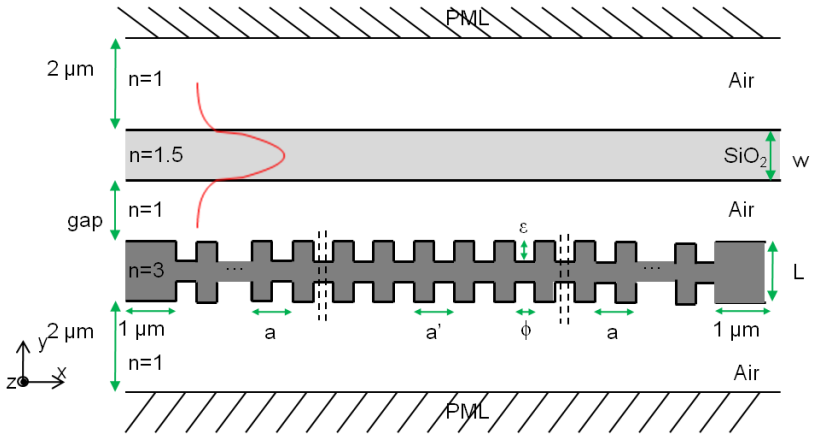

Figure 2.8: *Sketch of the 2D system, representing the cavity and fiber, simulated with CAMFR. The parameter values are: a=400 nm, a'=420 nm, ϕ=240 nm, $\epsilon = \pi\phi/8$=94 nm , L=250 nm. The red curve corresponds to the spatial profile of the injected field .*

The WG shown in fig. 2.8 (in dark grey) corresponds to the PhC while the fiber is modelled by a simple uniform slab, invariant both along the x and z-directions, fig. 2.8 in light grey. The fiber is represented by a SiO_2 (n=1.5) layer of thickness w and separated away from the WG (n=3) a distance called *gap*. The two PML layers are 2 μm over the SiO_2 and under the WG. Those spaces are filled with air. The cavity is a 1D heterostructure composed by an inner periodic WG (period a') and two outer periodic WGs (period a). Light confinement into the inner WG is obtained by a 20 nm-increasing a' with respect to a. The length of the inner WG is chosen to be 6 periods. The outer WGs constitute the cavity mirrors whose length has been set to 10 periods. We explore the coupling efficiency and the coupling quality factor for different fiber thickness (w) and air gap.

We first compute the solutions of the system without the fiber. In order to obtain the cavity modes, the band diagrams for the inner WG (red dots) and for the outer WG (black dots) are calculated, fig. 2.9.a. This gives a range of wavelengths for the cavity mode (1.290 $\mu m < \lambda <$1.355 μm), these wavelengths lying from the inner to the outher band edges. Then, the transmitted and reflected signal are computed within this wavelength range. For this, the injected field is set as the fundamental mode of the unstructured WG (fig.2.8 without the fiber). The transmitted and reflected signal in that mode are shown in fig. 2.9.b (black and red lines, respectively). We observe a resonance at $\lambda = 1.3295$ μm with a quality factor of $Q = 73888$. This wavelength is pointed out in the band diagram with a green circle (fig. 2.9.a). Note that this lies within the mirror band gap. Injecting the system resonantly ($\lambda = 1.3295$ μm) we plot the field spatial distribution in figs. 2.9.c and d. The intensity confinement in the cavity region can be observed.

Let us now consider the whole structure. We start calculating the band diagram of the inner WG (red dots) and the outer WG (black dots) in presence of the SiO_2 layer, fig. 2.10.a, which gives a range of wavelengths for the cavity mode (1.32 $\mu m < \lambda <$1.395 μm). The horizontal lines

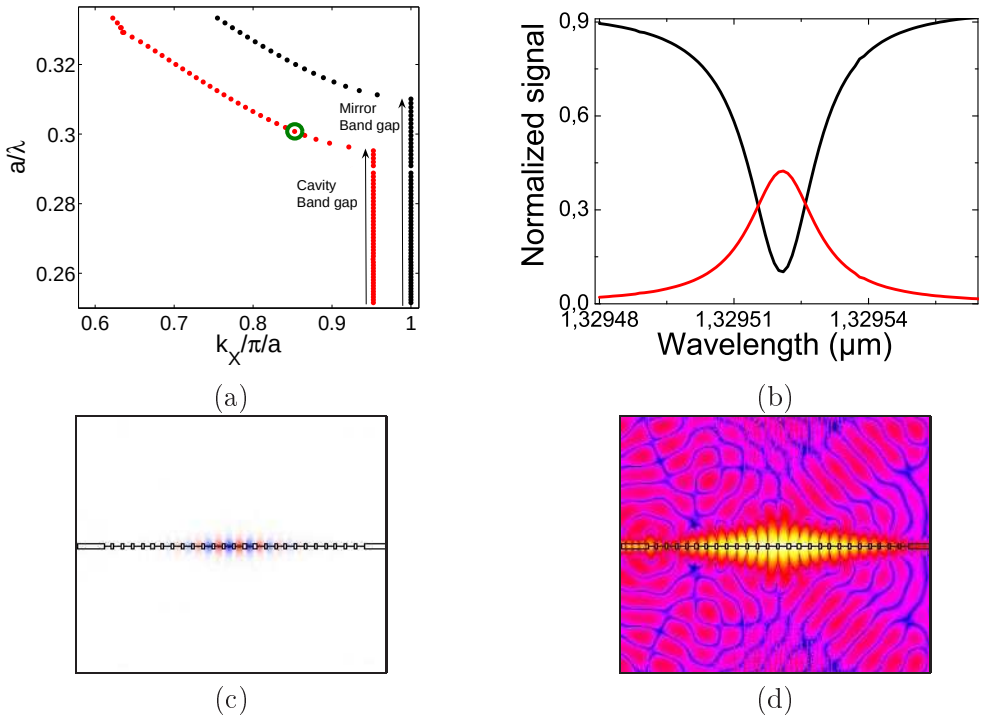

Figure 2.9: *(a) Band diagram for the periodic structure with a=400 nm in black dots and a'=420 nm red dots. Pointed out with a green circle we show the cavity mode position. (b) Transmitted and reflected normalized signals for the structure in fig. 2.8 without the fiber. The resonance is centered at* $\lambda = 1.3296$ *μm with a quality factor of* $Q_0 = 73888$. *(c) Field distribution in the structure for an injected signal in the fundamental mode at* $\lambda = 1.3295$ *μm. (d) Idem in logarithmic scale.*

in fig. 2.10.a show the position of the band gap of the inner and outer WGs (green and blue line, respectively) without the "fiber". Note that due to the presence of the fiber the band diagram shifts to longer wavelengths. Again, in order to study the transmitted and reflected signals, the injected field must be defined. The injection is launched through the fiber and it is set to the fundamental mode of the former $|\Psi_{0,fiber}\rangle$. The transmitted and reflected signals through the fiber are computed by projecting the transmitted and reflected fields on $|\Psi_{0,fiber}\rangle$. Total powers in reflection and transmission have also been computed. These signals contain information of the total energy crossing the right and left sides of the structure (fig. 2.8). Fig. 2.10.b shows the reflected and transmitted signal through the fiber (blue and green line, respectively) and the total ones (red and black lines, respectively) for $w = 1.5$ μm and $gap = 0$. A mode at $\lambda = 1.364$ μm is observed with a $Q_{loaded} = 520$. The position of the resonance wavelength in the band diagram is pointed out with a green circle (fig. 2.10.a). Note the difference between Q_{loaded} and Q_0: this means $Q_c << Q_0$ since $1/Q_{loaded} = 1/Q_0 + 1/Q_c$. From fig. 2.10.b we obtain that almost 50% of the total transmitted and reflected energy in resonance is not coupled through the fiber. The energy transfer between the fiber and the cavity is shown in fig. 2.10.c and d where we plot the field distribution in the structure for a resonant injection ($\lambda = 1.364$ μm). Note the absence of transmitted signal meaning the coupling is efficient.

Two different fiber thicknesses are studied in fig. 2.11.a, $w = 0.8$ μm and $w = 1.5$ μm, where the coupling efficiency (η) is calculated according to eqs. 2.31 end 2.36. We observe that

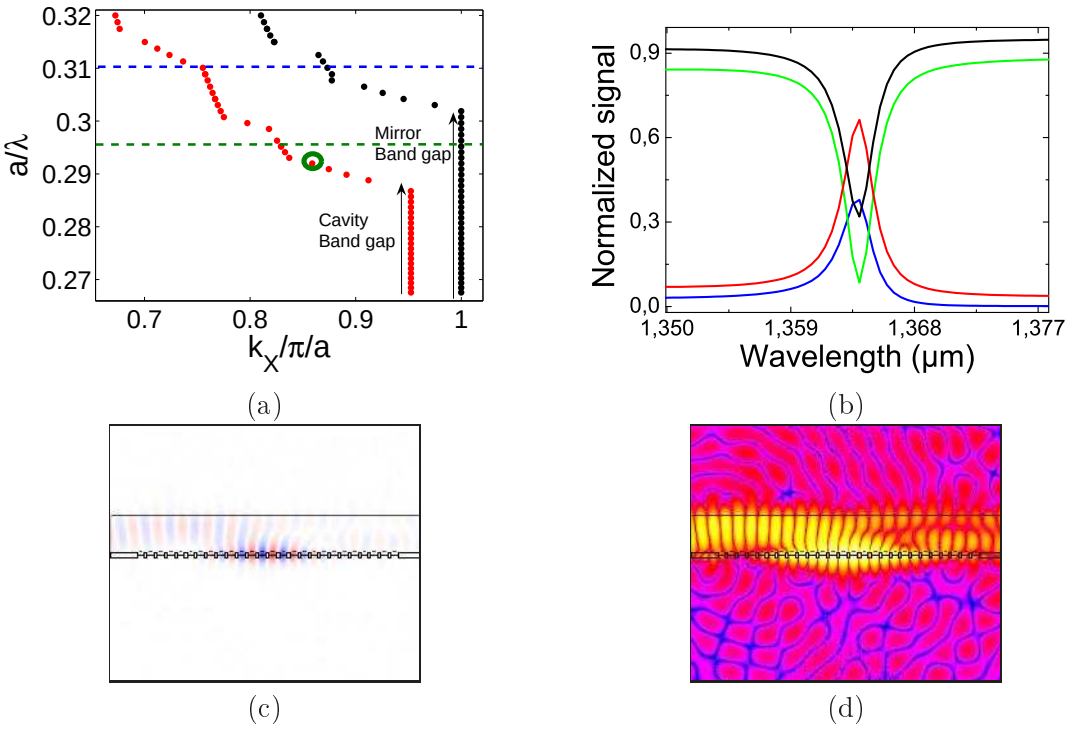

Figure 2.10: *(a) Band diagram for the periodic structure, this time in presence of the fiber, with a=400 nm (black dots) and a'=420 nm (red dots). The cavity mode position is highlighted with a green circle. The horizontal lines show the position of the band gap of the inner and outer WGs (fig. 2.9.a) without the fiber, green and blue line, respectively. (b) Reflected and transmitted normalized signals through the fiber, blue and green line, respectively, and over all the system modes, red and black line, respectively. The cavity mode is at* $\lambda = 1.364$ *μm and the resonance quality factor is* $Q = 520$*. (c) Field distribution in the structure while injecting through the fiber resonantly with the cavity mode (*$\lambda = 1.364$ *μm). (d) Idem in logarithmic scale.*

the maximum η for $w = 0.8$ μm is attained for a cavity-fiber distance different from zero, as it has also been found in [85]. Nevertheless, we find that for a wider fiber ($w = 1.5$ μm) the maximum η is achieved when cavity and fiber are in contact. Importantly, even if the efficiency is reduced with the fiber thickness, a maximum coupling of $\sim 70\%$ can still be achieved with $w = 1.5$ μm.

The coupling efficiency for different w when the cavity and the fiber are in contact (gap=0) are investigated in fig. 2.11.b. Although η decreases with w, an efficiency of $\sim 20\%$ can be achieved with a thickness of 3 μm. We will see in section 3.2.2 that this thickness corresponds to the experimental conditions. Let us stress that, since τ_c depends on the particular geometry of the cavity, we can expect differences when dealing with L3 cavities instead of 1D-heterostructures.

Fig. 2.12 shows the loaded quality factor (black dots) as a function of the air *gap* for $w = 1.5$ μm, directly calculated from the resonance width, $Q_{loaded} = \lambda/\Delta\lambda$. The coupling quality factor (Q_c) is given by eq. 2.37:

$$Q_c = \eta Q_{loaded} \tag{2.38}$$

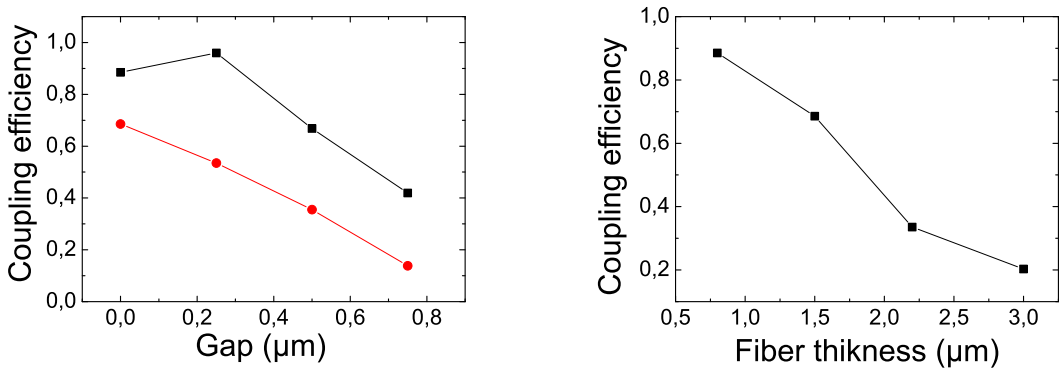

(a) (b)

Figure 2.11: *(a) Coupling efficiency as a function of the cavity-fiber distance (gap) for two different fiber thickness (w): (■) $w = 0.8$ μm and (●) $w = 1.5$ μm. (b) Coupling efficiency as a function of the fiber thickness while the cavity and the fiber are in contact (gap=0). The solid lines are guides to the eye.*

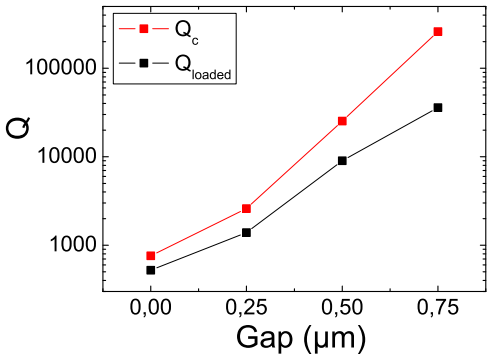

Figure 2.12: *(a) Loaded (Q_{loaded}) and coupling (Q_c) quality factors as a function of the air-gap for $w = 1.5$ μm, in red and black dots, respectively. The solid lines are guides to the eye.*

We observe an increase of Q_{loaded} and Q_c with the air gap, associated, as expected, to the coupling efficiency decrease with the fiber-WG separation (fig. 2.11.a). In addition, we have found that the cavity Q-factor Q_{rad} (which,in this case, is equal to Q_0 since no absorption is considered) obtained from eq. 2.37 is lower than the one without the fiber ($Q_{rad} < 74000$), and depends on the gap distance. We interpret this as additional fiber-induced losses in the cavity. This show that, in general, Q_{rad} can be lower than the intrinsic cavity Q-factor.
In conclusion, these simulations show that the intrinsic parameters of the cavity, ω_0 and Q_{rad}, may change due to the presence of the fiber. Thus, given a fiber-cavity configuration, with a certain coupling efficiency, the relevant parameters Q_{rad} and Q_c should be computed from eqs. 2.37 and 2.38; Q_{rad} cannot be determined from independent measurements without the fiber. Besides, the coupling efficiency as a function of different parameters of the system was studied. We have found that even for a fiber thickness of 3 μm a coupling efficiency of $\sim 20\%$ is achieved; we will see in following chapter that this configuration approaches the experimental conditions.

2.4 Conclusion

The main characteristics of a L3 cavity such as the mode position, the quality factor and the emission profile in near and far fields were obtained by means of FDTD simulations. Such simulations provided target design parameters for the fabrication of L3 cavities. Intrinsic quality factors of $\sim$ 23000 have been obtained for resonant cavity modes aroun 1.5 μm. Such high quality factors are compatible with efficient light coupling using a microfiber.

A theoretical model based on coupled mode theory was developed to characterize the coupling between a microfiber and a cavity. We have found that the coupling efficiency (η) depends on the taper-cavity coupling time (τ_c) and the cavity photon lifetime (τ_0) as $\eta = 1/(1 + \tau_c/\tau_0)$. In addition, the ratio τ_c/τ_0 can be easily related to the transmission through the taper at the cavity resonance (T) as: $T = 1/(1 + \tau_0/\tau_c)^2$. These results will be useful in the next chapter to quantify the coupling efficiency.

The simple formulas derived with CMT were tested with numerical simulations of a 1D-heterostructure cavity coupled to a 1D SiO_2 waveguide modelling the optical microfiber. We found that the presence of the fiber may alter the cavity intrinsic parameters such as the quality factor and the resonance wavelength. The fiber characteristics necessary to obtain efficient coupling conditions were studied. We found that even for a fiber thickness of 3 μm, when the fiber and the cavity are in contact, a coupling efficiency of $\sim$ 20% can be achieved. Remarkably, we will see in the next chapter that this value is in good agreement with the value found experimentally for the coupling efficiency of light into a L3 PhC nanocavity using a tapered optical fiber.

Chapter 3

A PhC cavity evanescently coupled to a tapered fiber

According to the results in chapter 2, efficient coupling between a microfiber and a cavity is possible provided the coupling quality factor is lower than the intrinsic quality factor. In this chapter we establish the experimental conditions for this to occur. In the first section we present, describe and characterise the sample. In the second section, we describe the fabrication and the nano-positioning system of the tapered fiber used to couple the cavity. Finally, we characterize the coupling efficiency.

3.1 Sample description

As it was mentioned in chapter 1, 2D photonic crystal nanocavities allow high qualities factors (up to 10^6 in the state of the art) meaning that they are, in principle, well adapted for evanescent coupling. In the following section we present a detailed description of a typical 2D PhC sample studied during this thesis.

3.1.1 Photonic crystal L3 cavity

The samples are 10 μm x 50 μm triangular lattice photonic crystals (PhC) of air holes in an InP suspended membrane , with a nanocavity in the center (fig. 3.1). The nanocavity is a modified L3 (three missing holes over a line of the PhC), where the two holes closing the cavity are shifted away by 0.15a. Noda et al. [67] have demonstrated that this shift increases the cavity quality factor of almost one order of magnitude.

As discussed in chapter 1, the QDs present high inhomogeneous broadening emission which allows to probe cavity modes in all this spectral range. This is one of the reasons that motivated the choice of QDs as the active material in the initial studies. In addition, as it has been mentioned in chapter 1, the absorption coefficient, which can lead to a reduction of the intrinsic quality factor, is lower in QDs than in QW materials allowing a higher coupling efficiency and thus an easier characterization of the coupling between the cavity and the fiber. The suspended InP membrane (262 nm-thick) thus incorporates a central single layer of self-assembled InAsP/InP quantum dots (QDs), fig. 3.2.a, whose density is $1.5 \times 10^{10} cm^{-2}$ and whose luminescence at 300 K is centered around 1.55 μm (fig. 3.2.b) with a 195-nm inhomogeneous broadening [107]. The membrane thickness ($\lambda/2n$) is such that the field maxima (@1550 nm) is located at the center of the membrane, where the active material is found. The whole structure, incorporating a GaInAs sacrificial layer under the InP, is grown by metalorganic vapour phase epitaxy (MOCVD). The

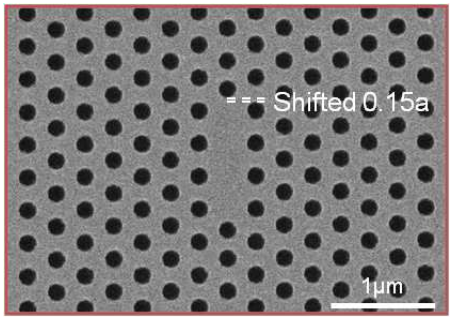

Figure 3.1: *MEB (electron beam microscopy) image of a modified L3 cavity (triangular lattice with period a=465 nm, holes radius=120 nm). The two holes closing the cavity are shifted away by 0.15a.*

air layer between the InP membrane and the substrate has a thickness of $\sim$ 1.16 μm. The QD luminescence cannot be obtained by means of photoluminescence measurements directly from the sample since the luminescence produced by the surrounding GaInAs completely masks the InAsP emission. Therefore, the photoluminiscence has been measured in a sample without InGaAs underneath (fig. 3.2), where the QDs were grown under the same procedure [108].

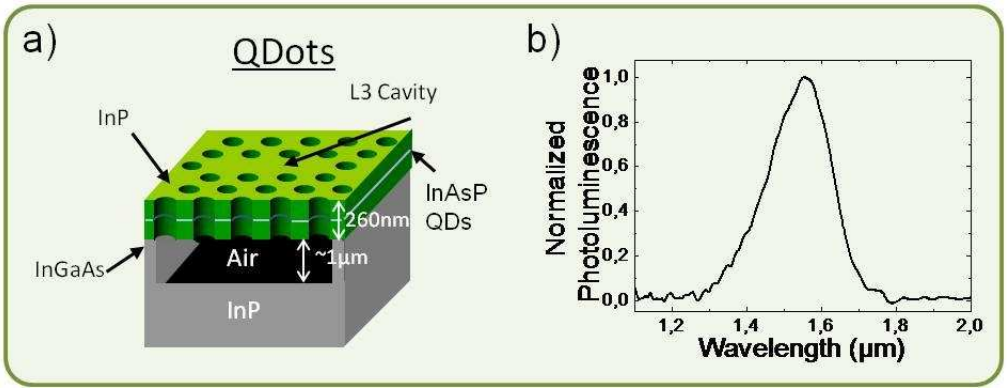

Figure 3.2: *Sketch of the photonic crystal-membrane sample. b) QDs photoluminescence spectrum [108].*

3.1.2 Sample fabrication

This section contains a summary of the fabrication steps. The samples were fabricated at the LPN clean room by Remy Braive and Isabel Sagnes. More details about the fabrication are given in [109].

The first step is the metalorganic vapour phase epitaxy (MOCVD) of the whole structure. This starts by the growth of an InGaAs sacrificial layer of 1.16 μm over an InP buffer, followed by an InP layer, which will form the suspended membrane. In the center of the latter the InAsP/InP quantum dots are grown and subsequently encapsulated with the InP. The InAsP layer ($\sim 2-3$ nm thickness) under the QDs is called the wetting layer (WL). The membrane total thickness is $\sim$260 nm and it corresponds to $\lambda/2n_{eff}$ whit n_{eff} the effective refractive index calculated as the weighted average of the refractive index of air and material. For details about the membrane thickness impact in the cavities modes and their emission diagram please refer to [110].

The second step is the fabrication of an etching mask in order to define the geometrical parameters of the 2D PhC. This mask is made of a 300 nm thickness layer of Si_3N_4 deposed at $300°C$ by PECVD (Plasma Enhanced Chemical Vapor Deposition) over the InP. The SiN is then covered by 450 nm of an electro-sensitive resin (PMMA, Polymethyl Methacrylate). The sample is positioned in an e-beam writer (LEICA EBPG 5000+) which allows to focus an electron beam over the resin following the structure design, with 2.5 nm precision. Then, using an appropriate chemical solution the isolated regions are dissolved.

After the resin isolation, the design is transferred into the nitride layer by a dry etching using a CPP-RIE (Capacitively Coupled Plasma-Reactive Ion Etching) which allows a directional etching. Then the motif is transferred to the semiconductor by a ICP-RIE (Inductively Coupled Plasma-Reactive Ion Etching). During this stage the InP memebrane is drilled by cylindrical air-holes (few hundreds nm depth) down to the InGaAs sacrificial layer.

Finally, in order to obtain the suspended membrane, the sacrificial layer is etched out in a wet atmosphere. Specifically, a $H_2SO_4 : H_2O_2 : H_2O$ chemical solution is able to penetrate into the sample trough the holes eventually dissolving the InGaAs.

3.1.3 Photoluminescence

Set up description

The experimental set up used to measure the photoluminescence spectrum of the QD samples is shown in fig. 3.3[1]. The photoemission of the active material (QDs) is used to identify the cavity mode under incoherent pumping @532 nm, with a CW, frequency doubled Nd:YAG laser. Indeed, the resonant mode filters the broadband luminescence giving a spectral narrow peak. The pump is focused onto the cavity by a large work-distance microscope objective ('Mitutuyo', M plan Apo NIR, X20, f=100 mm, $NA = 0.4$). The emission is collected by the same objective and send to either a CCD camera ('Pulnix', TM-6EX) in order to visualize the sample, or to a spectrograph/monochromator ('Princeton Instruments', Acton SP2500i, with a 600 g/mm grating 1.6 μm blaze and Ni cooled camera). After passing trough the spectrometer the signal is sent to an InGaAs 1D array spectroscopy camera ('Princeton Instruments', OMA V, spectral range 0.7 μm-1.6 μm, resolution FWHM: 0.315 nm).

Sample characterization

A typical spectrum of a L3 cavity sample is shown in fig. 3.4.a for a pump power of 41 μW. The PhC period and hole radius are a=445 nm and r=120 nm, respectively, giving a mode center at 1452 nm. The Q factor obtained from the FWHM of the cavity resonance gives 4800. It is important to point out that the measurement of the quality factor $Q = \lambda/\Delta\lambda$ by means of photoluminescence spectra has two limitations: one instrumental, since the FWHM of the emission peak is limited by the monochromator resolution; and one inherent to the system due to the material absorption, which leads to pump power dependent quality factors. Therefore, the Q measured for low pumping powers has to be considered as a lower bound limit approximation of the intrinsic quality factor.

[1]The QD photoluminescence was carried out in collaboration with Richard Hostein and Alexios Berveratos from LPN-PEQ group.

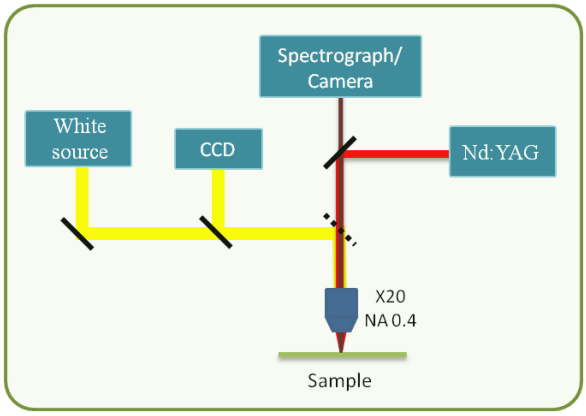

Figure 3.3: *Experimental set up sketch to obtain the photoluminescence spectrum of the sample. The sample is excited with a CW Nd:YAG laser (@532 nm) and the emission is sent to a spectrograph/camera.*

In order to study the laser effect, measurements of the collected intensity and the central wavelength of the resonance as a function of the injected power are performed, fig 3.4.b and c respectively. For lasers with a β factor lower than 1 (β= emission in the cavity mode/the whole emission), we expect a S-shaped curve for the emitted power. We also expect a change in the resonance wavelength as a function of the injected power in the following way: for an injected power under the laser threshold, a blue shift should be observed given by band filling effects (the carrier density increase changes the refractive index shifting the resonance to the blue, see section 4.2). Above the threshold, in turn, a red shift should be observed due to the membrane heating. Further increase of the pump power may induce a mechanical deformation of the membrane with a subsequent increase of optical losses and eventually complete destruction of the membrane. Since we did not observe neither a S-shape in fig.3.4.b nor a minimum in the wavelength shift in fig.3.4.c three posibilities can be considered: i) the system behaves as a laser with strong β factor ($\beta \sim 1$)[111]; ii) the threshold is at a lower power and we do not have enough sensitivity to observe it; iii) the sample does not show a laser effect. The usual method to identify laser emission is performing a second order correlation function of the emitted photons, which is out of the scope of this thesis. Though, let us stress the fact that laser emission in not a necessary condition for the existence of bistability or excitability, which are the phenomena sought in this work.

3.2 Tapered fiber assisted coupling

Among all the systems that can be used to couple light into the photonic crystal cavity, we chose the tapered fiber approach since it avoids insertion, propagation and absorption losses in a waveguide while it allows easily probing several cavities on a chip.

However, this coupling method requires a device allowing to control the taper position and movement with high precision (sub-μm resolution) and stability. We have implemented this technique for the first time at the LPN.

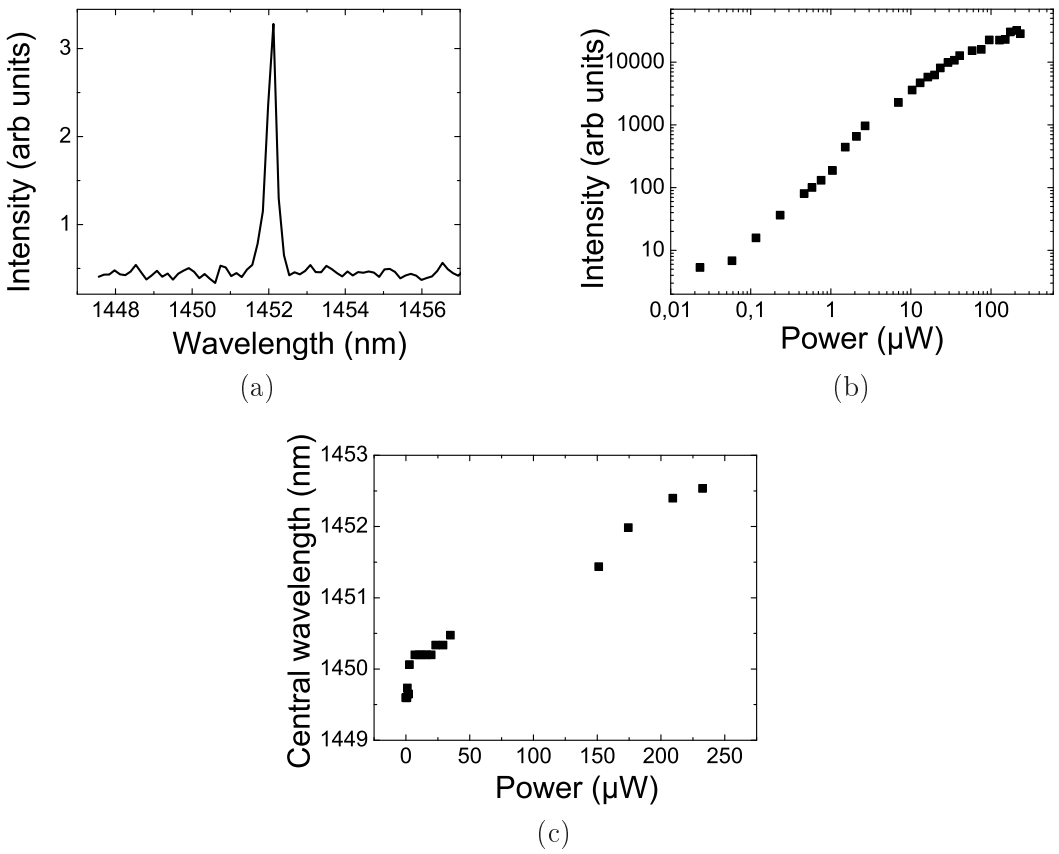

Figure 3.4: *(a) Photoluminescence spectrum of a L3 cavity (fig. 3.1.a) for 41 μW of pump power and 0.1 s of integration time. The mode is at $\lambda = 1452$ nm and the resonance quality factor is $Q \sim 4800$, limited by resolution. (b) Output intensity integral as a function of the pump power. Both axes are in logarithmic scale. (c) Resonance central wavelength as a function of the pump power.*

3.2.1 Tapered fiber fabrication and characterization

The first tapered fibers we used were commercial ones[2]. According to the literature [85, 112] the shape of the fiber is important to avoid losses in the bulk material, i.e. outside the PhC membrane. The first shape we tested was a loop, shown in fig 3.5.a. This configuration showed serious problems of instability, see fig. 3.5.b. The distance between the fiber and the sample cannot be controlled with precision at short distances since, closer than a certain value, the fiber sticks onto the sample. Thus, the fact of "attaching" and "detaching" the fiber from the sample made the loop change. As a next trial, an U-shape where the fiber was fixed on a small glass bar was tested, shown in fig 3.5.c.

This configuration was used to make the first characterization of the coupling between the fiber and the QD sample. At that time it became clear that the most efficient way to converge to a performant microfiber design was to get involved into the fabrication process ourselves, while taking benefit from the know how of a research team already involved in taper fabrica-

[2]A french company "LASEO" has fabricated customized tapered fibers on the basis of our specifications (size, shape and losses).

tion. For this reason, we started a collaboration with Laurent Bigot at the Laboratory PhLAM (Laboratoire de Physique des Lasers, Atomes et Molecules) in Lille. I participate, under his supervision, to the fabrication of the tapered fiber. Trying to reproduce old mounting techniques from LASEO, we noticed that fixing the taper onto a 5 mm-width bar was quite difficult. Finally we arrived to the most suitable configuration: the U-shape fixed on a microscope slide, fig. 3.6.a.

(a) (b) (c)

Figure 3.5: *(a) Image of the first tapered fiber we have tried: a loop shape. (b) Image of the same fiber coiled with itself. (c) Second type of fiber: an U-shape onto a 5 mm-wide bar.*

The fabrication consists firstly in removing the plastic jacket, exposing the 125 μm cladding, of a standard single-mode telecommunication fiber in a region of the order of 3 cm. After this, the fiber is fixed at both extremities and a gaz burner is positioned 1 mm under the naked fiber, fig. 3.6.b. The two fixed points pull out the fiber at 50 $\mu m/seg$ for 175 seconds until arriving to a minimum diameter between 1 and 3 μm. Once the fiber is tapered down it is bent in the narrow part forming an U-shape and then it is sticked on a microscope slide using UV glue in such a way that the thin curved segment (between 0.5-1 cm) is freely standing in air, see fig. 3.6.c. We have found that such length of the free standing segment achieves a good compromise between mechanical stability and physical constraints in the set-up. In addition, the curvature of the fiber at the stretched segment reduces the optical coupling to the substrate outside the photonic crystal membrane, thus decreasing optical losses [85]. Finally, two APC fiber pigtails were soldered at each fiber end.

The next step is the characterization of the taper. Losses are measured by means of a @1550 nm CW source. We have set the specifications for the maximal optical losses in the taper fiber to 10 dB. The fabricated tapers typically have between 3 db and 7 db. It is important to point out that the taper thickness also plays a dramatic role. We have found that for thickness lower than 1.5 μm-diameter the fiber becomes extremely unstable and fragile (losses rapidly increase with the use). On the other hand, for diameters larger than 4 μm, we verified that the evanescent tail out of the fiber is reduced and the coupling becomes inefficient. The tapers used during this work have diameters between 1.5 and 3 μm (fig. 3.6.a inset). It has been observed a degradation of the fiber (quantified by the losses) with the use: in general, the tapered fiber lifetime is ~ 3 months. The causes of degradation are, among others, the humidity and micro-fissures caused by the repeated contact with the sample (as discussed in the next paragraph). The fibers are fabricated in Lille and sent to Marcoussis by the post in an adequate package. Even though they seem very fragile, no taper has been broken down during the delivery.

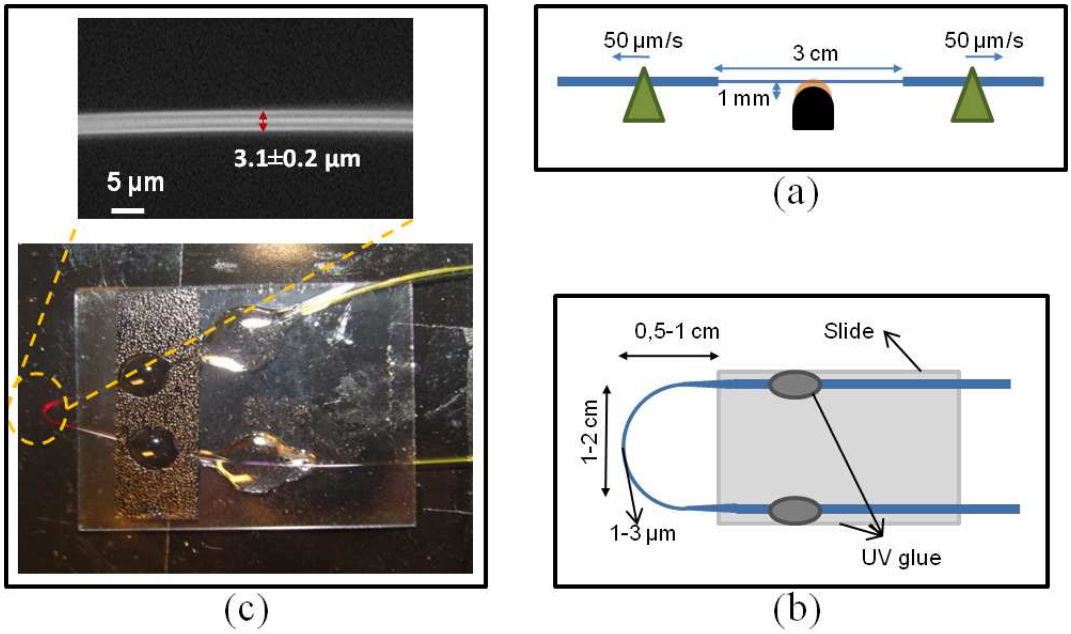

Figure 3.6: *(a) Image of the tapered fiber: final mounting. Inset: 50x microscope image of the thinner part of the fiber. (b) Sketch of the tapered fiber fabrication characteristics and (c) sketch of the mounting.*

3.2.2 Coupling efficiency

The microscope slide with the tapered fiber is fixed in a 3-axes stage with two PZT-driven axes (x-z), fig. 3.7. The piezoelectric is used to locate the fiber exactly over the cavity. Besides, the sample is also mounted over a PZT-driven axes that allows to move it in the x-y directions. Hwang et al. [85] have demonstrated that the maximal coupling efficiency is obtained for a PhC-taper vertical gap of 0.1 μm. However, fiber-sample distances as short as 0.1 μm cannot be fixed in our system since the fiber systematically sticks on the sample surface, most probably due to electrostatic forces originated by charges accumulated in the fiber. Nevertheless, we have chosen to work with the taper in contact with the cavity. The contact configuration ensures robustness to the system and reproducibility. Therefore, the fact that the taper is "stuck" to the sample by electrostatic forces guaranties the system stability during measurements. A picture of the whole sample is shown in fig. 3.8.a where each tiny square corresponds to a PhC and the red curved line to the tapered fiber. Fig. 3.8.b shows a picture of the PhC with the fiber positioned over de PhC cavity. In order to reduce mechanical vibrations of the taper due to air currents and decrease thermal fluctuations and humidity, the whole device (sample plus tapered fiber) is covered with an acrylic box.

To characterize the coupling efficiency we have used a 80 MHz repetition rate, 120 fs-duration pulsed probe beam from an OPO, optical parametric oscillator ('Opal', Spectra physics). The 30 nm-broad signal is centred at the cavity resonance wavelength and sent through a 50% coupler, to a fibered polarization controller and then through the tapered fiber, fig. 3.9. The polarization angle is changed by means of the polarization controller to optimize the optical coupling. The coupler splits the beam into two branches with equal intensity that allows measuring both the transmitted and the reflected signals. Both signals are sent to an optical spectrum analyser (OSA). Fig. 3.10 shows the transmitted and reflected intensity from an L3 cavity (a=465

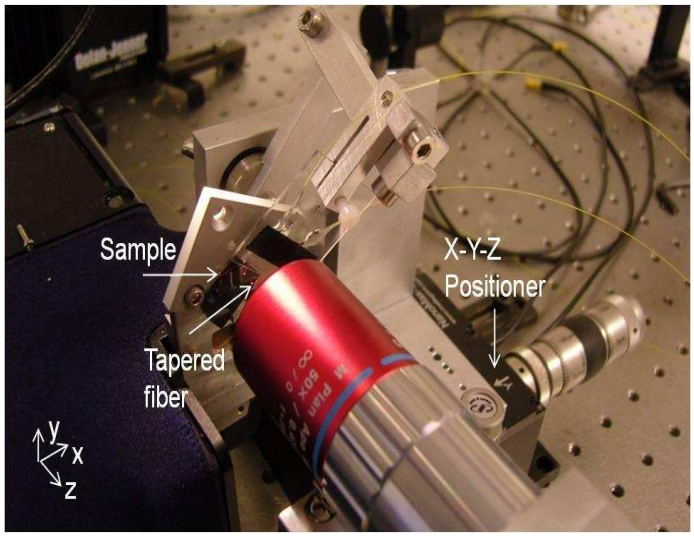

Figure 3.7: *(a) Set up to place the fiber over the PhC. A 3-axes stage (Nanomax) is used to precisely set the position of the fiber over the cavity.*

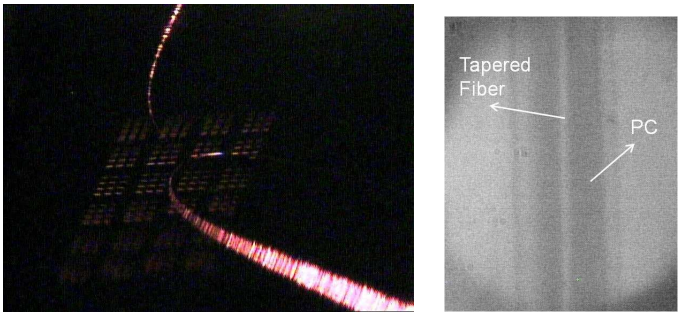

(a) (b)

Figure 3.8: *(a) Image of the whole sample and the tapered fiber. (b) Picture of the PhC membrane with the fiber positioned above the cavity.*

nm and r=120 nm) coupled by the tapered fiber. The resonance is centered at $\lambda = 1491.8$ nm and the loaded quality factor is $Q_{loaded} \sim 2400$. Note that the features of the experimental curves are in good agreement with the theoretical ones (fig. 2.6).

Using eqs. 2.31 and 2.36, we calculate the coupling efficiency (η) from fig. 3.10. The measured transmitted power in resonance is $P_{t,output} = 5.7$ nW and off resonance is $P_{off,output} \sim$11 nW, giving $\eta_c = 28\%$ and a coupling quality factor of $Q_c \sim 8500$, from eqs. 2.36 and 2.37, respectively. This value is in good agreement with the value found in section 2.3 by means of CAMFR simulations for a fiber 3 μm-thick which approximately corresponds to the diameter of the tapered fiber used here. This relative high coupling efficiency is of great interest in many applications, like efficient single photon sources, or light extraction of cavity based nano-lasers.

It is worth mentioning that the fiber, once tepered down, is not longer monomode meaning that a beating in the transmitted signal of the fiber is likely to be observed. COMSOL simulations were carried out[3] in order to obtain the modes of a standard (SMF28) fiber adiabatically tapered

[3]This simulations were done in collaboration with Nadia Belabas, LPN-PHOTONIQ, and Jean-Marie Moison,

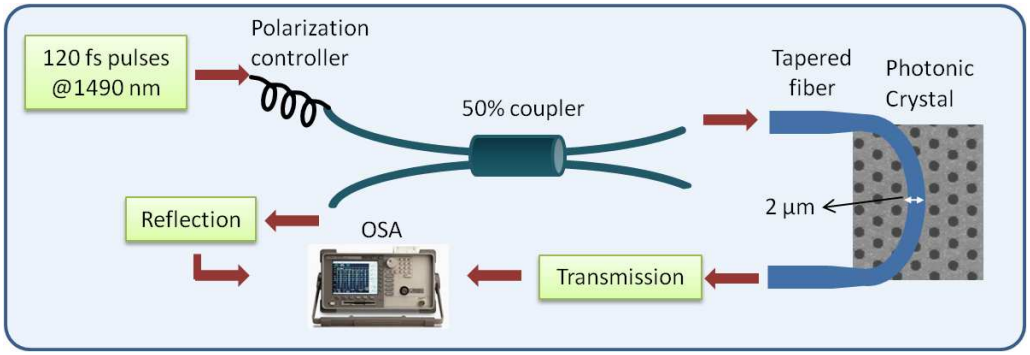

Figure 3.9: *Set up used to the characterise the coupling between the tapered fiber and the nanocavity. A MEB image of the L3 cavity is shown.*

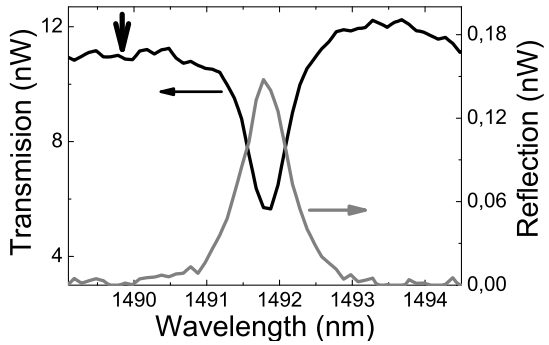

Figure 3.10: *Simultaneous transmitted and reflected signal. The thick arrow indicates the off resonance transmitted power used to estimate the coupling efficiency (see text).*

down to 3 μm. A fundamental mode with an effective refractive index (n_{eff}) of n_{eff}=1.4 and a first excited mode with n_{eff}=1.34 were found. This gives a beating in the signal with a period of: $\Delta\lambda = \lambda^2/(\Delta nL) = 3.7nm$, with $\Delta n = n_{eff,0} - n_{eff,1} = 0.06$, $\lambda = 1.49$ μm and L=1 cm. However, this beating is not observed in fig. 3.10 most probably due to a low contrast of the beating.

3.3 Conclusion

A Photonic crystal L3 nanocavity has been designed and fabricated. We estimated the intrinsic quality factor of at least 4800 (limited by the resolution of the spectrograph) by means of photoluminescence measurements. This gives us, according to the results of chapter 2, an estimation of the upper bound for the coupling quality factor (Q_c) necessary to obtain efficient coupling.

A fabrication process to taper down a commercial fiber was developed at the PhLAM laboratory. By this process, we succeed in fabricating tapered fibers with diameters between 1.5-3 μm and optical losess lower than 7db. Different mounting schemes of this fiber were studied, out of which the most adequate one was the U-shape mounted on a microscope slide. The fiber is first bent in the thinner part forming an U-shape and subsequently fixed onto a microscope slide. Besides, a positioning system with sub-μm resolution and high stability was designed and

LPN-PEQ-PHOTONIQ group.

assembled in order to locate the tapered fiber over the cavity with high precision.

The coupling between the cavity and the fiber was measured injecting a broad-band ($\sim$ 30 nm) signal through the fiber and measuring the transmitted/reflected signal. This broad signal was filtered by the cavity mode giving the cavity resonance. Applying this method, coupling efficiencies of $\sim$ 28% were achieved, which means that almost a third of the signal injected through the fiber is being coupled inside the cavity. This high coupling efficiency is of great interest in many applications, like efficient single photon sources, or light extraction of cavity based nano-lasers. In particular, in the next chapter, we will use this coupling scheme to obtain characteristic thermal and electronic times of the nanocavity in actives regimes.

Chapter 4

Application of the tapered fiber: measurement of relaxation times in active materials

The carriers excitation through an incoherent pump in active nanostructures can change the optical properties of the structure, and hence the intrinsic properties of the cavity, such as the cavity resonance frequency. Indeed, an optical pump allows to externally tuning the resonance wavelength. This phenomenon is interesting in the context of all-optical switching devices. In this chapter we apply the coupling method via a tapered fiber described before, to measure different characteristic times of the sample. In particular the thermal relaxation time in a PhC membrane and the characteristic electronic times are investigated. These measurements are based on the refractive index change, having a thermal or electronic origin, due to an incoherent pump. Both magnitudes will be of great interest in the following part where dynamical nonlinear regimes are studied.

4.1 Measurements of the characteristic thermal relaxation time

As it has been mentioned in chapter 1, photon emission and/or carrier induced nonlinearities are obtained through the excitation of electrons in semiconductor conduction bands or states. Electron and hole nonradiative recombination processes play a fundamental role in the relaxation of excited electronic populations. These are mediated by phonons which become a heat source. While heating turns out to be an unwanted effect in most photonic devices because of detrimental thermal loading (specially in photonic crystal suspended membranes), it can also be used as a mechanism for fast switching (up to 10 MHz-bandwidth) as long as the dimensions of optical cavities are small enough [113, 114, 27]. Moreover, in the context of novel nonlinear dynamical mechanisms relying on multiple time-scale processes, it has been demonstrated that the so-called thermo-optical excitable dynamics may lead to repetition rates as high as 1 GHz [89].

For all those situations, an insight into dynamics of heat dissipation is of central importance since it provides information about the characteristic time scales to take into account when pumping the sample in order to avoid heating up the material, i.e. by modulating the optical pump faster than the thermal relaxation time. In particular, quasi cw light injection for nonlinear operation or laser emission often requires the pump pulse to be longer than the carrier recombination lifetime, but shorter than the thermal time, as it has been implemented for instance in [115].

In the case of self-induced heating phenomena in micro and nano optical cavities (e.g., when the heat is produced by optical excitation of the resonant mode in the cavity) the characteristic heat dissipation times strongly depend on the cavity size. As it has been pointed out in [114], these scale with the characteristic cavity length, i.e. small cavities dissipate heat faster. The equilibrium temperature, in turn, scales with the inverse cavity length, mainly due to the reduced heat capacity of small cavities. Fast thermal processes are thus compatible with high thermal loading, showing the importance of thermal measurements in small cavities, such as photonic crystal nanocavities.

From the experimental point of view, while thermal loading can be estimated through measurements of thermally induced refractive index change, the thermal relaxation times cannot be obtained straightforwardly; this has been done so far through parameter fitting from nonlinear dynamical models [114, 27, 89]. This requires a complex set of equations coupling several variables, therefore, the fitted relaxation time becomes model-dependent. To avoid this, we have developed a novel method to directly measure the thermal relaxation time of a photonic crystal nanocavity, based on reflectivity measurements of a CW probe beam within the tapered fiber-assisted optical coupling scheme [97]. This measure allowed us to test the ability of the tapered fiber to extract interesting information of the system dynamics.

4.1.1 Experiment set up

The cavity is probed via the tapered fiber with the coupling characteristics mentioned in section 3.2 ($\eta_c = 28\%$), fig. 3.10. The CW probe power injected into the taper is set to a low level (< 1 mW) in order to prevent any self-induced thermal or electronic effects (the system shows nonlinear thermo-optical effects for injected powers higher than 1 mW, section 5.1). In order to produce heat, the cavity is optically pumped by the surface using a modulated CW beam at 800 nm focused down to a 3.2 $\mu m-$diameter spot (@$1/e^2$ of the intensity) by a long working distance microscope objective ('Mitutoyo', M Plan Apo NIR, X50, f=170 mm, $NA = 0.42$), fig. 4.1. This wavelength is mainly absorbed in the InP (bandgap wavelength ~900 nm @300 K).

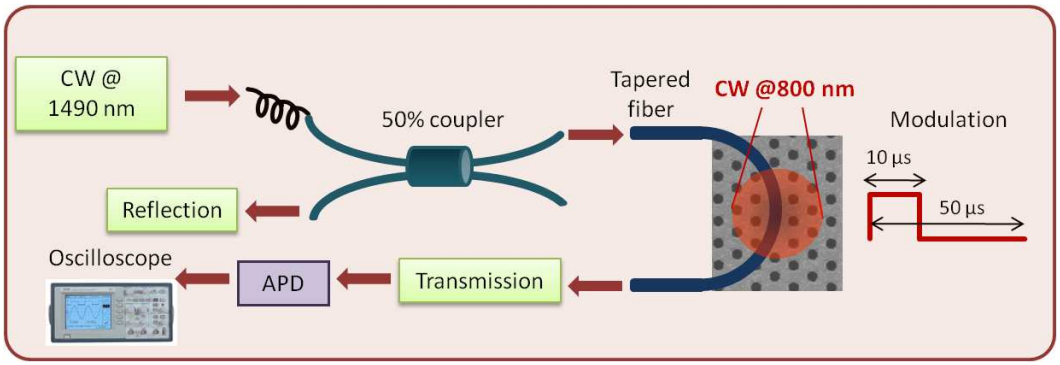

Figure 4.1: *Set up used to measure the thermal relaxation of a photonic crystal nanocavity.*

Non-radiative carrier relaxation processes are the central mechanisms producing heat in the membrane. Thermal effects increase the refractive index, shifting the resonance to longer wavelengths. Fig.4.2 shows the resonance spectrum for a pump power of 165 μW (on the sample) in red line and without pump in black line, measured as in section 3.2.2.

Thermal dynamics is measured as follows. The wavelength of a tunable laser ('Net Test',

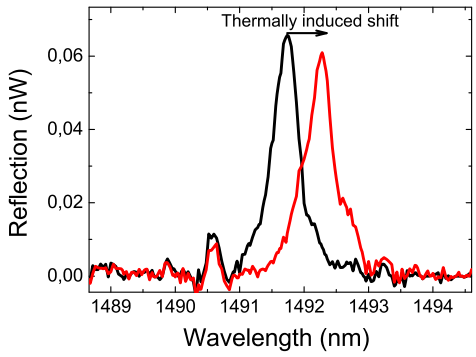

Figure 4.2: *Reflectivity spectrum of the cavity resonance without pump (black line), and with 165 μW pump (red line).*

Tunics Plus S, 1430 nm-1530 nm) is set at a given detuning $\Delta\lambda_0$ with respect to the resonance of the unpumped cavity ($\Delta\lambda_0 \equiv \lambda_c - \lambda_p$, where λ_c is the wavelength at the center of the resonance and λ_p the probe wavelength), probing the cavity-induced reflection. Heating up the cavity results in a thermally induced wavelength shift, producing a change in the reflected intensity of the probe light. A high sensitivity fiber coupled avalanche photodiode (APD, 'New Focus', model 1647) with a 15 kHz-1.1 GHz-bandwidth was used to temporally resolve the change of the reflected signal. Traces are recorded on a 400 MHz -bandwidth, 5 Gs/s, oscilloscope ('Lecroy', WaveRunner 44Xi). Upon 10 μs width-50 μs period square pump pulse excitation, the reflected signal exhibited either a drop-out followed by a recovery for $\Delta\lambda_0 \geq 0$ (i.e. blue detuning), or intensity peaks for $\Delta\lambda_0 < 0$ (red detuning). Both situations are directly related to the thermal dynamics of the resonance towards the equilibrium states. For a nearly resonant probe ($\Delta\lambda_0 = 0$, fig. 4.3.a), the signal decreased in the presence of the pump beam due to thermally-induced shift of the resonance. For red detuning, instead, the resonance "passes through" the injection wavelength leading to a maximum of intensity in the heating process, followed by a maximum in the cooling process (figs. 4.3.b-d).

In order to extract the characteristic thermal time from the time evolution of the reflected probe, the spectral shape of the resonance must be taken into account. The resonance can be fitted with a Lorentzian function. Considering the time dependence of the center of the resonance $\lambda_c(t)$, which contains the refractive index dependence with temperature, the time-dependent reflectivity $R(t)$ is thus modelled as $R(t) = 1/[1 + (\lambda_c - \lambda_p)^2/(\gamma/2)^2]$, where γ is the FWHM of the resonance. The resonance width γ is measured from the reflectivity signals as a function of the detuning. Since the APD detector cuts-off DC components, the reflected signal level was measured with respect to the signal drop out when the probe signal is turned off in fig 4.3.a-d. From fig. 4.4, the resonance width gives $\gamma = 0.33$ nm, corresponding to a quality factor of $Q_{loaded} \cong 4520$. The increase of the Q_{loaded} with respect to the one found in section 3.2.2 may be given to a decreased absorption due to the higher spectral power density used in this case compared to previous (broad-band) fs measurements. Let us stress that from the Q_{loaded} and the coupling efficiency (η) we can obtain the intrinsic quality factor (Q_{rad}), neglecting the absorption (i.e. $Q_0 = Q_{rad}$), as: $Q_{rad} = 1/(1-\eta)Q_{loaded}$, which gives $Q_{rad} = 6300$. The time dependent wavelength shift becomes:

$$\Delta\lambda(t) \equiv \lambda_c(t) - \lambda_p = \pm[R(t)^{-1} - 1]^{1/2}\gamma/2 \tag{4.1}$$

where the two roots indicate blue or red shift of the probe with respect to the cavity resonance.

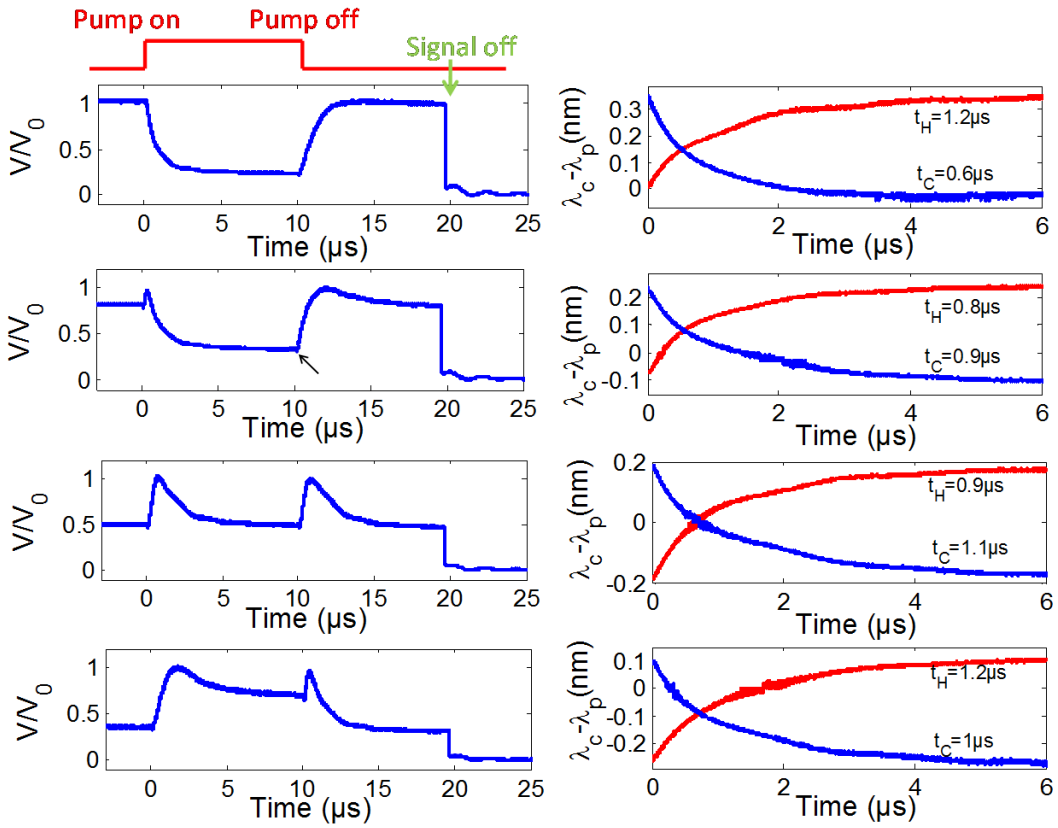

Figure 4.3: *Time evolution of the reflected square modulated (red line above) CW probe for different detunings. a) $\Delta\lambda_0 = 0$; b) $\Delta\lambda_0 = -0.08$ nm; c) $\Delta\lambda_0 = -0.21$ nm; d) $\Delta\lambda_0 = -0.33$ nm. e)-h) Thermal dynamics obtained from (a)-(d), taking into account the lorentzian shape of the resonance. The arrow in (c) indicates a small amplitude short peak corresponding to electronic blue-shift dynamics before the slow thermal dynamics takes place.*

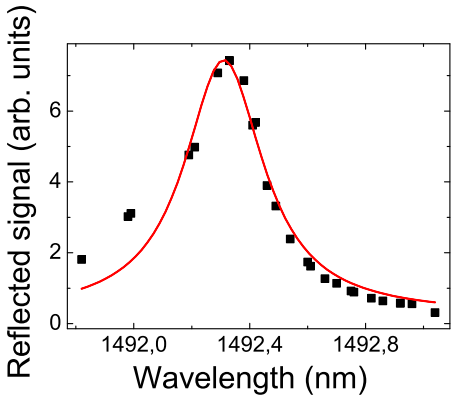

Figure 4.4: *Cavity resonance measure by means of the reflectivity decrease while switching off the signal. Fitted by a Lorentzian function. From the fitting, the resonance width gives 0.33 nm.*

It is worth to point out that the kinetics of the center of the resonance also contains an ultrafast process related to carrier-induced index variation. As we will see in section 4.2,

such processes decrease the refractive index blue-shifting the resonance in a time shorter than 1 ns, eventually being followed by a thermally driven red-shift. Therefore, they lead to short downward peaks for red detuning, and short upward peaks for blue detuning. Let us stress that such effects remain small in our measurements (see arrow in fig. 4.3.c).

From eq. 4.1, the time dependent detuning, $\Delta\lambda(t)$, is plotted in fig. 4.3.e-h, for the heating and cooling process. The slight noise in the signal at $\Delta\lambda \sim 0$ is due to the discontinuity of the two roots in the inverse of the lorentzian function. From those curves we obtain the characteristic time as the time for which the detuning decays 1/e of $|\Delta\lambda(0) - \Delta\lambda(\infty)|$, the difference between the initial detuning and its stationary value. The cooling and heating times for different detuning are similar, fig. 4.3.e-h. Considering that the characteristic times do not depend on the initial detuning, the average of the measured values for different detuning yields to $\tau_c = 0.9 \pm 0.2\ \mu s$ and $\tau_h = 1.0 \pm 0.2\ \mu s$ for the cooling and heating processes, respectively. We then conclude that there is no significant difference between these two times, provided the system is probed with a weak signal. Fig. 4.3.e shows that for the zero-detuning case the cooling time is about a factor 2 smaller compared to the other cases. For zero-detuning, indeed, the reflectivity time trace for the cooling process is mainly affected by the spectral tail at the blue side of the resonance, which is slightly different to the tail at the red side (see the slight asymmetry of the resonance in fig. 4.2), which may explain the substantial deviation for this situation. In spite of this, we stress the fact that our technique allows one to directly measure the dynamics of temperature in a nanocavity.

The characteristic times found ($\sim 1\ \mu s$) are in good agreement with the thermal dissipation time we have found using an alternative technique [116], so-called transient thermoreflectance imaging, which allows to investigate the spatial heat distribution with sub μs time resolution and sub μm spatial resolution[1]. Thermoreflectance methods rely on the relation between the temperature variation ΔT and the reflectivity variation ΔR_T of materials which, in first approximation, follows $\Delta R_T = (dR_T/dT)\Delta T$, where dR_T/dT is a constant which depends on the material. By means of a pump and probe technique and a CCD camera, images of the sample are taken for different pump-probe delay (τ). Fig. 4.5 shows the relative reflectivity changes (deconvolved with the normalized intensity of probe pulses) as a function of the delay (τ). The value of the relative reflectivity change is a spatial average on a 10 μm side square. The images are shown for τ equal to 30, 130, 500 and 1000 ns. Fitting the relative reflectivity changes by the convolution of an exponential $\Delta T_0 exp(-t/\tau_0)$with I_{Nprobe} (measured with a fast photodiode)[116], we found a thermal dissipation time of $\sim 1\ \mu s$. This measurement is in good agreement with our results and gives additional information about the spatial thermal distribution.

4.1.2 Discussion

The thermal dissipation time we have measured in the previous paragraphs, namely the dynamical relaxation process of the temperature in a PhC slab, characterizes a transient phenomenon towards the thermal equilibrium state. Classically, this is well described by the heat equation. Therefore, in order to obtain an analytical expression for the relaxation time (τ_{th}), the time dependent solutions of the heat equation are studied. This equation reads:

$$\partial T/\partial t = Q(r) + \alpha \nabla^2 T \tag{4.2}$$

[1]Time resolved thermo-reflectance measurements have been done in collaboration with Virginie Moreau, Gilles Tessier and Yannick De Wilde at the Institute Langevin.

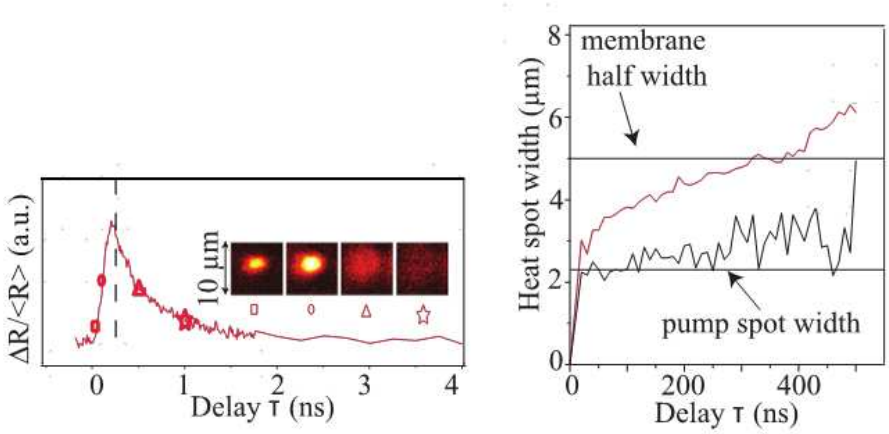

(a) (b)

Figure 4.5: *(a) Relative reflectivity change as a function of the delay (τ) when the pump is focused on the PhC membrane. Images of the relative reflectivity change are plotted for: $\tau = 30$ ns, 130 ns, 500 ns and 1000 ns. (b) Heat spot width as a function of the delay.*

where α is the thermal diffusivity, Q(r) is the heat source (per unit volume) symmetric under reflections $x \to -x$ and $y \to -y$, and T is the temperature increase with respect to the substrate temperature. The time dependent solutions are taken for a 2D rectangular membrane of size $2L_x \times 2L_y$, fig. 4.6.

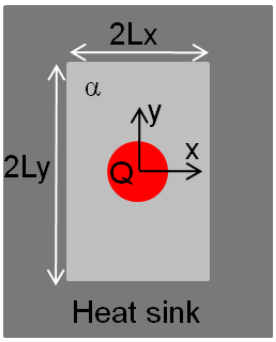

Figure 4.6: *Rectangular geometry for the calculation of transient dynamics in a 2D membrane.*

We set the following simplified boundary conditions: T(x=Lx)=T(y=Ly)=0 and $\partial T/\partial x|_{x=0} = \partial T/\partial y|_{y=0} = 0$ for symmetrical solutions. The general solution is a superposition of a particular (stationary) solution $T_{st}(r)$ and the homogeneous solution, $T(r,t) = T_{st}(r) + T_h(r,t)$. It can be easily showed that T_h can be expanded in Fourier series,

$$T_h(r,t) = \sum_{n,m=0}^{\infty} A_{nm} e^{-\sigma_{nm} t} cos(k_{xn}x) cos(k_{ym}y) \tag{4.3}$$

with $k_{xn} = (2n+1)\pi/2L_x$, $k_{yn} = (2n+1)\pi/2L_y$ and $\sigma_{nm}/\alpha = k_{xn}^2 + k_{ym}^2$. The amplitudes A_{nm} can be obtained from the initial conditions. In the case of the heating process ($Q(r) \neq 0$) the initial condition is $T^{(H)}(r, t=0) = 0$ meaning $T_h^{(H)}(r, t=0) = -T_{st}^{(H)}(r)$, and the coefficients $A_{nm}^{(H)}$ are calculated as the Fourier transform of $-T_{st}^{(H)}(r)$. Thus, the Fourier modes relax with

characteristic times given by

$$\tau_{th,nm} = 1/\sigma_{nm} = 1/\alpha(k_{xn}^2 + k_{ym}^2) = 4L_x^2 L_y^2/\alpha\pi^2[(2m+1)^2 L_x^2 + (2n+1)^2 L_y^2] \quad (4.4)$$

Note that higher order modes are dissipated faster. Therefore, we can expect the relaxation dynamics to be driven by the lowest order mode, provided it is efficiently excited. In our case, since $L_y >> L_x$, $\tau_{th,00} \approx 4L_x^2/\alpha\pi^2$; taking $\alpha = 0.372\ cm^2/s$ [117] then $\tau_{th,00} \sim 300$ ns, meaning that the smallest length governs the relaxation process. In addition, eq. 4.3 also accounts for cooling processes, whose dynamics is denoted by $T^{(C)}(r,t)$. In such a case the heat source is turned off (Q(r)=0) hence $T_{st}^{(C)}(r) = 0$ and the initial condition reads $T^{(C)}(r, t=0) = T_{st}^{(H)}(r)$. Therefore $A_{nm}^{(C)} = -A_{nm}^{(H)}$, hence $T^{(C)}(r,t) = -[T^{(H)}(r,t) - T_{st}^{(H)}(r)]$, which shows that the relaxation dynamics of the cooling process is the same as for the heating process.

The estimated relaxation time (τ_{th}) is about a factor 3 below the measured relaxation time. The discrepancy between these two values may be due to the strong approximations used in our simple model, in particular the temperature being fixed to the substrate temperature at the end of the membrane (perfect heat sink at L_x and L_y). Full 3D-finite element numerical simulations, as in [118], should be carried out in order to better account for thermal dynamics in this system.

4.2 Measurements of the carrier recombination time

Nonlinear effects of thermal origin were investigated in the preceding section. Here we will study relaxation times related to electronic refractive index change. This will give us information about the characteristic carrier recombination times in the nanostructures with possible applications in ultrafast optical switching.

All-optical ultrafast switches with chip-integration compatibility and efficient coupling to the external environment are at the heart of high-speed communications. Optical switches based on 2D PhC have already been proposed and investigated in III-V semiconductor-based materials in several configurations, including surface-resonant Bloch modes of a non defective 2D PhC, waveguides and cavities [119, 81, 91, 115]. Recently, fast switching capabilities of a PhC nanocavity were investigated using an evanescent coupling through a tapered fiber. A ~ 2 ns, ON−OFF switching time was demonstrated [120]. The performance and resolution were limited by the pulse duration and the detection bandwidth respectively. Indeed, the carrier induced nonlinear response is expected to allow ON−OFF switching times shorter than 2 ns at least by one order of magnitude [91]. In this section we present pump and probe measurements with 100 femtosecond time-resolution for all-fibered and surface pumping configurations [121]. As mentioned in sec. 3.2 our system contains three different semiconductors structures, all of them potentially contributing to index changes as a function of injected carriers: the (3-D) InP slab, a (2-D) wetting layer and a (0-D) QDs . The wavelength corresponding to their electronic bandgaps (λ_{gap}) are 0.92, 1.1 and 1.55 μm, respectively. The contribution of each semiconductor structure to carrier-induced nonlinear effects at the probe wavelength is discussed at the end of this section.

4.2.1 Pump and probe measurements

In order to achieve sub-ps time resolution compatible with electronically-induced active phenomena, a femtosecond pump and probe technique is implemented. Probe pulses (signal) with

120 fs-duration and 80 MHz-repetition rate are generated by an optical parametric oscillator at around 1490 nm. The probe power is kept below 250 nW at the input of the taper to avoid any nonlinear effect induced by the signal. As in section 3.2.2, using this broadband pulses ($\sim$ 30 nm-broad) to probe the nanocavity mode, we measure an optical resonance centered at 1491.5 nm with a FWHM of 0.6 nm corresponding to loaded quality factor of $Q_{loaded} \cong 2400$.

The active regime is achieved by optically injecting carriers using a 80 MHz-repetition rate, 100 fs-pulse duration Ti:Sa pump source. Pump pulses, emitted at $\lambda = 810$ nm, are absorbed in the InP ($\lambda_{gap} \sim 0.92\ \mu m$) inducing a carrier population that first relax to the wetting layer bang-edges ($\lambda_{gap} \sim 1.1\ \mu m$), fig. 4.7. As it has been shown elsewhere [91], this carrier density decreases the refractive index and induces the blue shift of the optical mode. In addition, a slow thermal effect also takes place with a time scale of the order of 1 μs, as described in section 4.1. Therefore, only the averaged thermal loading can be revealed by our measurements which, in turn, can fully resolve the ultrafast changes associated to the carrier dynamics. This was accomplished by analyzing the probe reflectivity/transmission intensity as a function of the delay between the pump and the probe pulses. Time delays are obtained by increasing or decreasing the probe path by means of a computer-controlled translation stage. The delay step is 7 fs and the maximum positive delay that can be reached is 1.3 ns. Both signals, reflected and transmitted, are measured with an optical spectrum analyser (OSA). In all the experiments the probe is sent through the tapered fiber, as describe in section 3.2.2, while two configurations were studied to pump the sample: surface pumping and through the tapered fiber.

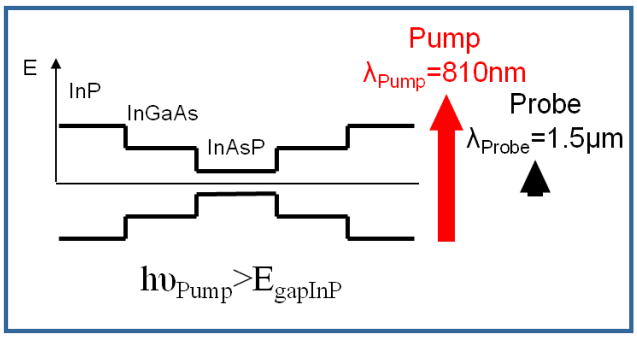

Figure 4.7: *Scheme of the energy levels of the different materials in the sample compared with the pump and probe energies.*

Surface pumping configuration

In a first set of experiments the free space propagating pump beam is sent to the 2D PhC by the surface, as described in fig 4.8. The pump beam is focused down via a 50x, long working distance (17 mm), microscope objective to a diameter of 3.2 μm (@$1/e^2$ of the intensity) shining the structure normally to the 2D PhC periodicity (red circle in fig. 4.8).

As the pump power is increased to 0.98 mW, a 3 nm red shift of the resonance is observed for negative or long positive delays ($>$ 1 ns). This red shift, associated to thermal effects, becomes a thermal offset for the linear regime. In the following, all electronically induced shifts are measured from this offset. Such blue shifts are only observed for positives delays within the picosecond to nanosecond time scale, which confirms its electronic origin [91, 120].

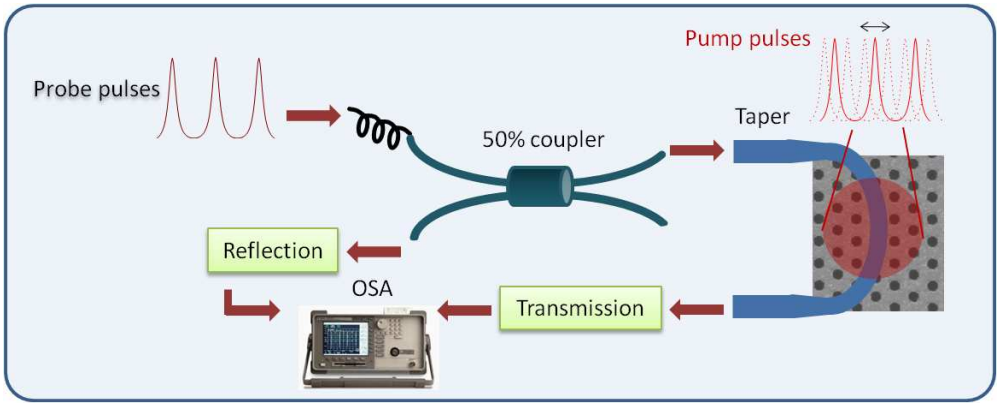

Figure 4.8: *Experimental setup for surface pump. A translation stage (non shown), allows to change the pump/probe delay.*

Fig. 4.9 shows the transmitted signal spectra with a pump power of 0.98 mW for different pump-probe delays. A maximum blue shift of 7 nm is obtained near pump-probe coincidence. This is consistent with the fact that the electronic density and the associated blue shift can be assumed to increase within a time of the order of the carrier relaxation time to the conduction and valence band edges ($\sim$ 1 ps). As the time delay is increased, the blue shift decreases due to carrier recombination. Clearly, the decrease of the blue shift as pump and probe delay is increased is related to the carrier recombination time for a given pump power.

In order to further analyse this temporal behavior and its dependence on the pump power, we measure the spectral shift $\Delta\lambda$ as a function of the pump-probe delay for different pumping powers (fig. 4.10.a). The observed rise time is of the order of 4 ps (except for the smallest power). As it was shown in ref. [122], this time is related to the photon lifetime in the cavity ($\sim$ 2 ps). A decrease of the total recovery time from $\sim 90 \pm 20$ ps to $\sim 30 \pm 5$ ps (measured at 1/e of the maximum) is observed as the pump power is increased from 0.3 mW to 1 mW (4.10.b). Note that both the blue shift and the ps time scale are clear signatures of the electronic nature of the nonlinear effect. Furthermore, the decrease of the recovery time with the pump power can be related to nonlinear terms in the carrier recombination process, such as bimolecular recombination [91], which will be discussed in detail at the end of this section.

Before describing the all fibered case, where the pump and the probe are injected via the tapered fiber, let us consider one interesting application of such ultrafast behavior: the all-optical control and switch of a CW signal. In order to implement such configuration, 490 $\mu W-$pump pulses are injected from the free space on the surface while a CW probe is coupled through the taper. The probe is modulated with 10 MHz repetition rate, with pulse duration of 90 ns and mean power of 235 μW. The modulation is applied to measure the signal contrast. Time traces are measured using a 15 kHz-1.1 GHz-bandwidth avalanche photodiode (APD). The mechanism underlying the control of the signal is simple and can be easily understood from the previous experiments. The resonance shift created by the pump pulse induces a change on the transmitted signal which can be switched on and off by means of the control (pump) pulses. Fig. 4.11.a shows the time trace of the transmitted signal for two different wavelengths. The periodicity of 12.5 ns corresponds to the pump repetition rate. Clearly, in the presence of the pump pulses the transmitted signal drops or increases depending on whether the probe wavelength is blue or red-shifted with respect to the cavity resonance, respectively. This is summarized in fig. 4.11.b,

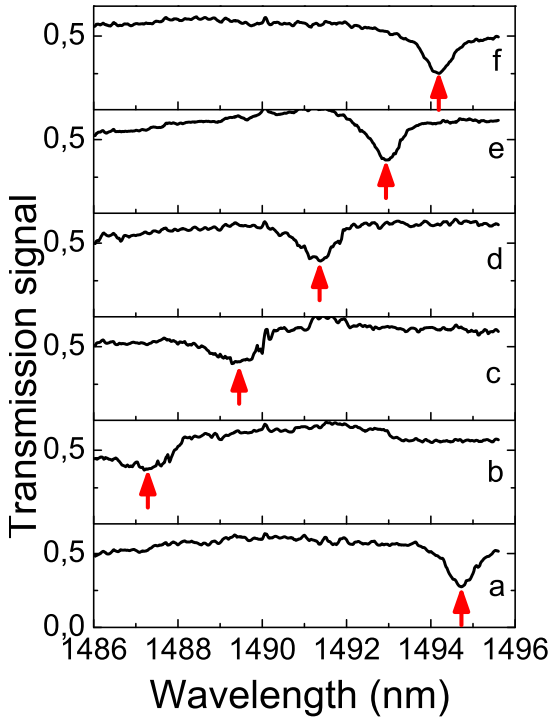

Figure 4.9: *Transmission spectrum for different pump and probe delays: a.* $\Delta t = -24$ *ps, b.* $\Delta t = 1$ *ps, c.* $\Delta t = 8$ *ps, d.* $\Delta t = 25$ *ps, e.* $\Delta t = 50$ *ps, f.* $\Delta t = 140$ *ps, with a vertical offset. The probe power at the input of the taper is 20 nW. The pump, with a power of 0.98 mW, is injected by the surface. The spectrum resolution is 0. 5nm. The red arrows point the resonance minimum.*

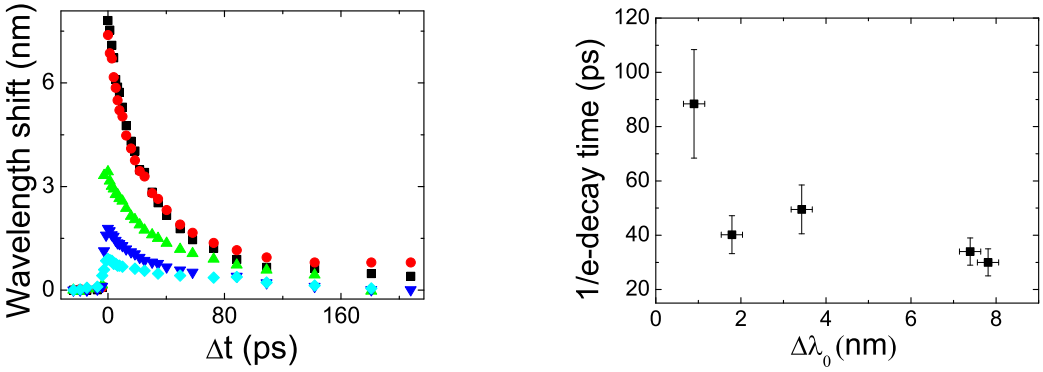

(a) (b)

Figure 4.10: *(a) Resonance shift as a function of the delay time for different pump powers, 0.28* mW(♦)*, 0.42* mW(▼)*,* $0.54mW$(▲)*, 0.67* mW(●) *and 0.98* mW(■)*. The rise time is* ~ 4 *ps, except for the smallest power where it is* ~ 7 *ps. (b) Dependence of the decay time (*Δt *at 1/e) with the pump power.*

which shows the variation of the transmitted peak amplitude (A), calculated from fig.4.11.a as: A=$100(a-b)/b$, as a function of the probe wavelength (black line) superimposed to the reso-

nance spectrum (red line) measured in the absence of pump pulses. A contrast as high as 20% is achieved as the probe is slightly shifted but close to the minimum of the resonance (fig. 4.11.b). This is a factor ~ 2 smaller than the contrast of the resonance in transmission calculated from fig. 4.11.b red line, which can be attributed to the limited bandwidth of the APD, resulting in a time convolution of the actual signal with the impulse response of the detector.

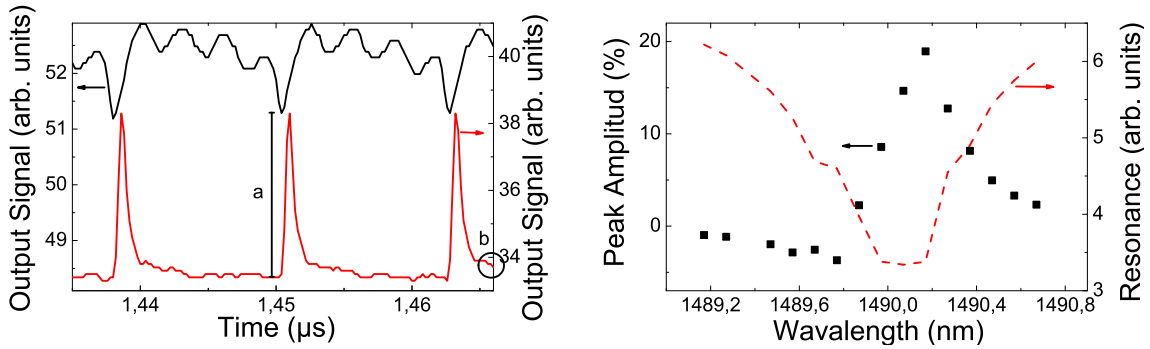

(a) (b)

Figure 4.11: *(a) Time resolved transmission, resolution 1 ns, for* $\Delta\lambda(\lambda_{inj} - \lambda_{res}) = -0.5$ *nm (black line) and* $\Delta\lambda = 0$ *(red line), each peak corresponds to the arrival of one pump pulse* ($\Delta t \sim 12.5$ *ns). (b) Transmitted amplitude spectrum in % with respect to the background signal* (■) *and cavity resonance (dash line).*

Fibered pump

One of the usual drawbacks of 2D PhC devices is to cross the bridge between the high efficient microscopic active devices and the macroscopic word. For this reason, we studied here the electronic characteristic time and the switching capabilities in an all fibered configuration.

In this experiment both the 100 fs-long 810 nm pump pulses and the 120 fs-long 1490 nm signal pulses are sent through the tapered fiber to the cavity, fig. 4.12. The pump power at the input of the fiber is fixed to ~ 2.5 mW, whereas the probe is kept below 250 μW to avoid probe-induced nonlinearities. Note that these values are measured at the input of the fiber and the actual pump and signal powers near the cavity are lowered due to both contact and propagation losses in the taper. From such losses we can estimate the power near the cavity (P_{in}) as $P_{in} = 0.26 P_{input}$, where P_{input} is the injected power at the input of the fiber. Both signals, pump and probe, propagate through 7 m of fiber until reaching the cavity.

The reflected signal spectrum is represented in fig. 4.13.a for different pump-probe delays. A maximum blue shift of 0.9 nm is obtained for the pump-probe coincidence. The linear resonance in this case is at 1494.3 nm. Although it is difficult to evaluate the actual pump intensity acting in the nanocavity region, an order of magnitude can be estimated from a comparison between the pumping powers in the two configurations (free-space and fiber-coupled) giving the same blue shift. Indeed, the blue shift achieved in the fibered pumping configuration (~ 1 nm) is close to the one obtained in the surface-pumping configuration for a pump power of 0.28 mW (fig. 4.10.a, (♦). Therefore, the pumping level in the fibered configuration is equivalent to ~ 0.28 mW shining the surface. As the InP coefficient of absorption at 810 nm is $\sim 33\%$ and considering the cavity surface with respect to the excitation surface, the absorbed pump power in

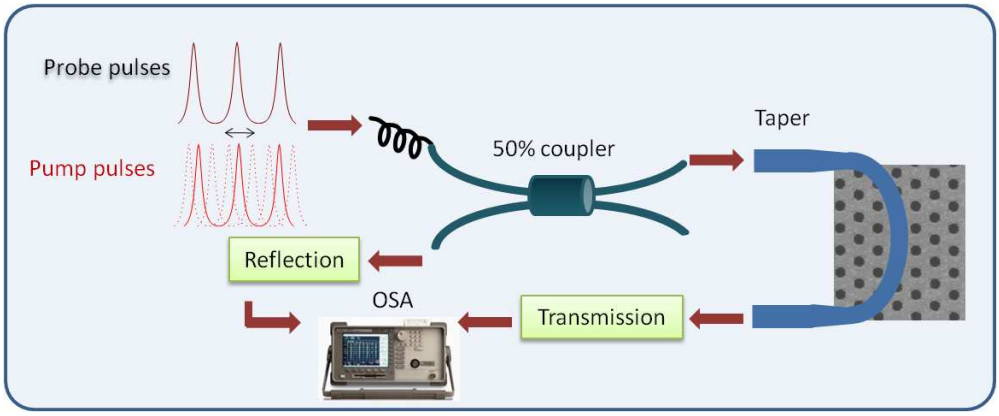

Figure 4.12: *Experimental setup for fibered pump. Using a translation stage, the pump pulses are delayed with respect to the probe pulses before being sent to the tapered fiber.*

the cavity region is reduced to $\sim 10\ \mu W$, which is of the same order of magnitude as in ref. [120].

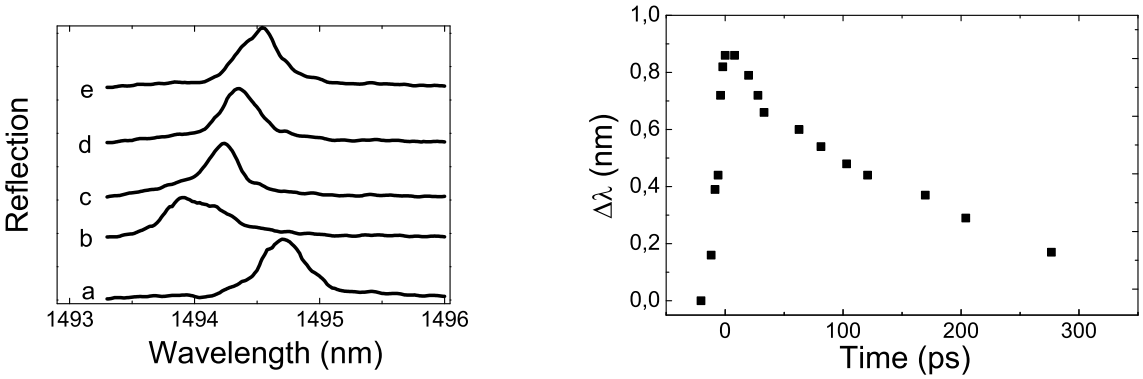

(a) (b)

Figure 4.13: *All fibered configuration. (a) Reflectivity intensity for different pump and probe delays: a. $\Delta t = -21$ ps, b. $\Delta t = 21$ ps, c. $\Delta t = 100$ ps, d. $\Delta t = 170$ ps, e. $\Delta t = 277$ ps, with a vertical offset, resolution 0.05 nm. The pump power was 2,5 mW at the input of the fiber. (b) Resonance shift as a function of pump-probe delays for all-fibered configuration (decay time at $1/e = 166$ ps and rise time 20 ps).*

We now consider the dynamics of the resonance wavelength shift in the fibered configuration. Fig. 4.13.b shows the time dependence of the blue shift in the experimental conditions of fig. 4.13.a. The rise time (switch ON) is ~ 20 ps and the decay time (switch OFF) is $\sim 170 \pm 15$ ps. These times are in the picosecond time scale and are still attributed to the carrier induced refractive index change as previously. However, they are longer compared to the ones measured in the surface-pump configuration. In both cases the signal is fiber coupled and there is no measurable effect associated to its intensity. Therefore, the increased ON and OFF times must be related to a linear and/or nonlinear dispersion associated to the propagation of the pump pulses in the fiber and the taper. In order to verify this hypothesis we further investigate the origin of the increase of the ON/OFF characteristic times as follows. First, we implement an autocorrelation measurement of the pump pulses at the output of the 7 m fiber-taper setup. Although their initial, free space, duration is ~ 100 fs, we find that pump pulses of 3 mW are

stretched to ~ 7 ps (fig. 4.14.a) after propagating through the fiber. This duration does not significantly change for all the pump pulse energies considered in the switching configuration. Next, we implement a surface pumping configuration with 7 ps-pump pulse duration in the following way: the pump pulses are temporally broaden to ~ 7 ps by taking benefit from the chromatic dispersion after propagating through a 7 m-long fiber and eventually sent to the sample in the same surface-pumping conditions of fig. 4.8. The measured rise and decay times are now ~ 20 ps and $\sim 115 \pm 20$ ps respectively [fig. 4.14.b (•)]. The rise time is close to the one measured in the all-fiber coupling configuration, whereas the decay time overlaps with the one obtained in the femtosecond surface pumping experiment for the same blue shift: (90 ± 20) ps. This builds confidence on the fact that the stretching of the pump pulses is at the origin of the increase of the ON responses. Indeed, by contrast with the 100-fs pump pulse in the surface-pumping configuration, which is shorter than all times scales of the system leading to free carrier relaxation, the 7-ps duration pump pulse is longer compared to the photon lifetime and approaches the fast carrier recombination time. The 20-ps rise time can thus be understood as resulting from the longer pumping pulse driving the system. However, the increase of the decay time in the fibered pump configuration with respect to surface pumping is more intriguing and could be related to a lower carrier density within the WL when pumping through the fiber, as discussed in the next paragraphs.

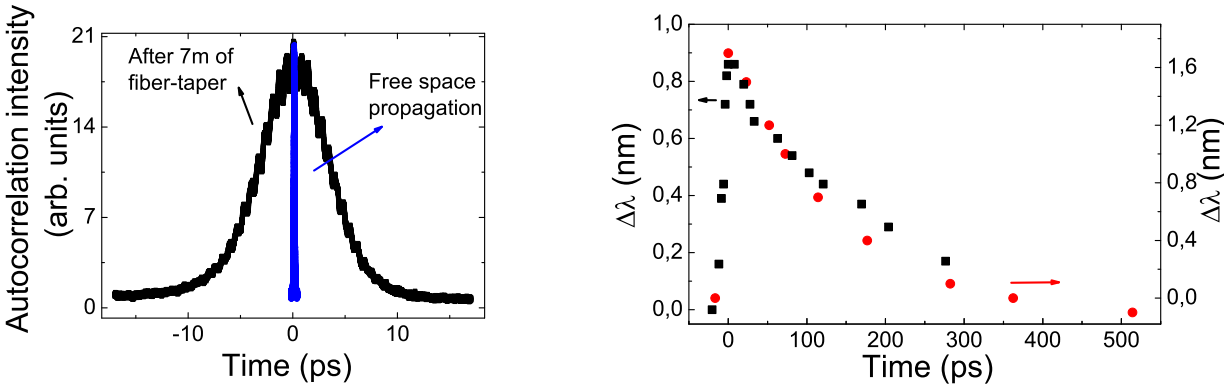

Figure 4.14: *(a) Autocorrelation measurement of pump pulses: free space propagation (blue line) and after 7 m of fiber-taper (black line). (b) Resonance shift as a function of pump-probe delays for all-fibered configuration (■) (decay time at $1/e = 166$ ps and rise time 20 ps) and for surface pumping with 7 ps-pump pulses duration (•) (decay and rise times: 150 ps and 20 ps, respectively).*

4.2.2 Discussion

The aim of this paragraph is to clarify the origin of the dynamics of the ON and OFF responses resulting from the femtosecond pump and probe experiments described above. For this porpose we use a simple and intuitive description based in the set of equation deduced in section 1.4. Since the pump-induced effects shift the resonance to the blue side of the spectrum, the leading nonlinear process is the decrease of the refractive index. Therefore, the active phenomena in play are mainly of electronic origin, i.e. they come from carrier-induced effects, which turn out to be dominant against (fast) red-shift processes, such as intrinsic Kerr effects. The injected carrier density in the surface pump experiment per unit power within the PhC slab, as deduced from

the experimental conditions, is typically

$$N_P \equiv \frac{N_{2D}}{P} = T\alpha_0 L/h\nu_p A \sim 10^{14} cm^{-2} mW^{-1} \tag{4.5}$$

where T is the pulse period of the femtosecond pulse-train, L is the membrane thickness, $h\nu_p$ is the pump photon energy, A is the surface of the pumped region ($A = \pi r^2$, with r=1.6 μm) and α_0 is the linear absorption coefficient at the pump wavelength ($\alpha_0 L \sim -ln(0.67) \sim 0.4$ [2], using that the fraction of the incident power absorbed at 800 nm is $\sim 33\%$ [123]). This density corresponds to an overall 3D density of $N_{3D} = N_{2D}/d \sim 10^{18}\ cm^{-3}$ injected carriers for $P \sim 0.3$ mW. Considering that the carrier diffusion in the InP is essentially governed by holes $D_h = 5\ cm^2/s$ [117], carriers are thus able to reach the wetting layer (WL) in $\sim (100\ nm)^2/D_h \sim 20$ ps; therefore only a fraction of the total carriers accounting for fast carriers will be eventually captured inside the WL in a time shorter than 20 ps. Such a fraction will be considered as a fitting parameter in our analysis.

We now analyse the contribution of each semiconductor layer or structure to carrier-induced nonlinear effects. For probe photon energies ($h\nu$) close enough to the bandgap energies (approximately $(E_g - h\nu)/E_g < 0.15$ for a III-V semiconductor), it has been shown that index change is dominated by band-filling effects [124], which is indeed the case of the QDs in our system. On the other hand, for very low photon energies with respect to the electronic bandgaps, $h\nu << E_g$, as it is the case of the InP, Drude effects are dominant. In the case of the wetting layer (WL) we can expect both band filling and Drude effects contributing to the decrease of refractive index (see section 1.2).

The refractive index change due to Drude effects for carrier densities close to transparency values ($N_{tr} \sim 10^{18}\ cm^{-3}$) can be estimated as large as $\Delta n/n \sim 0.001$ [124], leading to wavelength shifts of about $\Delta\lambda \sim \Gamma\lambda\Delta n/n < 1$ nm. Band-filling effects produce larger refractive index changes for a carrier density N_{tr}, both in bulk materials and in quantum wells (QWs). For instance in InAsP/InP QWs we have previously observed $\Delta n/n \sim 0.01$ for carrier densities close to QW transparency ($N_{2D} \sim 10^{12}\ cm^{-2}$) [91, 115]. In the case of quantum dots, however, the maximum carrier density that can be injected equals the QD density, $N_{QD} \sim 10^{10} cm^{-2}$. Taking into account that this remains at least two orders of magnitude below the carrier density in the WL, we can therefore conclude that refractive index change in the QDs, even if all the QD levels are occupied, can be neglected with respect to index change induced by carriers in the WL. From now on we thus consider that the nonlinear carrier-induced effects are produced by a carrier density confined within the WL. Furthermore, we assume that the refractive index change, hence the wavelength shift, can be considered to be a linear function of the carrier density, as usual:

$$\Delta\lambda = \Delta\lambda_N N \tag{4.6}$$

where $\Delta\lambda_N$ is taken constant and N is the 3D carrier density. Therefore, the dynamics of the wavelength shift, $\Delta\lambda(t)$, is considered proportional to the carrier dynamics, N(t).

We then study the carrier dynamics governing the observed time dependence of the wavelength shift (fig. 4.9.a). According to eq. 1.56 there are two components in the carrier dynamics, the recombination processes and the intracavity energy. Since in our experiments the probe power is kept low, we can neglect the contribution of the intracavity energy in front of the recombination processes. Therefore, two main recombination processes can be taken into account: a nonradiative recombination process with a time constant τ_{nr}, and a radiative recombination

[2] This expression is expected to hold for low pumping powers

process or bimolecular recombination at a rate BN, B being the bimolecular recombination coefficient, which is expected to play an important role especially for high carrier densities [91]. The corresponding rate equation for N(t) is

$$\frac{dN}{dt} = \frac{-N}{\tau_{nr}} - BN^2 \tag{4.7}$$

We solve eq. 4.7 analytically for femtosecond pumping. In such a case, carriers relax freely from an initial carrier density $N(t = t_{0+}) = N_0$ injected by the femtosecond pumping pulse centered at $t = t_0$, which has already been described as a kick-like pumping process [89, 93]. Defining $\Delta t = t - t_{0+}$, the solution of eq. 4.7 reads

$$N(\Delta t) = \frac{N_0 e^{-\Delta t/\tau_{nr}}}{1 + N_0 \tau_{nr} B(1 - e^{-\Delta t/\tau_{nr}})} \tag{4.8}$$

The decay time $\tau_{1/e}$ defined as the time for the decay of the carrier density at 1/e of the initial value, $N(\Delta t = \tau_{1/e}) = N_0/e$, can be readily found from eq. 4.8:

$$\tau_{1/e} = \tau_{nr} ln(\frac{e + N_0 \tau_{nr} B}{1 + N_0 \tau_{nr} B}) \tag{4.9}$$

Note that in the limit $BN_0 << (\tau_{nr})^{-1}$ we obtain $\tau_{1/e} \to \tau_{nr}$, meaning that for small bimolecular recombination rates, the nonradiative decay time is dominant.

Eqs. 4.8 and 4.9 can be re-written in terms of the (experimentally measured) initial wavelength shift ($\Delta\lambda_0$) by evaluating eq. 4.6 at $t = t_{0+}$, which gives $N_0 = \Delta\lambda_0/\Delta\lambda_N$. Using this, we have fitted eq. 4.8 to the experimental data in fig. 4.9.a with the fitting parameters $\widehat{B}$, $\Delta\lambda_0$ and τ_{nr}, where $\widehat{B} \equiv B/\Delta\lambda_N$. We notice that for the highest pump power, P=0.98 mW, the dynamics of $\Delta\lambda$ almost superimpose to that for P=0.67 mW, meaning that carrier saturation is playing an important role and therefore no additional information can be obtained from the data corresponding to P=0.98 mW. The excellent quality of the fits can be observed in fig. 4.15.a. We average out the parameter values resulting from fitting the four curves in fig. 4.9.a using a weighted average procedure. Normalized weights are defined assuming an ensemble of four independent measurements with weights w_i as usual, $w_i = (e_i^2 \sum 1/e_i^2)^{-1}$, where e_i is the standard deviation of the i-th fitted value. The weighted average gives $\langle\widehat{B}\rangle = (6.7 \pm 1)\ ns^{-1}nm^{-1}$ and $\langle\tau_{nr}\rangle = (0.12 \pm 0.03)$ ns, where the errors are given by the weighted standard deviation. The obtained nonradiative recombination time in this system is of the same order of magnitude as in previous measurements of 2D PhC samples with InAsP/InP QWs [91]. The accuracy of these two fitted parameters can be tested by comparing the experimental decay times to those obtained using eq. 4.9. This is shown in fig. 4.15.b. It can be observed that the dependency of the decay times on the initial carrier density is well reproduced by eq. 4.9 with the two averaged parameters $\langle\widehat{B}\rangle$ and $\langle\tau_{nr}\rangle$.

In order to relate $\langle\widehat{B}\rangle$ to the physical coefficient B, $\Delta\lambda_N$ has to be found. With this aim we first calculate the injected carrier density in the WL as a function of (small) pump power (P), $N_{0,WL} = (f/d)N_p P$, where f is the probability of carrier capture in the WL after diffusion and d is the WL thickness (d=0.6 nm). Next we relate the wavelength shift to the pump power for small P, $\Delta\lambda_0 \sim (3.2\ nm/mW)P$. As a result, $\Delta\lambda_N \sim (d/f) \times 1.3 \times 10^{-14}\ nm\ cm^2$. Using an already reported value for the bimolecular recombination coefficient in InP-based materials, $B \sim 3 \times 10^{-10}\ cm^3/s$ [93], the fraction of the total carrier population within the WL becomes $f \sim 0.02$. Considering that the remaining $(1 - f)$ carriers are within the InP, the ratio of the

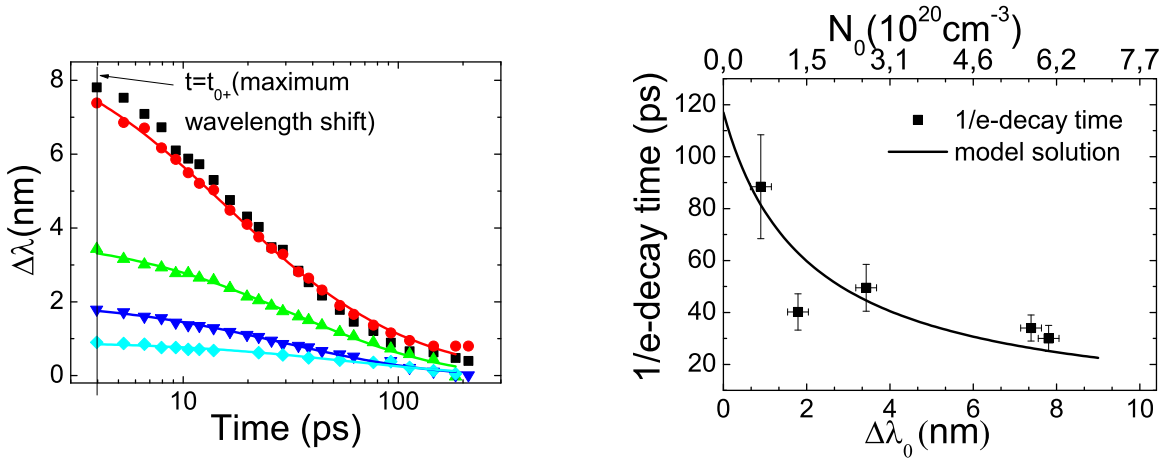

(a) (b)

Figure 4.15: *(a) Resonance shift as a function of the delay time (in logarithmic scale) for different pump powers, 0.28 mW(♦), 0.42 mW(▼), 0.54mW(▲), 0.67 mW(●) and 0.98 mW(■) fitted (solid line) using eq. 4.8, see text. The fitted parameters are:* $\tau_{nr} = (0.38 \pm 0.15)$ *ns and* $\widehat{B} = (6.6 \pm 0.3)$ $ns^{-1}nm^{-1}$ *for P=0.67 mW;*$\tau_{nr} = (0.13 \pm 0.03)$ *ns and* $\widehat{B} = (7 \pm 1)$ $ns^{-1}nm^{-1}$ *for P=0.54 mW;* $\tau_{nr} = (0.11 \pm 0.02)$ *ns and* $\widehat{B} = (14 \pm 2)$ $ns^{-1}nm^{-1}$ *for P=0.42 mW;* $\tau_{nr} = (0.17 \pm 0.1)$ *ns and* $\widehat{B} = (14 \pm 2)$ $ns^{-1}nm^{-1}$ *for P=0.28 mW. (b) Dependence of the decay time* (Δt *at* $1/e$) *with the pump power. Solid line: model solution for the decay time from eq. 4.9, using the weighted average of the fitted parameters in (a), namely* $\langle \widehat{B} \rangle = 6.74$ $ns^{-1}nm^{-1}$ *and* $\langle \tau_{nr} \rangle = 0.117$ *ns.*

density in the InP to that in the WL is $N_{0,InP}/N_{0,WL} \sim d(1-f)/Lf \sim 0.1$, meaning that even for such small fraction f, the carrier density in the WL is one order of magnitude larger than the density in the bulk. This justifies our early assumption that the main contribution of carrier-induced effects comes from the WL. In addition, we point out that the small fraction of the carrier density trapped within the WL in the observation time scale could be explained as a result of the rather small diffusion time of holes across the membrane, estimated above as ~ 20 ps.

As pointed out in sec. 4.2.1, in the case of the fibered pump configuration, the observed relaxation time of an initial wavelength shift of $\Delta\lambda_0 \sim 1$ nm is ~ 170 ps, whereas that for the same $\Delta\lambda_0$ in the surface configuration is ~ 90 ps. This could be explained under the hypothesis of a lower carrier density inside the WL in the fibered pump configuration, which might be related to a different pumped volume in this case with respect to free space pumping. Indeed, carriers are mostly injected close to the membrane surface in contact with the taper rather than throughout the whole membrane thickness as in the free space illumination. We can thus expect a smaller fraction of carriers being captured by the WL, and therefore a weaker bimolecular recombination effect leading to a slower decay time. The fact that a smaller carrier density in the WL for the fiber-pumping configuration gives the same $\Delta\lambda_0$ as in the surface pumping configuration could be explained as an additional blue shift induced by the remaining (1-f) carriers in the InP.

It is worth pointing out that radiative recombination governs carrier dynamics for the highest pumping powers used in this work. In particular, they are responsible for the shortest times that have been observed, that is, on the order of 30 ps, corresponding to the largest carrier densities. Also, since carrier saturation effects appear for $P > 0.7$ mW, it can be inferred that for the shortest observed time of 30 ps, a material limit is attained for ultrafast carrier-induced

switching processes in this class of systems. Notice that the shorter relaxation times observed here are of the same order of magnitude as those recently reported in resonantly pumped H0 cavities where carrier diffusion plays a main role in carrier relaxation due to small optical volume of the H0 cavity [125].

4.3 Conclusion

In order to test the performance of our taper-cavity-system, we have first developed a method to directly measure the thermal relaxation time of the nanocavity. This technique relies on reflectivity measurements of a CW probe beam coupled to the cavity through a tapered fiber, becoming sensitive to the thermally induced increase of the refractive index within the cavity. We applied this method to an InP-based nanocavity on a suspended membrane. Wavelength shifts up to 0.3 nm for 165 μW pumping power @800 nm were observed. The obtained values for the characteristic thermal times are close to 1 μs, more than a factor 3 compared to a rough estimation of the relaxation time of the fundamental mode in a rectangular 2D membrane, showing the relevance of the experimental measurements.

In a second experiment, time resolved pump and probe measurements with femtosecond resolution have been performed in order to investigate the electronic characteristic time of the system. The signal was evanescently coupled through the taper fibered, and the pump was either sent by the surface or through the tapered fiber. The optical pump provides ON/OFF switching of the transmitted or reflected signals with time features associated to the electronically induced refractive index change. In the surface pump configuration switching ON and OFF times of 4 and 30 ps, respectively, were measured. In the case of fiber-coupled pump pulses configuration, an all-fibered stable operation was achieved at the expense of increased ON and OFF switching times up to 20 ps and 170 ps, respectively. These values are still shorter by one order of magnitude than the previously reported ON/OFF switching times [120]. Through fitting the decay time of the nonlinear effect by means of rate equations for the carrier density we have explained the origin of the shortest overall switching times (35 ps) as a result of radiative carrier recombination inside the wetting layer. Moreover, we have shown that the increase of the rise time in the all-fibered configuration is a consequence of pump-pulse dispersion in the fiber. This could be pre-compensated at the input of the tapered fiber in order to retrieve the characteristic times measured in the surface pumping configuration, that is ON times as short as 4 ps. In addition to the switching capabilities, this kind of photonic crystal cavities with embedded quantum dots could be used as lasers sources with ultrafast tunability of the laser mode, taking benefit from the large carrier-induced nonlinear effects in the wetting layer described in section 4.2.

This electronic time together with the thermal relaxation time will be of major importance for the nonlinear dynamical studies discussed in the next part. These times are the characteristic lifetimes of the nonlinar phenomena we will see in the next chapters. In the following studies the refractive index change, thermal and/or electronic, is no longer given by an incoherent pump; instead, it will be induced by the intracavity energy.

Part II

NonLinear dynamics in photonic crystal cavities

In the previous part we have described, characterized and optimized a mechanism to efficiently couple light into a photonic crystal nanocavity. Using this mechanism nonlinear e-ffects of thermal and electronic origin were measured. These effects are given by refractive index changes shifting the resonance mode (to the red in the case of thermal effects and to the blue for electronic effects) due to an incoherent pump. In this part we will study the nonlinear effects given by a resonant injection with the photonic mode. Therefore, we focus on nonlinear dynamical regimes leaded by self-induced effects.

In the first chapter we study the nonlinear dynamical regimes ruled by a single material variable: thermal or electronic. In the first part of the chapter we explore the thermo-optical bistability; this regime is achieved provided the thermal nonlinear effects overcome the electronic ones. In the second part, we investigate the electronic bistability. In this case, thermal effects are avoided and only electronic nonlinearities are involved.

The nonlinear dynamical regime governed by two variables is studied in the second chapter. Both thermal and electronic effects are combined in order to obtain interesting phenomena such as self-sustained oscillations and excitability regime. Finally, the refractory time of the excitable cavity is measured. These studies represent the first reported demonstration of electronic excitability in a photonic crystal nanocavity.

Chapter 5

Nonlinear dynamical regimes involving a single dynamical variable: Optical bistability

In this chapter we will consider a particular class of dynamical effect, associated to the existence of an unique dynamical variable. Indeed, as long as the photon lifetime in the cavity is much shorter compared to the time scale of the material variable (i.e. carrier density or temperature) the former can be adiabatically eliminated leading to 1D phase spaces. Specially, we will focus on optical bistability (OB). OB is a key phenomenon in the road of all optical signal processing, in particular for optical memories. Two ingredients are needed in order to obtain bistable operation in an optical system: a resonance capable of localizing the light intensity in the spectral domain, and a nonlinear effect that changes the spectral response as a function of the injected intensity. Under certain conditions for the injection of a nearly resonant beam, two stable states for the transmission/reflection through the device can coexist. In the first section of this chapter we study the bistability given by thermal effects and in the second section by electronic effects, where thermallly-induced nonlinearities are avoided.

We have introduced the OB in section 1.2, where the constitutive equations have been detailed and the main behaviors have been discussed. We summarize here some key elements that are essential to set up and understand the experimental demonstration. The bistable regime in an optical device corresponds to the system showing two stable states of transmission/reflection, high and low, for a single input light intensity. In order to quantify this phenomenon, let us consider the steady states of the system (see section 1.2):

$$\frac{P_{out}}{P_0} = \frac{P_{in}/P_0}{1 + (P_{out}/P_0 \pm \delta)^2} \tag{5.1}$$

where P_{out} and P_{in} are the steady states of the transmitted and input power, respectively. P_0 is the "characteristic power of the cavity" and $\delta = \tau(\omega_0 - \omega_{in})$ is the detuning of the optical injection (ω_{in}) with respect to the resonance (ω_0). The bistable regime corresponds to the case where two critical points exist, which requires a detuning of $|\delta| > \sqrt{3}$. For negative nonlinearities, the positive sign in 5.1 holds and $\delta < -\sqrt{3}$, whereas for positive nonlinearities the negative sign must be consider and $\delta > -\sqrt{3}$. Under these conditions, a typical $P_{out}(P_{in})$ from eq. 5.1 is presented in fig. 5.1. Therefore, in order to obtain the bistable operation the system should be injected differently depending on the type of nonlinearity involved: with wavelengths on the red side of the resonance for thermal OB or on the blue side for electronic OB, fig. 5.2. We will

consider both situations in the following sections.

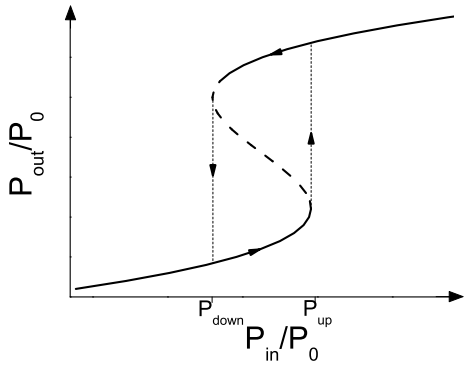

Figure 5.1: *Typical feature of a bistable optical system. The continuous line corresponds to the stable states while the dashed line to the unstable states. The arrows show the sense of the hysteresis cycle.*

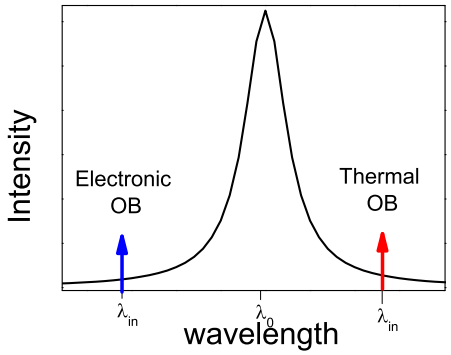

Figure 5.2: *Scheme of the injection wavelengths needed to obtain the thermal (red arrow) or electronic (blue arrow) bistability.*

The main change in these sections with respect to Part I is the near resonant pumping. The off resonant or incoherent pumping implemented in Part I produced a rigid shift of the cavity resonance. In the case of a resonant pumping, there is an interplay between the nonlinear shift and the enhancement of the intensity inside the cavity. The shift becomes stronger at the maximum of the electromagnetic field enhancement, corresponding at the cavity central frequency, and it is smaller at the resonance wings. As a result, the incident field induces a bending of the cavity resonance.

The thermal and electronic origin of the OB behavior will be identified by the dynamics of the switch between the upper and the lower states: slow with μs characteristic time for thermal OB and fast in the ps to ns scale for electronic OB.

Experimentally, this kind of behavior can be shown through a simple set up. The system is excited with firstly increasing and then decreasing power and the reflected/transmitted signal is collected. Under these conditions the system exhibits what we call the hysteresis cycle (black

arrows in fig. 5.1), which clearly shows the range of powers where the system presents two stable states for the same injected power.

5.1 Thermo-optical bistability

Thermo-optical bistability was studied in the sample described in section 3.2, under continuous wave (CW) excitation. The coupling into the resonance and the extraction of the signal are achieved via a tapered fiber as described in section 3.2.2. The OB phenomenon [82, 112] can be obtained through self-induced red shift of the resonance upon (large enough) CW injection from a single beam. The thermally-induced refractive index increase takes place for a nearly optically resonant CW injection, in the absence of any incoherent pump. In such a case, bistable operation can be expected provided that: i) the injection wavelength is red shifted with respect to the resonance; ii) the detuning between the injection beam and the cold resonance is larger (in modulus) than $\sim \sqrt{3}\gamma/2$, where γ is the FWHM of the resonance; iii) the injection power exceeds a given threshold. As long as the nonlinearity comes from a thermo-optical effect, the switching times should be related to the characteristic thermal relaxation time obtained before.

5.1.1 Set up description and results

In order to demonstrate the thermo-optical bistability through the hysteresis cycle, the output power as a function of input power for different detunings is investigated. Importantly, the power sweep in such measurements must be quasi-stationary, i.e. the duration of the power ramp must be much longer than the thermal relaxation time ($> 1\ \mu s$ according to section 4.1). Therefore, the CW input beam generated by a tunable laser ('Net Test', Tunics Plus S, 1430 nm-1530 nm) is modulated at 10 kHz, fig. 5.3. The modulation is obtained by feeding the laser through a low frequency modulation interface with a 10 kHz, 0-3.8 V, triangular signal, while keeping its current at 130 mA. Under this configuration the maximum power sent to the tapered fiber is 4.7 mW. In such conditions, the input modulation and the optical transmitted signal through the fiber are simultaneously measured as a function of time, the latter using a 3.5 GHz DC-coupled photoreceiver (DC-PD,'New Focus', model 1592). Both signals are registered in a 400 MHz-bandwidth, 5 Gs/s, oscilloscope ('Lecroy', WaveRunner 44Xi).

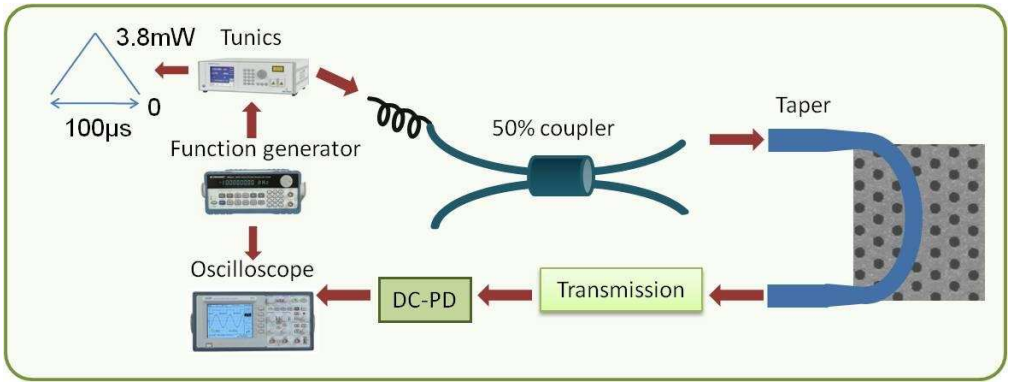

Figure 5.3: *Scheme of the experimental set up used to study the thermo-optical bistability.*

In order to determine the wavelength range for bistability operation we first characterize the cavity resonance using the experimental configuration described in section 3.2.2 where the use of 100 fs-duration OPO pulses allow to spectrally probe the cavity resonance through the

tapered fiber. The resonance spectrum is shown in fig. 5.4.a where the arrows indicate the spectral range explored in the thermo-optical bistability experiments.

Thermo-optical bistability was observed for injected powers greater than ~ 1 mW. The input and transmitted signals for a detuning of $\Delta\lambda = \lambda_0 - \lambda_{inj} = -0.56$ nm, where λ_0 is the linear cavity resonance and λ_{inj} the injected wavelength, are shown in fig. 5.4.b. The transmitted power in fig. 5.4.b reveals the thermo-optical bistable behavior. This is further highlighted in fig.5.4.c where the transmitted power as a function of the input power is plotted, showing the hysteresis cycle.

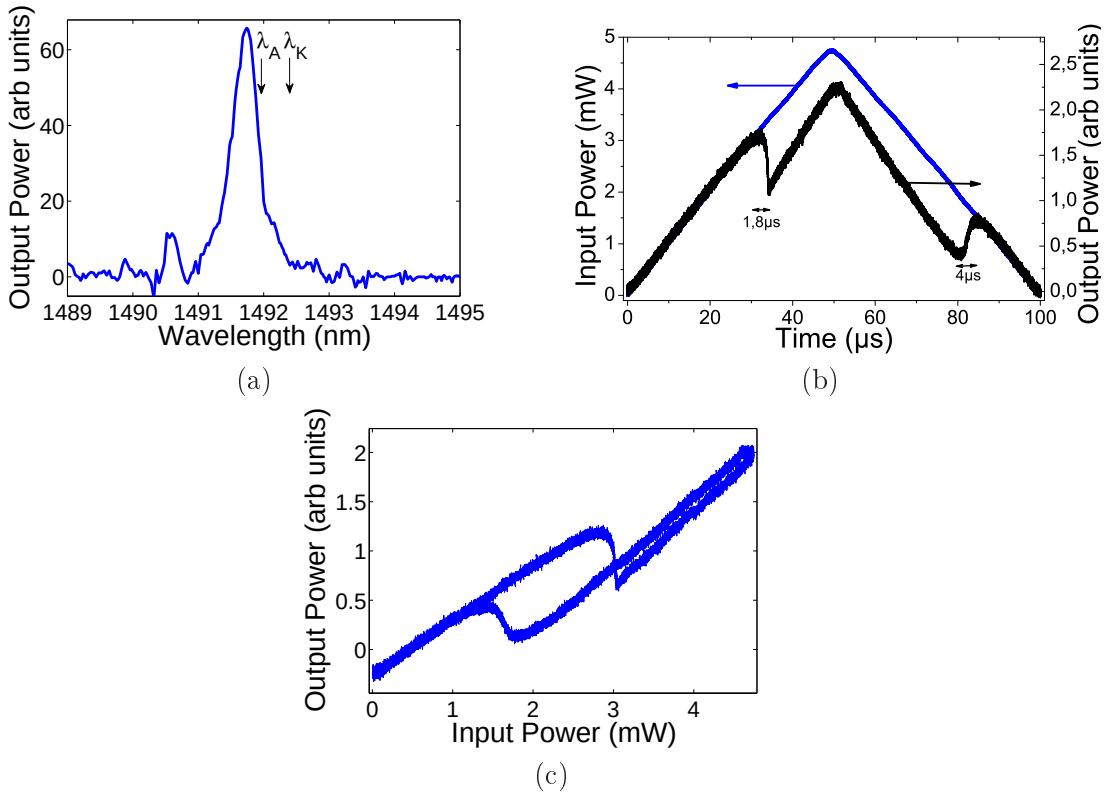

Figure 5.4: *(a) Reflectivity spectrum of the linear cavity resonance, and the wavelength range for the CW injection. (b) Time traces of input (blue line) and transmitted output (black line) powers for a detuning of $\Delta\lambda_0 = -0.56$ nm; durations of the switch processes are 1.8 μs and 4 μs for the on/off switching, respectively. (c) Hysteresis cycles showing the bistable behavior ($\Delta\lambda_0 = -0.56$ nm).*

Hysteresis loops are observed for $|\Delta\lambda| > 0.35$ nm. Fig. 5.5 shows the transmitted versus the input powers for different detunings. The loop size increases for larger detuning-values, up to $|\Delta\lambda| \sim 0.72$ nm where the maximum injection power remains below the bistability threshold. Note that the hysteresis cycle of fig. 5.4.c has the opposite direction than the cycle in fig. 5.1 due to the fact that the resonance in transmission is downwards (spectral dip). As discussed in section 1.2 (eq. 1.39), this sign of the nonlinearity yields to a bending of the resonance, towards higher wavelengths.

Switching on and off times have been measured as the time the system takes to shift from the higher to the lower value of the transmitted signal (heating up) and vice versa (cooling

down), respectively. The switch on time is 1.8 μs, whether the switch off time is 4 μs. Both are of the order of the 1 μs thermal characteristic time obtained with the pump and probe set up (see section 4.1), as expected. Though, the difference between switch on and off times is less intuitive. We discuss the origin of such difference in the following paragraphs.

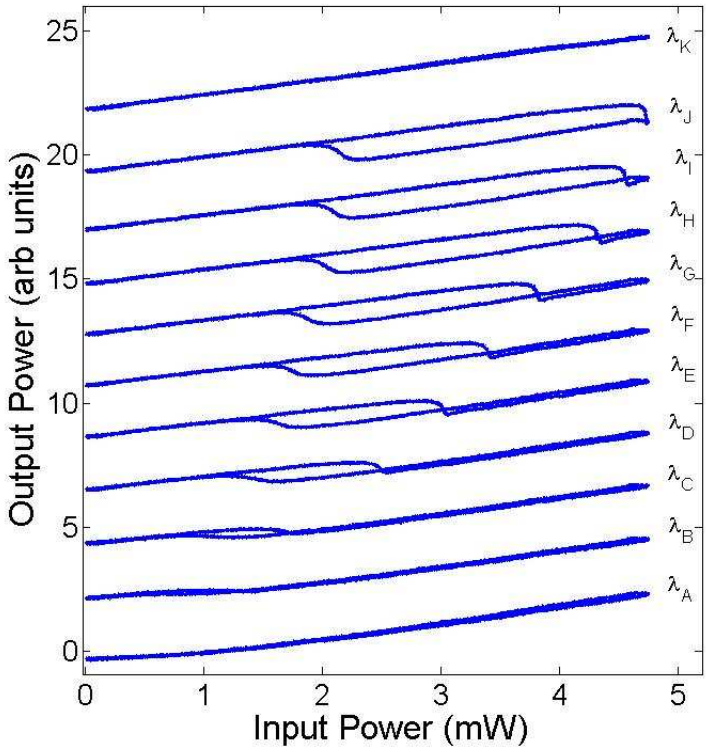

Figure 5.5: *Hysteresis cycles showing the bistable behavior. Detuning values with respect to the cavity resonance are, from λ_A to λ_K: -0.11, -0.27, - 0.36, -0.46, -0.52, -0.56, -0.6, -0.64, -0.66, -0.68 and -0.72 nm. The input power is measured at the tapered fiber input.*

5.1.2 Theoretical model

The difference between switch-on and switch-off times can be explained from simple considerations of dynamic thermo-optical nonlinearities. For this, we will apply the set of equations deduced in chapter 1.4 to the experimental conditions.

The dynamical equation for the intracavity energy (a) is given by eq. 1.41. However, according to the experiments, the contribution of electronic nonlinearities con be neglected. Then, eq. 1.41 yields

$$\frac{da}{dt} = [i(\omega_0 + \Delta\omega_{th}) - \frac{1}{\tau}]a + df \tag{5.2}$$

Replacing $a \to a'(t)e^{i\omega_{in}t}$, $t = t'/\tau$ and $f \to f'(t)e^{i\omega_{in}t}$ eq. 5.3 yields

$$\frac{da}{dt} = [i\delta(t) - 1]a + \tau df \tag{5.3}$$

where $\delta(t) = \tau(\omega_0 + \Delta\omega_{th} - \omega_{in}) = \delta_0 + \tau\Delta\omega_{th}$ and $d = j\ exp(j\phi/2)/\sqrt{\tau_c}$. Since the dynamics of $a(t)$ is much faster than thermal processes, its dynamical equation can be adiabatically eliminated. Moreover, we can relate the intracavity energy to the reflected power as $|a(t)|^2 = P_r(t)\tau_c$. Then, the stationary states of eq. 5.3 are given by

$$P_r(t) = \frac{\eta^2 P_{in}}{1 + \delta(t)^2} \tag{5.4}$$

which simply describes the Lorentzian shape of the resonance.

Considering the differential equation for the temperature dynamics (eq. 1.63) and the relation between $\Delta\omega_{th}$ and the temperature change (eq. 1.64), we obtain the equation for the dynamics of the resonance shift:

$$\frac{d\delta}{dt} = \frac{-1}{\tau_{th}}(\delta(t) - \delta_0 + \frac{P(t)}{P_0}) \tag{5.5}$$

with τ_{th} the characteristic relaxation time obtained in section 4.1 and $P_0 = U_{0,th}/\tau_c$ the outcoupled characteristic thermal power, see section 1.4, given by

$$P_0 \approx \frac{n_{g0}\rho\ C_p V_{cav}}{2Q_{loaded}(dn/dt)\tau_c\Gamma\alpha_0\tau_{dis}v_{g0}} \tag{5.6}$$

with $\tau_{dis,cav}$ the time scale for heat dissipation, which is approximated by $\tau_{dis,cav} \sim 186$ ns [97]. dn/dT can be taken from the tabulated values of the refractive index change per unit temperature as $dn/dT = n_T$ ($n_T/n \approx 0.63\ 10^{-4}K^{-1}$ @$300K$ for InP [96]).

The steady-states solutions of eqs. 5.4 and 5.5 can be graphically found by intersecting solutions of $d\delta/dt = 0$ from eq. 5.4 and eq. 5.5, fig. 5.6. Two stable states δ_{+st} and δ_{-st} coexist provided that $\delta_0 > \sqrt{3}$, and $P_{in} > P_{thr}$, where P_{thr} is the bistability threshold. The threshold in reflection can be approximated by $P_{r,thr} \sim P_0|\delta_0|$, fig. 5.6, which yields to a threshold for the injected power in the vicinity of the cavity of $P_{in,thr}^{(theo)} \sim P_0|\delta_0|/\eta^2$ according to CMT. $P_0 = 9.8$ μW is obtained as in section 1.4 (see caption in fig. 5.6) and δ_0 is obtained from the hysteresis cycle in fig. 5.5, considering λ_C, $\delta_0 = 2.2$ (using $\gamma = 0.33$ from section 4.1). This leads to $P_{in,thr}^{(theo)} = 210\ \mu W$, which is in good agreement with the value found experimentally for this detuning $P_{in,thr}^{(exp)} = 260\ \mu W$ (using that $P_{in} = 0.263P_{input}$, see caption in fig. 5.6).

Steady state relaxation dynamics can be obtained through the linearization of eq. 5.5 in the vicinity of the fixed points (see eq. 1.5 in the introduction), i.e. by setting $\delta \cong \delta_{st} + Aexp(-t/\tau_\pm)$ in eq. 5.5. The eigenvalues $\tau_\pm$ can be readily obtained:

$$\tau_\pm^{-1} = \tau_{th}^{-1}[1 + \frac{1}{P_0}\frac{dP}{d\delta}|_{\delta_{st}^\pm}] \tag{5.7}$$

Since P(t) has slopes with opposite signs at the two stable steady states (see fig. 5.6) corresponding to the switch on/off processes, namely positive (negative) slope for δ_{st}^+ (δ_{st}^-), therefore $\tau_+ < \tau_-$, consistent with the experimental observation of switch-on times shorter than switch-off times. With the parameters of fig. 5.6 we obtain $\tau_-/\tau_+ \approx 8.5$. Experimentally, the ratio of switch-on to switch-off times was ~ 2.2, which contains the information of the full i.e. nonlinear relaxation dynamics, whereas the calculated τ_-/τ_+ only accounts for the linear relaxation close

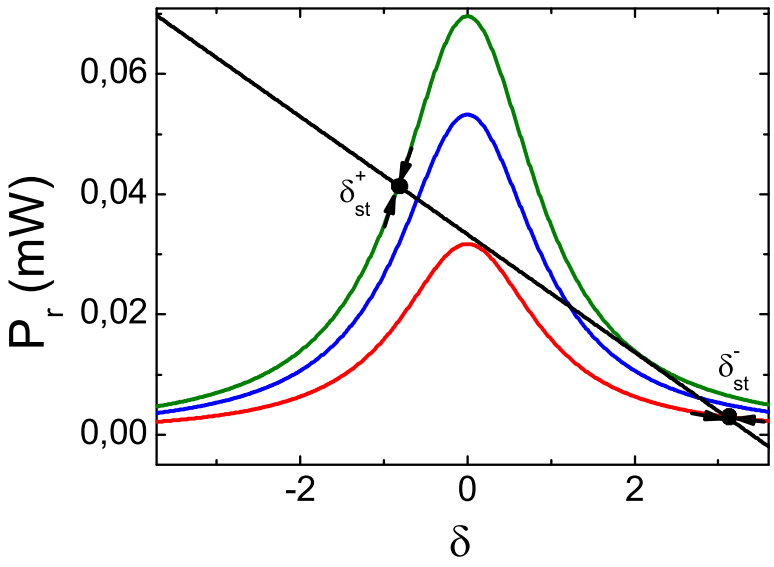

Figure 5.6: *Phase space for bistability conditions. Blue, green and red lines: stationary solutions of the reflected power (P) as a function of the normalized wavelength shift (δ) for: bistable conditions (P_{input} = 2 mW, blue) switch on conditions (P_{input} = 2.6 mW, green) and switch off conditions (P_{input} = 1.2 mW, red). Black line: stationary solutions of δ. The intersections of the black line with the curves give the steady states: $\delta_{st}^{+(-)}$ is the stable state for the switch on (off) process. The direction of the dynamical flow is indicated by the arrows. The opposite slopes of $dP/d\delta$ at the fixed points mathematically explain the difference in relaxation times (see text). The parameters are: $P_0 = 9.8\ \mu W$, calculated with $V_c = 0.08\ \mu m^3$, $\tau_{th} = 186$ ns, $\Gamma = 0.015$, $Q_{loaded} = 4520$, $\rho C_p = 1.5\ Jcm^{-3}K^{-1}$, $\delta_0 = 3.4$ and α=33 cm^{-1} (fitted parameter); and $P_{in} = 0.263 P_{input}$, with P_{input} the injected power into the fiber.*

to the steady states. We point out that the predicted difference in switching times given by eq. 5.7 is generic in bistable systems and can be expected to hold even for fast nonlinearities. Moreover, even in the absence of bistability, a high power input may affect the thermal dynamics in the way described by eq. 5.7 leading to a dependence of the thermal relaxation times to the equilibrium state δ_{st}. Unlike linear thermal dissipation regimes, studied in section 4.1, in the nonlinear regime heating and cooling processes may have different relaxation times provided the injected power is close to the characteristic power $P_{0,th}$.

5.2 Electronic bistability

Interesting nonlinear behaviors have been obtained for the sample depicted in fig. 3.2, such as, thermo-optical bistability and ultrafast optical switches provided by electronically-induced nonlinear effects. However, nonlinear dynamical mechanisms from an electronic origin, such as electronic bistability or excitability, were not observed in this sample. The absence of electronically driven nonlinear dynamical regimes can be attributed to a low absorption of the sample (the maximum absorption of the QDs is $\sim 10\ cm^{-1}$) together with the low confinement factor in QDs. In Yacomotti et al. [115] a nonlinear dynamical regime was observed in a sample with quantum wells (QWs) as active material. We can estimate the absorption (α) in their condition

through the quality factors with (Q_{lineal}) and without (Q_{rad}) absorption, $Q_{lineal} = 1763$ and $Q_{rad} = 3775$, respectively. From section 1.4, $1/Q_{lineal} = 1/Q_{rad} + 1/Q_a$, with $Q_a = \omega\tau_a/2$, the absorption quality factor, and $\tau_{a_0} = 2/v_{g_0}\alpha_0\Gamma$. Considering $\Gamma = 0.2$, the absorption in [115] allowing to achieve low-threshold electronic bistability was $\alpha \sim 200\ cm^{-1}$. Therefore, in order to obtain nonlinear dynamical regimes, the absorption needs to be increased at least one order of magnitude. In order to fulfill this requirement, samples with QW as active medium were fabricated taking benefit of the QW absorption, ranging from a few hundred of cm^{-1} to 5000 cm^{-1}, and the larger Γ factors.

The following part of this section first describes the main characteristics of such 2D PhC using QW as active medium. Then, we present the experimental demonstration of all-optical electronic bistability. The origin of this bistability is shown to be the fast electronic nonlinear index change.

5.2.1 Quantum Well samples

The geometrical parameters of the sample remain almost unchanged respect to the ones described in chapter 3; the main difference resides in the use of QWs as active material. The cavity is a L3-type cavity, where the two holes closing the cavity are shifted away by 0.15a. The PhC period and hole radius are a=450 nm and r=120 nm, respectively. In this case, the suspended InP membrane (265 nm-thick, $\lambda/2n$), grown by metalorganic vapour phase epitaxy (MOCVD), incorporates four central layers of InGaAs/InGaAsP QWs, fig. 5.7.a, each layer with a thickness of $\sim$ 13.5 nm and $\sim$ 16 nm for the well and the barrier, respectively. The QWs luminescence at 300 K, measured over an unetched region, close to the PhC, is centered at $\sim 1.51\ \mu m$ (fig. 5.7.b) with a spectral broadening of 75 nm. The membrane thickness ($\lambda/2n$) is such that the field maximum (@1550 nm) is located at the center of the membrane, matching the location of the active material. A $Si0_2$ sacrificial layer underneath is bonded on a Si substrate through a BCB layer [126]. A 1 μm air spacer, obtained after etching the sacrificial layer, lies between the InP membrane and the substrate.

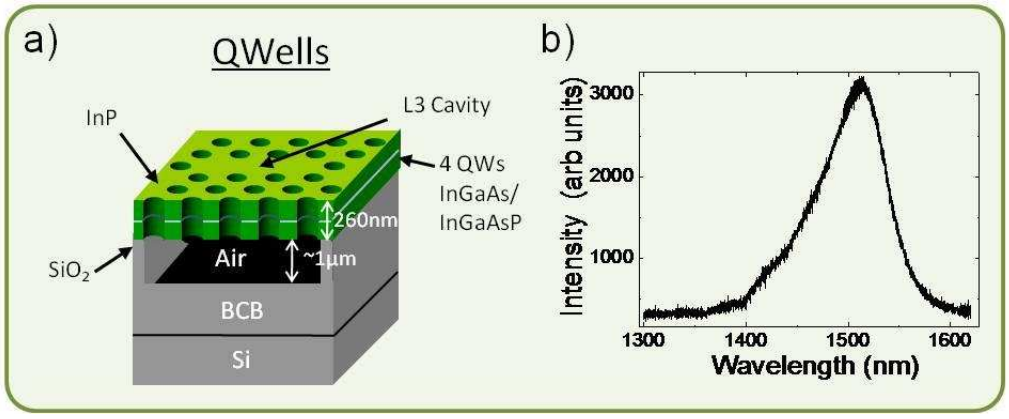

Figure 5.7: *(a) Qw sample scheme. (b) QWs photoluminescence spectrum.*

Sample fabrication

This section contains a summary of the fabrication steps. The samples were fabricated in the LPN clean room by Yacine Halioua, Frabice Raineri, Isabel Sagnes and Remy Braive. More

details about the fabrication process are given in [126].

The first step is the metalorganic vapour phase epitaxy (MOCVD) of the InP structure. This starts by the growth of an InGaAs etch stop over an InP substrate, followed by an InP layer, which will form the suspended membrane. In its center, four InGaAsP/InGaAs QWs are grown. The membrane total thickness is ~ 265 nm and it corresponds to $\lambda/2n_{eff}$ with n_{eff} the effective refractive index calculated as the weighted average of the refractive index of air and material. Finally, a 1 μm-thick sacrificial layer of $Si0_2$ is deposited over the InP active membrane. This structure is positioned (upside down) over a Si substrate coated with a benzocyclobutene (BCB) layer used for the bonding, see fig. 5.8. In order to polymerize the BCB and finalize the bonding, a hard bake is performed in a nitrogen atmosphere for 2h at 300°.

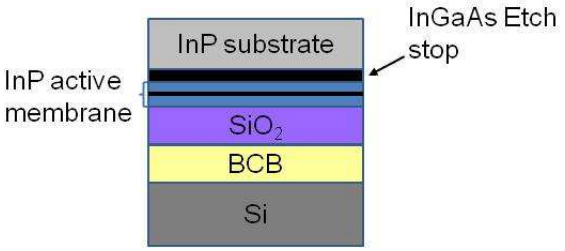

Figure 5.8: *(a) Sketch of the structure before the etching processes.*

Once hard baked, the InP substrate is removed by HCl wet etch. The InGaAs etch stop is removed using $H_2SO_4 : H_2O_2 : H_2O$ (3:1:1) leaving on top the InP layer with the QWs. The procedure to etch the holes is the one described in section 3.1.2. Once the InP active membrane is etched, the SiO_2 layer is removed under the PhC by HF wet etching in order to obtain the suspended membrane. Residual HF resting on the sample is removed by a supercritical drying technique.

Photoluminescence characterization

We first characterize photoluminiscence spectrum of the sample with QWs for different excitation intensities. The experimental set up, shown in fig. 5.9, is similar to the one described in sec. 3.1.3. The sample is pumped with a @810 nm, 80 MHz-repetition rate, 100 fs-pulse duration Ti:Sa source. The emission is collected with a 50x microscope objective ('Mitutoyo', M Plan Apo NIR, X50, $f = 170$ mm, $NA = 0.42$) and sent to a spectrometer, see sec. 3.1.3.

A typical spectrum of the L3-type cavity described above is shown in fig. 5.10.a, for a pump power of 15 μW. A mode centered at 1565 nm is observed. The quality factor obtained from the FWHM of the cavity resonance gives $Q \sim 1700$. As it has been discussed in section 3.1.3, the measured of the intrinsic quality factor has an inherent limitation due to the material absorption/gain, which leads to pump-dependent Q factors. In addition, both the limited spectral resolution and chirp effects from short-pulse photoluminescence results in broadening of the cavity peak. Therefore, the Q measurement from the FWHM for lower powers should be consider as a lower bound of the intrinsic quality factor. Indeed, we will see in the next paragraphs that injecting the system resonantly a quality factor of $Q_{loaded} \sim 3752$ is found. Measurements of the collected intensity (■) and the resonance central wavelength (●) as a function of the injected power are shown in fig 5.10.b. The overall behavior is similar to the one found for the QDs sample, sec. 3.1.3: an S-shape in fig. 5.10.b (black dots) is not observed and the FWHM

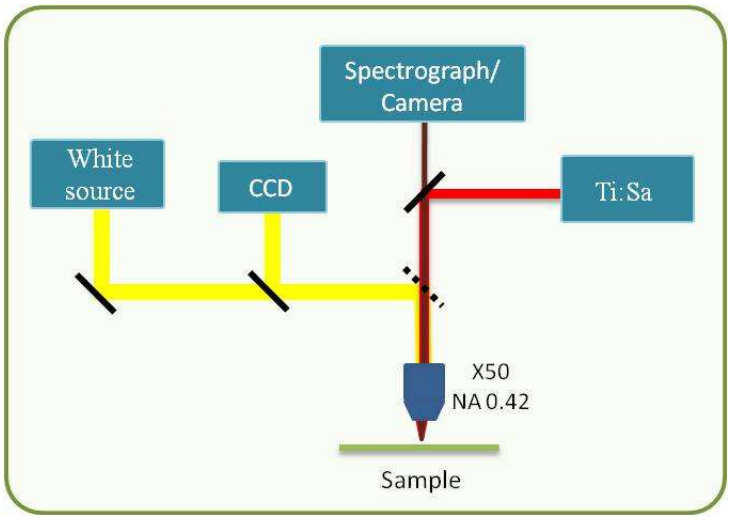

Figure 5.9: *(a) Sketch of the set up used to characterize the QWs sample.*

shows only an increase with the injected power. Therefore, there is no clear laser threshold-like behavior. As in the case of QD (sec. 3.1.3), three possible interpretations could be proposed: i) the system behaves as a high β factor ($\beta \sim 1$) laser [111]; ii) the threshold is at a power lower than those explored and we do not have enough sensitivity to measure it; iii) the sample does not show any laser effect. The usual method to identify laser emission is performing a second order correlation function, which is out of the scope of this thesis. However, it is important to point out that measurements carried out over a L3-type cavity in a QW PhC of same characteristics but a resonance centered at 1550 nm showed a possible laser threshold at 12 μW, fig. 5.10.c. As this resonance wavelength is closer to the QW maximum emission than the sample in fig. 5.10.a, we conclude that the lack of lasing effect comes from the strong detuning of the cavity mode with respect to the gain maximum. However, it is important to point out that laser emission is not a necessary condition for the existence of nonlinear dynamical regimes such as the bistability or the excitability, which are the effects sought in this work.

5.2.2 Bistability measurements

We have demonstrated in the previous section a thermo-optical bistability with switching times in the μs scale. These time scales are quite slow for fast information processing applications. In contrast, electronic nonlinearities allow faster switching, limited by the carrier lifetime which is in the ps to ns scale. Thus, an important task is to isolate electronically induced OB from the thermal effects.

Preliminary experiments to obtain the electronic bistable regime

In order to determine the wavelength range where the bistability can be achieved, let us begin with a detailed characterization of the linear resonance, meaning the resonance in the absence of gain and avoiding spectral broadening due to chirp effects. As previously, this is performed by coupling into the cavity, via the tapered fiber, a 30nm-broadband signal with a central wavelength of 1570 nm (as described in section 3.2.2). The reflected signal is collected and sent to an optical spectrum analyser (OSA). Fig 5.11.a shows the measured cavity resonance. The mode is centered at λ =1571.4 nm and its FWHM of 0.42 nm corresponds to a loaded quality factor

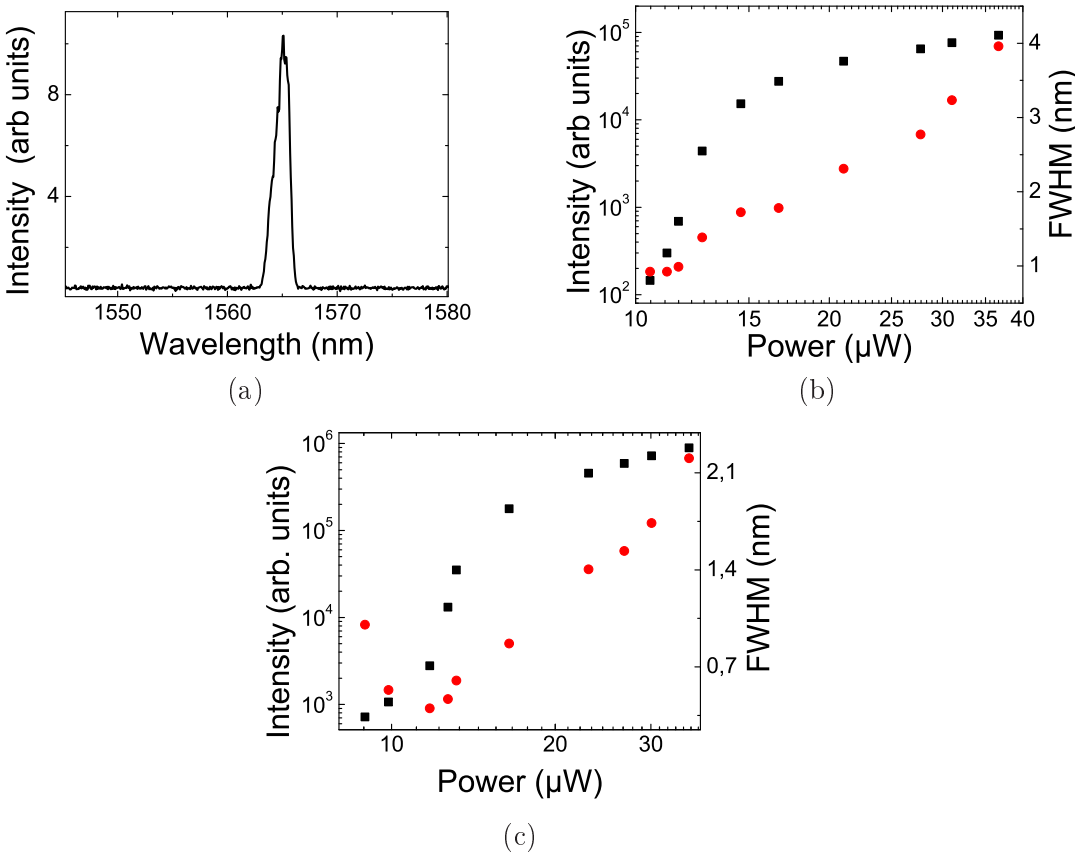

Figure 5.10: *(a) Photoluminescence spectrum of a L3-type cavity (fig. 5.9.a) for a pump power of 15 μW and 0.5 s of integration time. The mode is centered at λ =1565 nm and the resonance width is 1.7 nm (for this injected power). The PhC period and radius are: a=450 nm and r=120 nm, respectively. (b) Output intensity integral as a function of the pump power (■), both axes are in logarithmic scale. Resonance width as a function of the injected power (●). (c) Idem as (b) for a mode centered at λ =1565 nm. The PhC period is: a=445 nm.*

of $Q_{loaded} = 3752$. Note that the mode is red-shifted of about 6.4 nm with respect to fig. 5.10, which is due to the electronic nonlinear effects induced by the pump in the latter. The arrows in fig. 5.11.a show the spectral range of wavelength detunings used in the following experiment. As the injected power is increased, the resonance blue shifts and develops an asymmetric profile. A blue shift of 1.3 nm is obtained for an injected power of 214 μW, black line in fig. 5.11.b. This is ~ 3 times the FWHM of the linear resonance (fig. 5.11.a). The asymmetry of the resonance is a first hint of the electronic character of the response. After eq. 5.1 we can predict that a bistable operation should occur for optical injection blue-shifted by more than $\sqrt{3}\gamma/2$, with γ the linear resonance width (FWHM).

In order to further study the resonance asymmetry with the injected power, additional spectral measurements were carried out in the CW regime[1]. They allow discriminating the origin of the nonlinearity, i.e. thermal or electronic. Indeed, since a thermal effect increases the refractive index, a thermal bistability produces a bending of the resonance to the "red".

[1]These measurements were done in collaboration with Patricio Grinberg, Samir Haddadi and Kamel Bencheickh.

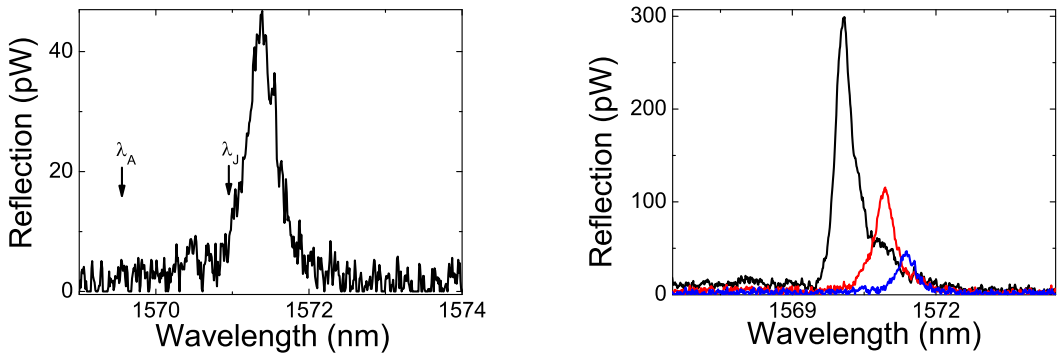

Figure 5.11: *(a) Reflected signal for a probe power of 95 μW. Arrows λ_A to λ_J indicate the wavelength range for the bistability experiment. The resonance is centered at $\lambda = 1571.4$ nm and the quality factor is $Q = 3752$. (b) Reflectivity spectrum of the system resonance for different probe powers: 214 μW (black line), 160 μW (red line) and 95 μW (blue line). Note the resonance blue-shifts as the probe power is increased. All the powers are measured at the input of the tapered fiber.*

Conversely, electronic nonlinearities decrease the refractive index bending the resonance to the "blue". Highly sensitive spectral measures were carried out to study these features.

The cavity is injected through the tapered fiber with a CW signal from a tunable laser, fig. 5.12. Before injection, the laser output is modulated with a AOM (acousto-optic modulator) driven at 10 MHz, 47 KHz repetition rate, 0-400 mV signal. This short-pulse-low duty cycle modulation minimizes the thermal loading. In order to increase the reflected signal detected with the APD, a Lock-in amplifier is used ('Stanford Research System', Model SR830 DSP). The lock-in and the tunable laser are driven through a GPIB interface using a Labview ('National instruments', 8.0) code.

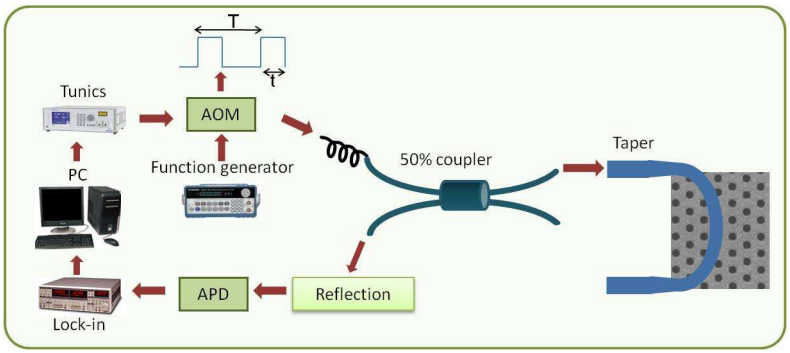

Figure 5.12: *Set up used to study the resonance bend with the injected power. Modulation period and pulse duration are: T=21 μs and t=100 ns, respectively.*

Fig. 5.13 shows the linear resonance (upper trace) obtained as in fig. 5.11 and the output signal as a function of the injected wavelength obtained from the modulated CW signal with a peak power of 0.5 mW. Note the strong asymmetry of the resonance, in particular the abrupt switch at the blue side that clearly demonstrates that the resonance bends to the blue. This

further confirms the electronic origin of the nonlinear behavior.

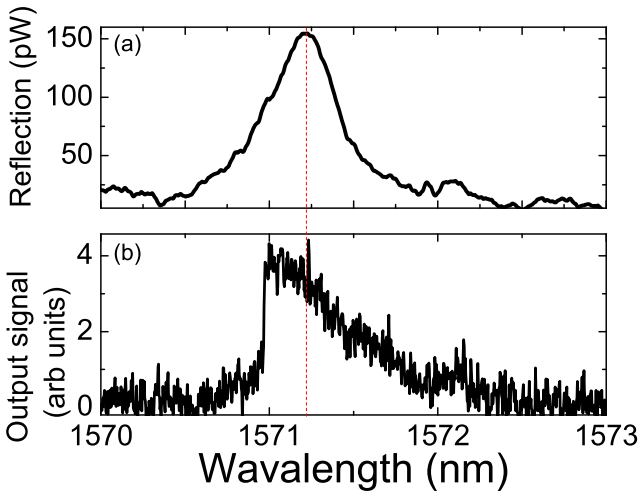

Figure 5.13: *Upper trace: Linear resonance obtained using the 30 nm-broadband resonant signal (as in fig.5.11), resolution: 0.05 nm. Lower trace: Resonance obtained by means of a CW modulated signal and a Lock-in detection. Peak power=0.5 mW, integration time: 300 ms, resolution: 5 pm. Note the resonance asymmetry and the abrupt switch at the blue side of the resonance.*

Using this technique the transmitted signal was also measured. The particular interest in the transmission signal is the measurement of the coupling efficiency. Injecting the system with powers higher than $\sim$200 μW (peak power) the resonance in transmission is asymmetric, fig. 5.14.a, indicating a bistable regime. As the injected power is decreased the resonance develops a symmetric profile (fig. 5.14.b). In this case the power is below the OB threshold and the linear resonance is obtained. From this transmitted signal we estimate a coupling efficiency (η), from eqs. 2.31 and 2.36, of $\eta \sim 7\%$. This value is four times lower than the efficiency found in section 3.2.2($\sim 28\%$). This decrease of the efficiency is attributed to both the QW absorption and the reduced coupling rate, i.e., increased Q_c respect to the system in section 3.2.2. Indeed, Q_c can be calculated from Q_{loaded} and η as $Q_c = Q_{loaded}/\eta$ which gives $Q_c = 53600$. This value is almost one order of magnitude higher than the Q_c found for the QD sample. In general, Q_c depends on the tapered fiber characteristics, on the fiber-cavity distance and on the cavity geometry. In this case the only difference respect to the QD sample is the tapered-fiber (the measurements in the QD and QW samples were developed with different tapered fibers). Therefore, the fiber used with the QW sample is less performant than the fiber used with the QD sample.

It is worth mentioning that the absorption quality factor can be calculated from the quality factor found in fig. 5.11.a, $Q_{loaded} = 3752$. For this, we will consider the intrinsic quality factor found in section 4.1, $Q_{rad} = 6300$, as an approximated value for the intrinsic Q in this sample. According to section 1.4, we can estimate the absorption quality factor (Q_a), as $1/Q_{loaded} = 1/Q_{rad} + 1/Q_a + 1/Q_c = 1/(1-\eta)Q_{rad} + 1/Q_a$. From this, we obtain $Q_a = 9760$, which can be used to calculate to τ_a giving $\tau_a = 0.15$ ps. The latter can be related to the absorption according to eq. 1.44, leading to $\alpha = 66\ cm^{-1}$. This value is lower than the calculated for Yacomotti et al. [115], most probably because in our case the cavity resonance is further away from the maximum of absorption of the QWs than in [115]. Let us stress that in the case of fig. 5.11.a the cavity quality factor is not limited by the presence of the fiber (due to the low

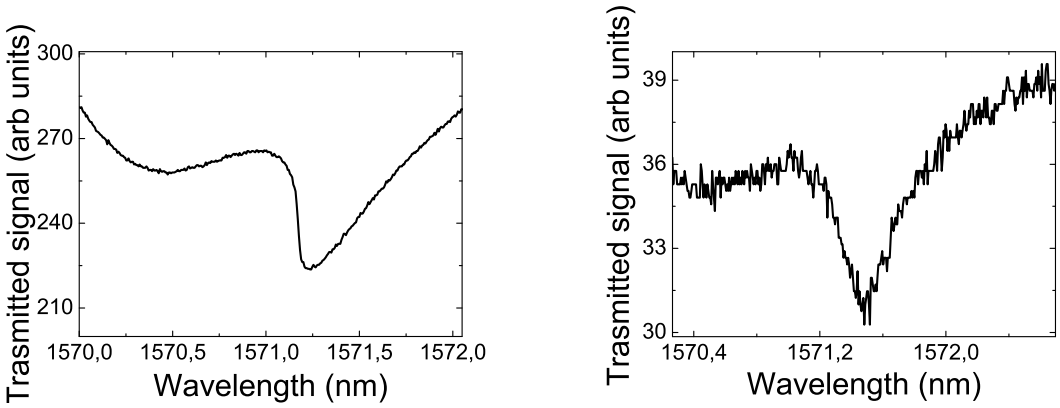

(a) (b)

Figure 5.14: *(a) Transmitted signal as a function of wavelength for an injected peak power of 600 μW. Note the asymmetry of the resonance. (b) Idem for a lower injected power (peak power=100 μW). Note the symmetry of the resonance, meaning that the injection is under the bistability threshold. A coupling efficiency of $\sim 7\%$ is obtained from this curve.*

coupling efficiency), i.e. $Q_0 \sim Q_{loaded}$; instead, it is the QW absorption that lowers the quality factor with respect to the intrinsic one by about a factor of 2.

Experimental set up to study electronic bistability

In order to obtain a clear signature of the OB operation the system is injected trough the tapered fiber with a CW nearly resonant signal modulated by a triangular amplitude modulation, fig. 5.15. This is done by sending the output of a tunable laser ('Yenista Optcis', Tunics Reference T100-ER, 1490 nm-1650 nm) to an optical amplifier ('Keopsys', model KPS-BT2) followed by an acousto-optic modulator (AOM, 'AA optoelectronic', MT 160). The optical amplifier is added since the AOM introduces $\sim$10 db losses. The modulation is obtained by feeding the AOM with triangular pulses of 4 MHz, 40 KHz repetition rate, 0$-$400 mV signal. Under this configuration the maximum power sent to the tapered fiber is 3.2 mW. This short-pulse-low duty cycle modulation is applied in order to minimize thermal effects that evolve in a μs scale (see sec. 4.1). In turn, they are quasi-stationary for the electronic time scale whose relaxation time is of the order of 200 ps (see sec. 4.2). The input and reflected signals collected through the tapered fiber are both measured as a function of time, by means of a 3.5 GHz DC-coupled photodiode and a 15 kHz-1.1 GHz bandwidth avalanche photodiode (APD, 'New focus', model 1647), respectively. These signals are registered in a 13 GHz-bandwidth oscilloscope ('Lecroy', WaveMaster 813Zi).

Demonstration of the electronic bistable regime

The time traces of the injected and reflected signals are presented in fig. 5.16. The triangular profile of the injected signal is shown in the upper trace (black line). The reflected signals for detunings $\Delta = \lambda_0 - \lambda_{in} = 1.5$, 1.7 and 1.9 nm, respectively, where λ_0 is the central wavelength of the linear resonance (λ_0 =1571.4 nm) are represented in blue, red and green lines, respectively. The bistable behavior is highlighted in fig.5.16.b where the reflected power is plotted as a function of the input power for a detuning of 1.7 nm (red curve in fig. 5.16.a), showing the hysteresis cycle. Note the sense of the loop, anticlockwise, which corresponds to a purely electronic bistability from a resonant upwards peak, as it is the case of the cavity mode measured

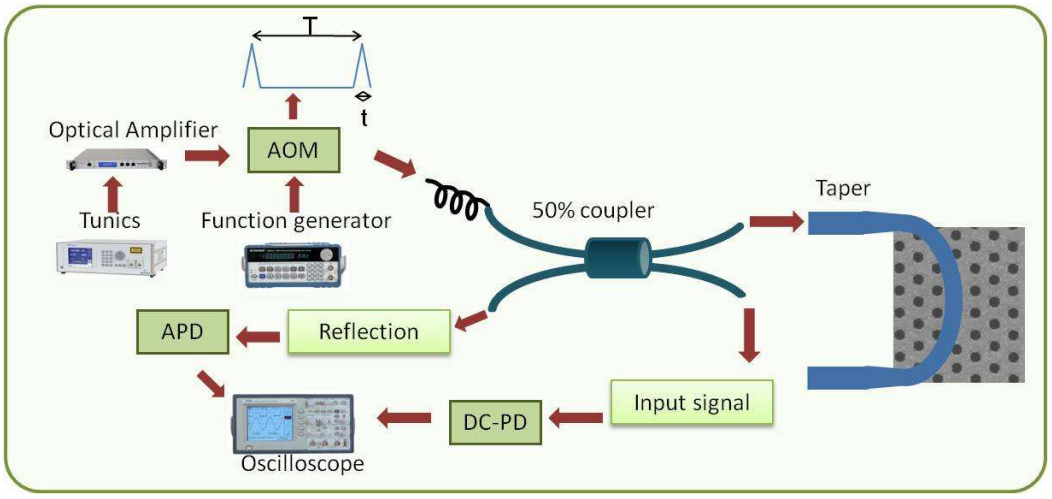

Figure 5.15: *Scheme of the experimental set up used to study electronic bistability. Modulation period and pulse duration are: T=25 μs and t=250 ns, respectively.*

in reflection. It is important to point out that thermal effects, if not completely avoided, can reverse the cycling sense of the hysteresis loop.

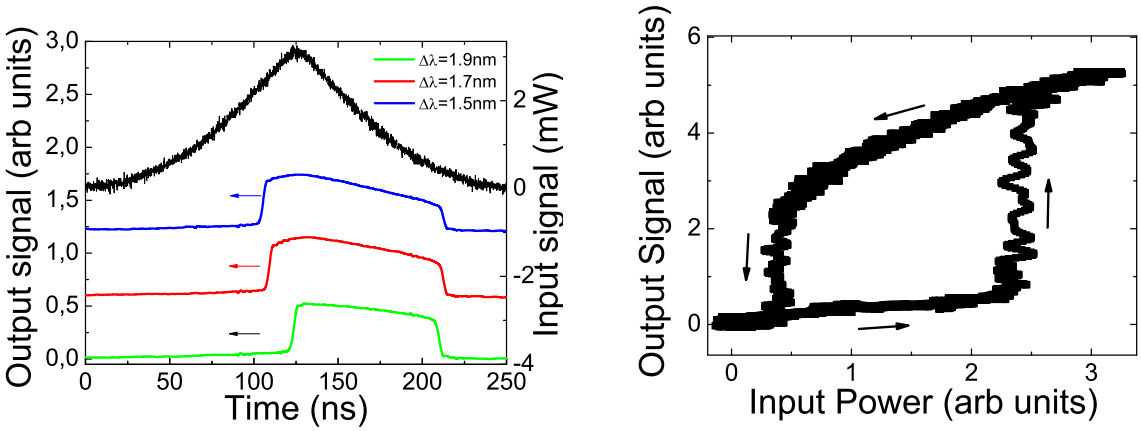

(a) (b)

Figure 5.16: *(a) Time traces of input (black line) and reflected (blue, red and green line) signals for detunings of $\Delta\lambda_0$ =1.5, 1.7 and 1.9 nm, respectively. (b) Hysteresis cycles showing bistable behavior ($\Delta\lambda_0$ =1.7 nm). The arrows show the sense of the cycle.*

Fig. 5.17 shows the reflected signal as a function of the input power for different detunings. Hysteresis loops are observed for detuning values between 1.9 and 0.4 nm. The loop size increases for larger $\Delta\lambda$, up to $\Delta\lambda \sim$1.9 nm; over this value no bistability is observed. The switching time is measured as the time widths between the minimum and the maximum of the switch processes and gives ∼6 ns for both switch on and off times. This value is 3 orders of magnitude faster than the switch in the thermo-optical bistability, which is an additional evidence of the electronic origin of the OB. Indeed, the switching time is limited here by the carrier recombination time. In a PhC this time is faster than the one associated to the bulk recombination time [127, 128], which is $\sim$ 2 ns [117]. This acceleration of the recombination process is attributed

to the increased surface recombination states in photonic crystal lattices. The etched sidewalls increase the overall surface area of the structure and decrease the carrier lifetime [129]. Thus, the recombination time in the structure is < 2 ns. In section 4.2, nonradiative recombinations times in the wetting layer of ~ 120 ps were found; even though it is not the same material and geometry it gives an order of magnitude for the recombination time. Besides, this time can also be estimated from [115] as ~ 200 ps, which corresponds to the same material but a different lattice and mode distribution.

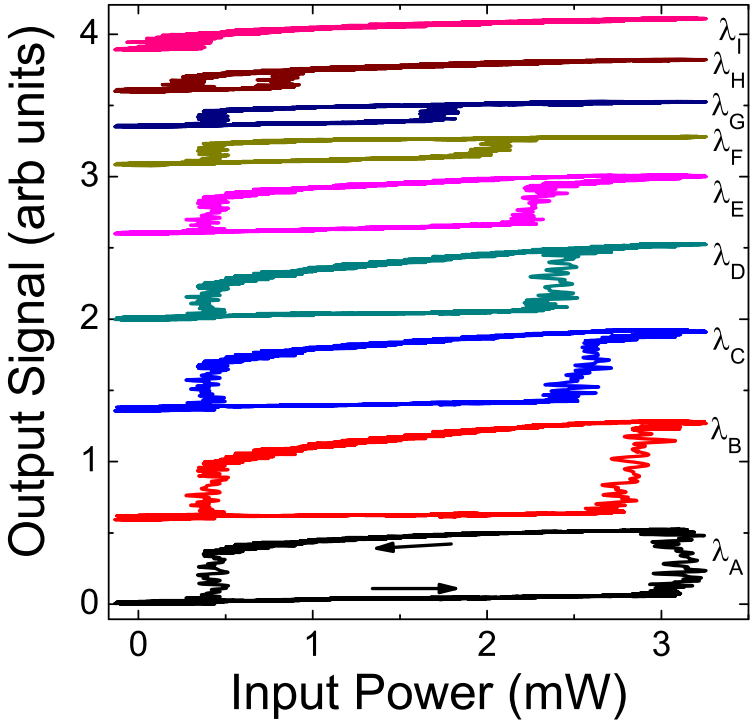

Figure 5.17: *Hysteresis cycles showing bistable behavior. Detuning-values with respect to the cavity resonance are, from λ_A to λ_I: 1.9, 1.8, 1.7, 1.5, 1.3, 1.1, 0.9, 0.7 and 0.4 nm. The input power is measured at the tapered fiber input. The durations of the switch processes is ~ 6 ns for the on and off switches.*

The minimum detuning for which the bistability is observed is $\Delta\lambda$ =0.4 nm, fig. 5.17. According to the theory the bistability can be observed for detunings larger (in modulus) than $\sqrt{3}$, with the detuning defined as $\delta = (\omega_0 - \omega_{in})/(\gamma/2)$. Using $Q_{loaded} = 3752$, $\lambda_0 = 1571.4$ nm (from fig. 5.11.b) and $\lambda_{inj} = 1571$ nm, $\delta \sim 1.83$ which is close to the minimum detuning necessary to the bistable behavior.

The incident powers were measured at the input of the tapered fiber. The actual intensity arriving to the cavity for a given injected power is difficult to determine. However, we can estimate this intensity by means of the tapered fiber losses. Thus, the power in the vicinity of the cavity is estimated as: $P_{in} \sim 0.57 P_{input}$, meaning that the bistability threshold from fig. 5.17 ($P_{injected,thr} = 0.3$ mW) is close to $P_{in,thr} \sim 170\ \mu W$. This is a rough estimation since it assumes that the losses are uniformly distributed along the fiber. From this value we can estimate the intrinsic threshold (independent of the coupling method), i.e. the power actually coupled

into the cavity, as the power in the vicinity (P_{in}) multiplied by the coupling efficiency (η). Then, the intrinsic threshold power $P_{intrinsic,thr}$ is given by $P_{intrinsic,thr} = \eta P_{in,thr} \sim 12\mu W$. This value is what we will consider as the bistability threshold. This value can be compared with the theoretical one ($P^{(theo)}_{intrinsic,thr}$) obtained from coupled mode theory and eq. 1.38 as $P^{(theo)}_{intrinsic,thr} \sim U_{0,e}|\delta_0|/\tau$, where $U_{0,e}$ is the characteristic intracavity energy, described in section 1.4, and $\delta_0 = 0.4\ nm/(0.42\ nm/2) = 1.9$, according to the experimental results. Thus, $P^{(theo)}_{intrinsic,thr} \sim 8\ \mu W$ in good agreement with the experimental results.

The intrinsic bistability threshold found ($\sim 12\mu W$), in good agreement with the value found by Kim et al. [87], is at least one order of magnitude smaller than the threshold of optical bistability in monolithic vertical cavities [24] and ring resonator devices [94]. This is due to a strong reduction of the mode volume in a PhC cavity. Indeed, according to [28, 21] the threshold scales as V/Q^2, with V the mode volume of the structure and Q its quality factor. Similar thresholds were obtained in Si PhC cavities by Notomi et al.[82]. In this case the mode volume was of the same order of magnitude while the quality factor was $Q \sim 33400$. The fact that our threshold compares well with the one found in [82] for Q factors ten times higher, is clearly related to the higher nonlinearity associated to the single photon absorption in contrast to the two-photon absorption in Si, as discussed in section 1.4. In other words, even when the quality factor is degraded by absorption, low threshold can still be achieved taking advantage of the large nonlinear coefficients in III-V semiconductors.

5.3 Conclusion

Optical bistability of two different physical origins were studied. In both cases the dynamics of the system is governed by a single dynamical variable. The dynamical variables studied here were: a slow variable given by the temperature change inside the cavity and a fast one given by carrier recombination in QWs.

Thermal dynamics has been investigated within a thermo-optical bistable regime. A bistable behavior has been observed for injected power higher than ~1 mW. The theoretical and experimental bistability threshold estimated and measured, respectively, at different points of the system are shown in table 5.1, i.e. input power (P_{input}); power in the vicinity of the cavity (P_{in}); and intrinsic threshold ($P_{intrinsic}$, the power that is coupled into the cavity). Switch-on/off times of 2 μs and 4 μs respectively (from the hot to the cold states) were measured. As expected, both are related to the 1 μs characteristic time measured in the linear regime. By means of a simple nonlinear dynamical representation we explained the origin of the difference in time between the switch-on and off processes. This difference can be mathematically explained by the opposite slopes of $dP/d\delta$ at the fixed points.

Fast optical bistability was observed in samples with QWs as active material. Low power threshold, $P_{in} \sim 12\ \mu W$, and fast switching times, $t \sim 6$ ns, were found. Since this time is three orders of magnitudes lower than the characteristic thermal time and the nonlinear refractive index is negative, we conclude that the nonlinear effects leading to bistable behavior is electronic. This was demonstrated through spectral measurements, where a bending of the resonance to the blue-side was observed. Looking at the resonance contrast in transmission we obtained a coupling efficiency of $\eta \sim 7\%$. Table 5.1 summarizes the theoretical/experimental threshold power estimated/measured at different points of the system. Note the similarities between the theoretical and experimental threshold. It is worth mentioning that, whereas for the theoretical

		P_{input}	P_{in}	$P_{intrinsic}$
Thermal	Theoretical		$\|\delta_0\|U_0/(\tau\eta)$=210 μW	$\|\delta_0\|U_0/\tau$=67 μW
	Experimental	1 mW	260 μW	83 μW
Electronic	Theoretical		$\|\delta_0\|U_0/(\tau\eta)$=114 μW	$\|\delta_0\|U_0/\tau$=8 μW
	Experimental	300 μW	170 μW	12 μW

Table 5.1: *Table summarizing the theoretical and experimental bistability threshold (of thermal and electronic origin) measured or estimated at different points in the system: power measured at the fiber input(P_{input}), power in the vicinity of the cavity (P_{in}) and power that is coupled into the cavity ($P_{intrinsic}$). $|\delta_0|$ for thermal and electronic bistability are: 2.2 and 1.9, respectively.*

thresholds of thermal origin one of the parameters arises from a fit (α) in the case of electronic effects all the parameters were obtained from the experimental data. The bistability threshold found, $P_{intrinsic,thr} = 12\,\mu W$, which is of the same order of magnitude that the threshold reported in [87], is at least one order of magnitude smaller than the threshold of optical bistability in monolithic vertical cavities[24] and ring resonator devices [94] mainly due to the small V/Q^2 ratios in PhCs.

Chapter 6

Nonlinear dynamical regimes involving both thermal and electronic dynamical variables

In the previous chapter we have investigated optical bistability originated either by thermal or electronic nonlinearities. A particular effort was devoted to isolate eletronic nonlinear response from the ubiquitous thermal effects. In this chapter, we investigate nonlinear dynamical regimes governed by the combination of thermal and electronic nonlinear effects. We will show that this combination can produce either self sustained oscillations or excitable responses, depending on the excitation conditions. Both regimes can be understood as the result of the interplay or competition between the effects of the two nonlinear dynamical variables. These behaviors are of interest in the context of optical information processing and all-optical devices.

6.1 Self-sustained oscillations

Self-sustained oscillations studied here are the consequence of the competition of two nonlinear responses of opposite sign and distinct time scales. In our case this competition is given by the positive and slow thermal nonlinearity and the negative and fast electronic nonlinearity.

Let us first analyse the origin of the self sustained oscillations from the OB cycles demonstrated in the previous chapter. If the system is injected with powers above the bistability threshold then a possible state of the system is in the upper branch of the hysteresis cycle. In this state, heating is enhanced, shifting the hysteresis cycle to higher injection powers. Therefore, a jump to the low reflectivity state is likely to occur, with a subsequent cooling. Hence, a jump back to the high reflectivity state takes place, giving rise to a periodic signal where the period is leaded by thermal effects. These self-pulsing oscillations were theoretically studied in detail by Yacomotti et al. [89] in the framework of the nonlinear dynamics of the field inside a resonator coupled to both electronic and thermal variables. The model proposed in [89] contains the slowly varying amplitude of the electromagnetic field (E) and carrier density (N). An example of the self-sustained oscillations is presented in fig 6.1.a. The oscillating regime can be seen in the phase portrait as an unstable fixed point solution and a stable limit cycle, fig. 6.1.b. Note the different times scales: the period, governed by the thermal time scale, and the rising and falling edges governed by the electronic time scale.

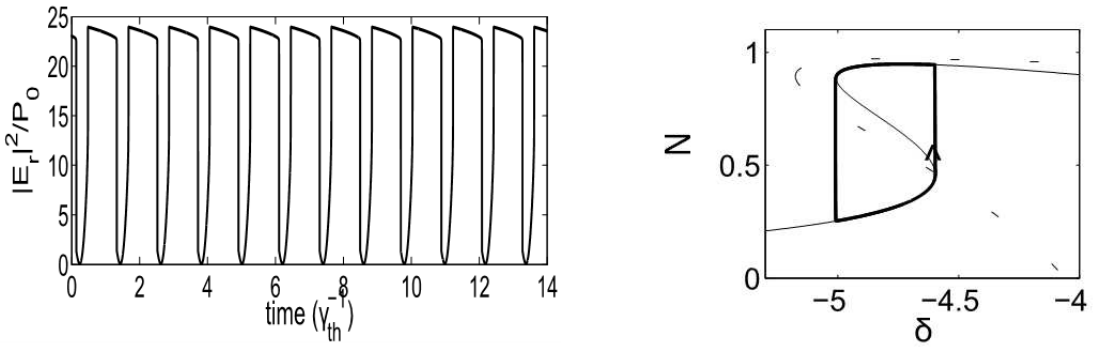

(a) (b)

Figure 6.1: *Solutions to the model proposed in [89]. (a) Time trace and (b) phase portrait for the reflected signal. δ denotes the detuning. x-axis unit in the time traces plot is $\tau_{th} = 0.84\ \mu s$.*

6.1.1 Self-sustained oscillations demonstration

In the previous chapter, thermal effects were avoided by the introduction of a slow modulation to the CW injection signal. This modulation prevents any accumulation of the excitation at the scale of thermal dynamics. In order to investigate the interplay of electronic and thermal dynamics, the modulation is now switched off in the set-up sketched in fig. 5.15, section 5.2. Injecting the cavity via the tapered fiber with a power above the threshold of the OB, the self-sustained oscillations presented in fig. 6.2 are observed, where the reflected signal as a function of time is plotted for different detunings. A shrinking of the pulse as the detuning increased is observed. The pulse duration is related to the initial position on the upper branch of the hysteresis cycle and its distance to the bistability threshold. As this position changes with the detuning, the pulse duration also changes.

Fig. 6.3 shows a zoom of a single pulse of λ_B in fig. 6.2 where the rise time and the pulse duration are depicted. Note that the pulse duration is in the time scale of the thermal processes (see section 4.1) while the rise time is of the order of the switching times found for the electronic bistability (see sec. 5.2.2). These times confirm the fact that in the self-sustained oscillations regime two dynamical variables are involved: thermal and electronic nonlinear effects.

Interesting enough, the presence of self-pulsing dynamics as the one observed here allows to predict the existence of excitability. Indeed, as far as the system is injected below the oscillatory threshold, pulses are no longer self-sustained. Instead, they can be triggered by adding a small external perturbation, as we will see in the next paragraphs.

6.2 Excitable regime

Excitability is a nonlinear dynamical mechanism underlying pulse-like responses to small perturbations in systems possessing one stable state. An excitable system reacts to an external perturbation in the form of all-or-none pulse responses, depending on whether the perturbation is above or below a certain threshold. In 2D PhC the excitable response can be considered as an action potential neuron-like ultrafast response. Excitable systems can switch from self-sustained oscillations to an excitable behavior as one control parameter is varied. In our case this control parameter is the injected power. In this section we present an experimental demonstration of excitable response in a 2D PhC nanocavity.

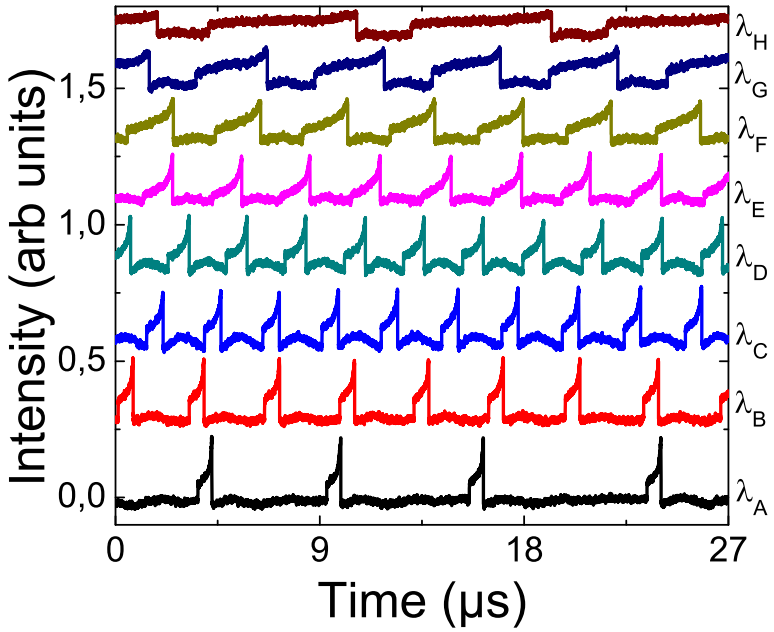

Figure 6.2: *Self-sustained oscillations. Reflected signals as a function of time for different detunings, from λ_A to λ_H: 1.8, 1.7, 1.6, 1.5, 1.4, 1.3, 1.2 and 1.1 nm. The input power, measured at the tapered fiber input, is 3.2 mW.*

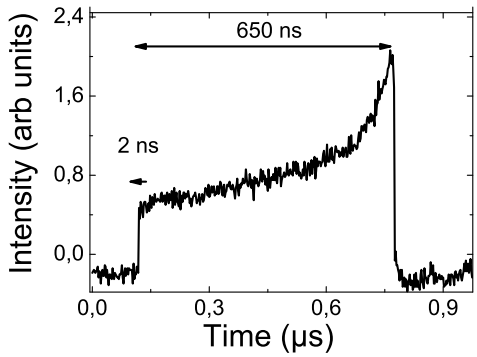

Figure 6.3: *Pulse isolated from a train of self-sustained oscillations for a detuning of 1.7 nm and 3.2 mW of injected power.*

6.2.1 General remarks

The type II excitability can be explained, as in the case of self-sustained oscillations, by considering slow thermal effects and fast electronic ones. Given the system in a stationary state, if a perturbation kicks it from the low to the high reflectivity branch of the hysteresis cycle, then heating is enhanced, shifting the hysteresis cycle to higher injection powers. Therefore, a jump back to the high reflectivity state is possible, with a subsequent cooling, giving rise to a closed dynamical cycle at the origin of a upwards pulse.

This dynamics was modeled in [89], for a Bloch-mode PhC (for which the response in

transmission and reflection are inverted with respect to our configuration). Fig. 6.4 shows the results in the phase portrait (fig. 6.4.a) and time traces (fig. 6.4.b). The excitability can be distinguished in the phase portrait as a stable fixed point and a trajectory that starts in a small neighborhood of the equilibrium state, leaves this region, and then returns to the quiescent state, fig. 6.4.a. Fig. 6.4.b shows the time traces for two different detunings showing the dependence of the pulse duration with the detuning.

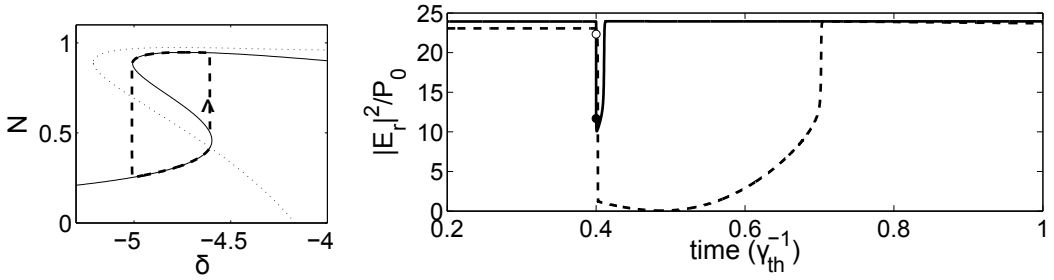

(a) (b)

Figure 6.4: *Solution to the model proposed in [89]. (a) Phase portraits and (b) time traces of the reflected power. δ denotes the detuning. x-axis unit in the time traces plot is $\tau_{th} = 0.84$ μs.*

6.2.2 Set up description

The experimental set up implemented to study the excitable behavior is shown in fig. 6.5. The system is injected through the fiber with a CW signal as previously. The injected power is kept below the threshold of self-sustained oscillations and an incoherent perturbation is sent by the surface. This perturbation induces the excitable response by kicking the system from the stable state. The perturbation beam is generated at 808 nm by a CW diode laser ('Thorlabs', L808P200). This is focused down via a 50x microscope objective to a diameter of ~ 4 μm ($@1/e^2$ of the intensity) illuminating the structure normally to the 2D PhC periodicity. The perturbation signal is modulated by means of a free-space AOM ('AA optoelectronic', MT350). The modulation is obtained by feeding the AOM with triangular pulses of 7.7 MHz, 40 KHz repetition rate, 0-1 V signal. This modulation is set in such a way that perturbation durations are shorter than the self-sustained oscillation period. The peak power attaining the sample is varied from 0 to 400 μW by changing the diode current.

6.2.3 Excitable response

For testing the excitable regime, the system is prepared with a detuning of $\Delta\lambda = 1.5$ nm. For this detuning the self-sustained oscillations threshold is 2.9 mW. Therefore, the signal power is set to 2.6 mW, at which the stable state corresponds to a low reflected power. We perturb this state by injecting the incoherent pump pulse by the surface. Fig. 6.6 shows the reflected signal as a function of time (lower trace). For perturbation powers lower than 1 μW, no output pulse is observed (black line). As the perturbation power is increased up to 20 μW a 2-μs-duration reflected pulse is observed (red line). The pulse characteristics remain essentially invariant for a further increase of the perturbation (fig. 6.6). The existence of a threshold and the invariance of the output pulse for different injected powers are strong evidences of the excitable nature of the reflected signal. This constitutes the first ever reported demonstration of excitable pulses in

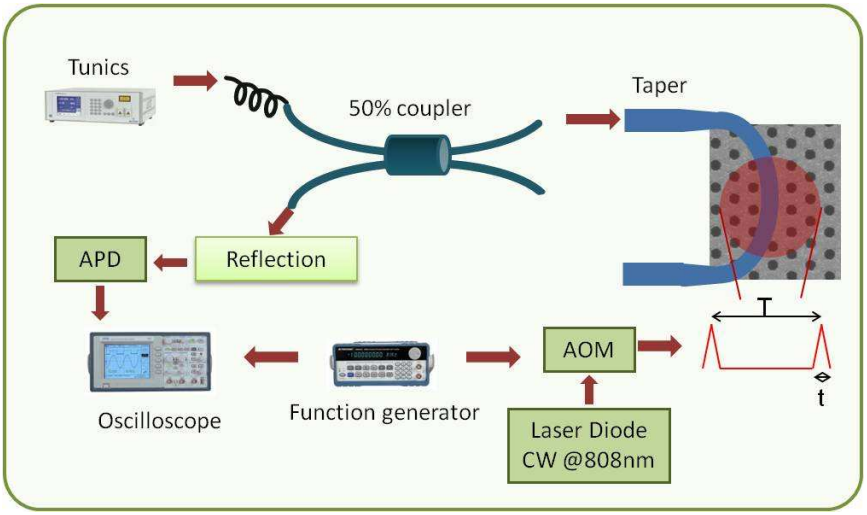

Figure 6.5: *Sketch of the set up used to study the excitable regime. Period and duration of the perturbation pulses are: T=25 μs and t=130 ns, respectively.*

an optical nanocavity.

As discussed in chapter 1 two main families of excitable regime are identified. In class II excitability the response is driven by the coexistence of a fast and slow times scales. From fig. 6.6, the pulse duration is $\sim 2\ \mu s$ and the rise time of the pulse is ~ 2 ns. Moreover, in the transition between excitability and self-sustained oscillations the pulses have a finite period, showing that the oscillations arise from a Hopf bifurcation as in Type II excitability. Instead, in Type I excitability, the oscillations arise from a saddle node bifurcation, thus, the pulses do not show a periodicity in the transition and they are sensitive to noise. Then, the optical response shows a slow and a fast dynamics which builds confidence on class II excitability.

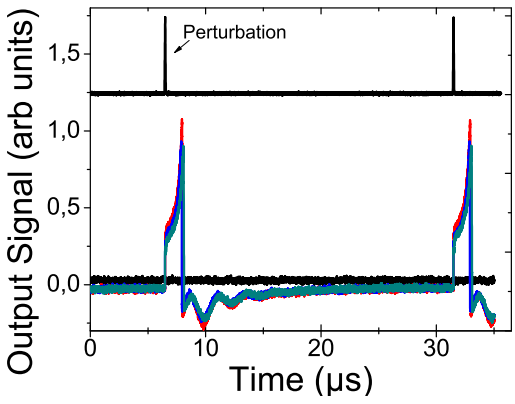

Figure 6.6: *Excitable responses (bottom traces) to 130ns-width, 40-KHz-repetition rate pulse perturbations (top trace) for different perturbation powers: 1 μW (black line), 20 μW (red line), 35 μW (blue line) and 46 μW (green line). The injected signal power is set at 2.6 mW and the detuning is* $\Delta\lambda = 1.5$ *nm.*

Fig. 6.7 shows the excitable response for different detunings. In all the cases the signal in-

tensity is kept below the self-sustained oscillations threshold by a factor 1.8 and the perturbation power is set above the largest excitability threshold, at 80 μW. We observe, as it was discussed for the self-sustained oscillations regime, a shrinking of the excitable pulse with the detuning. Besides, we can distinguish two behaviors: a fast and a slow, quasi-stationary, response. The fast and well contrasted response occurs for both high detunings and injected powers (fig 6.7, λ_A, λ_B and λ_C). An ultrafast pulse-like response can be interesting for applications in optoelectronic devices, such as optical switching, pulse reshaping [32] and in the context of excitable logic gates [130]. Slow, quasi-CW bistability but less contrasted pulses occur for low both detunings and injected signals (fig 6.7, λ_I). This quasi-steady-state bistability can be interesting for the applications of this system to long optical memories or sensors.

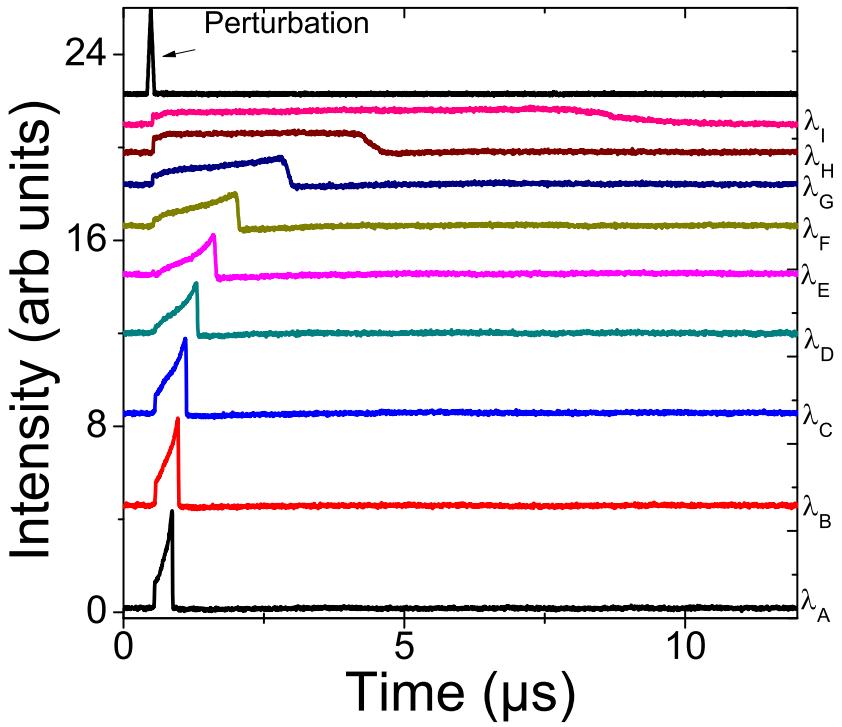

Figure 6.7: *Excitable responses (bottom traces) for different detunings. The injected power is set a factor 1.8 below the self-sustained oscillations threshold. The detunings and the injected powers, from λ_A to λ_I, are: 1.8 nm and 2.9 mW , 1.7 and 2.5 mW, 1.6 and 2.2 mW, 1.5 and 1.8 mW, 1.4 and 1.6 mW, 1.3 and 1.3 mW, 1.2 and 1.2 mW, 1.1 and 0.9 mW, and 1 nm and 0.8 mW, respectively. The top trace corresponds to the perturbation signal (peak power=80 μW).*

The optical pulses found in excitability measurements, as well as the pulses found in self-sustained oscillations, show a particular shape: an overshoot before the trailing edge. This shape is quite intriguing and could be the consequence of a quite different situation, e.g. a change in the pulse shape can be given by a particular type of hysteresis cycle such as optical bistability of Fano-like resonances [131]. These are often found in PhCs as the consequence of the coupling between a resonant mode and a quasi-continuum of radiative modes. Nevertheless, as the hysteresis cycles found in the bistability measurements show the regular S-shape, this particular pulses shape must have another origin. In order to gain more insight into this unexpected shape, additional bistability measurements, as depicted in section 5.2.2, are developed for longer

durations of the signal modulation. Fig. 6.8.a and b show the output signal (lower trace) and the input power (upper trace) as a function of time for two different modulation times: 11 μs and 10 μs with 1 μs time-out, respectively. A small upper peak at the end of the bistable pulse is observed in fig. 6.8.a and by adding a time-out this peak becomes more evident, fig. 6.8.b. Note the similarities between the shape of the bistable pulse (fig. 6.8.b) and the excitable pulse (fig. 6.6). The fact that the peak develops within constant injection time windows, and with μs time scales points to their thermal origin.

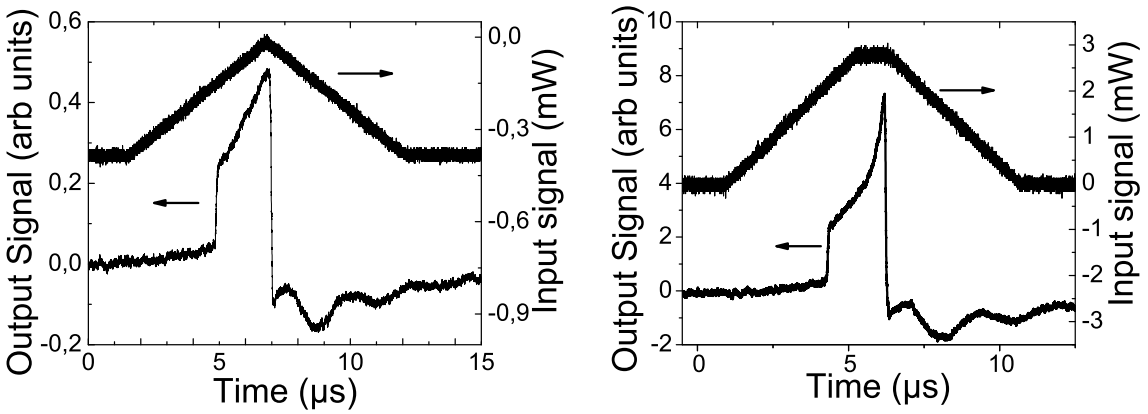

(a) (b)

Figure 6.8: *Bistability measurements for a longer signal modulation with constant injection intervals: (a) 11 μs and (b) 10 μs with 1 μs of time-out. Reflection signal (lower trace) and input signal (upper trace) as a function of time for a detuning of $\Delta\lambda_0 = 1.6$ nm. Note the similarities between the shape of the bistable pulse and the excitable pulse (fig. 6.6) specially the curve in (b).*

As discussed in chapter 1, another important characteristic of the excitable phenomenon is the existence of a "dead time" between two successive events, called refractory time (τ_r). This time is defined as the time it takes for an excitable system to be ready for a second stimulus once it returns to its resting state. In order to experimentally investigate this refractory time, two perturbation pulses are sent to the sample and the optical response is observed as a function of the delay between these two pulses. Fig. 6.9.a-d show the reflected signal and the perturbation signal as a function of time for three or four different delays and for detunings: $\Delta\lambda = 1.2, 1.1, 1, 0.9$ nm, respectively. We observe a clear dependence of the refractory times with the detuning: the higher the detuning, the shorter the refractory time. The obtained times are: $t_r \sim 2$ μs for $\Delta\lambda = 1.2$ nm, $t_r \sim 3$ μs for $\Delta\lambda = 1.1$ nm, $t_r \sim 4$ μs for $\Delta\lambda = 1$ nm and $t_r \sim 6$ μs for $\Delta\lambda = 0.9$ nm.

Fig. 6.10 shows the linear dependence of the refractory time with the excitable pulse duration (red line in fig. 6.10). Further theoretical work is necessary to understand this linear dependence. The refractory time has been studied in detail in biology for neurons (where it is in the ms range). To the best of our knowledge, this is the first time it is systematically investigated in a photonic system. This information can be relevant for applications of excitable optical system to all optical devices.

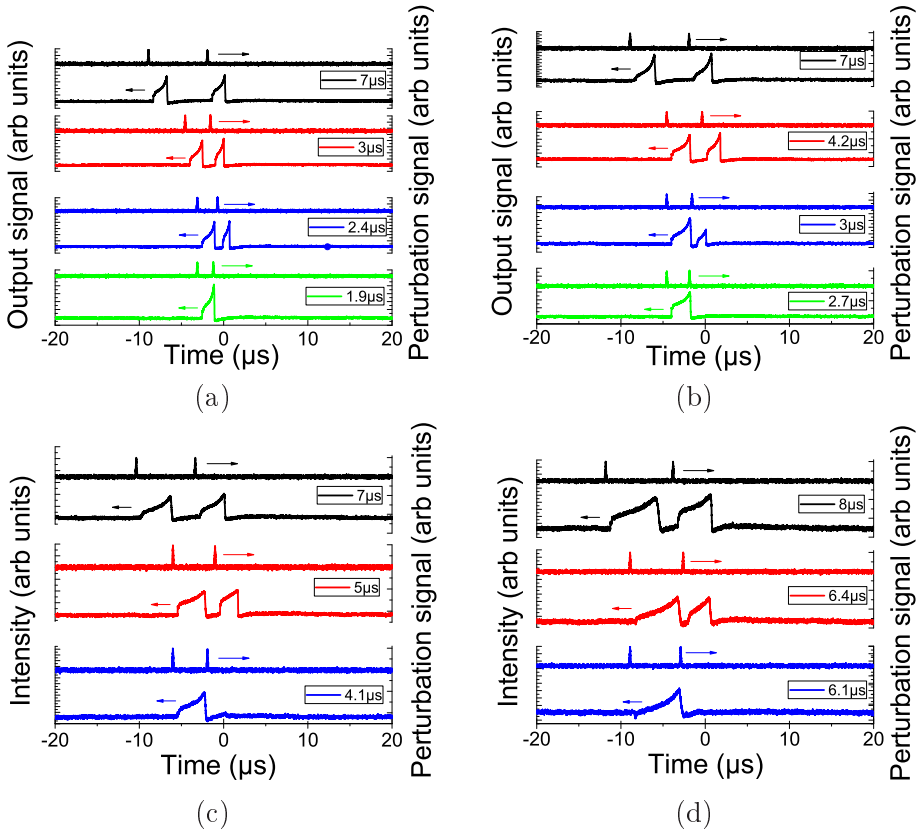

Figure 6.9: *Output signal and perturbation signal (lower and upper trace in each plot) as a function of time for different delays between perturbation pulses and for (a) $\Delta\lambda = 1.2$ nm, (b) $\Delta\lambda = 1.1$ nm, (c) $\Delta\lambda = 1$ nm and (d) $\Delta\lambda = 0.9$ nm. The refractory times are: (a) $t_r \sim 2$ μs, (b) $t_r \sim 3$ μs, (c) $t_r \sim 4$ μs and (d) $t_r \sim 6$ μs.*

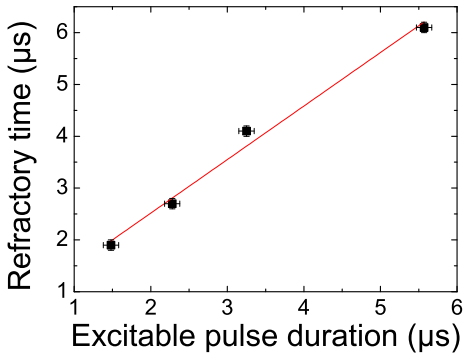

Figure 6.10: *Refractory time from fig. 6.9 as a function of the excitable pulse duration. Red line: linear fit (y=a+bx, with $a = (0,5 \pm 0,3)1/\mu s$ and $b = (1 \pm 0,1)$ μs).*

6.3 Conclusion

Self-sustained oscillations were experimentally demonstrated injecting a L3 PhC, containing QWs as active medium, with a CW signal above a certain threshold. A dependence of the pulse durations with the detuning was found, as it was already observed in [89] for a Bloch mode.

We have obtained an excitable regime by injecting, through the tapered fiber, a CW signal with a power below the self-sustained oscillation threshold, while an incoherent perturbation was sent by the surface. A dependence of the excitable pulse duration with the detuning was observed. In particular, a transition from quasi steady state bistbility to excitability was identified. Studies of the refractory time were carried out and a linear relation between this time and the duration of the excitable pulse was found. To our knowledge, this is the first time it is studied in a photonic system. The excitability and self-pulsing studies constitute the first ever reported demonstration of excitable pulses in a PhC nanocavity. The excitable and self-sustained oscillations behavior of the 2D PhC nanocavities can be of great interest in the development of photonic reservoir computing and all-optical circuits, such us clock recovery and pulse reshaping.

Part III

Nonlinear behaviors in evanescently coupled cavities

In the previous part we have obtained interesting nonlinear dynamical behaviors in L3 PhC cavities, such as electronic and thermal optical bistability, self-pulsing regimes and electronic excitability. In this part, we will focus on nonlinear dynamics in coupled cavities. In the first chapter, the evanescent coupling between PhC cavities is numerically investigated by means of FDTD simulations. Moreover, a theoretical model based on a coupled mode theory formalism is carried out in order to address the spontaneous symmetry breaking in nonlinear evanescently coupled cavities. In particular, the symmetry breaking in our experimental conditions is investigated.

In the second chapter, preliminary experimental studies on the coupling between two adjacent cavities etched in the same PhC are carried out by means of photoluminescence measurements. Conclusive studies of the coupling are developed through images of the near and far field emission profiles.

In the last chapter, we report on nonlinear dynamical measurements in two coupled L3 cavities. Bistable, self-sustained oscillations and excitable regimes are investigated. We finish this chapter by applying the theoretical formalism developed in the first chapter to the experimental conditions.

Chapter 7

Theoretical and numerical calculations of coupled cavities

Nonlinear coupled resonators can lead to interesting nonlinear behaviors such us symmetry breaking or pulse transmission in chains of excitable cavities. Symmetry breaking in all-optical devices attracts considerable attention due to its potential application to all-optical flip-flops. This phenomenon arises from the coupling of two identical nonlinear resonators under symmetrical excitation. When the incident field exceeds a certain value, the symmetric solution may no longer be stable and the system comes to a situation where the intensity inside each resonator is different. As a result, a non-symmetric state takes place, while linearly, the modes are completely delocalized in such a way that the intensity inside each resonator remains equal.

Once the symmetry breaking is achieved, e.g. more intensity in the right cavity than in the left one, a simple perturbation can switch the steady state to confine the intensity into the left cavity, giving rise to an optical flip-flop.

In previous works the symmetry breaking in cavitites with Kerr nonlinearity has been theoretically demonstrated by equally exciting both cavities from two separated ports [64], fig. 7.1. This system is interesting but quite difficult to reproduce experimentally since the excitation must be completely symmetric (in amplitude and phase). For this reason, in this section, we address symmetry breaking in two coupled cavities symmetrically excited through one single port. Such configuration is expected to considerably simplify the conditions for an experimental realization.

In the first part of this chapter we study the spatial field distribution of two linear coupled cavities by means of FDTD numerical simulations. In the second part the coupling between the two cavities and the external continuum is investigated through a Coupled Mode Theory (CMT) formalism. Finally, the parameters are adjusted in order to investigate the spontaneous symmetry breaking in two particular configurations, one of them accounting for the experimental conditions.

7.1 FDTD numerical simulations of two L3 coupled cavities

In order to study the evanescent coupling between cavities in a PhC, FDTD numerical simulations of two L3 cavities were carried out[1]. The method is the one discussed in section 2.1. The

[1]These calculations were done in collaboration with Timothy Karle, post-doc in our group.

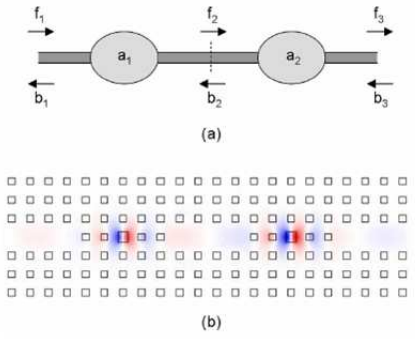

Figure 7.1: *(a) Sketch of the coupled cavities structure. (b) The PhC device, with a 4 period-long connecting WG. The electric field distribution is superimposed to illustrate the defect modes. Image from [64].*

simulated structure (see fig. 7.2) corresponds to two modified L3 cavities separated away by three rows of holes in the $\Gamma - M$ direction.

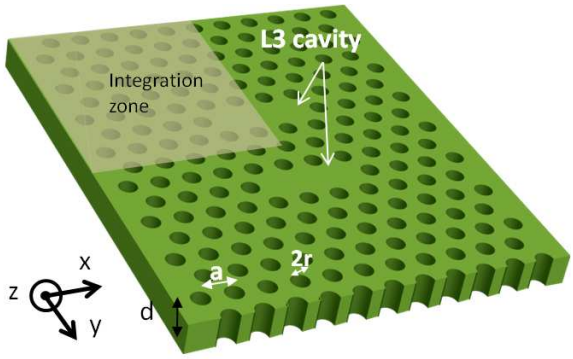

Figure 7.2: *Scheme of the two L3 cavities simulated in FDTD. The parameters are: a=435nm, r=0.3a for the period and holes radius, respectively.*

The simulation has a spatial resolution of $a/20 = 21.75$ nm in x and z-directions, $\sqrt{3}a/36 \simeq 20.9$ μm in y-direction, and a material refractive index of 3.3. The PhC period and hole radius are a=435 nm and r=0.3a, respectively; and the two holes closing the cavity are shifted away 0.15a. The dimensions of the sample are 28 periods (12.2 μm) in x-direction and 19 periods in y-direction (8.3 μm). The integration volume, shown in fig. 7.2 (grey area extends over half of the space in the z-direction), takes benefit from the symmetry of the structure . The electromagnetic field, calculated in this zone, is subsequently extended to the whole structure with the boundary conditions for the electric field shown in fig. 7.3. Fig. 7.3.a and b show the symmetry conditions of the y-polarization for the simulation of the symmetric and antisymmetric modes, respectively. The boundary conditions for the x-polarization are deduced from the latter. The system is excited with an electric dipole polarized in the y-direction located in the center of one of the cavities.

As a result of these simulations, two resonant modes were obtained, one at 1.596 μm with a quality factor of 18000 and the other one at 1.6 μm with $Q = 35000$. This resonance splitting results from the evanescent coupling between the cavities. The first mode corresponds to the

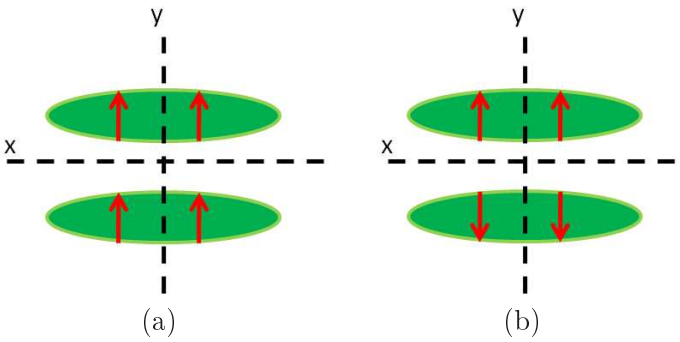

Figure 7.3: *Scheme of the boundary conditions for the electric field used in the FDTD simulations, for the y-polarization to simulate the symmetric (a) and antisymmetric mode (b), respectively.*

symmetric one while the second to the antisymmetric mode. The symmetry of the first mode (λ=1.596 μm) is shown in fig. 7.4.a. Note that the energy is confined in the cavities region, as expected, and the principal component of the electric field is polarized in the y-direction. It is important to point out that the symmetric mode is at higher energy than the antisymmetric one, contrary to the case of classic resonators such as micropillars and microrings. This will play an important role in the following.

The far field emission profile in k-space for the symmetric mode is shown in fig. 7.4.b, calculated as the spatial Fourier transform of the electromagnetic field monitored at twice the membrane thickness ($\sim 0.9\ \mu m$ from the membrane surface) in z-direction. We observe two lobes at $\sim 70°$. Note the emission profile is similar to the one found in section 2.1 (fig. 2.4) for a single cavity.

On the other hand, the mode centered at 1.6 μm reveals an antisymmetric spatial distribution of the field in the membrane, see fig. 7.5.a.

The emission profile of the antisymmetric mode in the far field has four lobes at $\sim 70°$, fig. 7.5.b. While the far field emission of the symmetric mode is hard to distinguish from the one of a single cavity, the emission of the antisymmetric mode is qualitatively different. The minimum of intensity at $k_y = 0$ arises from the destructive interference between the emission of each cavity since they are in anti-phase. This difference can be used to experimentally check the coupling between cavities, see chapter 8.

It is important to point out that the symmetric and antisymmetric modes only exist for the particular case where the two cavities are equivalent (i.e. equal resonance frequency and quality factor). Nevertheless, in a general case, where an asymmetry between the cavities takes place, the two modes of the system still present the same phase difference between the cavities as the symmetric ($\phi = 0$) and antisymmetric mode ($\phi = \pi$). These modes, for the general case, are usually called bonding ($\phi = 0$) and antibonding ($\phi = \pi$). We will return to this in section 8.4.

Typically, in coupled systems, the symmetric mode has less energy than the antisymmetric one, as the simple case of two masses coupled by a spring: the symmetric mode is the fundamental one. However, this is not imposed by any fundamental principle. According to the numerical simulations for two L3 cavities separated away in the $\Gamma - M$ direction the situation is the opposite one. In order to better understand this result, 2D FDTD numerical simulations of

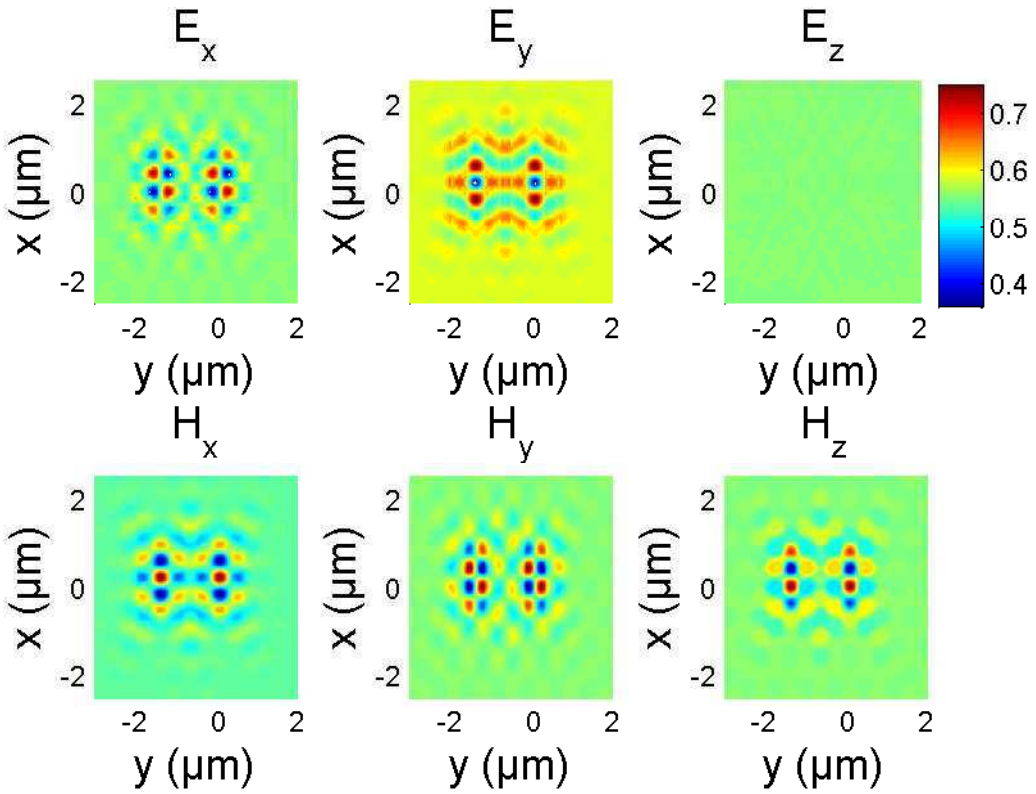

(a)

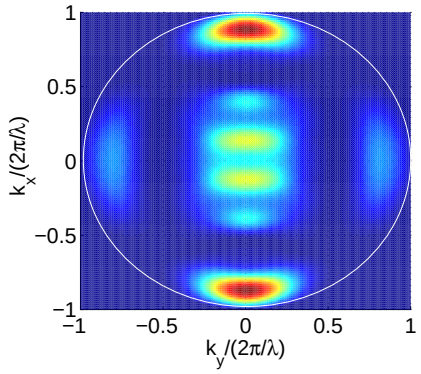

(b)

Figure 7.4: *(a) Spatial field distribution for the symmetric mode ($\lambda = 1.596$ μm) at the membrane center. (b) Far field emission profile of the symmetric mode calculated as the Fourier transform of the field stored on a monitor positioned at twice the lattice period (~ 0.9 μm from the membrane surface). Note the similarities with the emission profile of a single cavity (fig. 2.4)*

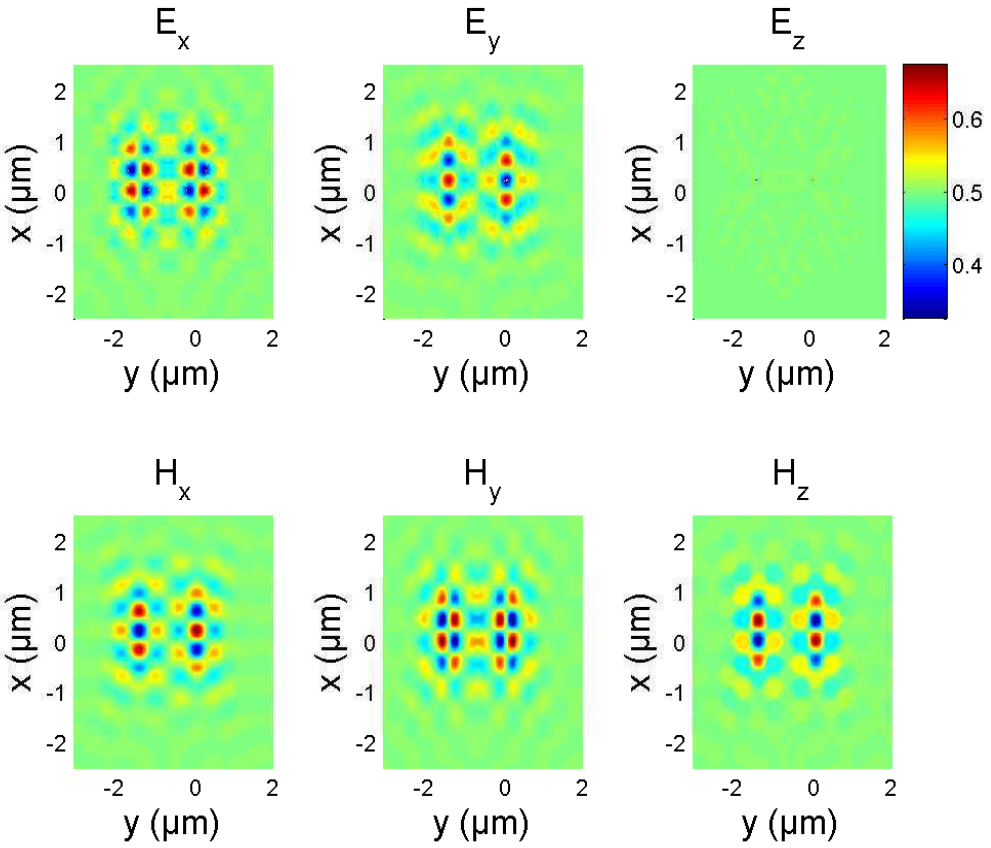

(a)

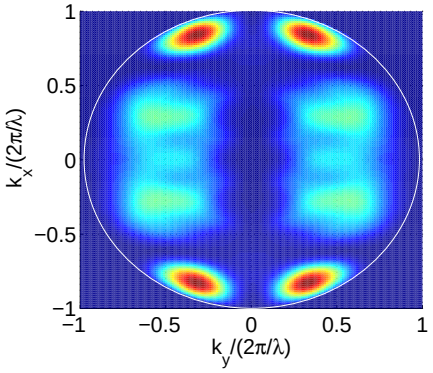

(b)

Figure 7.5: *(a) Spatial field distribution at the membrane center for the antisymmetric mode ($\lambda = 1.6$ μm). (b) Far field emission profile of the antisymmetric mode calculated as the Fourier transform of the field stored on a monitor positioned at twice the lattice period (~ 0.9 μm from the membrane surface).*

two W1 waveguides separated away by three rows of holes in the $\Gamma - M$ direction were carried out. Fig. 7.6 shows the band diagram of the coupled W1s. Note that there is a range of k where the splitting of modes is important and for which the symmetric mode is at lower wavelength than the antisymmetric one. In the case of cavities, since the mode is spatially confined, the (discrete) translation invariance is broken and the mode becomes confined at around $k \sim 0.4$. It can be observed that, for such k-value, the symmetric mode has higher energy than the antisymmetric one. For longer cavities, the central k-vector is expected to approach the edge of the Brillouin zone ($k = 0.5$): in such case, the situation would be reversed. It is worth mentioning that in general, according to [56] (fig. 1.33) the sign of the coupling, which determines the mode at higher energy, can be exchanged by changing the coupling configuration. This represents an advantage of PhC over other systems, such as microdisks or micropillars: the geometry can be chosen to tailor not only the coupling strength but also the coupling sign.

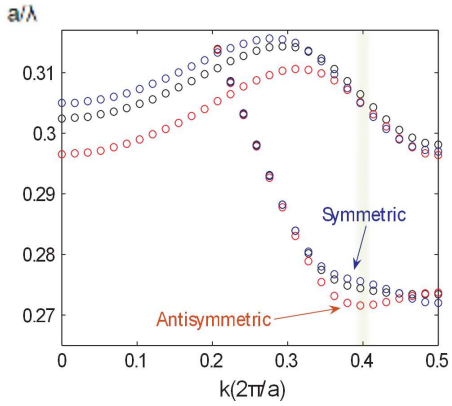

Figure 7.6: *Band diagram for two coupled W1 waveguides separated away by three rows of holes. Note there is a range of k where the splitting of modes is important and for which the symmetric mode is at lower wavelength than the antisymmetric one. The green region shows the mode confinement in k for a L3 cavity. The PhC period and radius are: 430 nm and 0.34a, respectively.*

7.2 Evanescently coupled linear cavities

Once the mutual coupling of PhC cavities has been numerically addressed, we investigate the coupling to the outside. In the following, we consider two evanescently coupled linear cavities coupled to the external continuum through n individual ports and m common ports (fig. 7.8.a). Each cavity has a coupling time to the ports τ.

The dynamical equations for this system are [132]:

$$\frac{da}{dt} = (j\Omega_0 - \Gamma)a + K^T|s_+\rangle \tag{7.1}$$

$$|s_-\rangle = C|s_+\rangle + Da \tag{7.2}$$

where a is the resonant field inside the cavities, $a = (a_1, a_2)$. Ω is a matrix with the resonant frequencies (ω_0) of the cavities and the evanescent coupling efficiency (κ) between them and Γ contains the losses. K and D are the coupling matrix from the ports to the cavities and vice versa. Using the same considerations as in section 2.2, it can be demonstrated that $K = D$.

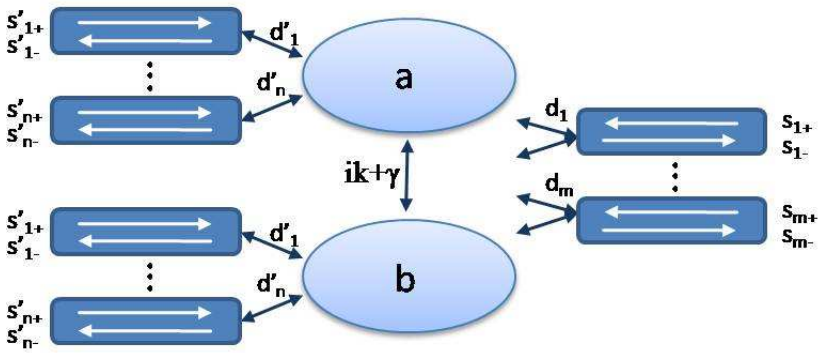

Figure 7.7: *Scheme of two coupled cavities coupled to the outside by n individual ports and m common ports.*

Taking the cavity modes as the basis we can express Ω, Γ and D as:

$$\Omega = \begin{pmatrix} w_0 & \kappa \\ \kappa & w_0 \end{pmatrix} \tag{7.3}$$

$$\Gamma = \begin{pmatrix} 1/\tau & -\gamma \\ -\gamma & 1/\tau \end{pmatrix} \tag{7.4}$$

$$D = \begin{pmatrix} d'_1 & 0 \\ \vdots & \vdots \\ d'_n & 0 \\ d_1 & d_1 \\ \vdots & \vdots \\ d_m & d_m \\ 0 & d'_1 \\ \vdots & \vdots \\ 0 & d'_n \end{pmatrix} \tag{7.5}$$

where d and d' are the coupling strengths between the cavities and the common or individual ports, respectively.

Considering $H = j\Omega - \Gamma$, the modes of the system are given by the eigenvectors of H. From eqs. 7.3 and 7.4, H is hermitian, then the eigenvectors form an orthogonal basis. Moreover, since the system is symmetric under reflection upon the x-axis, the eigenmodes are the symmetric and the antisymmetric ones. The wave amplitudes of the eigenmodes (c_S and c_A for the symmetric and antisymmetric modes respectively) oscillate with complex frequencies

$$\Omega_{S,A} = \omega_{S,A} + i/\tau_{S,A} \tag{7.6}$$

where $\omega_{S,A}$ and $1/\tau_{S,A}$ are given by:

$$\omega_{S,A} = \omega_0 \pm \kappa \tag{7.7}$$

$$1/\tau_{S,A} = 1/\tau \mp \gamma \tag{7.8}$$

Using $D^\dagger D = 2\Gamma$ [132], as in eq. 2.8, we obtain the relation between d, d', τ and γ given by:

$$\sum_{i=1}^{m} |d_i|^2 = -2\gamma \tag{7.9}$$

$$\sum_{i=1}^{n} |d'_i|^2 + \sum_{i=1}^{m} |d_i|^2 = \frac{2}{\tau} \tag{7.10}$$

In order to further simplify the calculations, we consider that the coupling strength of the individual/common ports are equal ($d'_1 = ... = d'_n = d' /\ d_1 = ... = d_m = d$). Eqs. 7.9 and 7.10 then read

$$m|d|^2 = -2\gamma \tag{7.11}$$

$$n|d'|^2 + m|d|^2 = \frac{2}{\tau} \tag{7.12}$$

Eq. 7.12 relates the modulus of d and d' with γ and τ. To relate the phases of d and d' with the system parameters, the matrix C must be defined. In eq. (7.2), C corresponds to the direct process, meaning the direct incoming field coupling to the ports. The direct process can either be resonant or given by evanescent coupling. These processes can be described by the followings unitary matrices C_r and C_e, respectively:

$$C_r = \begin{pmatrix} e^{j\phi'} & 0 & \dots & \dots & \dots & \dots & \dots & \dots & 0 \\ 0 & \ddots & & & & & & & \vdots \\ \vdots & & e^{j\phi'} & & & & & & \vdots \\ \vdots & & & e^{j\phi} & & & & & \vdots \\ \vdots & & & & \ddots & & & & \vdots \\ \vdots & & & & & e^{j\phi} & & & \vdots \\ \vdots & & & & & & e^{j\phi'} & & \vdots \\ \vdots & & & & & & & \ddots & 0 \\ 0 & \dots & \dots & \dots & \dots & \dots & \dots & 0 & e^{j\phi'} \end{pmatrix}; \tag{7.13}$$

$$C_e = \begin{pmatrix} 0 & \dots & e^{j\phi'} & 0 & \dots & \dots & \dots & \dots & 0 \\ & \ddots & & & & & & & \vdots \\ e^{j\phi'} & \dots & 0 & & & & & & \vdots \\ 0 & & & 0 & \dots & e^{j\phi} & & & \vdots \\ \vdots & & & & \ddots & & & & \vdots \\ \vdots & & & e^{j\phi} & \dots & 0 & & & 0 \\ \vdots & & & & & & 0 & \dots & e^{j\phi'} \\ \vdots & & & & & & & \ddots & \\ 0 & \dots & \dots & \dots & \dots & 0 & e^{j\phi'} & \dots & 0 \end{pmatrix} \tag{7.14}$$

where ϕ and ϕ' represent the phases, which depend on the properties of the ports. Applying eq. 2.16 ($CD^* = -D$) to eqs. 7.5 and 7.14 and writing d as $d = |d|exp(j\phi_d)$, $d' = |d'|exp(j\phi_{d'})$ we obtain:

$$e^{2j\phi_{d'}} = -e^{j\phi'}; \quad e^{2j\phi_d} = -e^{j\phi} \tag{7.15}$$

Eq. 7.15 leads to $\phi_d = \phi/2 + \pi/2$. Then $d = j|d|exp(j\phi/2)$.
This formalism has allowed us to find out the relation between different parameters in a system of linear coupled cavities. We will apply these results in the following section to the study of nonlinear coupled cavities.

7.3 Evanescently coupled nonlinear cavities

Here we consider two evanescently coupled nonlinear cavities coupled to the outside as in fig. 7.7. The dynamical equations are given by the set of equations deduced in section 1.4. Considering only an electronic nonlinear effect and adiabatically eliminating the differential equation for carrier density for simplicity (i.e. taking the steady states solution of eq. 1.56, section 1.4) , the dynamic equation for the intracavity energy is given by adding a nonlinear term to eq. 7.1 (see eq. 1.69 in section 1.4). Thus,

$$\frac{da_{1,2}}{dt} = [j(w_0 + \frac{|a_{1,2}|^2}{U_{0,e}\tau}) - \frac{1}{\tau}]a_{1,2} + (j\kappa + \gamma)a_{2,1} + df \tag{7.16}$$

with $U_{0,e} = \tau_{a_0}|a_{sat}|^2/\alpha_H\tau$ the characteristic intracavity energy for electronic bistable threshold, $d = j|d|exp(j\phi/2)$ and $|f|^2$ is the injected power through one common port. As previously discussed, given the negative sign of the nonlinearity, the intensity blue-shifts the resonance. Considering $a_{1,2}(t) = a'(t)e^{jwt}$, $f(t) = fe^{jwt}$ and $t' = t/\tau$ in Eq. (7.16) the steady states are given by [64]:

$$-\tau df = j(\delta + A) - 1)a'_1 + (j\tau\kappa + \tau\gamma)a'_2 \tag{7.17}$$

$$-\tau df = j(\delta + B) - 1)a'_2 + (j\tau\kappa + \tau\gamma)a'_1 \tag{7.18}$$

where $\delta = \tau(w_0 - w)$, $A = \frac{|a_1|^2}{U_{0,e}}$ and $B = \frac{|a_2|^2}{U_{0,e}}$. Equating the right sides of eqs. (7.17) and (7.18) and taking squared modulus, eqs. 7.17 and 7.18 give:

$$(A - B)[B^2 + (A + 2\alpha)B + A^2 + 2\Lambda A + \Lambda^2 + (1 + \tau\gamma)^2] = 0 \tag{7.19}$$

Here

$$\Lambda = \delta - \tau\kappa = \tau(\omega_A - \omega_0) \tag{7.20}$$

From Eq. (7.19) it is easy to show that a non-symmetric solution ($A \neq B$) is possible if $|\Lambda| > \sqrt{3}(1 + \tau\gamma)$ with A lying between the values $-2/3\Lambda \pm 2/3\sqrt{\Lambda^2 - 3(1 + \tau\gamma)^2}$. Moreover, since A must be positive by definition, Λ must be negative, thus $\Lambda < -\sqrt{3}(1 + \tau\gamma)$, which implies, according to eqs. 7.20 and 7.8, that $\tau_A(\omega_A - \omega_0) < -\sqrt{3}$. Surprisingly, this corresponds to the condition for bistability of the antisymmetric mode.
In the following we apply these results to two particular cases well suited for an experimental demonstration.

7.3.1 First case of study: Two cavities coupled to the external continuum by three ports

In these paragraphs we will consider the particular case where the cavities are coupled by three ports: two individual ports and a common one. It has already been demonstrated that spontaneous symmetry breaking takes place for two nonlinear PhC cavities coupled through a waveguide (see section 1.2.3). We will see that our particular case contains the system dynamics studied in [64], in the sense that parameters in [64] can be mapped to the parameters of our theory. Therefore, the solutions of [64] are formally equivalent to some set of solutions of eq. 7.16. Fig.

7.8.a shows a sketch of the system. Note that the coupling strength from one cavity to the left and right ports is considered to be the same. In this configuration n=1 and m=1; replacing these in eqs. 7.11 and 7.12, and further assuming $|d| = |d'|$ by construction, leads to:

$$\gamma = \frac{-1}{2\tau} \tag{7.21}$$

$$|d|^2 = \frac{1}{\tau} \tag{7.22}$$

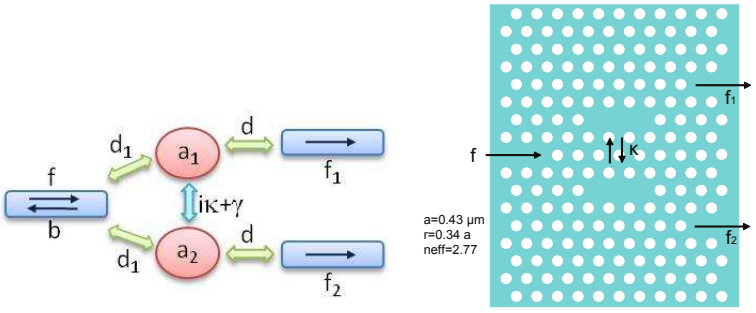

(a) (b)

Figure 7.8: *(a) Scheme of two coupled cavities coupled to the outside by two individual ports and one common port. (b) PC device compatible with (a).*

Replacing eq. 7.21 in the expression for $1/\tau_{S,A}$ (eq. 7.8) we obtain $1/\tau_S = 3/2\tau$ and $1/\tau_A = 1/2\tau$, so the antisymmetric mode has reduced losses with respect to the single cavity whereas the symmetric one has increased losses. Regarding $\Omega_{S/A}$, we obtain that for positives values of κ: $\Omega_a < w_0 < \Omega_s$. FDTD numerical simulations of section 7.1 have shown that this is the case of two evanescently coupled L3 cavities separated away in the $\Gamma - M$ direction by three rows of holes, fig. 7.8.b.

Replacing eqs. 7.21 and 7.22 in eq. 7.19, we obtain:

$$(A - B)[B^2 + (A + 2\alpha)B + A^2 + 2\Lambda A + \Lambda^2 + 1/4] = 0 \tag{7.23}$$

Note that eq. 7.23 is analogue to eq. 6 in [64] provided $\Lambda = \Delta'$. This allows us to identify $\tau\kappa = tg(\phi/2)/2$ where ϕ represents the phase that depends on the waveguide length and the PhC reflection properties in [64], fig. 7.1.b. Let us stress that this analogy is only obtained for the system of fig. 7.8, where $\gamma = -1/2\tau$, since γ changes for different system architectures. This means that the system in [64] can be mapped to a subset of solutions of a system of evanescently coupled cavities.

Replacing eqs. 7.21 and 7.22 in eqs. 7.17 and 7.18, taking squared modulus and combining both, we obtain the energy inside the cavities (A or B) as a function of the injected power ($P_{in} = |f|^2/P_0$, with $P_0 = U_{0,e}/(\tau^2|d|^2) = U_{0,e}/\tau$). This is represented in fig. 7.9 for different detunings and $\tau\kappa = 0.8$. This value corresponds to a resonance splitting of 0.8 times the resonance width. Fig. 7.9.a shows the energy inside the cavities vs the injected power for a detuning of $\delta = -0.2$. Note that the symmetric solution (orange line) becomes unstable for a certain input power and a stable non-symmetric solution appears (black line). This non-symmetric solution can be observed in the temporal simulations of fig. 7.9.b where the time trace of the energy

inside the cavities for $\delta = -0.2$ and an injected power of $P_{in}/P_0 = 2.5$ are plotted. The initial condition is set at the symmetric state $A_{in} = 0.65$ and, in order to achieve the breaking, a slight perturbation in the initial condition of the energy inside one of the cavities is added. Note that in fig. 7.9.b the system relaxes to the stationary sates A_1 and A_2 in fig. 7.9.a. For higher detuning (δ=-3) the curve becomes more complex and several steady states are possible for a single input power, fig. 7.9.c. This multi-stability is shown in fig. 7.9.d where the time trace for $\delta = -3$, $P_{in}/P_0 = 12.7$ and an initial condition of $A_{in} = 3.41$ is plotted. In fig. 7.9.d, at $t/\tau = 120$ a perturbation was added to the energy inside each cavity in order to make the system jump to the other stable branch. Let us stress that a large perturbation is needed in order to kick the system to the other branch. This means that the basin of attraction seems to be larger for the medium branches (A_1 and A_2) than for the external branches (A'_1 and A'_2).

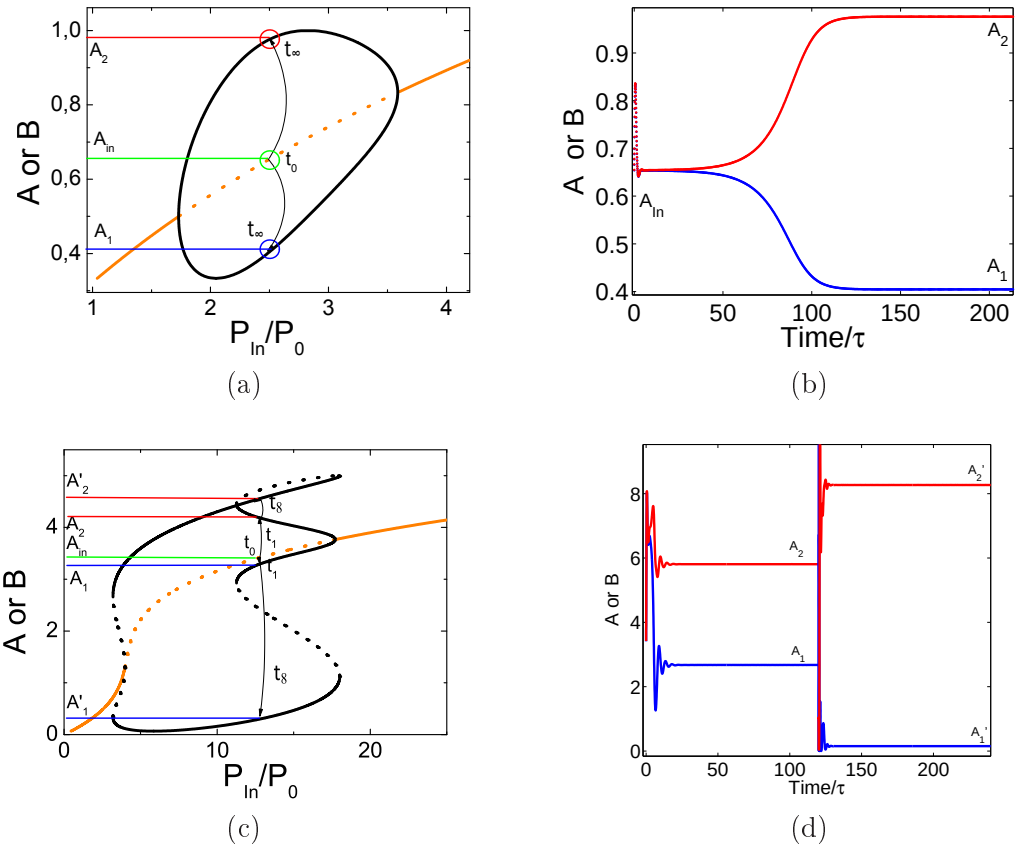

Figure 7.9: *Spontaneous symmetry breaking in two evanescent coupled cavities. (a) Energy inside the cavities as a function of the injected power for a detuning of $\delta = -0.2$ and a coupling efficiency of $\tau\kappa = 0.8$, showing two pitchfork bifurcations. The symmetric and non-symmetric solutions are shown in orange and black lines, respectively. Stable (unstable) states are shown with solid (dashed) lines. (b) Time traces of the energy inside the cavities for $\delta = -0.2$, injected power of $P_{in}/P_0 = 2.5$ and initial conditions of $A_{in} = B_{in} = 0.65$ plus a slight perturbation in one of the cavities. Note that the system relaxes to the stationary sates A_1 and A_2 in (a). (c) Idem as (a) for a detuning of $\delta = -3$ and $\tau\kappa = 0.8$, showing multi-stability. d) Idem as (b) for $\delta = -3$, $P_{in}/P_0 = 12.7$ and $A_{in} = 3.41$. At $t/\tau = 120$ a perturbation was added in order to make the system jump to the other stable branch (A'_1 and A'_2).*

In order to highlight the symmetry breaking, hysteresis cycles are calculated for the pa-

rameters in fig. 7.9. Fig. 7.10 shows the transmitted signals f_1 and f_2 (blue and red line, respectively) as a function of the injected power. For low detuning ($\delta = -0.2$), cycles are not observed (fig. 7.10.a), although, for higher detuning ($\delta = -3$) a complex hysteresis cycle is obtained revealing multi-stability.

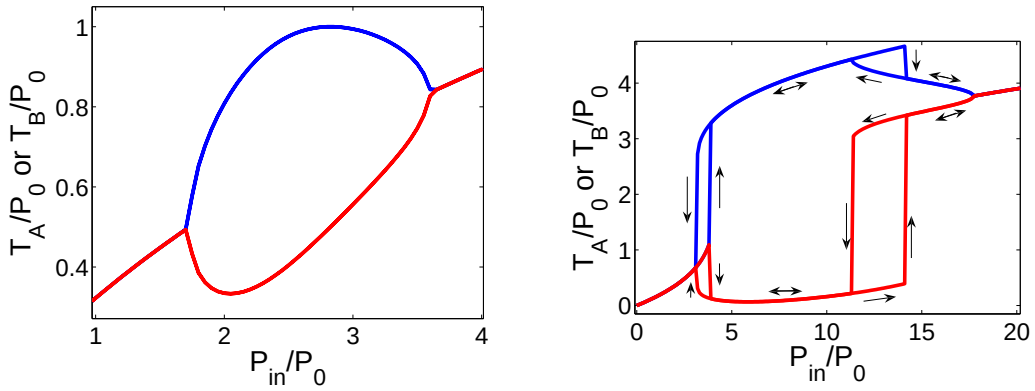

(a) (b)

Figure 7.10: *Hysteresis cycles for the parameters in fig. 7.9. Transmitted signals ($|f_1|^2$ in blue line and $|f_2|^2$ in red line) as a function of the input signal. The parameters values are: (a) $\delta = -0.2$ and $\tau\kappa = 0.8$ and (b) $\delta = -3$ and $\tau\kappa = 0.8$. The black arrows in (b) point out the cycle sense.*

The breaking of symmetry can also be seen in the spectral domain. The nonlinear spectral response is studied by analyzing the energy inside the cavities versus the detuning. For a very low injected power ($P_{in}/P_0 = 0.1$), fig. 7.11 (green line), the linear regime takes place. The resonance is centred at $\delta = -0.8$, which corresponds to the frequency of the symmetric mode. This can be expected since, as both cavities are injected with the same amplitude and phase, the only mode that can be excited in the linear regime is the symmetric one.

Increasing the injected power ($P_{in}/P_0 = 4$) the nonlinearity becomes stronger and the symmetric resonance blue-shifts and bends (fig. 7.11, orange line). Moreover, the spontaneous symmetry breaking is observed in fig. 7.11 (black line). Note the minimum detuning for which the breaking takes place satisfies the condition found in the previous section: $\Lambda < -\sqrt{3}(1+\tau\gamma)$. From fig. 7.11, the range of detunings for which the symmetry breaking exists become clear.

Phase Diagram

In order to obtain the set of parameters that give rise to the symmetry breaking, the phase diagram of the system in eq. 7.16 was studied. The space of parameters P_{in}/P_0 and $\tau\kappa$ of fig. 7.12.a shows the different bifurcations for the non-symmetric stable states (-saddle node (SN), -saddle repulsor (SR), -supercritical pitchfork (P), - subcritical pitchfork (SP)) and for the symmetric one (-saddle node (SNS), -saddle repulsor (SRS)). For different values of $\tau\kappa$ (at constant Λ), the P_{in}/P_0 at which a bifurcation occurs are plotted. Several regions can be distinguished. For strong coupling, $\tau\kappa \gtrsim 0.95$ (I zone in fig. 7.12.a), we observe symmetry breaking resulting from two pitchfork bifurcations (fig. 7.12.b). It is important to point out that the symmetry breaking threshold increases with the coupling strength. If $0 < \tau\kappa < 1$ (II zone in fig. 7.12.a)

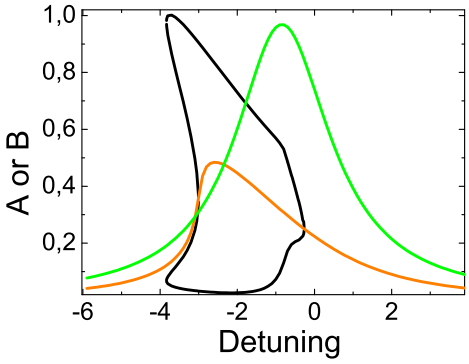

Figure 7.11: *Energy inside the cavities as a function of the detuning. For* $P_{in}/P_0 = 0.1$ *there is only one solution (symmetric) shown in green line. For an injected power of:* $P_{in}/P_0 = 4$*, the symmetric and non-symmetric solution are shown in orange and black lines, respectively. In all the cases* $\tau\kappa = 0.8$*. The green curve was multiplied by 80 in order to be shown in the same vertical scale.*

the symmetry breaking arises from a subcritical pitchfork bifurcation and the range of P_{in}/P_0 for which it exists is reduced (fig. 7.12.c). Finally, if $\tau\kappa < 0$ the non-symmetric stable states coexist with bistability of the symmetric stable states (III zone in fig. 7.12.d). Within regime III, the saddle node bifurcation delimiting the existence of non-symmetric states occurs at smaller P_{in}/P_0 values than the subcritical pitchfork bifurcation of the symmetric state. Therefore, non-symmetric states do not emerge from the symmetric state spontaneously, i. e. they are unlikely to be observed from hysteresis cycles in which P_{in} is progressively increased.

Indeed, symmetry breaking can be obtained in the system of fig. 7.8.a depending on the coupling strength. For strong coupling, the breaking of symmetry arises from two pitchfork bifurcations and a large range of P_{in}/P_0 for which this regime exists is observed.

The results in fig. 7.12 correspond to a particular configuration. Let us also address the limit $\tau\gamma = 0$ for which the symmetric and antisymmetric mode has equal losses. This represents the case of systems with "purely imaginary" coupling, such as micropillars. Fig. 7.13 shows the phase diagram for $\tau\gamma = 0$. As in fig. 7.12, three different regions can be distinguished: I) for strong coupling the symmetry breaking arises from a pitchfork bifurcation and the range of P_{in} for which it takes place is large; II) the symmetry breaking arises from a saddle node bifurcation and the P_{in} range for which it takes place is reduced; III) the stable states of the non-symmetric mode coexist with stable states of the symmetric mode, thus, they are unlikely to be observed from hysteresis cycles. From this result, we can conclude that symmetry breaking in a system with electronic (negative) nonlinearity, which blue-shifts the resonance wavelength, can only be obtained for positive couplings (i.e. $\omega_S > \omega_A$). Moreover, eq. 7.16 is invariant under the transformation $\tau\kappa \to -\tau\kappa$, $\delta \to -\delta$ and the change of the nonlinearity sign, $\Delta\omega_{NL} \to -\Delta\omega_{NL}$. Thus, according to fig. 7.13, with a positive nonlinearity the symmetry breaking can only be obtained for negative coupling coefficient (i.e. $\omega_S < \omega_A$).

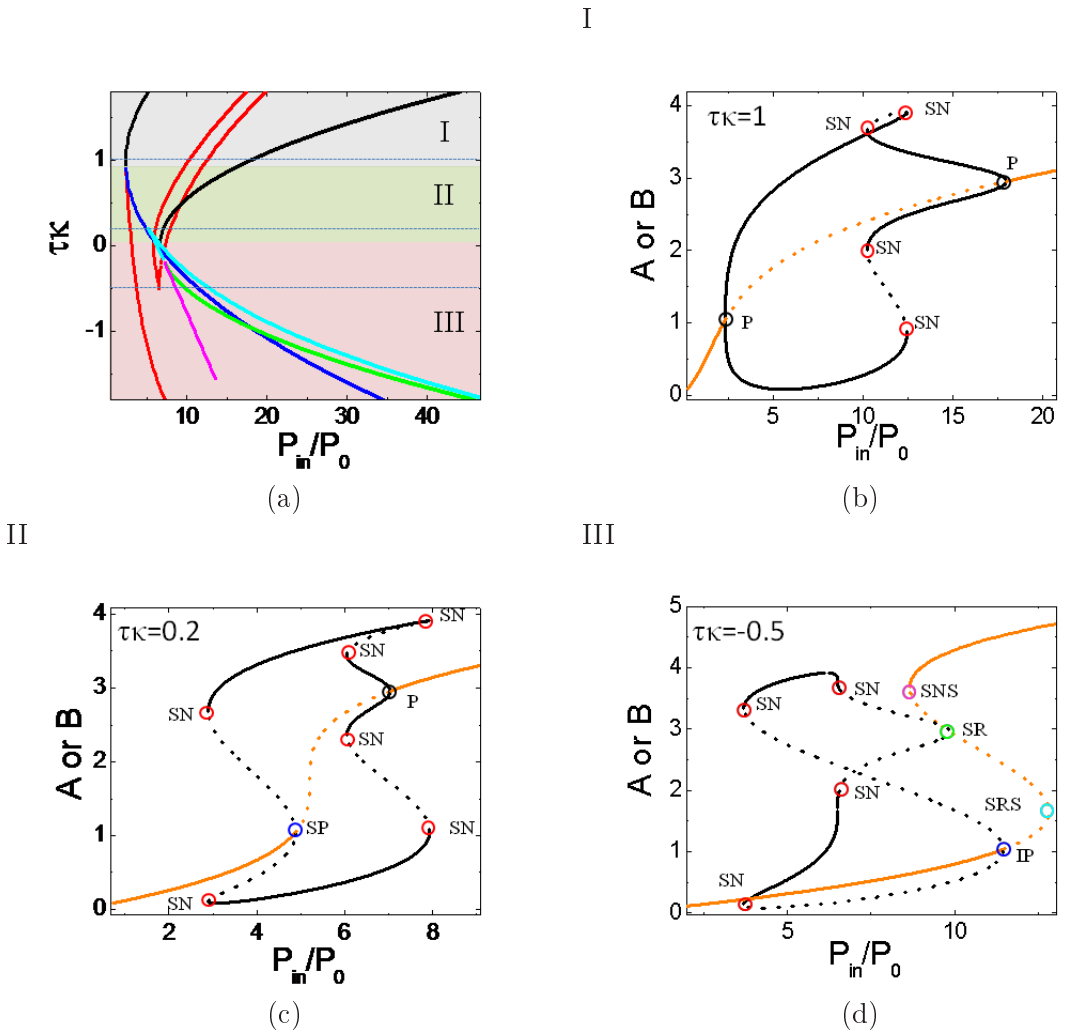

Figure 7.12: *(a) Phase diagram for a system with $\gamma = -0.5$. The bifurcations of the non-symmetric states are: -saddle node (SN), -saddle-repulsor (SR), -supercritical pitchfork (P), -subcritical pitchfork (SP). For the symmetric one: -saddle node (SNS), -saddle-repulsor (SRS). (b) Intensity inside the cavities as a function of the injected power. The symmetric and non-symmetric solution are shown in orange and black lines, respectively. Stable (unstable) states are shown with solid (dashed) line. $\tau\kappa = 1$. (c) $\tau\kappa = 0.3$. (d) $\tau\kappa = -0.3$. In all the cases $\Lambda = -3$. The bifurcation points are highlighted with open circles. The horizontal lines in (a) indicate the values of $\tau\kappa$ used in (b), (c) and (d).*

7.3.2 Second case of study: the experimental configuration

In the following we apply the theory developed in section 7.3 to the experimental configuration: a cavity coupled to the outside by a microfiber, fig. 7.14.a. This is a special case since, if no intrinsic losses are considered, m=2 and n=0 yielding to $\gamma = -1/\tau$ (from eq. 7.12). This means, from eq. 7.8, that the antisymmetric mode has no losses ($\tau_A = 0$). Therefore, this mode does not decay, which is unphysical. In order to add leaky ports to the antisymmetric mode, intrinsic losses as both individual and a common ports must be taken into account, fig. 7.14.b. The radiative common port accounts for the far field overlap of the radiative emission of the two cavities.

According to fig. 7.14.b, two common ports represent the fiber, with a coupling strength

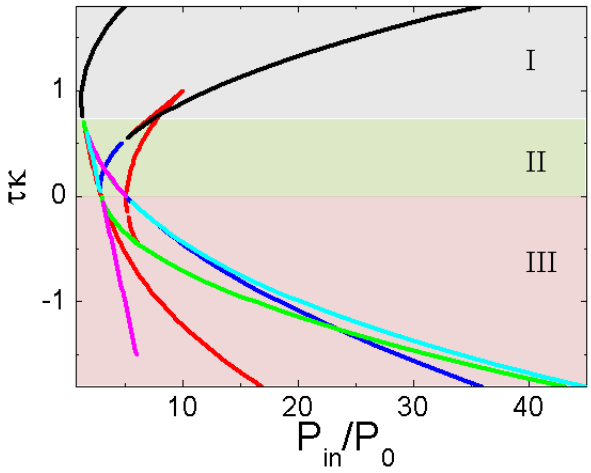

Figure 7.13: *Phase diagram for a system with $\gamma = 0$ and $\Lambda = -3$. The bifurcations of the non-symmetric states are: -saddle node (SN), -saddle-repulsor (SR), -supercritical pitchfork (P), -subcritical pitchfork (SP). For the symmetric one: -saddle node (SNS), -saddle-repulsor (SRS).*

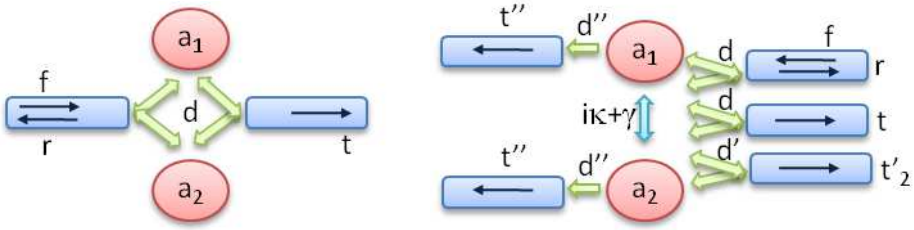

(a) (b)

Figure 7.14: *Scheme of the coupling between two cavities and the tapered fiber without (a) and with (b) intrinsic losses. In (b) each cavity is coupled to the external continuum by three common ports: the fiber (d) and radiative losses (d') and one individual port (the intrinsic losses, d").*

d, an additional port accounts for overlapping leakage from each cavity, with a coupling strength d', and two individual ports, with coupling strength d'', that represent the non-overlapping radiative losses of each cavity. The value of γ can be obtained considering first an undercoupled regime between the cavities and the fiber ($\tau_c \to \infty$), then, from eq. 7.8 we obtain:

$$\gamma_0 = \frac{1}{2}(\frac{1}{\tau_A} - \frac{1}{\tau_S}) = \frac{\omega_A}{4Q_A} - \frac{\omega_S}{4Q_S} \tag{7.24}$$

Considering the results of the simulation in section 7.1, $\omega_{A_0} = 1176.916$ THz, $\omega_{S_0} = 1180.102$ THz, $Q_{A_0} = 35000$, $Q_{S_0} = 18000$ and the results of the simulation for a single cavity ($Q_0 = 23000$ and ω_0=1178.562 THz, section 2.1) which are used to estimate $\tau \sim 39$ ps, we get $\tau\gamma_0 = -0.3$.

If now we add the fiber ($\tau_c \neq \infty$), eqs. 7.11 and 7.12 yield $\gamma = \gamma_0 - 1/\tau_c$. The experimental fiber-coupling conditions of section 5.2 correspond to the undercoupling regime, $\eta \simeq 0.07$, which gives $Q_0/Q_c \simeq 0.08$. Therefore we can approximate $\gamma \approx \gamma_0$.

Replacing in eq. 7.19 the value found for $\tau\gamma$ and keeping $\tau\kappa = -0.8$, we obtain the energy inside the cavities (A or B) as a function of the injected power for $\delta = -3$, fig. 7.15.a. Note

that the main features are similar to the ones shown in fig. 7.9.c meaning that the symmetry breaking is not significantly affected by γ. Fig. 7.15.b shows the time traces for an injected power of $P_{in}/P_0 = 9$. Similarly to the previous case (section 7.3.1), the system decays to the stationary sates A_1 and A_2 in fig. 7.15.a.

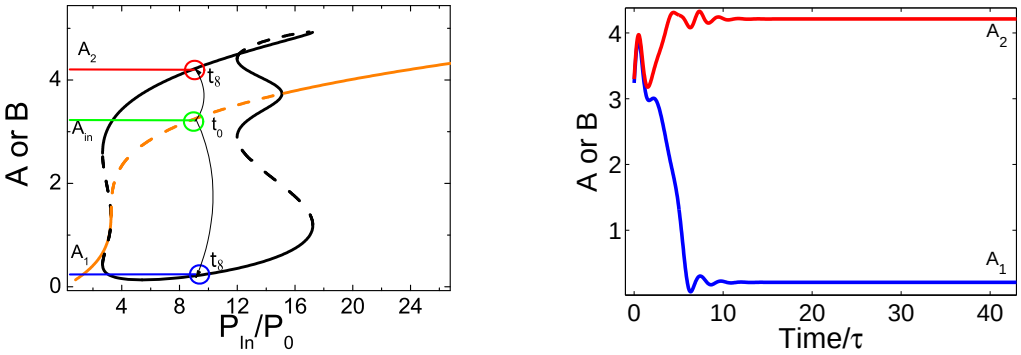

(a) (b)

Figure 7.15: *(a) Energy inside the cavities as a function of the injected power for a detuning of $\delta = -3$; $\tau\kappa = 0.8$ and $\tau\gamma = -0.3$. The symmetric and non-symmetric solutions are shown in orange and black lines, respectively. Stable (unstable) states are shown with solid (dashed) lines. (b) Time trace for an injected power of $P_{in}/P_0 = 9$; $\tau\kappa = 0.8$ and $\tau\gamma = -0.3$.*

In this configuration the measurable magnitude is no longer the energy in each cavity, but the output power given by the reflected ($|r|^2$) and transmitted ($|t|^2$) signals in the fiber. These are given by:

$$|S_-\rangle = C_e|S_+\rangle + Da \tag{7.25}$$

where

$$|S_-\rangle = \begin{pmatrix} r \\ t \\ t_1' \\ t_2' \\ t'' \end{pmatrix} \tag{7.26}$$

$$C_e = \begin{pmatrix} 0 & e^{j\phi} & 0 & 0 & 0 \\ e^{j\phi} & 0 & 0 & 0 & 0 \\ 0 & & & & \\ & & \ddots & & \\ & & & & 0 \end{pmatrix} \tag{7.27}$$

$$D = \begin{pmatrix} d & d \\ d & d \\ d' & d' \\ d'' & 0 \\ 0 & d'' \end{pmatrix} \tag{7.28}$$

The expression of C_e takes into account that the signal can only be injected through the fiber (as it is the case of cavities coupled trough a tapered fiber). Considering $|S_+\rangle = (f, 0, 0, 0, 0)$

(injection through the right side of the fiber) we obtain:

$$\frac{R}{P_0} = \frac{|r|^2}{P_0} = \frac{|a_1 + a_2|^2}{P_0 \tau} \tag{7.29}$$

where we used $d = ie^{j\phi/2}/\sqrt{\tau}$. Fig. 7.16 shows the hysteresis cycle measured in reflection (reflected signal as a function of the injected power). Note the difference with respect to bistable hysteresis cycles for a single cavity (fig. 5.17 in section 5.2). In particular, a change in slope of $R(P_{in})$ takes place when the system bifurcates from the symmetrical to non-symmetrical states. This shows, in principle, that the existence of spontaneous symmetry breaking can be detected from the features of the hysteresis cycle.

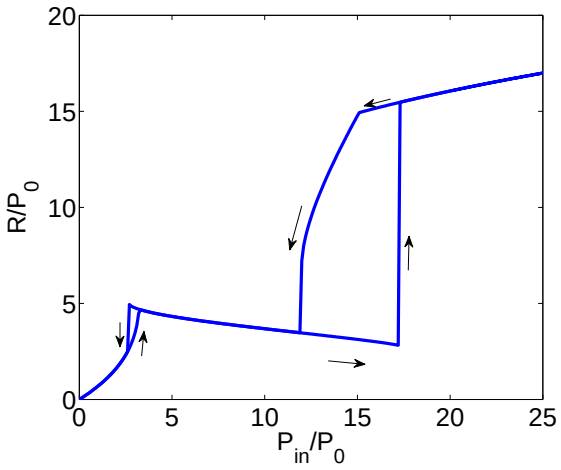

Figure 7.16: *Hysteresis cycle with the parameters in fig. 7.15. Reflected signal ($R=|r|^2$, from fig. 7.14.b) as a function of the input signal. The symmetry breaking can be detected from a dramatic change in the slope.*

7.4 Conclusion

The evanescent coupling between two L3 cavities separated by three rows of holes was determined by FDTD numerical simulations. Two resonant modes were found, separated away by ~ 4 nm, with different quality factors: $Q_S = 18000$ and $Q_A = 35000$. This corresponds to lower losses for the antisymmetric mode with respect to the symmetric one, which can be expected from the destructive/constructive interferences taking place for each mode.

A linear model based on a Coupled Mode Theory formalism was carried out in order to characterize the coupling between the cavities and the external ports. From this model the relation between the different parameters (τ, γ, κ and d) of the system was found. These results were used to develop a nonlinear model to study the symmetry breaking. We found that the spontaneous symmetry breaking can be achieved in a system where the two evanescently cavities are symmetrically excited by a single port. This result is important from an experimental point of view since, we believe, a demonstration of the symmetry breaking in this configuration is more viable than other configurations studied so far [64]. Indeed the possibility of symmetrically injecting the system through a single port substantially simplifies the experimental conditions.

This theoretical formalism was implemented to our experimental case: two cavities coupled to the outside via a tapered fiber. Spontaneous symmetry breaking was also found in this configuration. Therefore, choosing the appropriate parameters, the symmetry breaking might be achieved in our set up. In chapter 9 we will seek this phenomenon experimentally.

Chapter 8

Evanescent coupling between cavities

In the previous chapter we have shown, though FDTD numerical simulations, that evanescent coupling can be achieved between adjacent cavities in a PhC. Moreover, we used a coupled mode theory formalism to investigate the nonlinear regime of the coupled cavities and found that interesting nonlinear behaviors such as spontaneous symmetry breaking can be reached. We further demonstrated that these regimes are accessible within our experimental conditions, namely, two cavities coupled through a tapered fiber. Among the few works devoted to understanding optical coupling in PhC cavities, there is, to our knowledge, only one clear experimental demonstration by means of anti-crossing measurements of the mode splitting [79]. Here we tackle this problem using an alternative approach: the measurements of the relative phase coherence of the cavity fields.

The purpose of the present Chapter is to provide clear experimental evidence of the linear coupling between the cavities, as it was theoretically predicted in the previous one. These studies include spectral and spatial analysis, the latter both in the near and far fields. In order to simplify the access to the coupling parameters we first investigate cavities including QDs as the active medium. Indeed, the inhomogeneous broadening of the emission associated to the QD distribution allows to easily detect the cavity modes. Preliminary tests involving statistical studies of the spectral position of modes in samples with two cavities were carried out through photoluminescence experiments. Even though such studies are not conclusive for demonstrating optical coupling, they allow to build confidence on the observed mode splitting as a signature of coupling. In a second part we focus on L3 cavities including QW as active medium, that, following the results of Part II, are better suited for the nonlinear dynamical operation. Over these samples, near and far field emission profiles were investigated. These measurements constitute unequivocal evidence of evanescent coupling between the cavities.

8.1 Preliminary statistical studies of the coupling between cavities

The coupling between two adjacent identical cavities should manifest itself by the splitting of the initial mode into the symmetric and the antisymmetric ones. This splitting can be revealed via photoluminescence measurements. However, in general, technological imperfections may introduce a difference between the geometries of the cavities. This would end up with a two-peak photoluminescence spectrum which does not necessarily correspond to mode splitting. In a first series of experiments we have investigated the mode separation as a function of the PhC hole diameters and the distances between cavities. Here we present studies over L3 coupled

cavities and Noda-type adjacent cavities both including QDs as the active medium, since the inhomogeneously broadened emission of QDs allows to easily detect the position of the cavity modes.

8.1.1 Spectral studies of the emission of two L3 cavities

Samples analogous to the one described in section 3.1 including two adjacent L3 cavities etched in the same PhC were fabricated, fig. 8.1. The cavities are separated away by three rows of holes in the $\Gamma - M$ direction. In order to characterize these samples, photoluminescence spectra were measured. The cavities are pumped @532 nm with a CW, frequency doubled Nd:YAG laser and the emission is collected with a 20x microscope objective and send to a spectrometer/camera detection system, see sec. 3.1.3. A typical result is presented in Fig. 2.1. b where two resonances, labelled $\lambda_<$ and $\lambda_>$, are clearly visible.

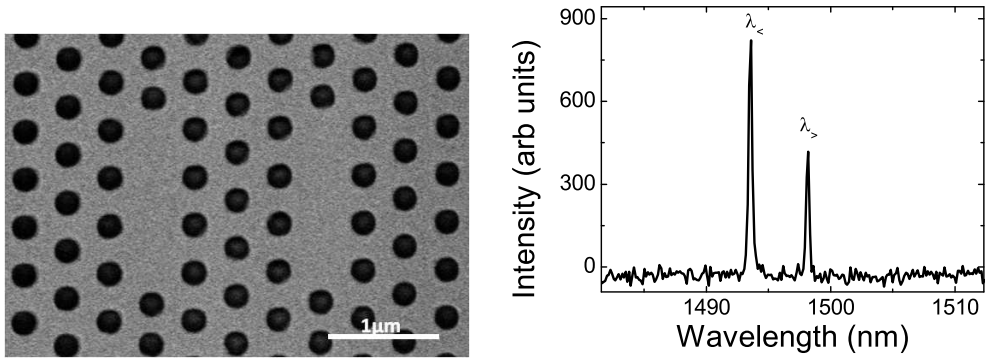

(a) (b)

Figure 8.1: *(a) MEB image of two L3 cavities in the same PhC separated away by three rows of holes in the* $\Gamma - M$ *direction. (b) Photoluminescence spectrum for a pump power of 23* μW *and an integration time of 0.1s.*

The spectral separation between peaks ($\lambda_> - \lambda_<$) is measured for 29 different PhCs containing two L3 cavities separated away be three rows of holes. For all the samples the lattice period, a=455nm, is kept constant, whereas the diameter is varied from 77 nm to 100 nm. Fig 8.2 shows the peak separation ($\lambda_> - \lambda_<$) for the whole set of samples. The average value gives $\lambda_> - \lambda_< = 5.1 \pm 0.7$ nm, in agreement with the FDTD numerical simulations of sec. 7.1 which gave $\Delta\lambda \sim 4$ nm. The small deviation from the average value ($\sim 14\%$) can be attributed to technological imperfections. The averaged distance between peaks, in turn, is most probably related to physical reasons: the mode splitting originated from the evanescent coupling. Then, according to section 7.1, $\lambda_<$ may correspond to the symmetric mode (λ_S) and $\lambda_>$ with the anti-symmetric one (λ_A). We will return to this discussion in section 8.4.

8.1.2 Spectral studies of the emission of two coupled cavities as a function of their separation

We now study the dependence of this splitting with the cavities separation. For this, we used Noda-type cavities (described in section 1.3). These were chosen for this study since the distance between cavities can be changed in a more "continuous" way compared to L3 cavities

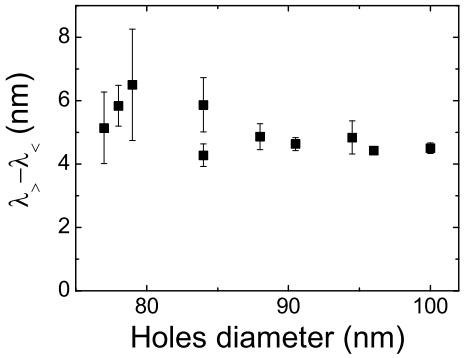

Figure 8.2: *Spectral distance between the modes of two L3 cavities in the same PhC as a function of the holes radius. The cavities are separated away by three rows of holes in the $\Gamma - M$ direction. The PhC period remains constant and equal to 455 nm.*

coupled in the $\Gamma - M$ direction. Indeed, Noda-type symmetrically coupled cavities can be obtained with p=1,2,..,N periods in between, while the number of holes between two L3 coupled cavities must be odd. A MEB image of a typical Noda-type cavity is presented in fig. 8.3. The PhC has a waveguide (W1) in the center and the cavities are given by a 20 nm-increase of the lattice period in the direction of the W1, along two periods, fig. 8.3. The barrier, given by the number of periods (p) between cavities, was varied from 2 to 20 (2, 3, 4, 5 and 20 periods).

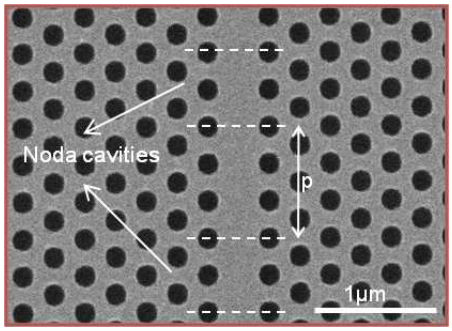

Figure 8.3: *MEB image of two Noda-20 cavities in the same waveguide separated away by three periods (p=3) of the photonic crystal. The cavity is obtained by a 20-nm increase of the lattice period.*

We proceed to the systematic measurement of the photoluminescence spectra for the different cavity separations. Typical results are shown in fig. 8.4.a. The $\lambda_> - \lambda_<$ wavelength splitting as a function of p is represented in fig. 8.4.b. Each point is the average of 4 sample measurements. For p=20 the cavities are separated by $\sim 9\ \mu m$ and we can consider that they are no longer coupled. Therefore, we can attribute the measured splitting to imperfections, always present in PhC fabricated with state of the art technologies. The evolution of $\Delta\lambda$ as a function of p between 2 and 5, can, in turn, be univoquely ascribed to the evolution of the coupling with the barrier thickness, in good agreement with eq. 7.7. These data are well fitted by a linear curve, which corresponds to consider a linear dependency of the coupling strength with the distance between cavities.

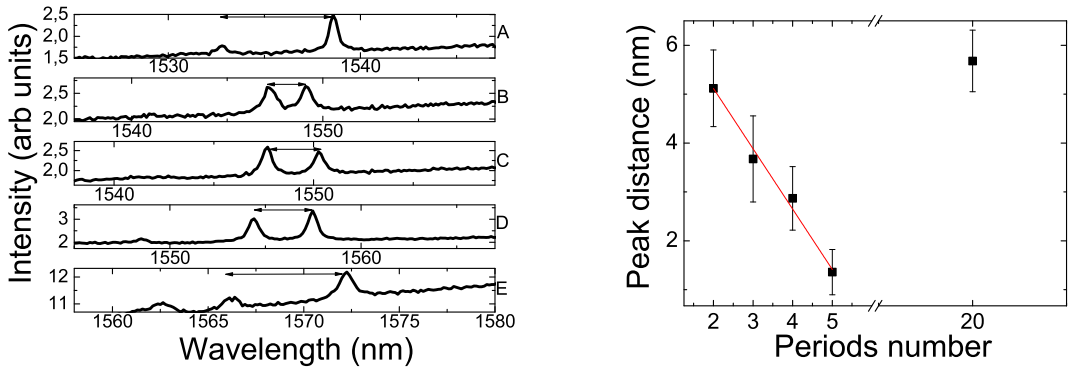

(a) (b)

Figure 8.4: *(a) Photoluminescence spectrum of two Noda-20 cavities. The number of periods of separation and the consequent wavelength splitting ($\Delta\lambda_{>-<}$) are: A. p=20, $\Delta\lambda_{>-<}$ =5.8 nm, B. p=5, $\Delta\lambda_{>-<}$=1.8 nm, C. p=4, $\Delta\lambda_{>-<}$=2.5 nm, D. p=3, $\Delta\lambda_{>-<}$=3.1 nm and E. p=2, $\Delta\lambda_{>-<}$=6 nm. (b) Peak distance ($\Delta\lambda_{>-<}$) as a function of the number of periods (p) between cavities. The value shown for each p corresponds to the average over four samples.*

8.2 Choosing the most appropriate type of cavity

In the previous paragraphs we have seen that Noda-20 cavities most probably show a splitting of the modes, which can be related to the evanescent coupling between cavities, and this splitting can be easily changed with the barrier thickness. Unfortunately, coupling tests with the tapered fiber have shown that the coupling is harder to achieve in this configuration since the angle between the fiber and the waveguide becomes critical. The tapered fiber needs to be parallel to the whole waveguide (which is 50 μm-long) while in the case of L3 cavities the fiber only needs to be parallel to the cavity ($\sim$ 1.5 μm-long).

In general, L3-type cavities (fig. 8.1) are much easier to couple with the tapered fiber compared to Noda-type cavities. Moreover, they are separated away in the direction perpendicular to the fiber, which is a necessary condition to guarantee a symmetric injection, mandatory for symmetry breaking experiments. For all these reasons, we have chosen this configuration to work with. Samples with two L3 cavities separated away by three and five rows of holes were fabricated. In the following we give a detailed characterization of these samples.

8.3 Photoluminescence of two cavities

The samples are analogue to the ones described in section 5.7 but, in this case, two L3 cavities are etched in the same PhC. As mentioned before, we incorporate 4 QWs as the active medium in order to increase the nonlinear response. Two different barrier thickness were studied: i) two L3 cavities separated away by three rows of holes in the $\Gamma - M$ direction and ii) five rows of holes. The $\Gamma - M$ direction corresponds to the direction perpendicular to the long axis of the cavity. MEB images of these two cases, i and ii, are shown in fig. 8.5.a and b, respectively.

The first natural characterisation of the samples are photoluminescence measurements, as presented in the previous sections. For this, the cavities are pumped with a @810 nm, 80 MHz-repetition rate, 100 fs-pulse duration Ti:Sa source. The emission is collected with a 50

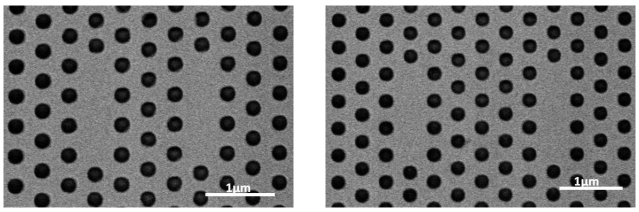

(a) (b)

Figure 8.5: *MEB images of samples with two L3 cavities separated away by three (a) and five (b) rows of holes in the $\Gamma - M$ direction. The period and hole radius are: a=450 nm and r=120 nm.*

x microscope objective and sent to a spectrometer, see sec. 3.1.3. Fig. 8.6.a and b show the spectrum obtained for the cavities separated away by 3 and 5 rows of holes, respectively. For a separation of three periods (fig. 8.6.b) we observe two peaks ($\lambda_<$ and $\lambda_>$) whose spectral separation is about 4 nm, in good agreement with the numerical simulations of section 7.1. Increasing the period number (p=5) only one peak is observed, meaning that either the coupling is weak, then the distance between the modes is smaller than the resonance width; or the cavities are not coupled at all. We will continue this discussion in the following sections.

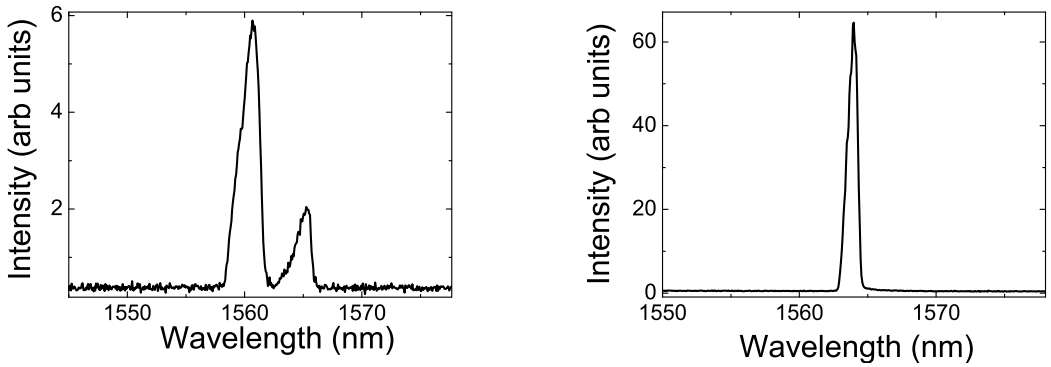

(a) (b)

Figure 8.6: *Photoluminescence spectrum of two L3 cavities separated away by three (a) and five (b) rows of holes, fig. 8.5.a and b. The injected power and integration time are: 30 μW and 0.2 s; 9 μW and 0.5 s, respectively.*

It is worth mentioning that PhCs with two L3 cavities separated away by one row of holes have also been fabricated and characterized. Photoluminescence measurements of this system show a mode splitting of $\sim$ 70 nm. This splitting is more than 140 times the FWHM of the cavity resonance and can be the signature of a very strong coupling regime, for which we cannot longer consider the coupling as a perturbation of each cavity. Therefore, the two cavities become a single one with a particular geometry. For this reason, in the following we will focus on the cavities separated by 3 and 5 rows of holes.

Measurements of the output intensity and the resonance width as a function of the pump power were carried out (not shown), in order to study the laser effect in i) and ii) (figs. 8.5.a and b, respectively). In the case of the cavities separated away three rows of holes, curves with similar features than in fig. 5.10 were obtained for both modes. Indeed, we arrive to the same three possibilities discussed in section 5.7. On the contrary, for the cavities separated away by

five rows of holes, a S-shape in the curve input vs output power and a decrease followed by an increase of the resonance width with the injected power were observed. Indeed, there is the possibility that the system shows a laser effect with a threshold at 8.5 μW. Second order correlation function should be performed in order to confirm this hypothesis.

The microfiber allows a nice method to further investigate the optical coupling between the cavities. In particular, the collection of the photoluminescence using the tapered fiber should be sensitive to the phase difference between the cavity fields. As it has been discussed in section 7.3, if the taper is positioned in the middle of the cavities, the anti-symmetric mode cannot be coupled through the fiber due to destructive interference. In order to test this experimentally, measurements of the coupling of photoluminescence of the $\lambda_<$ and $\lambda_>$ modes through the fiber were carried out for the sample with 3-holes barrier. The cavities are pumped by the surface and the fiber is positioned between them. The emission signal is simultaneously collected in free space and sent to the spectrometer and through the tapered fiber and sent to an optical spectrum analyser (OSA). Fig. 8.7.a and b show the two spectra. We observe a difference in the relative heights of the peaks in fig. 8.7.a and b. We stress that this difference was systematically observed, provided the fiber is positioned in the middle of the cavities. This result provides further evidence on the fact that the mode at higher wavelengths corresponds to the antisymmetric mode.

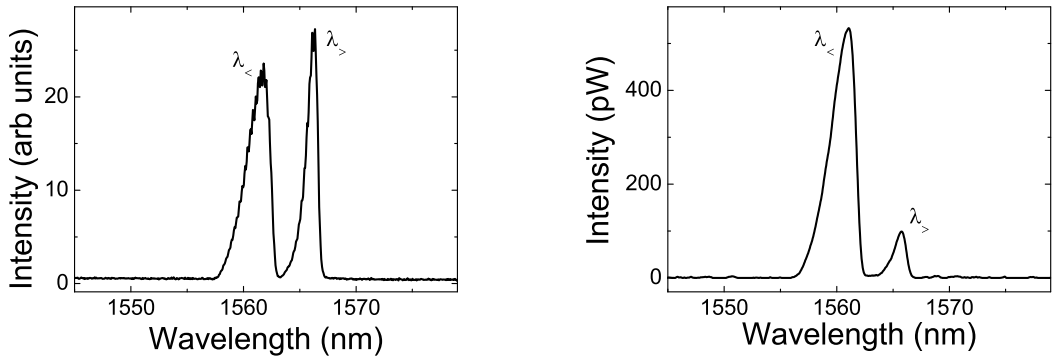

Figure 8.7: *Spectrum of the two L3 cavities separated away by 3 rows of holes measured in free space (a) and through the tapered fiber (b). Note the decrease of the relative height of the second peak in (b) respect to (a), consistent with the fact that the second mode corresponds to the antisymmetric mode. The pump power is 41 μW, the integration time in (a) is 0.5 s and the resolution in (b) is 0.05 nm.*

8.4 Emission profile of the coupled cavities

While building confidence in an optical coupling scenario, the previous experimental tests cannot be consider as experimental demonstration of mode coupling by themselves. Here we will seek a clear signature of mode coupling through the direct measurement of the symmetric and antisymmetric far field mode profiles. We will take advantage of the qualitative differences between the emission profile of the symmetric and antisymmetric modes to determine the existence of coupling between the cavities. According to the simulations of section 7.1, the emission angle is strong ($\sim 70°$). Therefore, in order to collect the intensity emitted by the sample, an objec-

tive with a high numerical aperture (NA) is used: a x160, NA=0.94, objective with 0.2 mm of working distance, which focuses the pump beam down to 1.5 μm. This microscope objective allows to collect angles up to 72°. The sample is pumped by the surface with the @ 810 nm, 100-fs pump duration, Ti:Sa laser. The emission is collected through the same optics and sent to a spectrometer and to an InGaAs CCD ('Sensor Unlimited', SU320), as sketched in fig. 8.8. Focusing down the signal emitted by the sample over the InGaAs camera the near field emission is obtained, while the far field emission is given by the image of the back focal plane of the objective (which is located near the back pupil of the objective). In the experimental set up we obtain the far field images by adding a lens behind the objective (f1 in fig. 8.8). This lens is located at a distance $f1$, which corresponds to its focal distance, of the back focal plane of the objective.

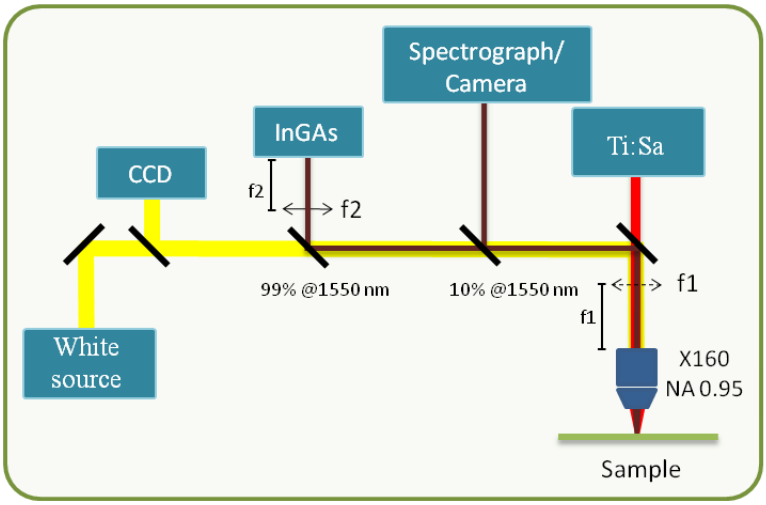

Figure 8.8: *Sketch of the device used to measure the near and far field emission profiles of the samples by either removing or adding f1.* $f1 = f2 = 250$ *mm.*

8.4.1 Emission profile of a single cavity

Let us start by characterizing the emission of a single cavity. The measured far field emission of the sample and the calculated far field using the FDTD (see section 2.1) are shown in fig. 8.9.a and b, respectively. The white line corresponds to the light cone (emission at 90°) while the dashed white line corresponds to the maximum angle collected in our set up ($\sim 72°$). Note that part of the main lobes (fig. 8.9.b) are cut by the NA of the objective. In spite of this, two lobes in the vertical direction can be distinguished, in very good agreement with the numerical results. Fig. 8.9.c and d show the near field emission and the photoluminescence spectrum, respectively. The dashed white line in fig. 8.9.c represents the cavity position and it allows to check that the near field emission is located at the cavity center. Finally, fig. 8.9.e shows the near field emission found by the FDTD simulations. Only the principal component of the electromagnetic field is represented: the electric field polarized in the y-direction (E_y). It is worth mentioning that, as the objective presents a high numerical aperture and a short working distance, the position of the focus becomes very sensitive. For this reason, it is very difficult to track the actual near field profile, which is highly dependent on the distance to the focal plane. In the following, although we will present the near field measurements, we will focus our attention on the far field measurements. They are much less sensitive to the alignment with re-

spect to the focal plane, and contain the information about the relative phase of the cavity fields.

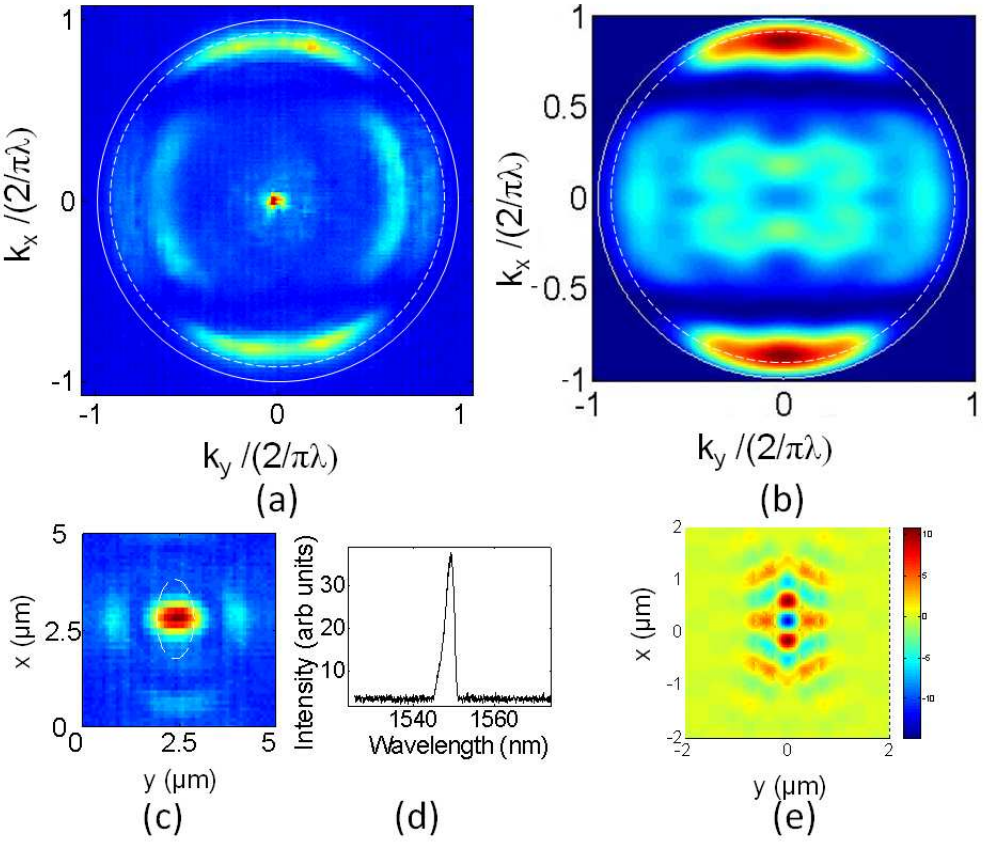

Figure 8.9: *Experimental (a) and numerical (b) (provided by FDTD simulations) far field emission profiles of a single L3 cavity. The white line in both figures corresponds to an emission at* 90° *while the dashed white line corresponds to the maximum angle collected in our set up (*$\sim$ 72°*). (c)-(d) Experimental near field emission and photoluminescence spectrum (for an injected power of 38* μW *and 0.2 s of integration time). (e) Numerical near field profile of a single L3 cavity.*

The bright point in the center of the image in fig. 8.9.a corresponds to the luminescence of the QW that is not being filtered by the cavity mode, since it is observed even when pumping outside of the cavity region. This emission propagates as a plane wave which corresponds to the origin of the Fourier space.

8.4.2 Near and Far Field images of two L3 cavities separated away by 3 rows of holes

Three different situations associated to the pumping conditions can be tested in the case of two cavities separated away by three rows of holes (fig. 8.5.b): I) pumping the "left" cavity, II) pumping in the middle, III) pumping the "right" cavity, as sketched in fig. 8.10. In situations I and III a single peak is observed, while for II, two peaks separated away by 4 nm are obtained, fig. 8.10.

Fig. 8.11.a and b show the far field emission for I and III, respectively. Note the similarities with the far field emission of a single cavity. Furthermore, the near field emission in both

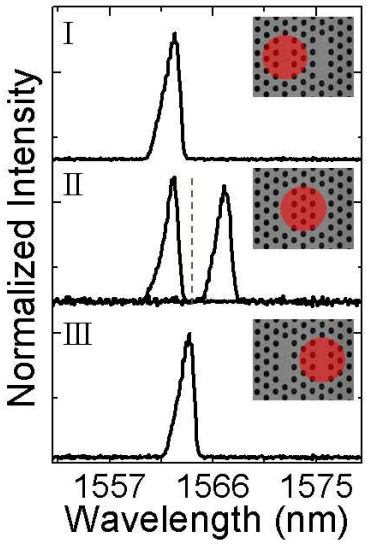

Figure 8.10: *Photoluminescence spectrum acquired for different pump localization (inset) for two L3 cavities separated away by three rows of holes. The dashed line denotes the cut off wavelength of a bandpass filter used to characterize the emission of each mode separately.*

situations shows that the intensity is more concentrated in one of the cavities than in the other one. Fig. 8.11.d shows the corresponding spectra, in black and red lines, for situations I and III, respectively. We observe a slight difference in the central wavelength. However, the actual spectral separation is hard to establish since the resonance wavelength depends on the intensity, hence on the focus. The fact that only one peak in the spectrum is observed shows that only one mode is effectively being excited. In the following section we will come back to this discussion.

On the other hand, when the two cavities are pumped in between, two modes are observed with an spectral separation of 4 nm (fig. 8.10.II). In these conditions we placed a bandpass filter before the spectrograph and the InGaAs CCD in order to selectively detect one of the two modes. Fig. 8.12.a shows the far field emission of the mode at lower wavelength; we will call this mode $\lambda_<$. According to the numerical simulations of section 7.1, this mode should be the symmetric one. Fig. 8.12.b shows the far field emission of the symmetric mode calculated by FDTD simulations. Fig. 8.12.c and d show the near field and the photoluminescence spectrum of this mode. Note that both cavities are "turned on", in agreement with the near field found in the simulations of the symmetric mode (fig. 8.12.e). We attribute the differences in the features on figs. 8.12.c and e to the focal issues already mentioned. We note some similarities between the far field of $\lambda_<$ and the one of the symmetric mode, 8.12.a and b, respectively. However, since both the far field emission of the symmetric mode and of a single cavity present two lobes, it is difficult to qualitatively distinguish between these two cases. The spectral separation between modes ($\sim$ 4 nm) is in good agreement with the value found trough numerical simulations for the separation between the symmetric and antisymmetric modes of coupled cavities. This strongly suggest that the symmetric mode is the one being excited.

Selecting only the mode at higher wavelengths ($\lambda_>$, see fig. 8.6.b), we observe a qualitatively different far field emission. Fig. 8.13.a and b show the far field emission of $\lambda_>$ and the

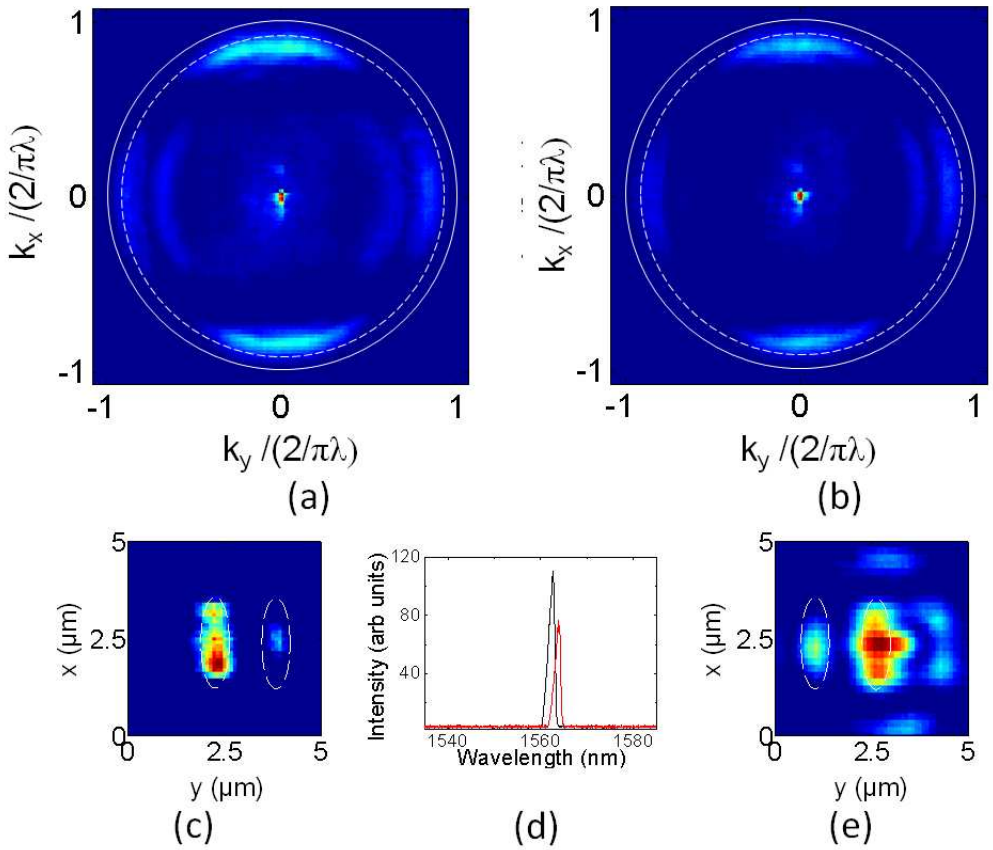

Figure 8.11: *(a)-(b) Experimental far field emission profile of two L3 cavities separated away by three rows of holes when pumping the left and right cavity, respectively. (c) Experimental near field emission while pumping the left cavity. (d) Photoluminescence spectrum (for an injected power of 24 μW and 0.2 s of integration time) when pumping the left (black line) and right (red line) cavity. (e) Experimental near field emission when pumping the right cavity.*

one of the anti-symmetric mode obtained by FDTD simulations. Note the excellent agreement between these two images. Fig. 8.13.c and d show the near field and the photoluminescence spectrum of this mode. Note that both cavities are emitting, in agreement with the simulations of the anti-symmetric mode (fig. 8.12.e). Indeed, looking at fig. 8.13.a and c and considering the fact that $\lambda_>$ is at higher wavelengths, we conclude that this mode corresponds to the anti-symmetric mode of two coupled cavities. The fingerprints of optical coupling are clearly contained in the far field of the antisymmetric mode.

8.4.3 Near and far field images of two L3 cavities separated away by 5 rows of holes

In the case of two cavities separated away by 5 rows of holes, as in the previous case, we can test three different situations: I) pumping the "left" cavity, II) pumping in the middle, III) pumping the "right" cavity, as sketched in fig. 8.14. In I and III a single peak is observed, while for II two overlapping peaks are obtained, fig. 8.14.

Fig. 8.15.a and b show the far field emission for I and III, respectively. The near field

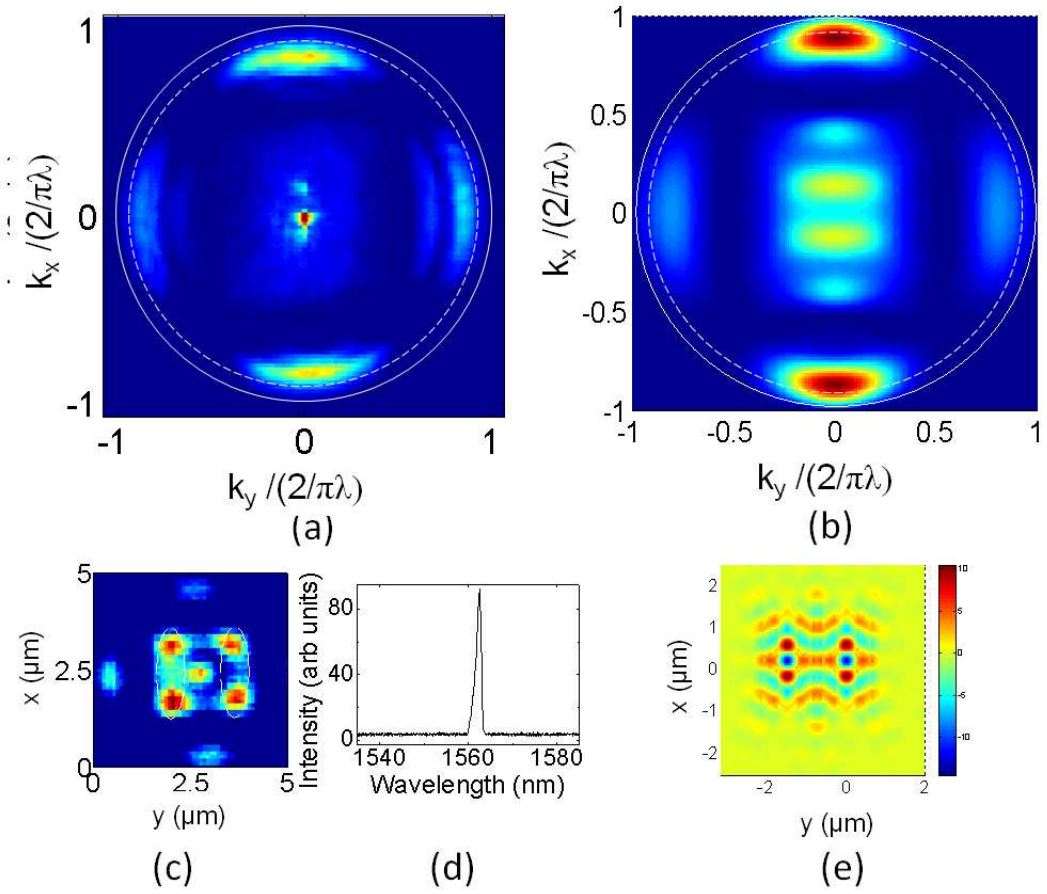

Figure 8.12: *Experimental far field emission profiles of two L3 cavities separated by 3 rows of holes when pumping in the middle and collecting only the emission of the mode at lower wavelength ($\lambda_<$, fig. 8.6.a). (b) Numerical (provided by FDTD simulations) far field emission of the symmetric mode of coupled cavities. (c)-(d) Experimental near field emission and photoluminescence spectrum (for an injected power of 100 μW and 0.2 s of integration time). (e) Numerical calculations of the near field of the symmetric mode.*

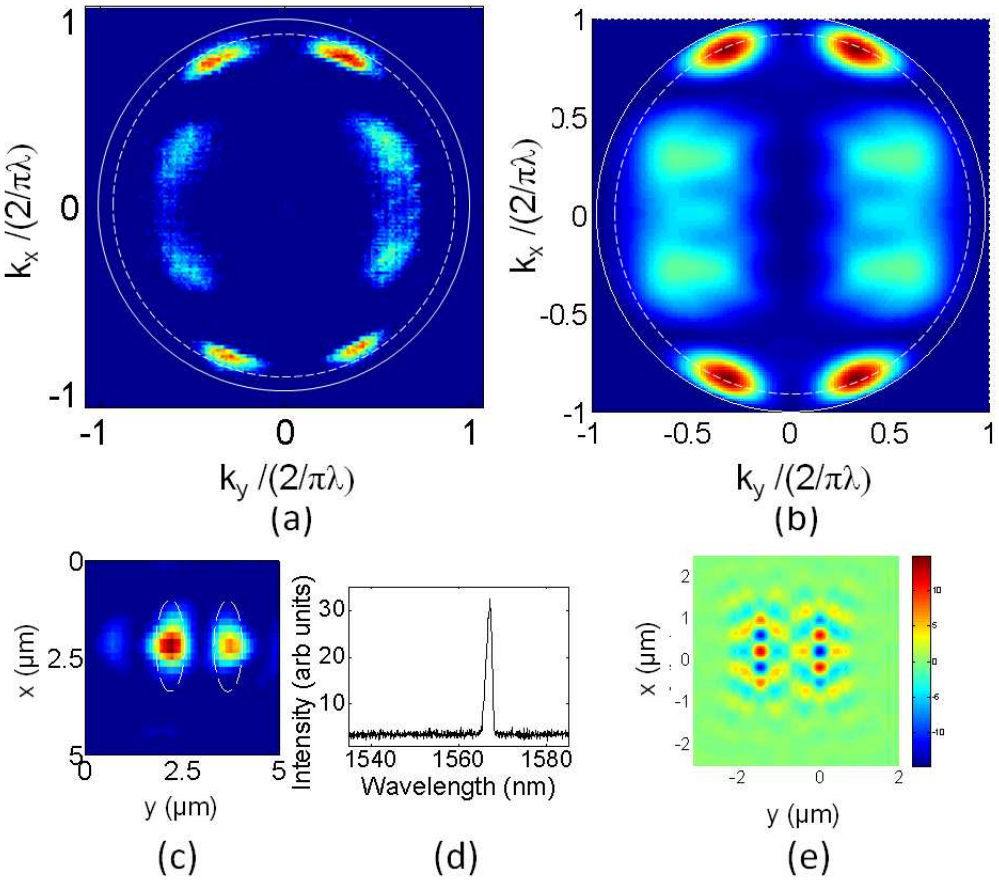

Figure 8.13: *Experimental far field emission profile of two L3 cavities separated by 3 rows of holes when pumping in the middle and collecting only the emission of the mode at higher wavelength ($\lambda_>$, fig. 8.6.a). (b) Numerical (provided by FDTD simulations) far field emission of the antisymmetric mode of coupled cavities. (c)-(d) Experimental near field emission and photoluminescence spectrum (for an injected power of 47 μW and 0.2 s of integration time). (e) Numerical calculations of the near field of the antisymmetric mode.*

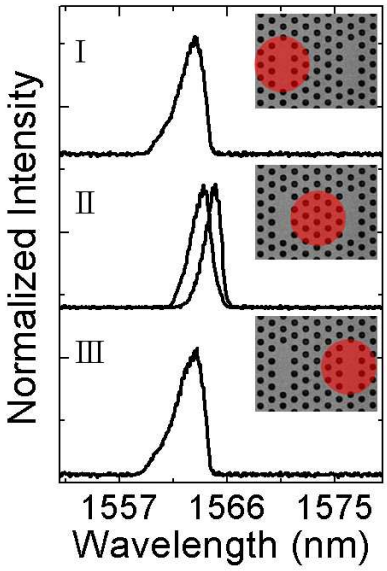

Figure 8.14: *Photoluminescence spectrum for different pump localizations (inset) for two L3 cavities separated away by five rows of holes. Note that also in this case two modes are observed in II.*

emission for I and III is plotted in figs. 8.15.c and e, respectively, while fig. 8.15.d shows the spectra of both configurations (I in black line and III in red line). The overlap of the both resonances is clearly observed. As in the case of fig. 8.11, only one mode is being excited. In the following section we will discuss the origin of the suppression of the second mode when the pump beams excites only one cavity.

Pumping the system in the center, at high powers, two modes are observed separated away by ~ 1 nm, see fig. 8.14.II. The spectral separation between them is shorter than their width which makes them difficult to collect separately. Even more, the spectrum oscillates between these two modes constantly: a mode competition takes place. The emission profile also oscillates between two different patterns. Fig. 8.16.a shows the far field emission while maximizing the signal of the mode at lower wavelengths. In order to compare this result with the theory, FDTD numerical simulations as the ones depicted in section 8.11 were carried out for two L3 cavities separated away by 5 rows of holes. This simulation shows the symmetric mode centered at $\lambda_S = 1599.3$ nm with a quality factor of $Q_S = 23300$ and the antisymmetric mode center at $\lambda_A = 1600$ nm with $Q_A = 28000$. Fig. 8.16.b shows the far field emission found in this simulation for the symmetric mode. Note the similarities between fig. 8.16.a and b. The experimental near field of this mode is plotted in fig. 8.16.c: both cavities are "turned on", in agreement with the near field found in the simulations (fig. 8.16.d). All these observations indicate that the $\lambda_<$-mode indeed corresponds to the symmetric one. We will return to this discussion in the next section.

Furthermore, the far field emission obtained by maximizing the signal of the mode at higher wavelengths, fig. 8.17.a, is in good agreement with the far field found in the numerical simulations for the antisymmetric mode, fig. 8.17.b. In addition, the near field emission, fig. 8.17.c, shows the intensity delocalized in both cavities as in the numerical simulations, fig. 8.17.e.

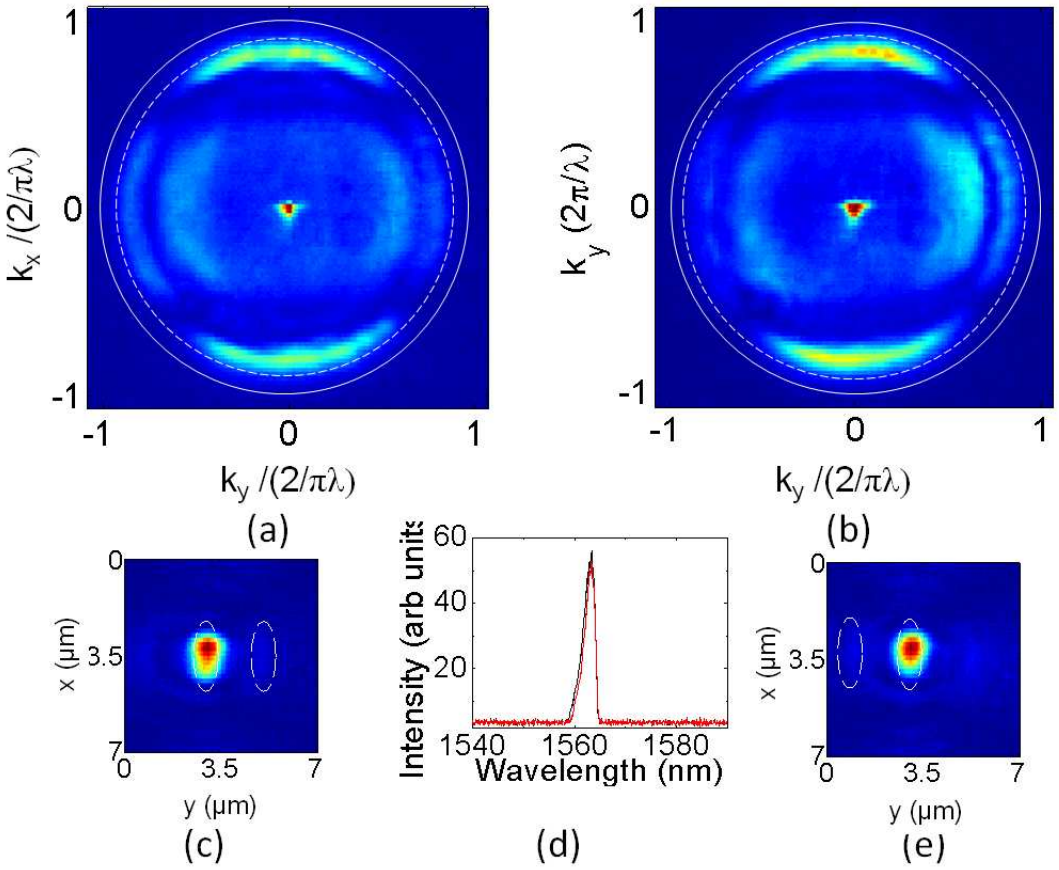

Figure 8.15: *(a)-(b) Experimental far field emission profile of two L3 cavities separated away by five rows of holes when pumping the left and right cavity, respectively. (c) Experimental near field emission while pumping the left cavity. (d) Photoluminescence spectrum (for an injected power of 47 μW and 0.2 s of integration time) when pumping the left (black line) and right (red line) cavity. (e) Experimental near field emission when pumping the right cavity.*

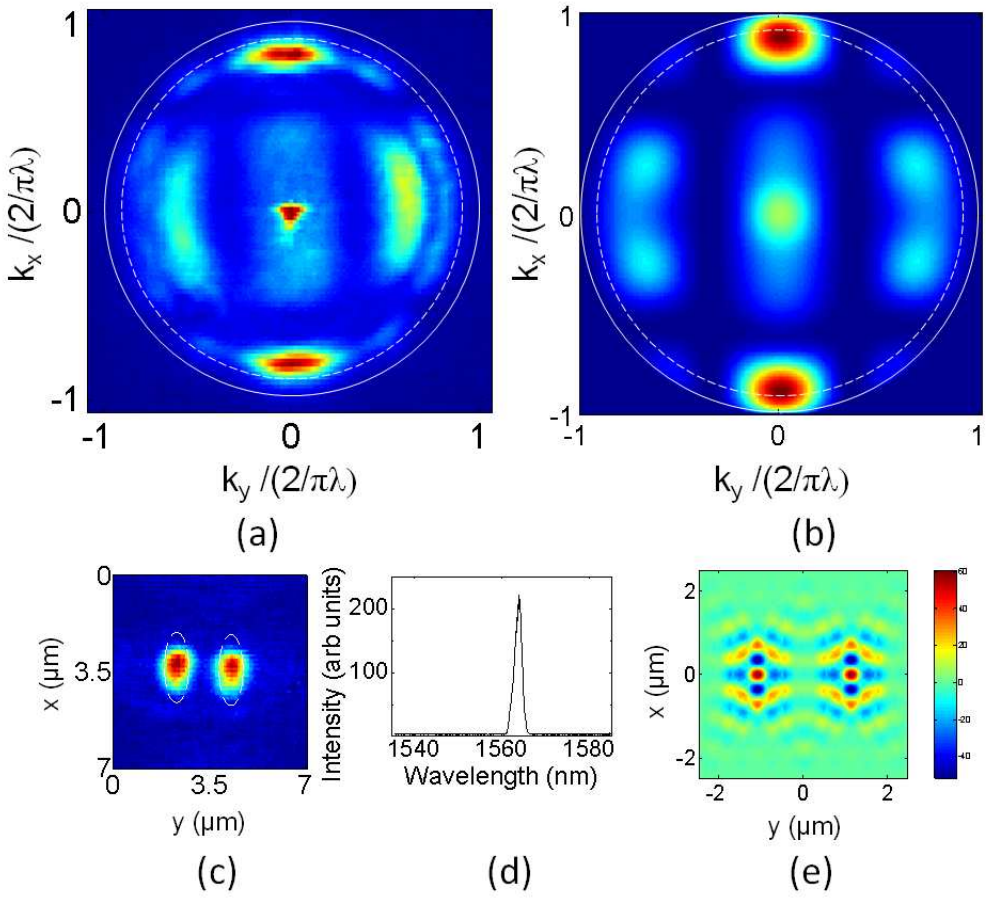

Figure 8.16: *(a) Experimental far field emission profile of two L3 cavities separated by 5 rows of holes when pumping in the middle and maximizing the emission of the mode at lower wavelength. (b) Numerical (provided by FDTD simulations) far field emission of the symmetric mode of coupled cavities. (c)-(d) Experimental near field emission and photoluminescence spectrum (for an injected power of 140 μW and 0.2 s of integration time). (e) Numerical calculations of the near field of the symmetric mode.*

The excellent agreement between figs. 8.17.a and b and the fact that this mode is red-shifted respect to the cavity mode (fig. 8.17.d) lead us to conclude that this $\lambda_>$-mode indeed corresponds to the antisymmetric mode of the coupled cavity system.

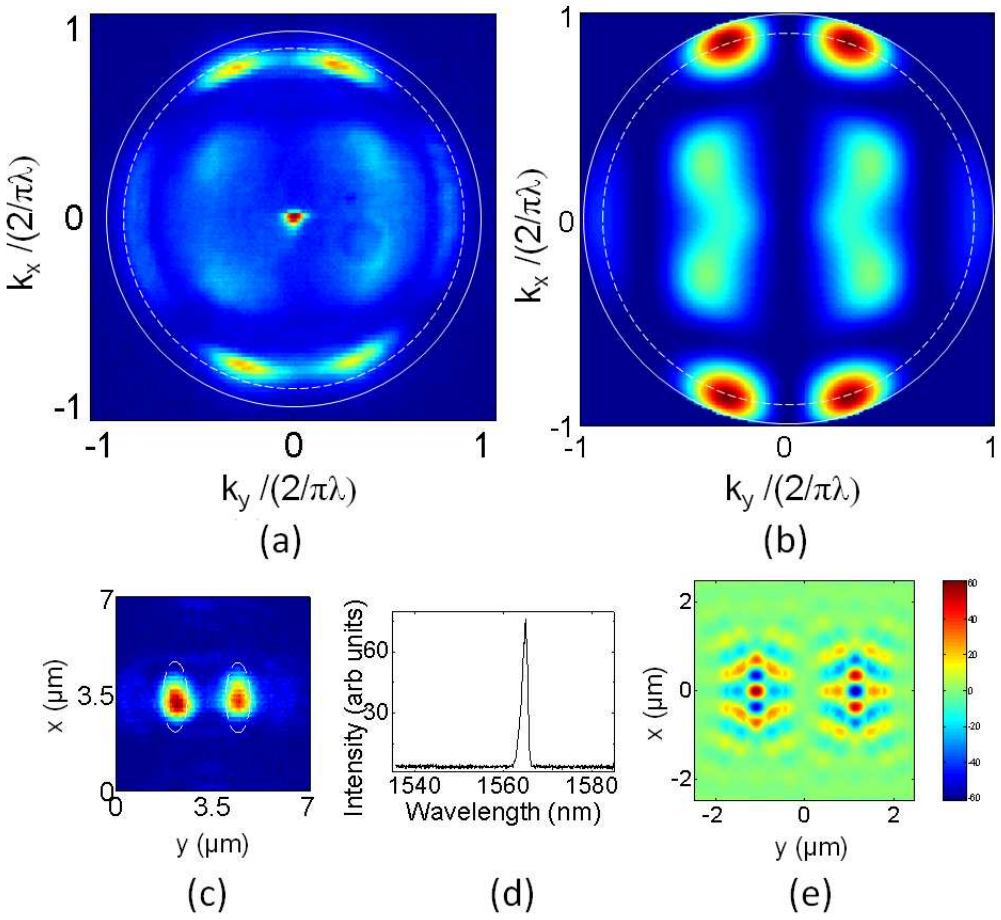

Figure 8.17: *(a) Experimental far field emission profile of two L3 cavity separated by 5 rows of holes when pumping in the middle and maximizing the emission of the mode at higher wavelength. (b) Numerical (provided by FDTD simulations) far field emission of the antisymmetric mode of coupled cavities. (c)-(d) Experimental near field emission and photoluminescence spectrum (for an injected power of 140 μW and 0.2 s of integration time). (e) Numerical calculations of the near field of the antisymmetric mode.*

8.4.4 Discussion

In the previous paragraphs the near and far field emissions of two L3 cavities in a same photonic crystal separated away by three (p=3) or five (p=5) rows of holes were measured. In order to compare the images found through numerical simulations and the experimental ones, we have measured the FWHM of the lobes observed in the images. For this, we measured the intensity profile along a circle concentric with the image, whose radius corresponds to the maximum of intensity of the lobe. Fig. 8.18.a and b show the measurement of the lobe width.

Table 8.1 summarizes the theoretical and experimental lobe widths for the different pump

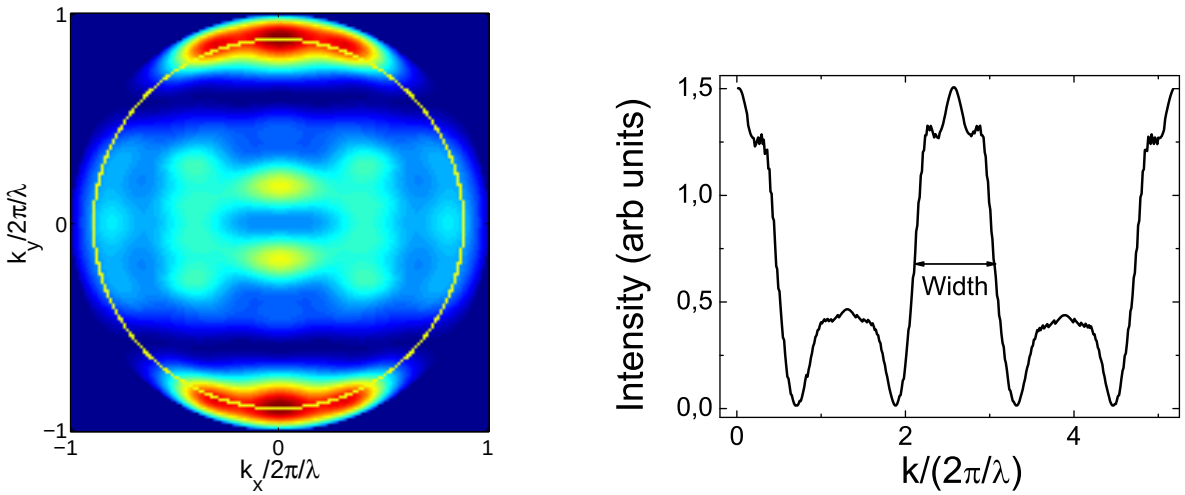

Figure 8.18: *(a) Image of the far field emission profile for a single cavity found through FDTD numerical simulations. The yellow line corresponds to the circle for which the intensity profile was obtained in order to measured the lobe width. (b) Intensity profile corresponding to the yellow line in (a).*

configurations. The difference between the lobe width of the theoretical and experimental image for a single cavity may be due to the numerical aperture of the objective which cuts the lobes in the latter. For coupled cavities, let us first focus on the $\lambda_<$-mode. In the experimental case, for p=3, no significant differences are observed between the lobes width while pumping the left, the right cavity, and in the middle. This would indicate that, in all these cases, the same mode is being observed. Moreover, this lobe width is smaller than the width of the lobe of a single cavity and it is in good agreement with the theoretical width of the symmetric mode. This indicates that it would correspond to the bonding mode in nonidentical coupled cavities due to the asymmetrical pumping; we will return to this discussion in the following paragraphs. However, in the experimental case for p=5, a strong difference between the case where the pump is centered in one of the cavities and the case where it is centered in the middle is observed. Even more, in the first case the lobe width is close to the one found for a single cavity. Hence, the bonding mode is only observed when the pump is centered between the cavities for p=5, and this turns out to be the symmetric mode. Let us stress the agreement between the theoretical and experimental values, both for p=3 and p=5, in the centered pumping configurations. For p=5, even stronger similarities are observed for the $\lambda_>$-mode. The difference between the lobes width in the theoretical and experimental images for p=3, in the case of the antisymmetric mode, may be due to the numerical aperture of the objective. As the two cavities are closer for p=3 than for p=5, the angular separation between the two maxima in the y-direction becomes larger, and thus, the NA becomes more critical.

In order to understand the absence of the $\lambda_>$-mode when the pump in centered over one cavity, the impact of an asymmetry between the cavities induced by the pump was investigated. First of all, pumping one of the cavities reduces its absorption inducing a difference in the quality factor with respect to the other one. However, we have estimated that this absorption-saturation effect induces a change in the quality factors of about a factor 2; and we have verified that this difference does not significantly affect the coupling. On the other hand, we have also observed that

						
			$\lambda_<$	$\lambda_<$	$\lambda_<$	$\lambda_>$
L3 single	Theoretical	0.9				
	Experimental	0.7				
L3 Coupled p=3	Theoretical				0.5	0.4
	Experimental		0.6	0.5	0.5	0.2
L3 Coupled p=5	Theoretical				0.3	0.3
	Experimental		0.8	0.7	0.3	0.3

Table 8.1: *Comparison between the lobe widths of the theoretical and experimental far field emission profile images, in units of $k/(2\pi/\lambda)$, for the different samples and pump configurations. the agreement theoretical/experimental is very good in all the cases except: the experimental width of $\lambda_>$-mode for p=3, which may be due to a cut off effect of the NA; and the lobe widths of $\lambda_<$-mode, which indicates that the energy is mostly localized in one cavity.*

the pump induces a frequency blue-shift. This shift may be important, according to the results of chapter 5: the linear resonance obtained with the tapered fiber is systematically red-shifted of about ~ 6 nm with respect to the resonance measured in photoluminescence experiments. This shift leads to a difference in the resonance frequency of each cavity. This difference may not be as high as ~ 6 nm when pumping one of the cavities, since some of the carriers excited by the pump reach the second cavity by diffusion, but it may still be important. In order to study the coupling between the cavities when such difference is induced, the frequencies of the hybrid modes and their amplitudes were calculated as a function of the frequency difference between the cavities. Within this aim, we have computed the eigenvalues and eigenvectors of the following system:

$$\begin{aligned} \frac{da_1}{dt} &= (i\tau\omega_1 - 1)a_1 + \tau\gamma a_2 + i\tau\kappa a_2 \\ \frac{da_2}{dt} &= (i\tau\omega_2 - 1)a_2 + \tau\gamma a_1 + i\tau\kappa a_1 \end{aligned} \tag{8.1}$$

Two eigenmodes are obtained from eq. 8.1: a mode for which the phase difference between the cavities is zero, usually called bonding (with wavelength λ_0), and one with a phase difference of π, called anti-bonding (with wavelength λ_π). These modes become the syummetric ($\lambda_0 = \lambda_S$) and antisymmetric ($\lambda_\pi = \lambda_A$) as far as the system is symmetric, i.e. $\lambda_1 = \lambda_2$. Fig. 8.19.a shows λ_π and λ_0 as a function of the difference of the resonance wavelengths for p=3. For this situation we set the parameters $\tau\kappa = 10$ and $\tau\gamma = -0.3$ as it will be deduced in the next chapter. Let us assume that only the cavity 2 is pumped, hence $a_1(t=0) = 0$ and $a_2(t=0) = 1$ and $\lambda_2 < \lambda_1$ due to the pumping induced blue-shift. We define the energy in each cavity as:

$$E_{1,2} = \int_0^\infty |a_{1,2}|^2 dt \tag{8.2}$$

and

$$\begin{pmatrix} a_1(t) \\ a_2(t) \end{pmatrix} = C_0 \overrightarrow{v_0} e^{i\Omega_0 t} + C_\pi \overrightarrow{v_\pi} e^{i\Omega_\pi t} \tag{8.3}$$

where $\overrightarrow{v_{0,\pi}}$ is the bonding (anti-bonding) eigenvector. The energy transfer (E_1/E_2) between the second cavity and the first one, and the ratio of the bonding (C_0) to the anti-bonding (C_π) modes are plotted in fig. 8.19.b as a function of the $\lambda_2 - \lambda_1$. In the case $\lambda_1 - \lambda_2$=4 nm, less than half of the intensity is being transferred and the bonding mode is excited a factor 5 more

than the anti-bonding mode. This may be the reason why we observed more intensity in one of the cavities and, in the spectrum, only the bonding mode is being observed.

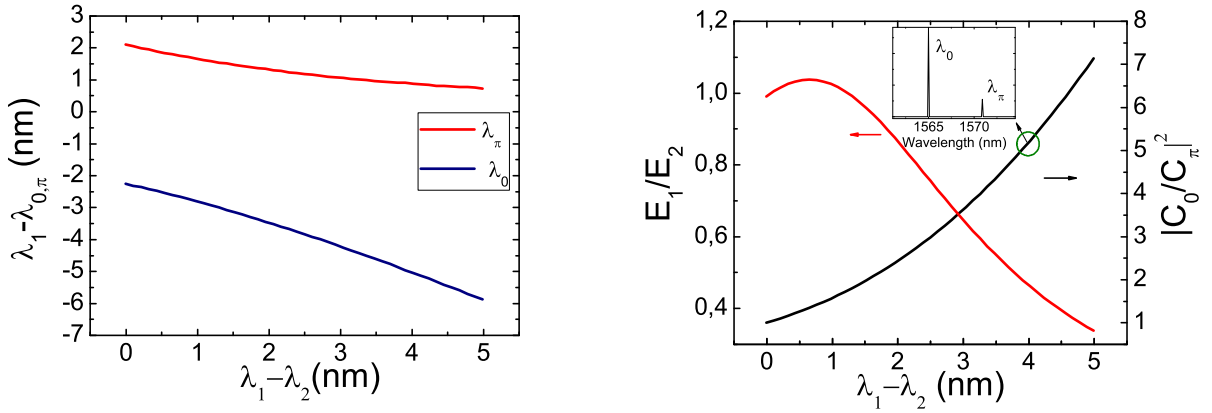

(a) (b)

Figure 8.19: *(a) Wavelength of the bonding (λ_0) and anti-bonding (λ_π) mode as a function of the difference between the resonance wavelength of each cavity ($\lambda_1 - \lambda_2$) for p=3. (b) Energy transfer between the excited cavity (E_2) and the other one (E_1) and ratio of the amplitudes of the bonging and anti-bonging modes as a function of $\lambda_1 - \lambda_2$.*

The wavelength of the bonding (λ_0) and anti-bonding (λ_π) modes are plotted in fig. 8.20 as a function of the difference of the resonance wavelengths for p=5 (which gives $\tau\kappa = 2.5$ and $\tau\gamma = -0.014$ as we will see in the next chapter). We observed that for $\lambda_1 - \lambda_2$=4 nm λ_0 and λ_π approach the values of the resonance wavelengths of each cavity, meaning the energy is strongly localized in one of the cavities. This is shown in fig. 8.20 where the energy transfer (E_1/E_2) between the second cavity (the one excited) and the first one, and the ratio of amplitudes of the bonding and anti-bonding modes are plotted as a function of $\lambda_1 - \lambda_2$. For $\lambda_1 - \lambda_2$=4 nm only 3% of the energy is being transferred from the excited cavity to the other and the bonding mode is excited 50 times more than the anti-bonding one. This is the reason why the anti-bonding mode is not observed when only one cavity is pumped. Indeed, since the energy is highly concentrated in one of the cavities the far field emission profile is essentially equivalent to the one of a single cavity.

8.5 Conclusion

The evanescent coupling between cavities has been studied in different systems using different methods. Through statistical analysis of the resonance position in two L3 cavities separated away by three rows of holes in the $\Gamma - M$ direction, we found an averaged (for different hole radius) mode splitting of ~ 5 nm which is a first, but not conclusive, evidence of coupling. Studies on the photoluminescence spectrum of Noda-type cavities separated away by 2, 3, 4, 5 and 20 periods showed the dependence of the mode splitting with the barrier thickness, in good agreement with the theory. This provides further evidence pointing to splitted modes rather than non-interacting cavities.

We decided to work with L3-types cavities separated away by three and five rows, mainly because they are easier to inject through the tapered fiber. By means of photoluminescence

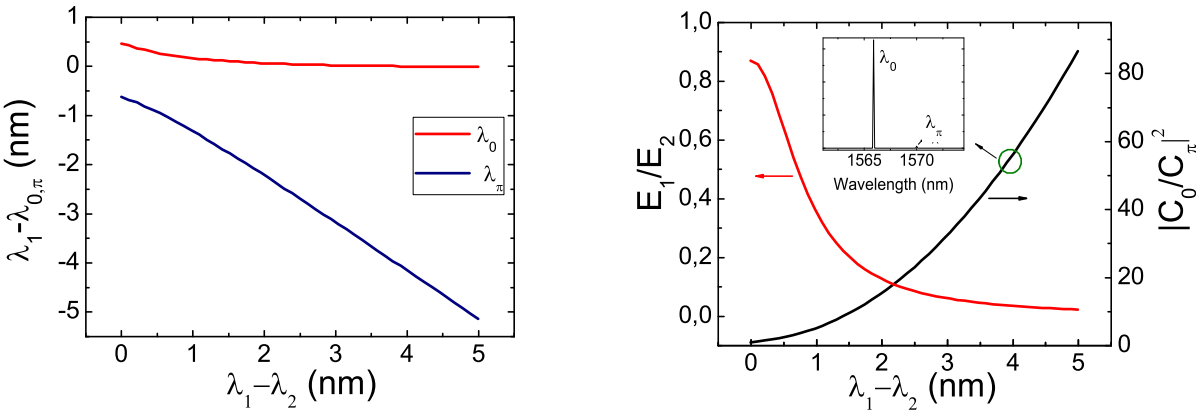

Figure 8.20: *(a) Wavelength of the symmetric (λ_S) and antisymmetric (λ_A) mode as a function of the difference between the resonance wavelength of each cavity ($\lambda_1 - \lambda_2$) for p=5. (b) Energy transfer between the cavity (E_2) that is excited and the other (E_1) and ratio of the amplitudes of the bonging and anti-bonging modes as a function of $\lambda_1 - \lambda_2$.*

measurements, we observed, for p=3 and around $\lambda \sim 1565$ nm, two modes separated by ~ 4 nm. Experiments of photoluminescence collected with the tapered fiber have shown a difference in the relative height of the modes measured in free space and through the tapered fiber. The amplitude of the second peak was systematically smaller than that of the first one. This is expected for the antisymmetric mode, since, as the fields in each cavity are in anti-phase they cannot couple to the same port (in the case of the fiber located in the middle of the cavities). This is a further result allowing to build confidence on the evanescently coupled cavities scenario.

In order to provide a clear experimental signature of coupling, near and far field emission profiles were measured using an InGaAs CCD and a high NA objective. Far field emission profiles of a single cavity were studied and an excellent agreement between experimental and simulated results has been obtained. Analyzing the far field emission, when pumping in the middle of the cavities, two modes are observed separated away by 4 nm. Collecting only the mode at higher wavelength, the far field emission profile presents a minimum of intensity in the center ($k_y = 0$), in good agreement with the far field emission pattern of two cavities emitting with a phase different of π. Therefore, we conclude that this mode corresponds to the antisymmetric mode of coupled cavities. This constitutes concluding evidence of evanescent coupling. Different analysis were implemented in order to study the origin of the mode observed when the pump is centered in one of the cavities: i) the comparison of the width of the lobes observed in the experimental and simulated images; and ii) the analysis of the eigenvalues and eigenvectors of the system in presence of a difference in the resonance frequency of each cavity. We have found that, when pumping one of the cavities, a pump-induced blue shift externally breaks the symmetry, making the bonding mode significantly more excited than the anti-bonding one. Moreover, this asymmetry leads to a strong localization of the energy in the cavity that is being pumped. In conclusion, when the pump is centered in one of the cavities, the dominating mode is the bonding one. This effect is particularly enhanced in the case of p=5: the coupling becomes negligible and the excited mode almost corresponds to the one of the cavity that is being excited.

The analysis of the near and far field emission profile to determine the coupling between

resonators is commonly used in optics. However, this type of analysis has never been reported in PhC cavities, perhaps due to collection issues. To our knowledge, the results presented, together with previous anticrossing measurements [79], are the only conclusive demonstrations of optical coupling in PhC cavities.

In the following chapter we apply our system to the study of nonlinear dynamics in PhC coupled nanocavities.

Chapter 9

Towards experimental demonstration of spontaneous symmetry breaking

In this section we present nonlinear dynamical measurements performed in the samples of coupled cavities described in section 8.6. Systematic studies are carried out only for the cavities separated away by 3 rows of holes. In this case, modes are clearly splitted allowing us to study the optical response for injection wavelengths near each resonance. In the last part of this chapter, we relate the experimental results to the the theory developed in section 7.2.

9.1 Nonlinear dynamics in two L3 cavities separated away by five rows of holes

In order to study the spontaneous symmetry breaking in evanescently coupled cavities, the hysteresis cycles are studied since, according to section 7.3.2 they can be distinguished from bistability of a single cavity.

In the case of cavities separated away by five rows of holes, measurements of nonlinear dynamical regimes give behaviors comparable to the ones found in chapter 6, section 6, for a single cavity. It is worth mentioning that, since the cavities are separated away $\sim 2.4\ \mu m$, which is approximately the fiber width, simultaneously coupling both cavities with the fiber is quite difficult. Moreover, a symmetrical injection is not guaranteed. Even though, placing the fiber above one of the cavities, one mode is observed. For this mode we observed bistability, excitability and self-pulsing regimes but without any evidence of symmetry breaking. Most probably, this may be due to the fact that the injection is not symmetric in this case.

9.2 Nonlinear dynamics in two L3 cavities separated away by three rows of holes

Here we look for the spontaneous symmetry breaking in the evanescently coupled cavities of fig. 8.5.a. Nonlinear dynamical mechanisms such as bistability, self-sustained oscillations and excitability are studied. Special attention is focussed on hysteresis cycles which are the observable that may contain fingerprints of symmetry breaking.

Let us start by characterizing the linear resonances, meaning the spectral features in the absence of absorption saturation and/or refractive index nonlinear effects. The cavities are

injected through the tapered fiber using a 30 nm-broadband resonant signal (as described in section 3.2.2). The reflected signal is collected and sent to an optical spectrum analyzer (OSA). According to the discussion of section 8.3, the fiber must be positioned asymmetrically with respect to the cavities in order to excite the antisymmetric mode of the system. Fig. 9.1.a and b show the spectra when the fiber is placed between the cavities and closer to one of them, respectively; as a consequence, $\lambda_<$ (the symmetric mode, $\lambda_< = \lambda_S$) is observed in fig. 9.1.a and $\lambda_>$ (the antisymmetric mode, $\lambda_> = \lambda_A$) is observed in fig. 9.1.b. We observe λ_S centered at $\lambda_S = 1567.5$ nm with a loaded quality factor of $Q_{S,loaded} = 4236$ and the antisymmetric one center at $\lambda_A = 1571.5$ nm with $Q_{A,loaded} = 5069$. As expected, the antisymmetric mode has a higher quality factor. The arrows in fig. 9.1 correspond to the spectral range of wavelength detuning used in the next experiments (section 9.2.1). This detuning range satisfies the condition to obtain symmetry breaking which is, according to section 7.3, $\tau_A(\omega_A - \omega_0) < -\sqrt{3}$.

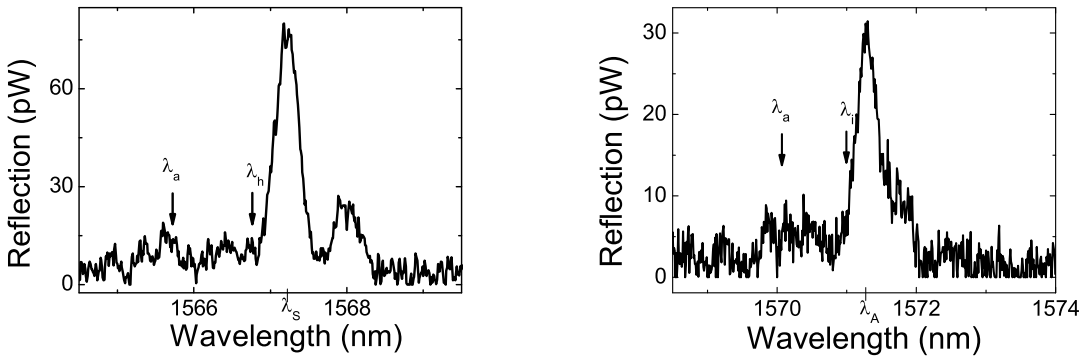

Figure 9.1: *(a) Reflectivity spectrum of (a) λ_S and (b) the antisymmetric modes of the system. The modes in (a) and (b) are centered at $\lambda_S = 1567.5$ nm with $Q_{S,loaded} = 4236$ and $\lambda_A = 1571.5$ nm with $Q_{A,loaded} = 5069$, respectively. Injected power=107 μW and resolution= 0.05 nm. The arrows correspond to the spectral range of wavelength detuning used in CW experiments of section 9.2.1.*

9.2.1 Nonlinear dynamical response at low wavelengths

In the following we investigate the nonlinear dynamical regimes of the system for injected wavelengths near the first (i.e. symmetric) mode, fig. 9.1.a. In order to study the bistable regime the system is injected through the tapered fiber with a modulated CW signal. The modulation is given by triangular pulses of 4 MHz, 40 KHz repetition rate. The experimental set up is the one described in section 5.2.2. Fast optical bistability is observed for injection powers greater than ~ 0.2 mW. The input (black line) and reflected signal (blue, red and green line) for detunings ($\Delta\lambda = \lambda_0 - \lambda_{inj}$) between 1.2 nm and 1.5 nm are shown in fig. 9.2.a. The bistable behavior is highlighted in fig.9.2.b where the reflected power is plotted as a function of the input power for a detuning of 1.4 nm (red curve in fig. 9.2.a), showing the hysteresis cycle.

Hysteresis loops are observed for detuning values between 1.5 and 0.4 nm. Fig. 9.3 shows the reflected signal as a function of the input power for different detunings. The loop size increases for larger detuning-values, up to $\Delta\lambda \sim 1.5$ nm; over this value no bistability is observed for the range of power used here. The switching time is measured as the time widths between

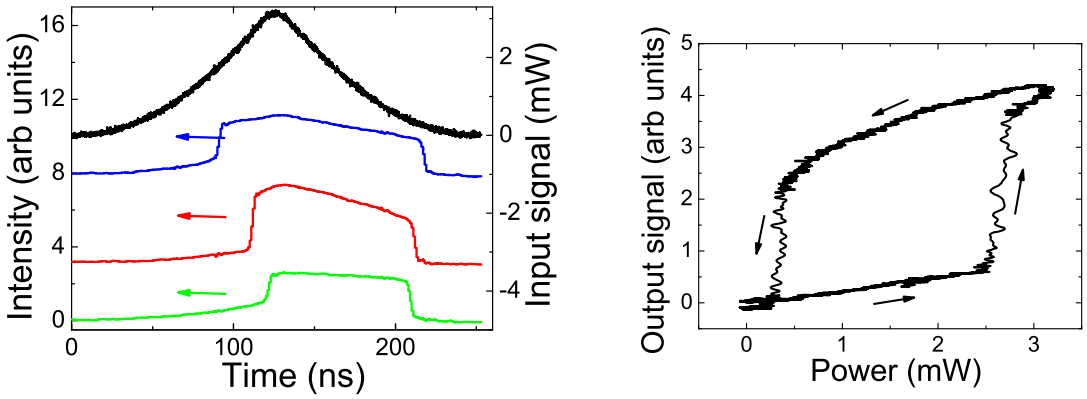

(a) (b)

Figure 9.2: *(a) Time traces of input (black line) and reflected (blue, red and green line) signals for a detuning of $\Delta\lambda$ =1.2, 1.4 and 1.5 nm, respectively. (b) Hysteresis cycles showing bistable behavior ($\Delta\lambda$ =1.4 nm). The arrows indicate the sense of the cycle.*

the minimum and the maximum of the switch processes and gives ∼4 ns for the switch on and off times, meaning that the effect leading the bistability is electronic. Note the similarities between these curves and the ones found in section 5.2.2 (fig. 5.17): no evidence of symmetry breaking is observed in these measurements.

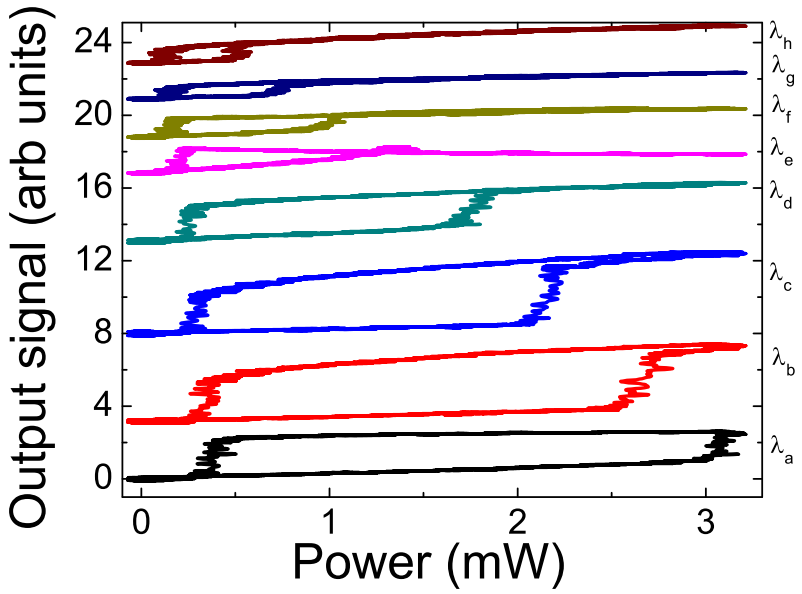

Figure 9.3: *Hysteresis cycles showing bistable behavior. Detuning-values with respect to the cavity resonance are, from λ_a to λ_h: 1.5, 1.4, 1.3, 1.2, 1, 0.8, 0.6 and 0.4 nm. The input power is measured at the tapered fiber input. The duration of the switch processes is ∼ 4 ns for the on and off switches.*

In the following, self sustained oscillations and excitability are studied. Turning off the signal modulation and injecting the system with a CW beam above the bistability threshold,

self-sustained oscillations are obtained. Fig. 9.4 shows the reflected signals as function of time for different detunings. Note the similarities with the oscillations found for a single cavity (fig. 6.2).

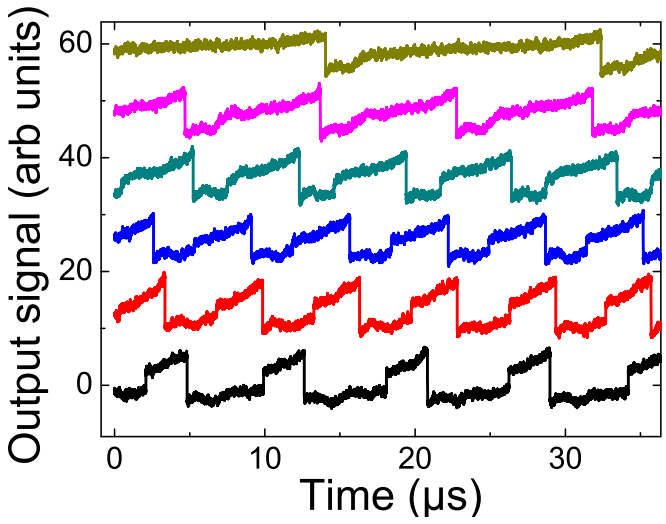

Figure 9.4: *Self-sustained oscillations. Reflected signals as a function of time for different detunings, from λ_a to λ_f: 1.3, 1.2, 1.1, 1, 0.9 and 0.8 nm. The input power, measured at the tapered fiber input, is 2.5 mW.*

Let us now focus on excitability. In the case that both cavities are excitable, the response to a perturbation of one of the cavities may act as a perturbation for the second cavity. Indeed, two excitable pulses may be observed, provided the response time is longer than the pulse itself; otherwise, larger pulses could be obtained. In the experiments, an excitable regime was also observed decreasing the injected power under the bistability threshold and adding an incoherent perturbation by the surface as described in section 6.2. Fig. 9.5 shows the reflected signal as a function of time for a detuning of 1.3 nm. For perturbation powers lower than 4 μW, no output pulse is observed. However, for higher powers an excitable pulse in the reflected signal is obtained. Once again, no qualitative difference is observed with respect to the excitable pulses of a single cavity (fig. 6.6).

It is worth mentioning that in this case, where the fiber is positioned symmetrically respect to the cavities as in the case studied in section 7.3.2, we have also studied the system response under injected wavelengths close to the antisymmetric mode. This is because, according to the results of section 7.3, the symmetry breaking is achieved for detunings that satisfy the bistability condition of the antisymmetric mode $\tau_A(\omega_A - \omega_0) < -\sqrt{3}$. However, no evidence of symmetry breaking was found.

In summary, even when a hybrid mode is likely to be excited in this case, the behavior of the system in figs. 9.3, 9.4 and 9.5 cannot be distinguished from that of a single cavity. Moreover, features of the hysteresis cycle as the ones predicted by the CMT model (see section 7.2) have not been observed. Therefore, no evidence of spontaneous symmetry breaking was obtained. In conclusion, the bistable, self-pulsing and excitable regimes experimentally observed correspond to non-linear dynamical scenarios involving the symmetric mode of the coupled-cavity system.

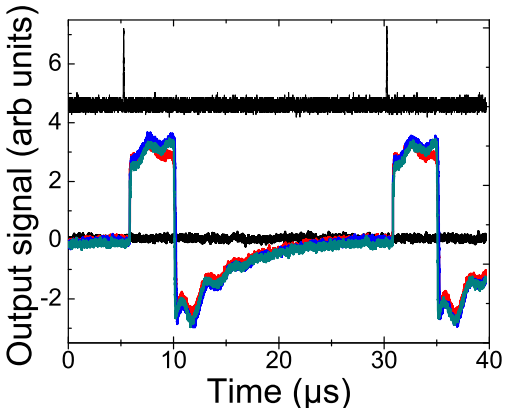

Figure 9.5: *Excitable responses (bottom traces) to 130ns-width, 40-KHz-repetition rate pulse perturbations (top trace) for different perturbation powers: 4 μW (black line), 60 μW (red line), 80 μW (blue line) and 100 μW (green line). The injected signal power is set at 0.8 mW and the detuning is* $\Delta\lambda = 1.3$ *nm.*

9.2.2 Nonlinear dynamical response at high wavelengths

In the following we repeat the experiments described in the previous paragraphs for injected wavelengths near the wavelength of the antisymmetric mode (the wavelength range shown in fig. 9.1.b). In this case, the fiber is positioned closer to one of the cavities in order to excite the antisymmetric mode.

A fast optical bistable regime is observed for injection powers greater than ~ 0.7 mW. Fig. 9.6.a shows the input (black line) and reflected signal (blue, red and green line) for detunings ($\Delta\lambda = \lambda_0 - \lambda_{inj}$) between 0.6 nm and 1.1 nm. The bistable behavior is highlighted in fig.9.6.b where the reflected power it is plotted as a function of the input power for a detuning of 1.1 nm (green curve in fig. 9.6.a), showing the hysteresis cycle.

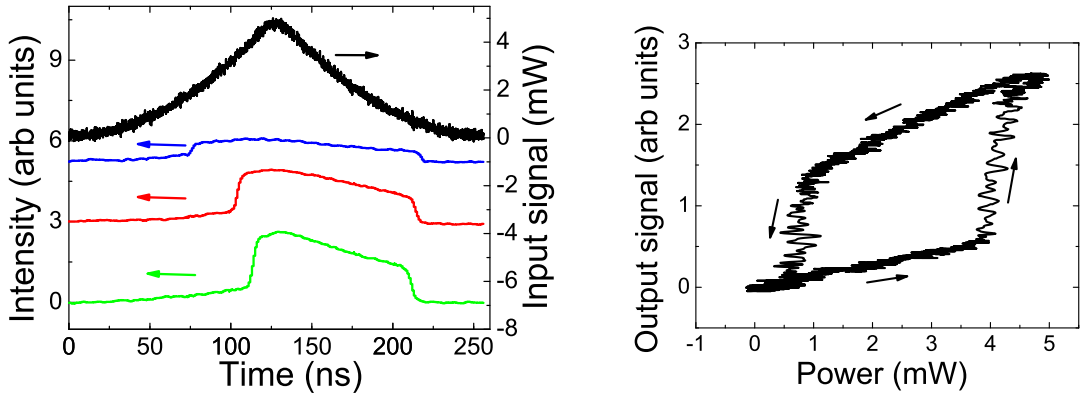

(a) (b)

Figure 9.6: *(a) Time traces of input (black line) and reflected (blue, red and green line) signals for a detuning of* $\Delta\lambda_0$ *=0.6, 1 and 1.1 nm, respectively. (b) Hysteresis cycles showing bistable behavior (*$\Delta\lambda_0$ *=1.1 nm). The arrows indicate the sense of the cycle.*

Hysteresis loops are observed for detunings between 0.3 and 1.2 nm. Fig. 9.7 shows the reflected signal as a function of the input power for different detunings. The switching times are ∼7 ns for the switch on and off times, consistent with electronic effects leading to optical bistability. Also in this case, the curves are similar to the ones found for a single cavity.

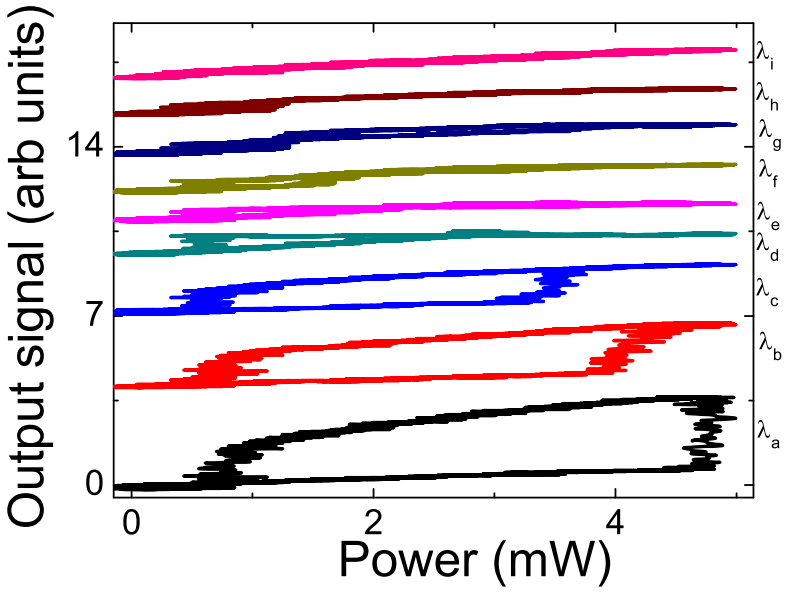

Figure 9.7: *Hysteresis cycles showing bistable behavior. Detuning-values with respect to the cavity resonance are, from λ_a to λ_i: 1.2, 1.1, 1, 0.9, 0.7, 0.5, 0.4 and 0.3 nm. The input power is measured at the tapered fiber input. The durations of the switch processes is ∼ 7 ns for the on and off switches.*

Self-sustained oscillations are also observed for detunings between 0.8 and 1.1 nm, fig. 9.8. The shape of the pulses is similar to the one found in fig. 6.2.

All the aformentioned results show that, injecting the system with wavelengths near the mode at lower and higher wavelengths, no evidence of spontaneous symmetry breaking is obtained. In the following section we discuss possible reasons for the absence of this phenomenon.

9.3 Discussion

In order to further understand the experimental results, we adjust the parameters of the theory developed in section 7.2 to match the experimental conditions, for the structures shown in fig. 8.5 coupled through a microfiber.

9.3.1 L3 cavities separated away by three rows of holes

Let us begin with the L3 cavities separated away by three rows of holes. In order to apply the formalism to the experimental case, we need to obtain the values of $\tau\gamma$, $\tau\kappa$ and δ from the experimental results. $\tau\kappa$ can be found from the wavelength splitting. Considering $\lambda_< = \lambda_S$, this splitting is ∼ 4 nm (see fig. 8.6.b). Then $\tau\kappa$ is given by (according to eq. 7.7):

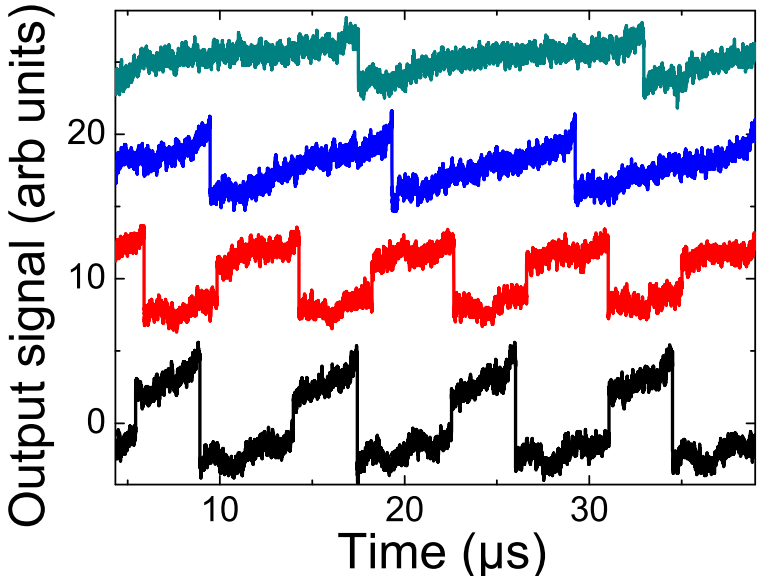

Figure 9.8: *Self-sustained oscillations. Reflected signals as a function of time for different detuning, from λ_a to λ_d: 1.1, 1, 0.9 and 0.8 nm. The input power, measured at the fiber taper input, is 4.8 mW.*

$$\tau\kappa = \tau\frac{(\omega_S - \omega_A)}{2} \sim \frac{(\lambda_S - \lambda_A)}{\Delta\lambda_{FWHM}} \tag{9.1}$$

where $\Delta\lambda_{FWHM}$ corresponds to the resonance width, which in the experimental case is ~ 0.4 nm. Hence, $\tau\kappa \sim 10$.

Regarding $\tau\gamma$, as we have seen in section 7.3, it can be obtained from the difference in the quality factor of the symmetric and antisymmetric modes (eq. 7.24). Therefore, we measure these quality factors from the resonance spectra in figs. 9.1.a and b, respectively, giving $Q_S = 4236$ and $Q_A = 5069$. τ is estimated from the quality factor of the single L3 cavity (section 5.7) as $\tau \sim 6$ ps. This leads to $\tau\gamma = -0.3$, in good agreement with the value of $\tau\gamma$ calculated through the FDTD numerical simulations of section 7.1. Considering one of the detuning values used in the experiment of fig. 9.3 ($\Delta\lambda = 1.1$ nm) we calculate δ as: $\delta = \tau(\omega_0 - \omega) = \tau(\omega_S - \omega_{in} - \kappa) = -15$, yielding to $\Lambda = \delta - \tau\kappa = -25$. Fig. 9.9.a shows the energy inside each cavity as a function of the injected signal. Note that the symmetry breaking threshold is a factor 30 higher than the threshold found for $\tau\kappa = 0.8$ (fig. 7.9). Experimentally, however, the injected powers are kept low in order to avoid damaging the sample. Fig. 9.9.b shows a zoom of the area depicted in red in fig. 9.9.a. We observe a bistable regime for the symmetric mode with a threshold 10 times lower than the symmetry breaking threshold, meaning that, with the injected powers used in this experiment, we can only see the bistability of the symmetric mode.

In order to get better insight into the experimental hysteresis cycles found in fig. 9.3, calculations of the reflected signal as a function of the injected power are carried out. Using eq. 7.29 we plot, in fig. 9.10, the hysteresis cycle for the parameters of fig. 9.9. The hysteresis cycle corresponding to bistability of the symmetric mode is observed. In addition, fast oscillations are observed close to the pitchfork bifurcation since no stable fixed point exists for $P_{in}/P_0 \gtrsim 100$

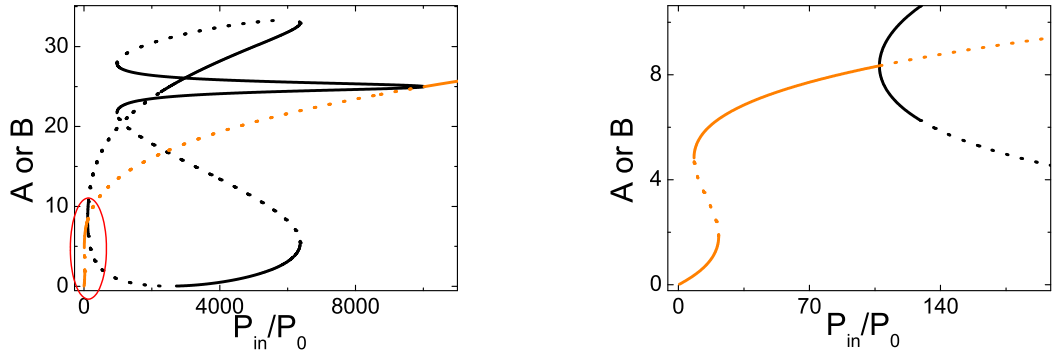

Figure 9.9: *(a) Intracavity energy as a function of the injected power for* $\tau\kappa = 10$, $\tau\gamma = -0.3$ *and* δ*=-15. The symmetric and non-symmetric solutions are shown in orange and black lines, respectively. Stable (unstable) states are shown with solid (dashed) line. (b) Zoom of the region depicted by the red circle in (a).*

(fig. 9.9.b). Note the similarities with the experimental curves shown in fig. 9.2. We can conclude that for high $\tau\kappa$ values, i.e. very strong coupling between cavities, the symmetry breaking may only take place for injected powers as high as ~ 10 times the bistability threshold of the symmetric mode.

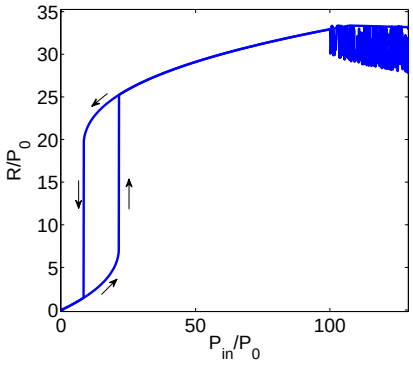

Figure 9.10: *Theoretical hysteresis cycle. Reflected signal as a function of the injected power for* $\tau\kappa = 10$, $\tau\gamma = -0.3$ *and* δ*=-15. Note the fast oscillations for* $P_{in}/P_0 \gtrsim 100$*, which take place after the pitchfork bifurcation leading to symmetry breaking.*

For larger detunings with respect to the low wavelength mode, $\Delta\lambda = 1.8$ nm, which gives δ=-19 ($\Lambda = -29$), the energy inside the cavities as a function of the injected signal becomes more complex, fig. 9.11.a. For injected power ratios higher than 23, almost all the fixed points are unstable, probably due to secondary (Hopf) bifurcations. Fig. 9.11.b shows the time trace for an injected power of P_{in}/P_0=50: note that the signals oscillate in antiphase meaning there is ultrafast exchange of energy between the cavities. Remarkably, deterministic caos seems to take place in this signal. Therefore, by changing some parameters, the system may show a chaotic behavior, such as the Lorenz attractor reported in [133], or periodic or quasi-periodic oscillations, such as Josephson oscillations, which are expected to occur in coupled Bose-Einstein condensates such as polariton systems [134]. The oscillations of fig. 9.11.b were not observed experimentally,

most probably due to the limited bandwidth of the detector.

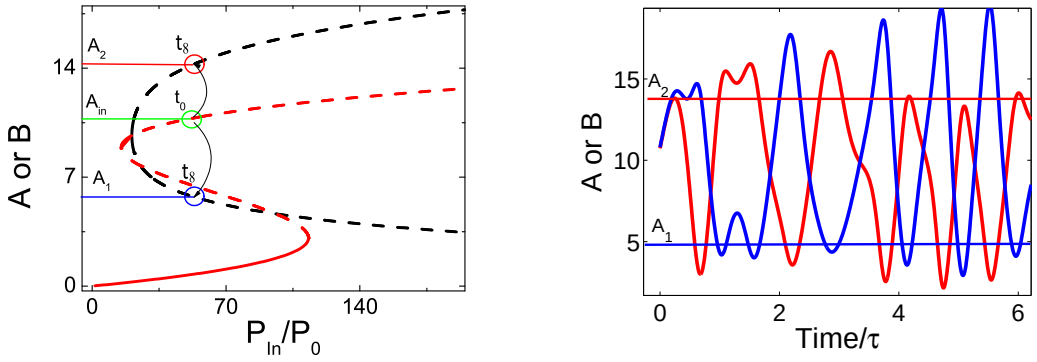

(a) (b)

Figure 9.11: *(a) Intracavity energy as a function of the injected power for* $\tau\kappa = 10$, $\tau\gamma = -0.3$ *and* δ*=-19. The symmetric and non-symmetric solutions are shown in orange and black lines, respectively. Stable (unstable) states are shown with solid (dashed) line. (b) Time traces of the energy inside the cavities for an injected power of* $P_{in}/P_0 = 50$ *and initial conditions for the intracavity energy of* $A_{in} = 11$.

In order to compare this case with the one studied in section 7.3.1, let us consider lower detunings, say, in such a way that $\Lambda = -3$ as in fig. 7.13; hence $\delta = 7$. Since $\tau\kappa = 10$, this case corresponds to region I in fig. 7.13. Even though fig. 7.13 was obtained for $\tau\gamma = 0$ we have verified that the latter does not qualitatively change the phase diagram of the system. Fig. 9.12 shows the intracavity energy of each cavity as a function of the injected signal. Note that the symmetry breaking threshold is $\sim 300P_0$, as expected from fig. 7.13. This may be the reason why, even for injected wavelengths near the antisymmetric mode, no evidence of symmetry breaking was observed.

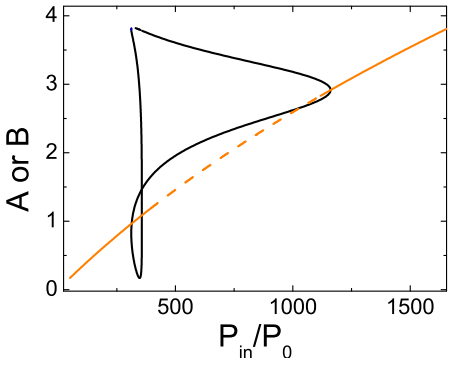

Figure 9.12: *(a) Intracavity energy as a function of the injected power for* $\tau\kappa = 10$, $\tau\gamma = -0.3$ *and* δ*=7 (*$\Lambda = -3$ *as in fig. 7.12.a). The symmetric and non-symmetric solutions are shown in orange and black lines, respectively. Stable (unstable) states are shown with solid (dashed) line.*

In the case of injected wavelengths close to λ_A of section 9.2.2, recall that the fiber is shifted from the geometrical center of the cavities in order to observe the antisymmetric mode.

Therefore, the theory developed in section 7.3 cannot be applied since the injection is considered symmetric, for which the antisymmetric mode cannot be excited in the linear regime. Therefore, in the present case, no spontaneous symmetry breaking is expected since the symmetry is already broken: only nonlinear dynamical behaviors of the antisymmetric state are observed.

9.3.2 L3 cavities separated away by five rows of holes

We proceed as before to understand the experimental results found for the cavities separated away by five rows of holes. In this case, the resonant modes overlap, as discussed in section 8.3 and they cannot be isolated; hence, we cannot obtain the value of γ from the difference in the quality factors of the symmetric and antisymmetric modes. For this reason, we will consider the results of the numerical simulations (see section 8.4.3) since we have seen, in the case p=3, that the value found for $\tau\gamma$ from the experience and from the simulations are in good agreement. The numerical simulations give $Q_S = 23300$ and $Q_A = 28000$ yielding to $\tau\gamma = -0.014$.

The spectral separation between the symmetric and antisymmetric modes can be approximated by ~ 1 nm, according to section 8.4.3, giving $\tau\kappa = 2.5$. In order to compare this case with fig. 7.13, let us consider $\delta = -0.5$ which gives $\Lambda = -3$. Fig. 9.13.a shows the energy inside the cavities as a function of the input power. This case corresponds to region I in fig. 7.13, where the symmetry breaking arises from a pitchfork bifurcations. More importantly, the symmetry breaking can be distinguished in the reflected signal vs input signal plot as the absence of hysteresis cycles and a marked change in the slope of the curve at $P_{in}/P_0 \approx 10$ as shown in fig. 9.13.b. Moreover, this change in the slope becomes more evident as the detuning is increased. Fig. 9.13.c shows the intracavity energy for each cavity as a function of the injected signal for $\tau\kappa = 2.5$, $\tau\gamma = -0.014$ and $\delta = -3$. Note that the features of the curve become more complex. In this case, the symmetry breaking can be distinguished by a marked change in the slope followed by a hysteresis cycle as shown in fig. 9.13.d. Also note that the change in the slope is obtained for reasonable injected powers, i.e. 10 times the characteristic power (P_0). Therefore this configuration is the most suitable for obtaining the spontaneous symmetry breaking. Experimentally, a major difficulty arises from the large separation of the cavities: the fiber-assisted coupling method appears to be no longer efficient in this case.

9.4 Conclusions

Nonlinear dynamical regimes were studied in evanescently coupled cavities. Bistable, self-pulsing and excitable operation were observed in two L3 cavities separated away by three and five rows of holes in the $\Gamma - M$ direction. Unfortunately, no evidence of spontaneous symmetry breaking was observed.

Through these experimental results we have obtained the necessary parameters to adjust the nonlinear model developed in chapter 7 to the experimental conditions. We have found that, in the case of the cavities separated away by three rows of holes (p=3), the detuning values chosen in the experiment, i.e. blue detuning with respect to the symmetric mode, lead to ultrafast oscillating dynamics. Even if these regimes can take place in our system, they would not have been revealed in our measurements due to experimental limitations. In addition, within symmetrical excitation conditions, injecting the system at lower δ (i.e. near the antisymmetric mode), symmetry breaking threshold about 120 times higher than the characteristic power P_0 are obtained, i.e. about 70 times higher than the onset of bistability ($P_{onset} \sim \sqrt{3}P_0$). Therefore,

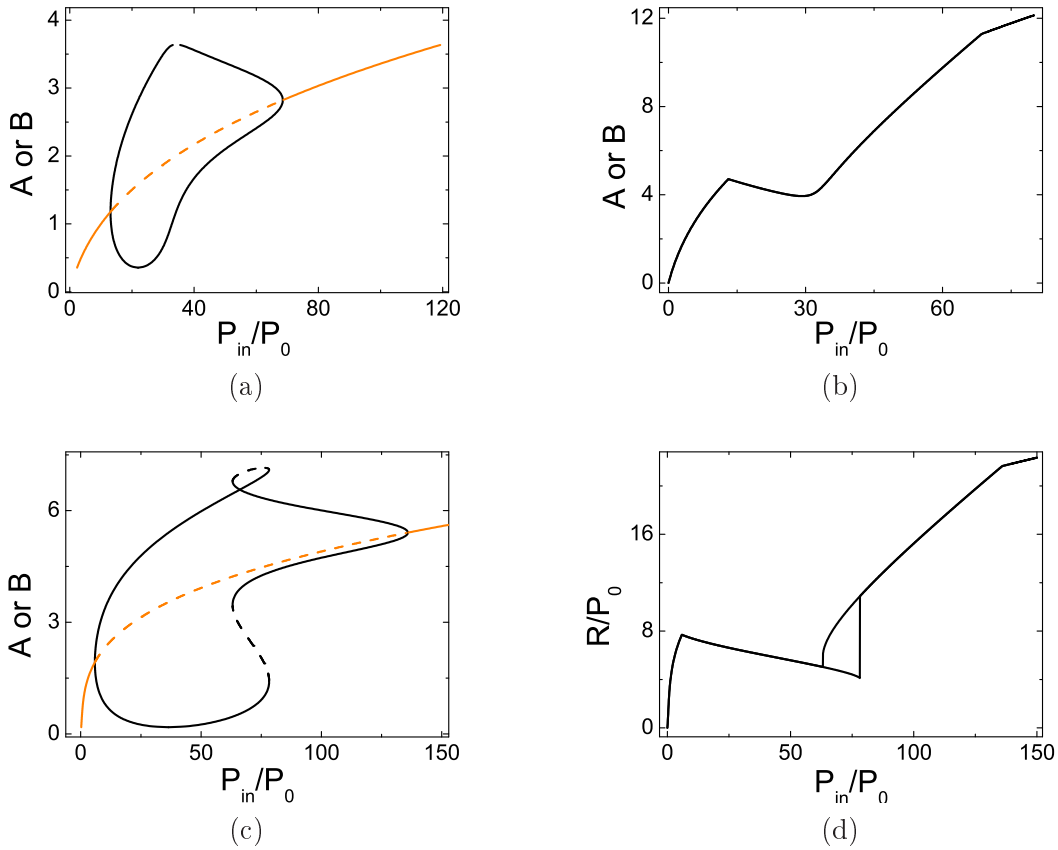

Figure 9.13: *(a) Energy inside each cavity as a function of the injected power for* $\tau\kappa = 2.5$, $\tau\gamma = -0.014$ *and* $\delta = -0.5$ $(\Lambda = -3)$. *The symmetric and non-symmetric solution are shown in orange and black lines, respectively. Stable (unstable) states are shown with solid (dashed) line.(b) Hysteresis cycle. Reflected signal as a function of the injected power for* $\tau\kappa = 2.5$, $\tau\gamma = -0.014$ *and* $\delta = -0.5$. *(c) Idem as (a) for* $\delta = -3$ $(\Lambda = -5.5)$. *(d) Idem as (b) for* $\delta = -3$. *Note the symmetry breaking can be distinguished from a change in the slop of the curve (d) followed by an hysteresis cycle.*

with the power levels used in our experiments (low in order to avoid damaging the sample) no symmetry breaking can be obtained. Though, in the case p=5, the cavities are less coupled and the theory predicts that the symmetry breaking takes place for injected powers compatible with the experimental conditions, i.e. of about 6 times the onset of bistability. Moreover, according to the theory, the symmetry breaking can be distinguished from slope discontinuities in the hysteresis cycle.

Still, L3 cavities separated away by 5 rows of holes have a main drawback: the distance between the cavities, which is of the same order than the tapered fiber thickness, prevent to efficiently coupled the cavities. A method to decrease the cavity distance without increasing the coupling strength is highly desirable; we will return to this subject in the Prospects.

In conclusion, thanks to these studies, all the ingredients needed to obtain symmetry breaking in coupled PhC nanocavities in a near future have been determined.

Chapter 10

Conclusions and Prospects

10.1 Conclusions

Nonlinear optics is being increasingly studied since its beginning fifty years ago. Among all the nonlinear phenomena that can be observed in optical systems, optical bistability have been extensively investigated in the last decades, mostly due to its potential for optical memories and switching. In optical bistability the system allows two possibles output signals for an equal injection. By definition, bistability only deals with static regimes and one dynamical variable, but it is often the precursor of exciting dynamical regimes, which can be encountered in several natural systems including neurons, cardiac tissues and chemical reactions. Dynamical nonliearities allow rich and complex non-stationary phenomena such as excitability and self-sustained oscillations. In a self-sustained oscillations regime the nonlinear system reacts emitting a periodical signal while excited with a CW beam. In the excitable regime the system develops all-or-none calibrated optical responses to a small perturbation. In both cases the nonlinear dynamics arises from the competition between the evolution of two dynamical variables with different time scales.

It is well known that nonlinear effects can be enhanced in optical resonators. During the past decade, small size optical resonators came to maturity, thanks to an enormous amount of work both technological and numerical to anticipate and engineer their optical properties. Among them, 2D PhC nanocavities share the advantage of attaining small mode volumes $\lesssim (\lambda^3/n)^3$, high quality factors up to 10^6 and the potential of being connected in complex architectures by clever PhC designs.

Only few works were devoted to the understanding and implementation of nonlinear dynamics in nanoresonators. They have mostly focussed on optical bistability of thermal origin, mainly because thermal effects in ultra-small cavities are usually dominant against ultra-fast nonlinearities. Electronic nonlinearities in nanoresonators are more difficult to achieve and observe due to both technological issues and small signals in play with fast time scales (ps-ns scale). Even tough, some works have recently demonstrated bistability of electronic origin in PhC nanocavities [87, 88]. However, more complex dynamical nonlinear scenarios are quasi unexplored in 2D PhC. In particular, excitability and self-pulsing regimes in PhC nanocavities have never been reported.

The main objective of this PhD thesis was to explore, for the first time, self-sustained oscillations and excitability in photonic crystal nanocavities. We achieved such nonlinear dynamical regimes by introducing a competition between the electronic and thermal dynamics in suspended membrane 2D PhC nanocavities with QWs as active media.

Due to the complexity of the possible scenarios, a first effort was devoted to develop a

model able to capture the combined effect of the cavity and the nonlinear responses. For this, we have developed an original coupled mode approach that includes the intracavity energy, the carrier dynamics and temperature variation in a generic cavity filled with III-V semiconductor material. This model allows the study of different regimes in optical resonators such as bistability (which involves at least a single nonlinear variable) and excitability (which involves at least two nonlinear variables).

In a second step we have experimentally investigated the role of each dynamical variable separately. Although thermal and electronic effects have been widely studied, they are strongly dependent on the particularities of the 2D PhC design and technology. Therefore, measurements of the thermal relaxation times in a L3 cavity with QDs as active medium were carried out. Through an innovative technique, exploiting the reflected signal change due to an incoherent pump, a thermal relaxation time of the order of 1 μs was obtained in good agreement with thermo-reflectance measurements developed in [116]. On the other hand, through a pump and probe technique we have measured the electronic recombination time. Times of the order of 30 ps were found. This short time is associated to bimolecular recombination processes in the wetting layer. These times are the time scales of the regimes sought in this work: bistability, excitability and self-pulsing.

Coupling high light intensity levels inside nanocavities for nonlinear dynamical studies is a challenging task: efficient input coupling methods are required. With this aim, we have developed a tapered fiber approach to efficiently inject light into the cavity mode. The coupling method consists in evanescent coupling between the tapered fiber and the nanocavity. Coupling efficiencies of the order of 28% in samples with QDs as active materials and 7% in samples with QW were achieved. Even with 7% coupling efficiencies we have been able to study nonlinear dynamical regimes in PhC nanocavities for input powers in the fiber of less than 1 mW.

Bistable regimes governed by thermal or electronic effects were studied. In particular, a fast bistable switching of electronic origin was obtained in samples with QWs as active media. Bistable thresholds as low as $\sim 10\ \mu W$ coupled into the cavity were measured, in good agreement with the values reported by Notomi et al. [82] and Kim et al. [87].

We capitalized on these results in order to investigate nonlinear dynamical responses associated to the competition between electronic and thermal nonlinear variables. Namely, nonlinear dynamical regimes involving both thermal and electronic nonlinear effects were investigated. We have experimentally demonstrated self-pulsing and excitable behavior in this sample. These results represent the first ever reported demonstration of excitability and self-sustained oscillations in photonic crystal nanocavities, which might open a door to future applications of this cavities to all optical devices.

A second objective of this PhD thesis was to explore the conditions to obtain symmetry breaking in coupled nonlinear nanocavities. Symmetry breaking is a fundamental phenomenon that has never been demonstrated in PhC resonators. This phenomenon is characterized by a non-symmetric response of the cavities under a symmetrical injection. We first developed an analytical model based on coupled mode theory (CMT). Through this model, we have obtained that symmetry breaking takes place for a wide range of input powers, in cavities coupled to the external continuum by three ports and, more importantly, in the experimental configuration: two cavities coupled to the outside by a tapered fiber.

In order to study this phenomenon experimentally, different types of coupled cavities were fabricated and investigated. For L3 adjacent cavities, we have obtained conclusive evidence of

evanescent coupling through far field emission profile images. To our knowledge, this is the first reported study of the coupling between cavities in PhC by means of near and far field emission profile images. Moreover, it is the first conclusive evidence of the existence of a phase coherence between the fields inside each cavity. This theoretical and experimental results set the basis for the demonstration of symmetry breaking in a near future.

10.2 Prospects

During this PHD thesis the conditions for the experimental demonstration of spontaneous symmetry breaking were determined from theoretical and experimental studies. Unfortunately, the final experimental demonstration was elusive, mainly due to the lack of time to optimize the cavity coupling conditions. Simulations and experiments have shown that the most likely problem is the coupling strength : too strong for cavities separated by 3 rows of holes and, for those separated by 5 rows of holes, the fiber-assisted coupling method may be poorly adapted due to the increase of the fiber-cavity distance; symmetrical injection into the system may not be guaranteed in such a case. We think that symmetry breaking will be demonstrated in a near future thanks to an improved control of the coupling strength. One possible way of controlling this coupling is to change the diameter of the holes between the cavities. Therefore, a short term prospect is the systematic study, through numerical simulations, of the mode splitting as a function of the size of holes in the barrier between the cavities.

The tapered fiber coupling method, used in this work, allowed demonstrating both self-sustained oscillations and excitability in the 2D PhC nanocavities. However, this method presents some drawbacks, such as the impossibility to excite the two cavities simultaneously while detecting separately their emissions. This becomes important for the symmetry breaking measurements, for which the symmetric excitation of the cavities is mandatory and the detection of the state of each cavity can give an insight on the localization of light. Besides, in order to study the coupling between cavities, it may be interesting to inject one of the cavities and study the transfer of energy between them by collecting the output signal from the other one. Another drawback of this coupling method is the threshold increase of nonlinear behaviors due to the relatively low coupling efficiency. Therefore, a mid-term prospect is the implementation of a recently proposed method that would replace the tapered fiber coupling system, as explain below.

Due to the strong solid angle of the emission diagram of L3 nanocavities, their input/output coupling by the surface is quite inefficient even when a high numerical aperture objective is used. This is the reason why the coupling via a tapered fiber was implemented. Several works have studied the "beam-shaping" in PhC devices [135, 136, 137], in particular, recent works have investigated high-Q photonic crystal nanocavities with a tailored radiation pattern [138, 139, 140]. This type of cavities allow to collect 80% of the radiated power by optics having a numerical aperture of 0.6. Such maximization of the in- and out-coupling efficiency into a narrow emission cone is obtained by properly modifying the holes around the cavity. The basic idea, called band-folding technique, is illustrated in fig. 10.1a. and b. The near field of an optimized PhC cavity is distributed as close as possible to the border of the Brillouin zone (BZ) ($k_x = \pi/a$). If a period 2a is superimposed to the original structure, the distribution of the near field in the reciprocal space is folded with respect to $k_x = \pi/(2a)$ and therefore a replica of the distribution near the first BZ appears at $k_x = 0$. Consequently, radiation is now leaked mainly vertically and the amount of leakage is controlled by the amplitude of the subharmonics with period 2a [138]. Figs. 10.1.c and d show the L3 cavity without and with modification of the period, respectively. The radiation pattern for the cavity in figs. 10.1.c and d are shown in figs. 10.1.e and f, respectively [139]. Note the highly directive emission of the cavity where

the band folding was implemented. It is important to mention that, due to this modification of the holes period, the quality factor of the structure is reduced by about a factor 4. This value is of the same order than the reduction of the cavity quality factor due to the coupling with a tapered fiber with a coupling efficiency of $\eta = 80\%$ (according to the CMT formalism developed in chapter 2). Such geometry would not only provide an alternative channel for light injection but also enable selective measurements of the radiation from each cavity with low cross-talk.

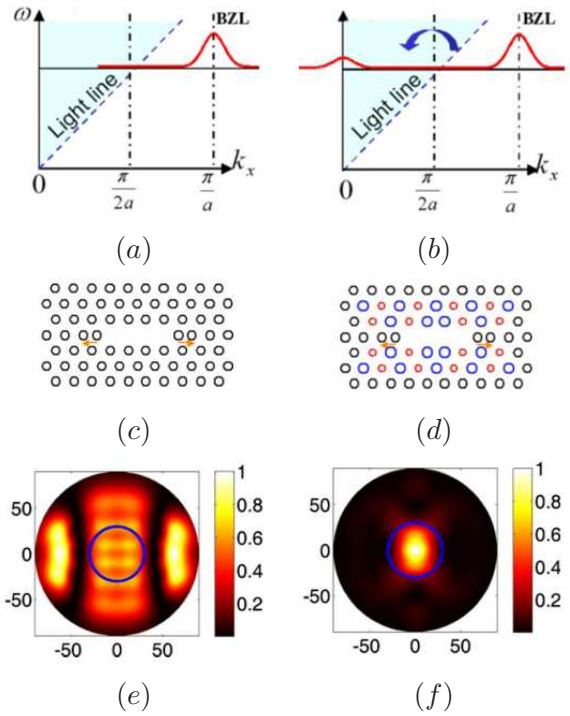

Figure 10.1: *Principle of band folding: (a) schematic representation of the near field distribution in the reciprocal space for an optimized cavity; (b) band-folded distribution (Image from [138]). Scheme of a L3 cavity with standard design (c) and with implementation of the band folding (d) through additional sub-harmonic modulation. Radiation pattern with broad emission for the standard L3 design (e) and highly directive for the modified (f)(Image from [139]).*

A further advantage of exciting the cavities by the surface is the possibility of simultaneously exciting an array of cavities. Whereas the tapered fiber allows to symmetrically inject at most two cavities, a surface injection scheme would allow to inject several cavities "in parallel", provided the excitation spot is large enough. Since, above threshold, an excitable pulse is independent of the excitation intensity, robust pulse transmission can be expected through cavity chains, giving interesting prospects for delay line applications and even original all-optical logical gates. From the nonlinear dynamical point of view, chains of coupled cavities can be used to study the propagation of nonlinear wavefronts, fig 10.2. In this context, this work opens the door for investigating interesting and applicable (e.g. all-optical devices) behaviors in two nonlinear cavities in a short term, as well as arrays of excitable cavities in a mid-to-long term.

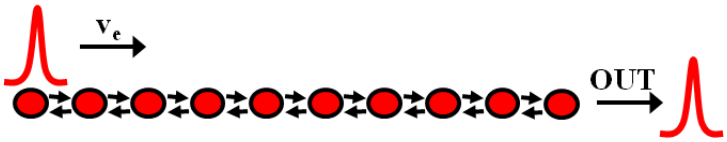

Figure 10.2: *Excitable wave travelling through the nanocavities.*

Publications

Publications related with this thesis:

[1] M. Brunstein, A. M. Yacomotti, R. Braive, I. Sagnes, F. Raineri, L. Bigot and J.A. Levenson, *Excitability and self-pulsing in a 2D InP-based Photonic Crystal Nanocavity*, submitted to Phys. Rev. Lett. E

[2] M. Brunstein, T Karle, R. Braive, I. Sagnes, F. Raineri, J. Bloch, J.A. Levenson and A. M. Yacomotti, *Radiation pattern from coupled Photonic crystal nanocaviites*, submited to Appl. Phys. Lett.

[3] M. Brunstein, A. M. Yacomotti, R. Braive, I. Sagnes, L. Bigot and J.A. Levenson, *All-optical, all-fibered ultrafast switching in 2D InP-based photonic crystal nanocavity*, IEEE Photonics journal, 2, 642-651, 2010.

[5] V. Moreau,G Tessier, F. Raineri, M. Brunstein, A. Yacomotti, R. Raj, I. Sagnes, A. Levenson and Y. De Wilde, *Transient thermoreflectance imaging of active photonic crystals*, Appl. Phys. Lett. 96, 091103 (2010).

[6] M. Brunstein, R. Braive, R. Hostein, A. Beveratos, I. Robert-Philip, I. Sagnes, T. J. Karle, A. M. Yacomotti, J. A. Levenson, V. Moreau, G. Tessier and Y. De Wilde, *Thermo-optical dynamics in an optically pumped Photonic Crystal nano-cavity*, Optics Express, Vol. 17, Issue 19, pp. 17118-17129 (2009)

Others publications:

[7] L. C. Estrada, O. E. Martinez, M. Brunstein, S. Bouchoule, L. Le-Gratiet, A. Talneau, I. Sagnes, P. Monnier, J. A. Levenson, and A. M. Yacomotti , Small volume excitation and enhancement of dye fluorescence on a 2D photonic crystal surface, Optics Express, Vol. 18, Issue 4, pp. 3693-3699 (2010)

Bibliography

[1] C. Hilborn Robert. *Chaos and nonlinear dynamics: an introduction for scientists and engineers.* New York, 2000.

[2] S. H. Strogatz. *Nonlinear dynamics and chaos.* 1994.

[3] H. Haken. *Synergetics, 3er edition.* Berlin, 1983.

[4] J. D. Murray. *Mathematical Biology.* New York, 1990.

[5] A. Rabinovitch and I. Rogachevskii. Threshold, excitability and isochrones in the Bonhoeffer–van der Pol system. *Chaos: An Interdisciplinary Journal of Nonlinear Science*, 9(4):880–886, 1999.

[6] Izhikevich EM. Neural excitability, spiking and bursting. *Int J Bif Chaos*, 10(6):1171–1266, 2000.

[7] Nikola Burić, Ines Grozdanović, and Nebojša Vasović. Type I vs. type II excitable systems with delayed coupling. *Chaos, Solitons & Fractals*, 23(4):1221–1233, February 2005.

[8] D. Terman and D. Wang. Global competition and local cooperation in a network of neural oscillators. *Physica D: Nonlinear Phenomena*, 81(1-2):148–176, February 1995.

[9] D. Taylor, P. Holmes, and A. H. Cohen. *Excitable Oscillators as Models for Central Pattern Generators. Series on Stability, Vibration and Control of Systems, Series B.* Singapore, 1997.

[10] Johan L. A. Dubbeldam, Bernd Krauskopf, and Daan Lenstra. Excitability and coherence resonance in lasers with saturable absorber. *Physical Review E*, 60(6):6580–6588, December 1999.

[11] A. L. Hodgkin and A. F. Huxley. A quantitative description of membrane current and its application to conduction and excitation in nerve. *The Journal of Physiology*, 117(4):500–544, August 1952.

[12] R. W. Boyd. *Nonlinear optics, third edition.* 2008.

[13] Jon Opsal, Michael W. Taylor, W. Lee Smith, and Allan Rosencwaig. Temporal behavior of modulated optical reflectance in silicon. *Journal of Applied Physics*, 61(1):240–248, 1987.

[14] K. J. Yee, D. Lee, X. Liu, W. L. Lim, M. Dobrowolska, J. K. Furdyna, Y. S. Lim, K. G. Lee, Y. H. Ahn, and D. S. Kim. Optical studies of carrier and phonon dynamics in Ga[sub 1 - x]Mn[sub x]As. *Journal of Applied Physics*, 98(11):113509+, 2005.

[15] Y. H. Lee, A. Chavez Pirson, S. W. Koch, H. M. Gibbs, S. H. Park, J. Morhange, A. Jeffery, N. Peyghambarian, L. Banyai, A. C. Gossard, and W. Wiegmann. Room-Temperature Optical Nonlinearities in GaAs. *Physical Review Letters*, 57(19):2446–2449, November 1986.

[16] Grundmann Marius. *The physics of semiconductors, second edition.* Berlin, 2010.

[17] A. Szöke, V. Daneu, J. Goldhar, and N. A. Kurnit. Bistable optical element and its applications. *Applied Physics Letters*, 15(11):376–379, 1969.

[18] H. M. Gibbs, S. L. McCall, and T. N. C. Venkatesan. Differential Gain and Bistability Using a Sodium-Filled Fabry-Perot Interferometer. *Physical Review Letters*, 36(19):1135–1138, May 1976.

[19] Shanhui Fan, Wonjoo Suh, and J. D. Joannopoulos. Temporal coupled-mode theory for the Fano resonance in optical resonators. *J. Opt. Soc. Am. A*, 20(3):569–572, March 2003.

[20] Björn Maes, Peter Bienstman, and Roel Baets. Switching in coupled nonlinear photonic-crystal resonators. *J. Opt. Soc. Am. B*, 22(8):1778–1784, August 2005.

[21] Marin Soljačić, Mihai Ibanescu, Steven G. Johnson, Yoel Fink, and J. D. Joannopoulos. Optimal bistable switching in nonlinear photonic crystals. *Physical Review E*, 66(5):055601+, November 2002.

[22] R. Kuszelewicz, J. L. Oudar, J. C. Michel, and R. Azoulay. Monolithic GaAs/AlAs optical bistable [e-acute]talons with improved switching characteristics. *Applied Physics Letters*, 53(22):2138–2140, 1988.

[23] B. G. Sfez, J. L. Oudar, J. C. Michel, R. Kuszelewicz, and R. Azoulay. External-beam switching in monolithic bistable GaAs quantum well [e-acute]talons. *Applied Physics Letters*, 57(18):1849–1851, 1990.

[24] J. P. Debray, E. Lugagne Delpon, G. Le Roux, J. L. Oudar, and M. Quillec. Low threshold InGaAlAs monolithic vertical cavity bistable device at 1.5 mu m wavelength. *Applied Physics Letters*, 70(21):2858–2860, 1997.

[25] T. Elsass, K. Gauthron, G. Beaudoin, I. Sagnes, R. Kuszelewicz, and S. Barbay. Fast manipulation of laser localized structures in a monolithic vertical cavity with saturable absorber. *Applied Physics B: Lasers and Optics*, 98(2):327–331, February 2010.

[26] T. Rivera, F. R. Ladan, A. Izraël, R. Azoulay, R. Kuszelewicz, and J. L. Oudar. Reduced threshold all-optical bistability in etched quantum well microresonators. *Applied Physics Letters*, 64(7):869–871, 1994.

[27] Thomas J. Johnson, Matthew Borselli, and Oskar Painter. Self-induced optical modulation of the transmission through a high-Q silicon microdisk resonator. *Optics Express*, 14(2):817+, 2006.

[28] E. Centeno and D. Felbacq. Optical bistability in finite-size nonlinear bidimensional photonic crystals doped by a microcavity. *Physical Review B*, 62(12):R7683–R7686, September 2000.

[29] Stéphane Barland, Oreste Piro, Massimo Giudici, Jorge R. Tredicce, and Salvador Balle. Experimental evidence of van der Pol–Fitzhugh–Nagumo dynamics in semiconductor optical amplifiers. *Physical Review E*, 68(3):036209+, September 2003.

[30] Tal Carmon, Hossein Rokhsari, Lan Yang, Tobias J. Kippenberg, and Kerry J. Vahala. Temporal Behavior of Radiation-Pressure-Induced Vibrations of an Optical Microcavity Phonon Mode. *Physical Review Letters*, 94(22):223902+, June 2005.

[31] Eiichi Kuramochi, Masaya Notomi, Satoshi Mitsugi, Akihiko Shinya, Takasumi Tanabe, and Toshifumi Watanabe. Ultrahigh-Q photonic crystal nanocavities realized by the local width modulation of a line defect. *Applied Physics Letters*, 88(4):041112+, 2006.

[32] V. Z. Tronciu and R. A. Abram. Excitability of excitons and biexcitons in a ring cavity. *Physical Review E*, 65(2):026616+, January 2002.

[33] Bjorn Maes, Martin Fiers, and Peter Bienstman. Self-pulsing and chaos in short chains of coupled nonlinear microcavities. *Physical Review A*, 80(3):033805+, September 2009.

[34] H. Jaeger and H. Haas. Harnessing Nonlinearity: Predicting Chaotic Systems and Saving Energy in Wireless Communication. *Science*, 304(5667):78–80, April 2004.

[35] Wolfgang Maass, Thomas Natschläger, and Henry Markram. Real-Time Computing Without Stable States: A New Framework for Neural Computation Based on Perturbations. *Neural Computation*, 14(11):2531–2560, November 2002.

[36] Kristof Vandoorne, Wouter Dierckx, Benjamin Schrauwen, David Verstraeten, Roel Baets, Peter Bienstman, and Jan Van Campenhout. Toward optical signal processing using Photonic Reservoir Computing. *Optics Express*, 16(15):11182+.

[37] B. Krauskopf, K. Schneiderb, J. Sieber, S. Wieczorekc, and M. Wolfrumb. Excitability and self-pulsations near homoclinic bifurcations in semiconductor laser systems. *Optics Communications*, 215(4-6):367–379, January 2003.

[38] Lukasz Olejniczak, Krassimir Panajotov, Hugo Thienpont, and Marc Sciamanna. Self-pulsations and excitability in optically injected quantum-dot lasers: Impact of the excited states and spontaneous emission noise. *Physical Review A*, 82(2):023807+, August 2010.

[39] O. V. Ushakov, N. Korneyev, M. Radziunas, H. J. Wünsche, and F. Henneberger. Excitability of chaotic transients in a semiconductor laser. *EPL (Europhysics Letters)*, pages 30004+, August 2007.

[40] J. Dubbeldam and B. Krausfopf. Self-pulsations of lasers with saturable absorber: dynamics and bifurcations. *Optics Communications*, 159(4-6):325–338, January 1999.

[41] H. MacKenzie, J. Reid, H. Alattar, and E. Abraham. Regenerative pulsations in an InSb bistable etalon. *Optics Communications*, 60(3):181–186, November 1986.

[42] M. Giudici, C. Green, G. Giacomelli, U. Nespolo, and J. R. Tredicce. Andronov bifurcation and excitability in semiconductor lasers with optical feedback. *Physical Review E*, 55(6):6414–6418, June 1997.

[43] A. M. Yacomotti, M. C. Eguia, J. Aliaga, O. E. Martinez, G. B. Mindlin, and A. Lipsich. Interspike Time Distribution in Noise Driven Excitable Systems. *Physical Review Letters*, 83(2):292–295, July 1999.

[44] Francesco Marino, Massimo Giudici, Stéphane Barland, and Salvador Balle. Experimental Evidence of Stochastic Resonance in an Excitable Optical System. *Physical Review Letters*, 88(4):040601+, January 2002.

[45] H. J. Wünsche, O. Brox, M. Radziunas, and F. Henneberger. Excitability of a Semiconductor Laser by a Two-Mode Homoclinic Bifurcation. *Physical Review Letters*, 88(2):023901+, December 2001.

[46] Miguel A. Larotonda, Alejandro Hnilo, Jorge M. Mendez, and Alejandro M. Yacomotti. Experimental investigation on excitability in a laser with a saturable absorber. *Physical Review A*, 65(3):033812+, February 2002.

[47] F. Plaza, M. G. Velarde, F. T. Arecchi, S. Boccaletti, M. Ciofini, and R. Meucci. Excitability following an avalanche-collapse process. *EPL (Europhysics Letters)*, pages 85+, April 1997.

[48] Francesco Marino, Gustau Catalán, Pedro Sánchez, Salvador Balle, and Oreste Piro. Thermo-Optical "Canard Orbits" and Excitable Limit Cycles. *Physical Review Letters*, 92(7):073901+, February 2004.

[49] Stefano Beri, Lilia Mashall, Lendert Gelens, Guy Van der Sande, Gabor Mezosi, Marc Sorel, Jan Danckaert, and Guy Verschaffelt. Excitability in optical systems close to Z2Z2-symmetry. *Physics Letters A*, 374(5):739–743, January 2010.

[50] L. Gelens, L. Mashal, S. Beri, W. Coomans, G. Van der Sande, J. Danckaert, and G. Verschaffelt. Excitability in semiconductor microring lasers: Experimental and theoretical pulse characterization. *Physical Review A*, 82(6):063841+, December 2010.

[51] B. Kelleher, D. Goulding, S. P. Hegarty, G. Huyet, Ding-Yi Cong, A. Martinez, A. Lemaître, A. Ramdane, M. Fischer, F. Gerschütz, and J. Koeth. Excitable phase slips in an injection-locked single-mode quantum-dot laser. *Optics Letters*, 34(4):440+, February 2009.

[52] Thomas D. Happ, Martin Kamp, Alfred Forchel, Anatolii V. Bazhenov, Ilja I. Tartakovskii, Alexander Gorbunov, and Vladimir D. Kulakovskii. Coupling of point-defect microcavities in two-dimensional photonic-crystal slabs. *Journal of the Optical Society of America B*, 20(2):373+, February 2003.

[53] Satoru Ishii, Kengo Nozaki, and Toshihiko Baba. Photonic Molecules in Photonic Crystals. *Japanese Journal of Applied Physics*, 45(No. 8A):6108–6111, August 2006.

[54] D. O'Brien, M. D. Settle, T. Karle, A. Michaeli, M. Salib, and T. F. Krauss. Coupled photonic crystal heterostructure nanocavities. *Optics Express*, 15(3):1228+.

[55] Kirill A. Atlasov, Karl F. Karlsson, Alok Rudra, Benjamin Dwir, and Eli Kapon. Wavelength and loss splitting in directly coupled photonic-crystal defect microcavities. *Optics Express*, 16(20):16255–16264, September 2008.

[56] A. R. A. Chalcraft, S. Lam, B. D. Jones, D. Szymanski, R. Oulton, A. C. T. Thijssen, M. S. Skolnick, D. M. Whittaker, T. F. Krauss, and A. M. Fox. Mode structure of coupled L3 photonic crystal cavities. *Optics Express*, 19(6):5670+.

[57] Atsuo Nakagawa, Satoru Ishii, and Toshihiko Baba. Photonic molecule laser composed of GaInAsP microdisks. *Applied Physics Letters*, 86(4):041112+, 2005.

[58] Fengnian Xia, Lidija Sekaric, and Yurii Vlasov. Ultracompact optical buffers on a silicon chip. *Nature Photonics*, 1(1):65–71, December 2006.

[59] M. Benyoucef, S. Kiravittaya, Y. F. Mei, A. Rastelli, and O. G. Schmidt. Strongly coupled semiconductor microcavities: A route to couple artificial atoms over micrometric distances. *Physical Review B*, 77(3):035108+, January 2008.

[60] Hsuan Lin, Jhih-Hao Chen, Shih-Shing Chao, Ming-Cheng Lo, Sheng-Di Lin, and Wen-Hao Chang. Strong coupling of different cavity modes in photonic molecules formed by two adjacent microdisk microcavities. *Optics Express*, 18(23):23948+.

[61] B. M. Möller, U. Woggon, M. V. Artemyev, and R. Wannemacher. Photonic molecules doped with semiconductor nanocrystals. *Physical Review B*, 70(11):115323+, September 2004.

[62] Adrien Dousse, Jan Suffczynski, Alexios Beveratos, Olivier Krebs, Aristide Lemaitre, Isabelle Sagnes, Jacqueline Bloch, Paul Voisin, and Pascale Senellart. Ultrabright source of entangled photon pairs. *Nature*, 466(7303):217–220, July 2010.

[63] Marin Soljačić, Steven G. Johnson, Shanhui Fan, Mihai Ibanescu, Erich Ippen, and J. D. Joannopoulos. Photonic-crystal slow-light enhancement of nonlinear phase sensitivity. *Journal of the Optical Society of America B*, 19(9):2052+.

[64] Björn Maes, Marin Soljacic, John D. Joannopoulos, Peter Bienstman, Roel Baets, Simon-Pierre Gorza, and Marc Haelterman. Switching through symmetry breaking in coupled nonlinear micro-cavities. *Opt. Express*, 14(22):10678–10683, October 2006.

[65] John D. Joannopoulos, Steven G. Johnson, Joshua N. Winn, and Robert D. Meade. *Photonic Crystals: Molding the Flow of Light. second edition.* 2008.

[66] O. Painter, J. Vučkovič, and A. Scherer. Defect modes of a two-dimensional photonic crystal in an optically thin dielectric slab. *Journal of the Optical Society of America B*, 16(2):275–285, February 1999.

[67] Yoshihiro Akahane, Takashi Asano, Bong-Shik Song, and Susumu Noda. High-Q photonic nanocavity in a two-dimensional photonic crystal. *Nature*, 425(6961):944–947, October 2003.

[68] Christophe Sauvan, Philippe Lalanne, and Jean-Paul Hugonin. Photonics: Tuning holes in photonic-crystal nanocavities. *Nature*, 429(6988), May 2004.

[69] C. Sauvan, P. Lalanne, and J. P. Hugonin. Slow-wave effect and mode-profile matching in photonic crystal microcavities. *Physical Review B*, 71(16):165118+, April 2005.

[70] Bong-Shik Song, Susumu Noda, Takashi Asano, and Yoshihiro Akahane. Ultra-high-Q photonic double-heterostructure nanocavity. *Nature Materials*, 4(3):207–210, February 2005.

[71] R. Herrmann, T. Sunner, T. Hein, A. Löffler, M. Kamp, and A. Forchel. Ultrahigh-quality photonic crystal cavity in GaAs. *Opt. Lett.*, 31(9):1229–1231, 2006.

[72] Evelin Weidner, Sylvain Combrié, Nguyen Vi Quynh Tran, Alfredo De Rossi, Julien Nagle, Simone Cassette, Anne Talneau, and Henri Benisty. Achievement of ultrahigh quality factors in GaAs photonic crystal membrane nanocavity. *Applied Physics Letters*, 89(22):221104+, 2006.

[73] Hatice Altug, Dirk Englund, and Jelena Vuckovic. Ultrafast photonic crystal nanocavity laser. *Nature Physics*, 2(7):484–488, July 2006.

[74] S. Mookherjea and A. Yariv. Coupled resonator optical waveguides. *IEEE Journal of Selected Topics in Quantum Electronics*, 8(3):448–456, May 2002.

[75] Sergei V. Zhukovsky, Dmitry N. Chigrin, Andrei V. Lavrinenko, and Johann Kroha. Switchable Lasing in Multimode Microcavities. *Physical Review Letters*, 99(7):073902+, August 2007.

[76] S. Ishii, A. Nakagawa, and T. Baba. Modal characteristics and bistability in twin microdisk photonic molecule lasers. *IEEE Journal of Selected Topics in Quantum Electronics*, 12(1):71–77, January 2006.

[77] Martin T. Hill, Harmen J. S. Dorren, Tjibbe de Vries, Xaveer J. M. Leijtens, Jan H. den Besten, Barry Smalbrugge, Yok-Siang Oei, Hans Binsma, Giok-Djan Khoe, and Meint K. Smit. A fast low-power optical memory based on coupled micro-ring lasers. *Nature*, 432(7014):206–209, November 2004.

[78] Masaya Notomi, Eiichi Kuramochi, and Takasumi Tanabe. Large-scale arrays of ultrahigh-Q coupled nanocavities. *Nature Photonics*, 2(12):741–747, November 2008.

[79] Silvia Vignolini, Francesco Riboli, Francesca Intonti, Diederik S. Wiersma, Laurent Balet, Lianhe H. Li, Marco Francardi, Annamaria Gerardino, Andrea Fiore, and Massimo Gurioli. Mode hybridization in photonic crystal molecules. *Applied Physics Letters*, 97(6):063101+, 2010.

[80] C. J. M. Smith, R. M. De La Rue, M. Rattier, S. Olivier, H. Benisty, C. Weisbuch, T. F. Krauss, R. Houdré, and U. Oesterle. Coupled guide and cavity in a two-dimensional photonic crystal. *Applied Physics Letters*, 78(11):1487–1489, 2001.

[81] Nakamura Hitoshi, Yoshimasa Sugimoto, Kyozo Kanamoto, Naoki Ikeda, Yu Tanaka, Yusui Nakamura, Shunsuke Ohkouchi, Yoshinori Watanabe, Kuon Inoue, Hiroshi Ishikawa, and Kiyoshi Asakawa. Ultra-fast photonic crystal/quantum dot alloptical switch for future photonic networks. *Opt. Express*, 12(26):6606–6614, December 2004.

[82] Masaya Notomi, Akihiko Shinya, Satoshi Mitsugi, Goh Kira, Eiichi Kuramochi, and Takasumi Tanabe. Optical bistable switching action of Si high-Q photonic-crystal nanocavities. *Opt. Express*, 13(7):2678–2687, April 2005.

[83] Paul E. Barclay, Kartik Srinivasan, and Oskar Painter. Design of photonic crystal waveguides for evanescent coupling to optical fiber tapers and integration with high-Q cavities. *Journal of the Optical Society of America B*, 20(11):2274+.

[84] Guk-Hyun Kim, Yong-Hee Lee, Akihiko Shinya, and Masaya Notomi. Coupling of small, low-loss hexapole mode with photonic crystal slab waveguide mode. *Optics Express*, 12(26):6624+, 2004.

[85] In K. Hwang, Sun K. Kim, Jin K. Yang, Se H. Kim, Sang H. Lee, and Yong H. Lee. Curved-microfiber photon coupling for photonic crystal light emitter. *Applied Physics Letters*, 87(13):131107+, 2005.

[86] Takasumi Tanabe, Masaya Notomi, Satoshi Mitsugi, Akihiko Shinya, and Eiichi Kuramochi. Fast bistable all-optical switch and memory on a silicon photonic crystal on-chip. *Optics Letters*, 30(19):2575–2577, October 2005.

[87] Myung K. Kim, In K. Hwang, Se H. Kim, Hyun J. Chang, and Yong H. Lee. All-optical bistable switching in curved microfiber-coupled photonic crystal resonators. *Applied Physics Letters*, 90(16):161118+, 2007.

[88] M. Notomi, T. Tanabe, A. Shinya, E. Kuramochi, H. Taniyama, S. Mitsugi, and M. Morita. Nonlinear and adiabatic control of high-Qphotonic crystal nanocavities. *Opt. Express*, 15(26):17458–17481, December 2007.

[89] A. M. Yacomotti, P. Monnier, F. Raineri, Ben B. Bakir, C. Seassal, R. Raj, and J. A. Levenson. Fast Thermo-Optical Excitability in a Two-Dimensional Photonic Crystal. *Physical Review Letters*, 97(14):143904+, October 2006.

[90] E. Rosencher and B. Vinter. *Optoelectronique*. Paris, 2002.

[91] F. Raineri, Crina Cojocaru, P. Monnier, A. Levenson, R. Raj, C. Seassal, X. Letartre, and P. Viktorovitch. Ultrafast dynamics of the third-order nonlinear response in a two-dimensional InP-based photonic crystal. *Applied Physics Letters*, 85(11):1880–1882, 2004.

[92] Edited by Eli Kapon. *Semiconductor laser I: Fundamentals*. 1999.

[93] Fabrice Raineri, Alejandro M. Yacomotti, Timothy J. Karle, Richard Hostein, Remy Braive, Alexios Beveratos, Isabelle Sagnes, and Rama Raj. Dynamics of band-edge photonic crystal lasers. *Opt. Express*, 17(5):3165–3172, March 2009.

[94] G. R. Olbright, N. Peyghambarian, H. M. Gibbs, H. A. Macleod, and F. Van Milligen. Microsecond room-temperature optical bistability and crosstalk studies in ZnS and ZnSe interference filters with visible light and milliwatt powers. *Applied Physics Letters*, 45(10):1031–1033, 1984.

[95] A. R. A. Chalcraft, S. Lam, D. O'Brien, T. F. Krauss, M. Sahin, D. Szymanski, D. Sanvitto, R. Oulton, M. S. Skolnick, A. M. Fox, D. M. Whittaker, H. Y. Liu, and M. Hopkinson. Mode structure of the L3 photonic crystal cavity. *Applied Physics Letters*, 90(24):241117+, 2007.

[96] Francesco G. Della Corte, Giuseppe Cocorullo, Mario Iodice, and Ivo Rendina. Temperature dependence of the thermo-optic coefficient of InP, GaAs, and SiC from room temperature to 600 K at the wavelength of 1.5 mu m. *Applied Physics Letters*, 77(11):1614–1616, 2000.

[97] M. Brunstein, R. Braive, R. Hostein, A. Beveratos, I. Rober-Philip, I. Sagnes, T. J. Karle, A. M. Yacomotti, J. A. Levenson, V. Moreau, G. Tessier, and Y. De Wilde. Thermo-optical dynamics in an optically pumped Photonic Crystal nano-cavity. *Opt. Express*, 17(19):17118–17129, September 2009.

[98] K. S. Kim, R. H. Stolen, W. A. Reed, and K. W. Quoi. Measurement of the nonlinear index of silica-core and dispersion-shifted fibers. *Optics Letters*, 19(4):257–259, February 1994.

[99] A. Taflove and S. C. Hagness. *Computational Electrodynamics: The Finite-Difference Time-Domain Method, 2nd ed.* Artech House, 2000.

[100] Allen Taflove. Application of the Finite-Difference Time-Domain Method to Sinusoidal Steady-State Electromagnetic-Penetration Problems. *IEEE Transactions on Electromagnetic Compatibility*, EMC-22(3):191–202, August 1980.

[101] Vladimir A. Mandelshtam and Howard S. Taylor. Harmonic inversion of time signals and its applications. *The Journal of Chemical Physics*, 107(17):6756–6769, 1997.

[102] http://ab-initio.mit.edu/wiki/index.php/Harminv.

[103] Qiang Li, Tao Wang, Yikai Su, Min Yan, and Min Qiu. Coupled mode theory analysis of mode-splitting in coupled cavity system. *Opt. Express*, 18(8):8367–8382, April 2010.

[104] Peter Bienstman. *Rigorous and efficient modelling of wavelength scale photonic components*. PhD thesis.

[105] http://camfr.sourceforge.net/index.html.

[106] http://camfr.sourceforge.net/principles/index.html.

[107] A. Michon, R. Hostein, G. Patriarche, N. Gogneau, G. Beaudoin, A. Beveratos, I. Robert-Philip, S. Laurent, S. Sauvage, P. Boucaud, and I. Sagnes. Metal organic vapor phase epitaxy of InAsP/InP(001) quantum dots for 1.55âĨ¼m applications: Growth, structural, and optical properties. *Journal of Applied Physics*, 104(4):043504+, 2008.

[108] Richard Hostein. *Étude des propriétés optiques et dynamiques des boîtes quantiques InAsP/InP(001); Application à la réalisation de sources de photons uniques et lasers à cristaux photoniques émettant à 1.5 Âμm. PhDthesis*, 2009.

[109] R. Braive, L. Le Gratiet, S. Guilet, G. Patriarche, A. LemaıÌtre, A. Beveratos, I. Robert-Philip, and I. Sagnes. Inductively coupled plasma etching of GaAs suspended photonic crystal cavities. Journal of Vacuum Science & Technology B: Microelectronics and Nanometer Structures*, 27(4):1909+, 2009.*

[110] Stephan Laurent. Cavité à bande interdite photonique bidimensionelle et application à une source de photons uniques indiscernables. *PhD thesis, 2006.*

[111] F. De Martini, M. Marrocco, and D. Murra. Transverse quantum correlations in the active microscopic cavity. Physical Review Letters*, 65(15):1853–1856, October 1990.*

[112] Paul Barclay, Kartik Srinivasan, and Oskar Painter. Nonlinear response of silicon photonic crystal microresonators excited via an integrated waveguide and fiber taper. Opt. Express*, 13(3):801–820, February 2005.*

[113] Yurii A. Vlasov, Martin O'Boyle, Hendrik F. Hamann, and Sharee J. McNab. Active control of slow light on a chip with photonic crystal waveguides. Nature*, 438(7064):65–69, November 2005.*

[114] Tal Carmon, Lan Yang, and Kerry J. Vahala. Dynamical thermal behavior and thermal self-stability of microcavities. Optics Express*, 12(20):4742–4750, October 2004.*

[115] A. M. Yacomotti, F. Raineri, G. Vecchi, P. Monnier, R. Raj, A. Levenson, Ben B. Bakir, C. Seassal, X. Letartre, P. Viktorovitch, L. Di Cioccio, and J. M. Fedeli. All-optical bistable band-edge Bloch modes in a two-dimensional photonic crystal. Applied Physics Letters*, 88(23):231107+, 2006.*

[116] Virginie Moreau, Gilles Tessier, Fabrice Raineri, Maia Brunstein, Alejandro Yacomotti, Rama Raj, Isabelle Sagnes, Ariel Levenson, and Yannick De Wilde. Transient thermoreflectance imaging of active photonic crystals. Applied Physics Letters*, 96(9):091103+, 2010.*

[117] http://www.ioffe.rssi.ru/SVA/NSM/Semicond/InP/electric.html#Basic.

[118] M. T. Tinker and J. B. Lee. Thermal and optical simulation of a photonic crystal light modulator based on the thermo-optic shift of the cut-off frequency. Optics Express, *13(18):7174+, 2005.*

[119] C. Soukoulis. Photonic Crystals and Light Localization in the 21st Century. *Boston, 2001.*

[120] In-Kag Hwang, Myung-Ki Kim, and Yong-Hee Lee. All-Optical Switching in InGaAsP–InP Photonic Crystal Resonator Coupled With Microfiber. IEEE Photonics Technology Letters, *19(19):1535–1537, October 2007.*

[121] M. Brunstein, A. M. Yacomotti, R. Braive, S. Barbay, I. Sagnes, L. Bigot, L. Le-Gratiet, and J. A. Levenson. All-Optical, All-Fibered Ultrafast Switching in 2-D InP-Based Photonic Crystal Nanocavity. IEEE Photonics Journal, *2(4):642–651, August 2010.*

[122] A. M. Yacomotti, F. Raineri, C. Cojocaru, P. Monnier, J. A. Levenson, and R. Raj. Nonadiabatic Dynamics of the Electromagnetic Field and Charge Carriers in High-Q Photonic Crystal Resonators. Physical Review Letters, *96(9):093901+, March 2006.*

[123] F. Raineri, G. Vecchi, A. M. Yacomotti, C. Seassal, P. Viktorovitch, R. Raj, and A. Levenson. Doubly resonant photonic crystal for efficient laser operation: Pumping and lasing at low group velocity photonic modes. Applied Physics Letters, *86(1):011116+, 2005.*

[124] Jessica P. Mondia, Hong W. Tan, Stefan Linden, Henry M. van Driel, and Jeff F. Young. Ultrafast tuning of two-dimensional planar photonic-crystal waveguides via free-carrier injection and the optical Kerr effect. Journal of the Optical Society of America B, *22(11):2480+.*

[125] Kengo Nozaki, Takasumi Tanabe, Akihiko Shinya, Shinji Matsuo, Tomonari Sato, Hideaki Taniyama, and Masaya Notomi. Sub-femtojoule all-optical switching using a photonic-crystal nanocavity. Nature Photonics, *4(7):477–483, May 2010.*

[126] T. J. Karle, Y. Halioua, F. Raineri, P. Monnier, R. Braive, L. Le Gratiet, G. Beaudoin, I. Sagnes, G. Roelkens, F. van Laere, D. Van Thourhout, and R. Raj. Heterogeneous integration and precise alignment of InP-based photonic crystal lasers to complementary metal-oxide semiconductor fabricated silicon-on-insulator wire waveguides. Journal of Applied Physics, *107(6):063103+, 2010.*

[127] Alain Haché and Martin Bourgeois. Ultrafast all-optical switching in a silicon-based photonic crystal. Applied Physics Letters, *77(25):4089–4091, 2000.*

[128] S. W. Leonard, H. M. van Driel, J. Schilling, and R. B. Wehrspohn. Ultrafast band-edge tuning of a two-dimensional silicon photonic crystal via free-carrier injection. Physical Review B, *66(16):161102+, October 2002.*

[129] J. F. Holzman, P. Strasser, R. Wuest, F. Robin, D. Erni, and H. Jackel. Picosecond free-carrier recombination in indium phosphide photonic crystals. pages 570–573.

[130] Adrian Jacobo, Damia Gomila, Pere Colet, and Manuel A. Matias. All Optical Logical Operations Using Excitable Cavity Solitons. pages 122–123, January 2010.

[131] Li Li, Xinlu Zhang, and Lixue Chen. Optical bistability and Fano-like resonance transmission in a ring cavity-coupled Michelson interferometer. Journal of Optics A: Pure and Applied Optics, *10(7):075305+, July 2008.*

[132] Wonjoo Suh, Zheng Wang, and Shanhui Fan. Temporal coupled-mode theory and the presence of non-orthogonal modes in lossless multimode cavities. IEEE Journal of Quantum Electronics, *40(10):1511–1518, October 2004.*

[133] P. Coullet and N. Vandenberghe. Chaotic self-trapping of a weakly irreversible double Bose condensate. Physical Review E, *64(2):025202+, July 2001.*

[134] K. G. Lagoudakis, B. Pietka, M. Wouters, R. André, and B. Deveaud Plédran. Coherent Oscillations in an Exciton-Polariton Josephson Junction. Physical Review Letters, *105(12):120403+, September 2010.*

[135] P. Gellie, W. Maineult, A. Andronico, G. Leo, C. Sirtori, S. Barbieri, Y. Chassagneux, J. R. Coudevylle, R. Colombelli, S. P. Khanna, E. H. Linfield, and A. G. Davies. Effect of transverse mode structure on the far field pattern of metal-metal terahertz quantum cascade lasers. Journal of Applied Physics, *104(12):124513+, 2008.*

[136] Wilfried Maineult, Pierre Gellie, Alessio Andronico, Pascal Filloux, Giuseppe Leo, Carlo Sirtori, Stefano Barbieri, Emilien Peytavit, Tahsin Akalin, Jean F. Lampin, Harvey E. Beere, and David A. Ritchie. Metal-metal terahertz quantum cascade laser with micro-transverse-electromagnetic-horn antenna. Applied Physics Letters, *93(18):183508+, 2008.*

[137] Gregoire Sevin, Daivid Fowler, Gangyi Xu, Francois H. Julien, Raffaele Colombelli, Suraj P. Khanna, Edmund H. Linfield, and A. Giles Davies. Optimized surface-emitting photonic-crystal terahertz quantum cascade lasers with reduced resonator dimensions. Applied Physics Letters, *97(13):131101+, 2010.*

[138] Nguyen Vi Quynh Tran, Sylvain Combrié, and Alfredo De Rossi. Directive emission from high- Q photonic crystal cavities through band folding. Physical Review B, *79(4):041101+, January 2009.*

[139] Nguyen Vi Quynh Tran, Sylvain Combrié, Pierre Colman, Alfredo De Rossi, and Ting Mei. Vertical high emission in photonic crystal nanocavities by band-folding design. Physical Review B, *82(7):075120+, August 2010.*

[140] Simone L. Portalupi, Matteo Galli, Christopher Reardon, Thomas Krauss, Liam O'Faolain, Lucio C. Andreani, and Dario Gerace. Planar photonic crystal cavities with far-field optimization for high coupling efficiency and quality factor. Optics Express, *18(15):16064–16073, July 2010.*